University of Trento

Faculty of Mathematical, Physical and Natural Sciences

Doctoral School in Physics, XXV Cycle

FINAL THESIS

DEVELOPMENT AND STUDY OF A DENSE ARRAY CONCENTRATION PHOTOVOLTAIC (CPV) SYSTEM

Supervisor

Prof. Roberto S. Brusa

Candidate

Massimo Eccher

ACADEMIC YEAR 2012-2013

Abstract

In the past several years there has been a growing commercial interest in Concentration PhotoVoltaics (CPV) thanks to its promise of low cost electrical power generation. While the technology of CPV using point-focus Fresnel-like optical elements is reaching maturity, the systems based on dense array receivers still need further scientific progress. This thesis explores the field of CPV applied to a parabolic concentrator prototype and to a dense array receiver made of multijunction solar cells.

The solar concentrator, completely designed and built at the University of Trento, is characterized, in order to get the illumination distribution on the PV receiver. The non-uniformity in incident flux results in a current mismatch among cells and strongly impacts the system performance. In order to solve this issue, we have proposed a new type of electrical connection by fitting each cell of the array with an individual DC-DC converter. This method is shown to increase the power transfer efficiency with respect to classical series connection, at least for the tested illumination levels and unbalances. The other main problem with dense array systems is the reliability of the PV receiver, with special attention to the high thermal flux to be dissipated. Several types of water-cooled receivers have been built, with different material configurations that were previously studied with 3D thermal modeling. In particular the building of a multi-cell receiver has required the design of the insulation/interconnection between the cells, the tuning of the cell soldering and the realization of front contact connections.

Acknowledgements

So many people have helped me to accomplish this PhD project that I even don't know where to begin. My heartfelt thankfulness goes to those who have sustained me side-by-side in my daily work: Ale for his brilliant ideas, Marco for the support in any kind of issue, Mariacher and Lea for many precious discussions about physics, Pippa for having solved more than one hitch in front of my PC. I am indebted to all of them. Thanks very much to Emanuele for a long list of things. Of course I have to acknowledge the guidance of my advisor, Roberto S. Brusa, who wanted and made possible this thesis.

Thanks above all to Gianni and Miriana who are inspiration for everything I do. Grazie

Contents

Chapter 1

Introduction

1.1 Why PV in concentration?

The idea of photovoltaics in concentration is about as old as the first activities in flat photovoltaics. Concentrating the sunlight by optical devices like lenses or mirrors reduces the area of expensive solar cells or modules, and, moreover, increases their efficiency. One disadvantage of concentrating photovoltaics (CPV), that is the necessity to track the sun's orbit, is partly compensated by a longer exposition time of the cells during the day.

In the 70s, PV cells were so expensive that the idea of substituting them with optical elements became an attractive option. In 1975 a national program was launched in the USA, led by Sandia National Laboratories (DOE) to develop ideas and concentration photovoltaic prototypes [Burgess and Pritchard, 1978]. Almost every type of concentrating technology was explored during this period, including reflective dishes (Boeing), reflective troughs (Acurex), point-focus Fresnel lenses (RCA, Varian, Motorola, Martin Marietta), linear Fresnel lenses (E-Systems), luminescent concentrators (Owens-Illinois), compound parabolic concentrators (Sun Trac, University of Chicago). System efficiencies for these prototypes ranged from 5% for the reflective trough systems to 10% for point-focus Fresnel systems [Boes, 1980]. In spite of the rapid progress of CPV technologies in the 80s, they played a minor role for more than 25 years. The market was not prepared to build the large facilities that CPV would require, given its little modularity (100 kW) and the need to economically compete at this scale with the energy from conventional power stations. The modularity limit was not strictly related to the CPV concept, but arose from the use of

structures with tracking, which can only be profitable in plants of several kW [Sala and Antòn, 2011] and are not suited for smaller application like roof systems, for example.

It was only recently that a number of companies started to commercialize CPV systems. The main reasons for this development are: 1) PV production and application have grown into a size where larger systems are desirable and 2) high quality III-V semiconductor compounds offer the option of high performance solar cells with efficiencies of more than 40 %, that in the future may reach 50 %.

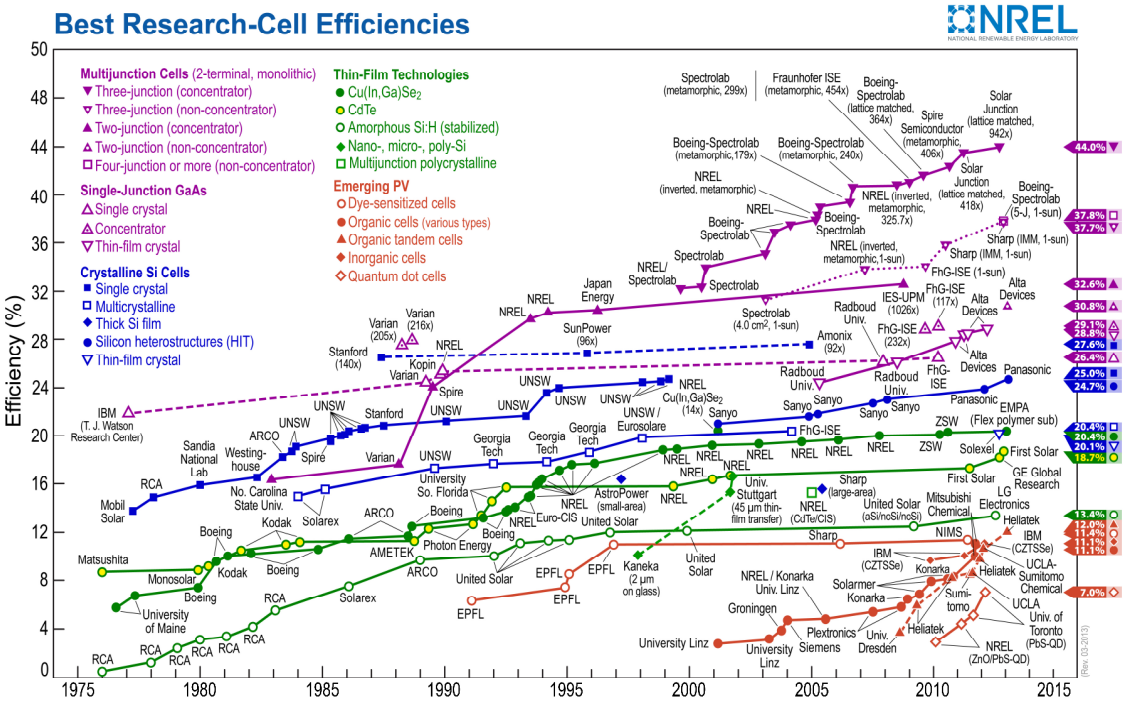

Figure 1.1: historic summary of research-cells efficiency records (http://www.nrel.gov/ncpv/).

Multijunction (MJ) solar cells are currently favored over single junction cells, as they are more efficient, have a better response to high concentration and lower temperature coefficient (lower loss in efficiency with an increase in temperature). Though the cost of MJ solar cells is roughly 100 times that of silicon cells of the same area, the small cell area employed makes the relative costs of cells in each system comparable. In this way efficiency becomes a more important parameter that cost itself. Recently, research-level MJ cells have reached a laboratory efficiency of 44 %, as can be seen in Figure 1.1. Their Si counterpart, made of a high-quality single crystal

material, designed for flat PV modules, has reached a maximum of 25 %.

It can also be outlined that the MJ technology is showing the fastest growing performance among the existing PV cells. This steep cell efficiency trajectory directly results in CPV panel efficiencies close to 40% by the end of the decade. In Figure 1.2 the efficiency of the module considers the efficiency reduction due to optical losses and mismatch problem given by the series/parallel association of the cells. The system efficiency is instead the relationship between the global AC power generated by the system and the incident sunlight energy. There is barely data from modules and systems efficiencies, because very few of them have been published as the companies are reluctant to give any additional information of their products, apart from the electrical parameters. For such reasons, it only can be indicated that the present concentration module efficiency is located in the range of 25–30%, while the efficiency of the present systems is around 25%.

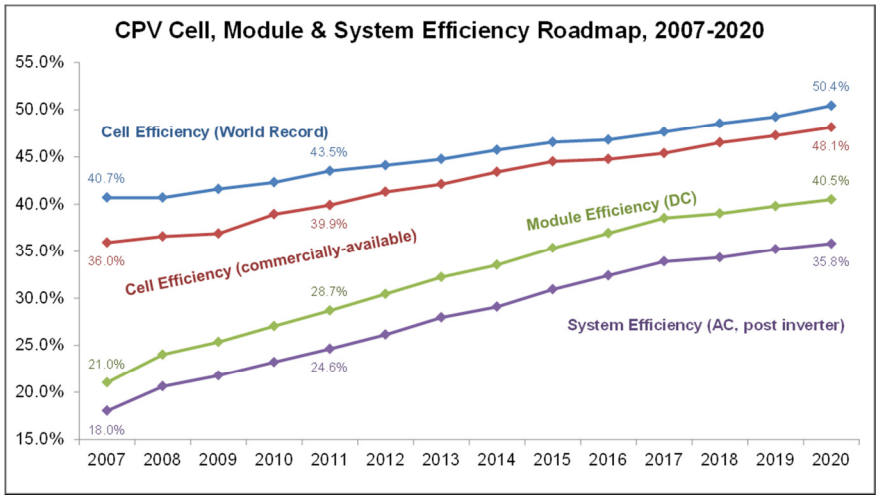

Figure 1.2: CPV cell, module and system efficiency roadmap, 2007-2020 (Source: GTM research, CPV Consortium, October 2011, www.pv-insider.com).

1.2 Current status of CPV

In the last 10 years, the solar industry has broadened up, and the CPV industry is now growing rapidly. With the overall PV market growing in the 30 GWp/y range, the

production of CPV systems has reached a production volume of more than 100 MWp/y (source: 2010-2015 CPV Consortium 2010 Report). The High Concentration Photovoltaic (HCPV, > 300 X) systems have the best perspective on cost reduction in its target market and that's why most of the companies are investing in this technology [Pérez-Higuuras et al., 2011]. The LCOE (Levelized Cost of Energy), which is the cost of 1 kWh from the system during its life time, is probably the most useful measure for comparing and ranking solar installations. For HCPV systems, the LCOE has been reported to vary between 0.14 $/kWh and 0.50 $/kWh [Mokri and Emziane, 2011] and large margins are forecasted. For a comparison, crystalline PV is today around 0.24 $/kWh [Hazlehurst].

Presently about three dozen companies are producing HCPV systems and some companies are working on MW-scale installations. Each has done its own assessment of which designs will find the best trade-off between performance, cost and reliability. In [Zubi et al., 2009] the most important companies developing and commercializing HCPV systems are listed; 15 out of 21 in this list use Fresnel lenses. Currently, the CPV pipeline is dominated by three system manufacturers (Concentrix Solar, Amonix, and SolFocus) that are briefly introduced in the following.

Concentrix Solar

A successful HCPV system using the Fresnel lens is the one commercialized by the German company Concentrix Solar. This company was founded in 2005 as a spin-off aiming to manufacture concentrator systems based on the FLATCON (Fresnel Lens All-glass Tandem cell CONcentrator) technology, which that was initially developed at the Fraunhofer Institute in cooperation with the Ioffe Institute in St. Petersburg.

The developed module uses tiny circular cells of 2.3 mm diameter (Figure 2.2), which are soldered on a copper plate and subsequently glued on a glass sheet. While the other system developers using the Fresnel lens apply a homogenizer device in order to enhance light homogeneity on the cell, the Concentrix lens is designed for use without a homogenizer. Energy amortization time for the FLATCON system has been investigated by the Fraunhofer Institute and is 8-12 months for sunny locations. This is even lower than thin-film PV. While the expected lifetime is 25 years, the company gives a 20 years warranty for its modules (www.concentrix-solar.de).

Amonix

Amonix, Inc. is a company founded in 1989 in California which manufactures CPV commercial solar power systems. In 1994 Amonix developed a 20-kW point-focus Fresnel lens array based on Si solar cell intended for the utility market. It has an innovative integral-backplane module design that greatly reduces the number of parts by incorporating the wiring and cell package as a part of the module back [Garboushian, 1994].

In 2007, the company began incorporating multijunction solar cell technology into its modular design. The Amonix CPV system uses Fresnel lenses with a concentration of 500 X. It is composed of seven proprietary MegaModulesTM, each with 36 acrylic lenses and 36 MJ solar cells. A dual-axis mounting structure tracks the sun throughout the day as the lenses collect sunlight. In July 2012, Amonix set the world record for photovoltaic module efficiency at 34.2% (best measured) and 33.5% (full regression analysis) under nominal operating conditions, verified by the National Renewable Energy Laboratory [Kurtz, 2012].

Solfocus

SolFocus is leading supplier of CPV systems headquartered in San Jose, California. The system developed by Solfocus includes a primary mirror (Micro-Dish), a secondary reflector and a non-imaging homogenizer (Figure 1.3) to focus the direct solar radiation 650 times on a 1 cm^2 III-V cell. The secondary reflector has its shadow on the center of the Micro-Dish, where the cell and the homogenizer are located. One module includes 20 Micro-Dish units, while the system consists of 28 modules mounted on a conventional dual-axis azimuth-elevation tracker. According to [Photon, 2008] the panel efficiency is 25% and the system efficiency is 23%; currently Solfocus declares 29% and 27%, respectively. The 2 percentage points difference include the losses through the inverter and the energy consumed by the tracking system. The company declares that this system provide the lowest levelized cost of energy (LCOE) in high sun regions.

Figure 1.3: Solfocus module showing the micro-dishes and the full system made of 30 modules.

1.3 Motivation of the thesis

The I.d.E.A laboratory at the Department of Physics of the University of Trento entered the field of solar energy in 2006, with the designing and building of a solar concentrator prototype. This concentrator prototype, which tracks the sun along a polar mount roll axis, is basically a portion of a full parabolic dish made of three reflective paraboloidal sectors, having 0.8 m^2 area each. Parabolic dishes have been successfully used in concentration solar power (CSP) applications but they are not so common in concentration photovoltaic (CPV) systems due to the typical Gaussian shape of the generated light profile. Several technical barriers (optical efficiency, sun-tracking, thermal management, light homogeneity, packaging) still remain; some of them are approached in the present work and constitute the core of the thesis.

The first objective of this thesis was the evaluation of the performance of the concentrator, which is required to properly design a PV receiver and which also serves for other solar energy projects. In fact, regardless of the kind of solar energy application, the receiver has to consider the main parameters that define the illumination spot at the focal plane, i.e. the total solar flux, the peak and average power densities, the distribution of the concentrated light and the dimensions of the

spot. These spot properties allow assessing the optical efficiency of the concentrator and give an insight into the quality of the optical components. It follows that the work of characterization is also needed to have an evaluation of the solar modules manufacturing process, which was completely developed by our group [Bettonte et al., 2007].

In CPV systems, the non-uniformity in solar flux incident on the cells results from the inherent optical behavior of the concentrator and due to tracking inaccuracies. This is less of an issue in single optic/single cell systems, as long as optical elements are well aligned and all produce the same incident power on the cells. In dense array CPV systems, the power on the cells can be very different and this is the main reason why most of CPV companies have forsaken the development of dense-arrays in favor of Fresnel-like systems. In fact, the current mismatch among the cells in the array can lead to severe degradation in system performance, as well as danger of cell damage due to reverse-bias operation and overheating. A possible solution is to use a secondary optical element (SOE), which can improve the light homogeneity but which also inflict optical losses. The common method to protect cell from reverse bias damage is to install bypass diodes parallel to each cell. This measure protects cells against damage but does not fully recover the power loss due to current mismatch; moreover this is not practical for the realization of the array itself.

The source for the series mismatch problem is the fact that PV cells typically offer low voltage (around 3 V for III–V multijunction cells), and therefore need to be connected in series to produce an overall high voltage of the module. We propose a different approach to solve the problem of current mismatching, which consist in using two new types of electrical connections for the cells. These type of connections have the advantage of making unnecessary the SOE (or at least of limiting the restriction on the its design) and the bypass diodes. We want to demonstrate that these connections, making use of DC-DC converter modules, can increase the power transfer to the load with respect to an array realized with series or parallel connections.

The realization of the photovoltaic receiver is another main issue in CPV systems. A dense-array receiver is basically a parquet of solar cells, which has to be arranged in way of reducing the spacing between the cells. While single cells typically only need passive cooling, densely packed modules present greater problems for cooling

because each of the cells only has its rear side available for heat sinking. This means that, in principle, the entire thermal load must be dissipated in a direction normal to the module surface. This generally implies that passive cooling cannot be used in these configurations at their typical concentration levels. The selection of materials for the receiver (hosting the PV cells) has to satisfy both the requirement of low thermal resistance, electrical insulation and release of thermo-mechanical stress that may break the cells. The aim of the present work was to understand which material are good candidate for the cell-to-sink interconnect. The building of a working CPV receiver implies to take special care to the tuning of the cell fixing and to the realization of the front contact interconnections between the cells. All these issues must to be dealt since they seriously impact the reliability and the performance of a CPV dense array. In the current state of development we are not interested in building an optimal receiver in terms of light collection efficiency (spacing between cells and between connections), but we want to realize a device that allows performing consistent test operations for an array of MJ cells under concentration. This way the goal is to build a quite robust receiver that will stand several working cycles under outdoor operation and that will prevent cell heating.

1.4 Outline

Chapter 2

The primary types of concentrators and the main features to consider for the design of a CPV system are discussed. These characteristics include the type of optic, the concentration level and the type of sun-tracking. A more detailed explanation of the parabolic concentrator geometry is given. Finally, our parabolic concentrator prototype and the process to realize the solar modules are described.

Chapter 3

Solar collectors quality is dependent on the reflectance properties of the mirror

material in addition to the durability and geometrical deviations from the designed shape. In the first part of this chapter some characterization methods that have been used for CPV concentrators are presented. The experimental work to evaluate the performance of our solar collector is then reported. In particular we have measured the reflectance properties of the mirror, the illumination profile and the total power at the focus plane. To measure the optical efficiency of the collector, a flat plate calorimeter was built.

Chapter 4

Multijunction (MJ) solar cells made of III-V materials are the most suitable devices for CPV applications, since they have the highest efficiencies and the best response to high temperatures. The concept beneath the MJ approach, which is basic to understand what is required for the building of dense array PV receivers, is here presented. After that, the characteristics of the Spectrolab MJ cells we have used are described. The current-voltage curves at different illumination levels for one of these cells have been measured in the concentrator system.

Chapter 5

This chapter is focused on the solution of the cell current matching problem, which is typical for CPV dense array systems. The effects of current mismatch are firstly exposed and a theoretical analysis for a mismatched multi-cell array is made. Two new types of electrical connections are proposed, making use of DC-DC converter modules. They have the advantage of a non-zero number of degrees of freedom (as regard to electrical working point of the cells), oppositely to parallel or series connection. These two types of connection are compared with classical connections with some examples of operative conditions.

Chapter 6

The subject of this chapter is the experimental proof of the new type of connection (2^{nd} type), that was already predicted in Chapter 5. The first experiment here presented has been performed indoor and made use of devices that have PV cell-equivalent circuit. The second experiment has been performed with PV cells under non-uniform

concentrated solar light. The comparison with the I-V for the series connected circuit shows the potential advantages, in terms of electrical power delivered to load, given by the new type of connection.

Chapter 7

The present chapter treats the thermal management of a dense array CPV receiver; the effects of the heat on solar cells and the thermal behavior of different material for the subcomponent are introduced. The different types of receiver and material configurations are analyzed with a 3D thermal modeling. In the last part our trials to build a working multi-cell assembly are presented, with a description of the whole manufacturing process we have developed.

Chapter 2

Concentration PhotoVoltaic (CPV) systems

2.1 Introduction

A photovoltaic concentrator always has two main and elements: a collector, capable of redirecting the rays of the sun towards a smaller area, and a special solar cell receiving the concentrated sunlight. There are systems sometimes called concentrators that use flat mirrors to intensify the light onto conventional panels, but they won't be handled in the present chapter.

This chapter relies on the characteristics of a CPV system that are not proper of the PV converter, that are the type of optic, the concentration level and the type of sun-tracking. The main objective is to provide a basic understanding of these characteristics. Firstly, in Section 2.2, the primary types of concentrators are discussed as regard to the main features to be considered for the design of a CPV system. In Section 2.3, some theoretical concepts are introduced: the thermodynamical limit of concentration, the definition of optical efficiency and the reflective parabolic design. In section 2.4, the parabolic concentrator prototype designed and built at the University of Trento (Department of Physics) is described. The optical components of this concentrator are reflective parabolic modules that could be assembled in a full dish. Their method of construction (patent [Bettonte, 2007]) is the subject of Section 2.5.

2.2 Basic types of concentrators

The PV concentrators have many more characteristic parameters than the flat modules, and they can be classified under many more possible criteria. For example they can be roughly divided in two main categories with respect to the concentration level they achieve:

i) High concentration (>300 X, HCPV) point point-focus systems with highly efficient III-V cells (>35%) and with a high specific cost.

ii) Low or medium concentration (2-60 X) with silicon cells of up to 20-22% efficiency and at low cost.

Beyond this, concentrators may be classified depending on the optical means used to concentrate the light, the number of axes of the tracking of the sun, the mechanical mechanism that affects the tracking, and so on. The major types are here discussed, and the basic features are described.

2.2.1 Types of optic

Refractive lenses or reflective dishes and troughs are the classical types of optics that are used in concentrators. In case of reflective optic, Fresnel lenses are usually chosen, since conventional spherical lenses would be too thick and costly to be practical. This type of lens reduces the amount of material required compared to a spherical lens by dividing the lens into a set of concentric annular sections (flat or curved), resulting into a thinner profile. Fresnel lenses may be made either point-focus, in which case they have circular symmetry about their axis, or linear focus, in which the lens has a constant cross section along a transverse axis. Point-focus lenses usually use one cell behind each lens (see Figure 2.1 a), whereas line-focus lenses have a linear array of cells (Figure 2.2 b).

The most used material of choice for the lens is usually Acrylic plastic (polymethyl methacrylate, PMM), which molds well and has shown good weatherability. Nevertheless, there remain some long-term durability concerns for PMMA, and so attempts to make the lens from glass have been made.

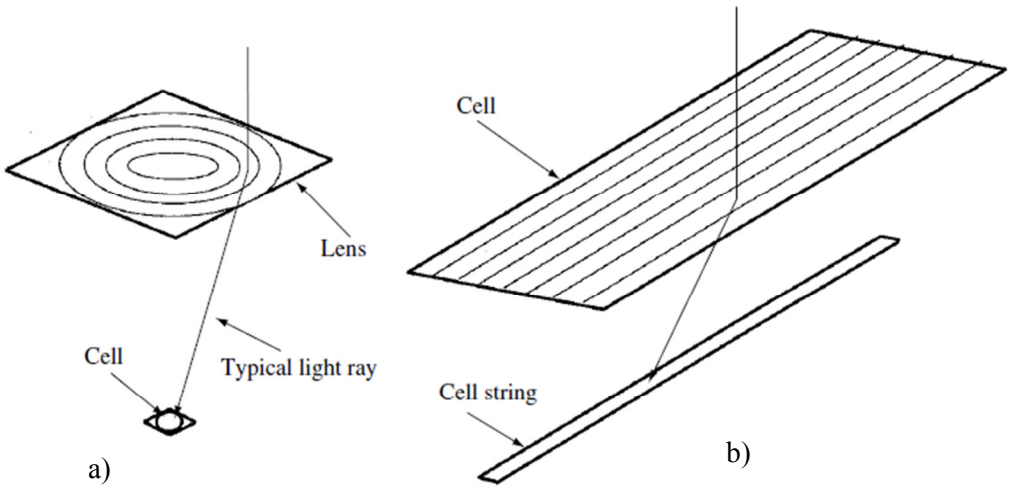

Figure 2.1: basic Fresnel lens configuration: a) point focus and b) linear Fresnel lens.

Fresnel lenses are usually incorporated into modules that contain multiple lenses in parquet, a housing to protect the backside of the lens, and the cells. The cell may incorporate a secondary optical element (SOE) whose purpose is to further concentrate the light or to make the image more uniform. The picture of Figure 2.2 shows a concentrator module with Flatcon^{R} technology developed at the Frauenhofer Institute (Freiburg, Germany), whose lenses are designed to work without secondary optics.

Nowadays Fresnel lens is the most applied CPV optics (see for example the 800 kW installation of Sol3g in Flix, Terragona [www.sol3g.com] or the Flatcon^{R} system commercialized by Concentrix Solar [Bett et al., 2005]). Amongs the advantages of Fresnel type system, we find the light homogeneity between the cells, the possibility of using passive cooling and, given the large space between the cells, the ease of

Figure 2.2: Flatcon^{R} module filled with smoke to visualize the cone of light from each Fresnel lens to the cells [Jaus et al., 2006].

assembly (electrical connection, soldering of the cells and bypass diodes).

The alternative to refractive lenses is to use reflective mirrors. A reflective surface with the shape of a parabola will focus all light parallel to the parabola's axis to a point located at the parabola's focus. Like lenses, parabolas come in a point-focus configuration (which is formed by rotating the parabola around its axis and creating a paraboloid) and line-focus configuration (which is formed by translating the parabola perpendicular to its axis). These configurations are illustrated in Figure 2.3.

The illumination spot produced by a parabolic dish has to be absorbed by a dense array receiver in which several III-V cells are integrated. Due to the larger focus, active cooling is necessary. In theory, useful heat could result here, but taking into account that a low receiver temperature improves efficiency and cell operating conditions, the cogeneration options shrink. The limits of combining power and heat generation in PV systems are detailed in [Photon International, 2008]. The advantages of grouping the III-V cells lie rather in the more advanced management that can be assumed for a receiver with respect to a single cell. If properly engineered, this can be transformed into an efficiency and reliability advantage. To our knowledge, anyway, at now no CPV systems based on parabolic dish have demonstrated efficiency and reliability advantage.

2.2.2 Concentration ratio

There is not a unique definition of concentration ratio in use. There are several definitions of concentration ratio in use. The most common is *geometric concentration ratio* (X). This is defined as the entrance aperture (area of the primary lens or mirror, A_{conc}) divided by exit aperture (area of the receiver, A_{rec})

$$C = A_{conc}/A_{rec} \tag{2.1}$$

When a single cell is used, the exit aperture is the active cell area, which is the region of the cell that is designed to be illuminated. Unlike in most non-concentrating systems, the entire cell need not be illuminated by the primary lens; in fact the non-illuminated edge of the cell is often provided with busbars for electrical connection, and this need not result in an efficiency loss as would be the case in a flat-plate module.

Another measure of concentration is *intensity concentration* (suns). Since standard peak solar irradiance is often set at 1000 W/m^2, the concentration expressed in suns is defined as the ratio of the average intensity of the focused light on the cell active area divided by 1000 W/m^2 (0.1 W/cm^2). For example, if 10 W were focused onto a cell of 2 cm^2 active area, the intensity concentration would be 50 suns. In actuality, whereas the global solar flux is often close to 0.1 W/cm^2, the direct solar flux is typically less.

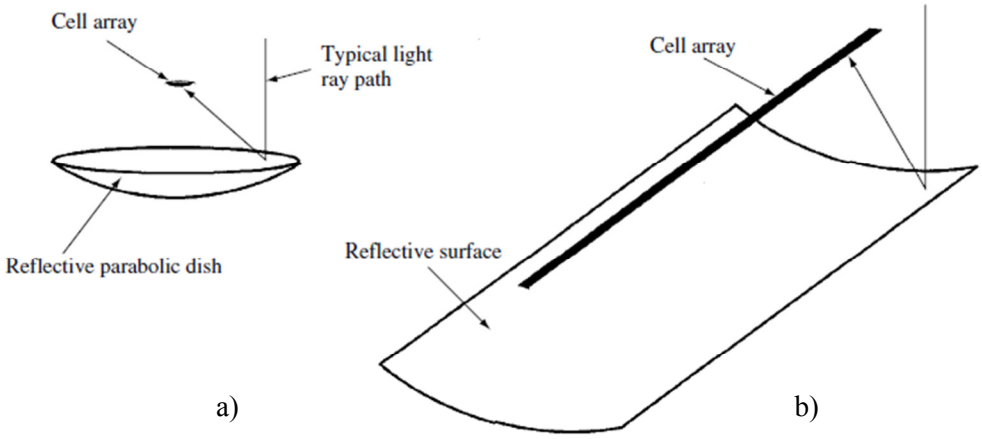

Figure 2.3: Reflective cocentrator configurations; a) paraboloiid or parabolic dish, b) linear parabolic trough.

The difference is the radiation that is scattered by the atmosphere or clouds, and comes from directions other than the sun (diffuse solar flux). Typically, the direct radiation is around 0.085 W/cm^2 on a clear day, so many concentrator systems are rated at this level, i. If the lens had a transmission of 85%, then the intensity concentration would be 0.85 $\times$ 0.85 = 0.72 of the geometric concentration. In the above example the cell would be illuminated at 36 suns.

2.2.3 Types of tracking

Even if it possible to provide some concentration without sun-tracking, tracking is needed for medium and high concentration systems. The optics in CPV modules accept the direct component of the incoming light and therefore must be oriented appropriately to maximize the energy collected.

In case of point-focus optics, the optical components are generally required to track

along two axes in order to be always pointed at the sun. From a mechanical standpoint, two-axis tracking is more complex than one-axis tracking; however, point-focus systems can obtain higher concentration ratios and thus lower cell cost. Line-focus reflective troughs need only track along one axis such that the image falls along the focus line. Linear Fresnel concentrators suffer severe optical aberrations when the sun is not perpendicular to the lens' translation axis. This generally limits linear Fresnel systems to two-axis tracking.

The two main categories of two-axis trackers are shown in Figure 2.4. The pedestal form showed in Figure 2.4 (a) uses a central pedestal supporting a flat tracking array structure. Tracking is usually effected by a gearbox, which tracks the array along a vertical axis (the azimuth rotation) and along a horizontal axis (the elevation rotation). The other form of two-axis tracking is the roll-tilt structure of Figure 2.4 (b). The roll

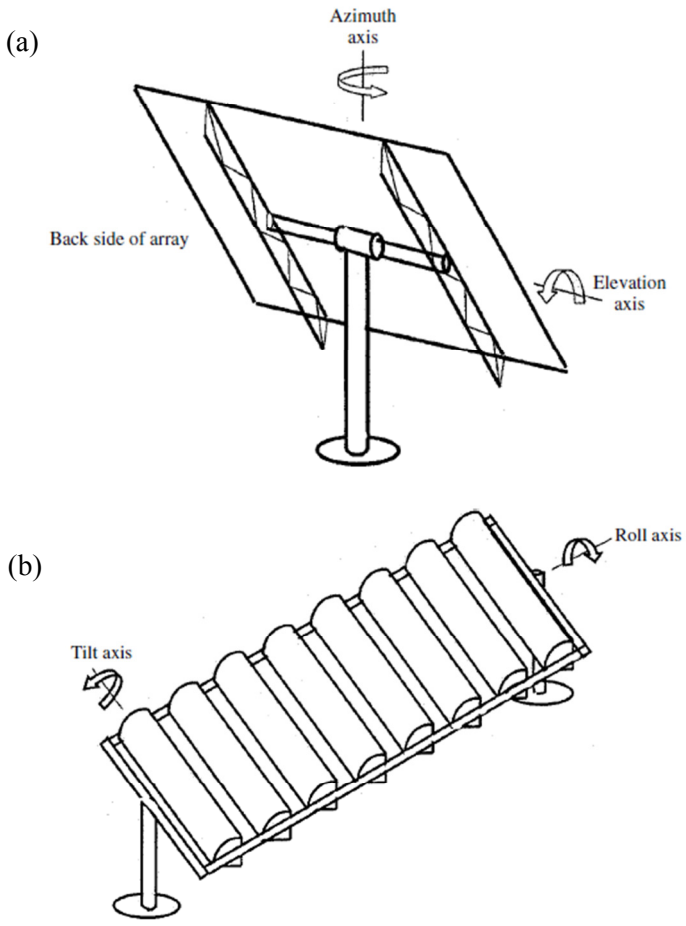

Figure 2.4: two-axis trackers; (a) pedestal arrangement and (b) roll-tilt arrangement.

axis is usually placed in a north–south direction, as this minimizes shadowing by adjacent modules along the roll axis. The selection of tracker type is dependent on many factors including installation size, land constraints, latitude, wind loads and ease of installation [Swanson, 2003].

2.3 Concentration concepts

2.3.1 Thermodynamic limit

One of the remarkable theorems of non-imaging optics is that there exists a relationship between the maximum angle that is accepted by the concentrator and the maximum concentration that is obtainable, $C_{\max}$. Consider the schematic representation of a concentrator Figure 2.5. The light that hits the entrance aperture, of area A_{conc}, at an angle less than $\theta_{max,in}$ from the normal is transmitted to the exit

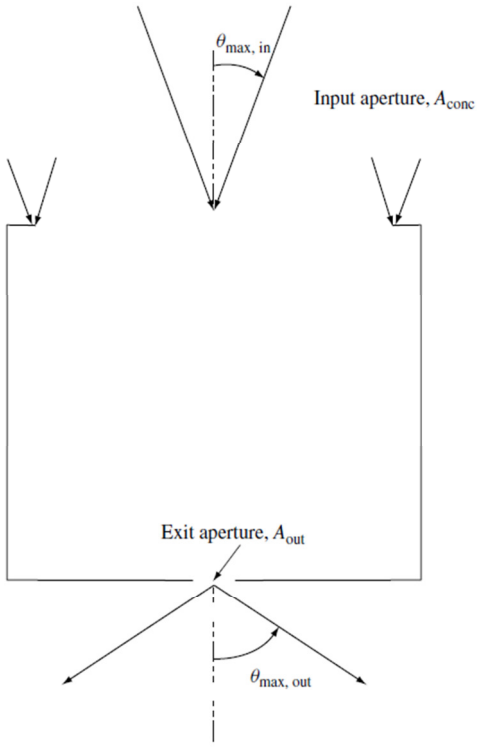

Figure 2.5: schematic representation of a generalized concentrator.

aperture where the receiver of area A_{rec} is located (PV cells in our case), emerging at an angle less than $\theta_{max,out}$ to the normal of the receiver. For two-axis, or three-dimensional, the following relationship holds for the geometrical concentration:

$$C = A_{conc}/A_{rec} \leq C_{max} = \sin^2(\theta_{max,out})/\sin^2(\theta_{max,in}) \quad (2.2)$$

which, by considering the Snell's law of refraction, becomes

$$C = A_{conc}/A_{rec} \leq C_{max} = n^2\sin^2(\theta_{max,out})/\sin^2(\theta_{max,in}) \quad (2.3)$$

if the receiver is immersed in a dielectric medium of index of refraction n [Sala and Anton, 2011]. A concentrator that achieves this maximum is called an *ideal* concentrator. The maximum it could be is 90◦, but angles approaching this result in many rays striking the receiver at grazing angles. This may prove impractical, since such rays are prone to have high reflectance and can easily miss the target owing to mechanical alignment errors. The above equation, for $\theta_{max,out}$ = 90° becomes[1]

$$C = \frac{A_{conc}}{A_{rec}} \leq C_{max} = n^2/\sin^2(\theta_{max,in}). \quad (2.4)$$

If one designs a concentrator that accepts as a maximum input angle the half angle of the sun as seen from the Earth, 0.27°, then it could have a maximum concentration of about 45 000. Interestingly, the concentration of 40 000 restores the radiative power density at the receiver to that at the surface of the sun. If we assume to have a hot spherical radiator (the sun) that is radiating black-body radiation, and an insulated black body as receiver, a simple proof of the above equations can be derived [Swanson, 2003].

2.3.2 Optical efficiency

Not all the light captured by a real concentrator reaches the solar cell: a part of it is lost. We define the *optical efficiency* as:

[1] The designers, however, recommend not to design concentrators with very large exit angles just to gain higher concentration ratio.

$$\eta_{op} = \frac{P_{rec}}{P_{conc}} \tag{2.5}$$

where P_{rec} is the light power on the receiver and P_{conc} is the light power at the entrance of the concentrator.

By considering Equation 2.1, we have

$$\eta_{op} = \frac{I_{rec}\, A_{rec}}{I_D\, A_{conc}} = \frac{I_{rec}}{I_D\ C} \tag{2.6}$$

where I_{rec} is the average irradiance on the receiver surface (on W/m^2) and I_D is the direct normal irradiance.

The values of the optical efficiency of the normal systems are not usually more than 85%. It is a fundamental parameter because it influences both the efficiency of the cell and the cost of the system. The η_{op} values falls as the number of interfaces that the light has to cross is increased; for example for each air‑glass interface that the light crosses, the power is reduced to 96%, the reflections on the aluminum are reduced by 85% and with silver by 90%.

2.3.3 The parabolic concentrator

In Figure 2.6 is shown a scematic for a reflective parabolic concentrator, which could represent the cross section of either a two-dimensional linear parabolic trough or of a three-dimensional paraboloid of revolution.

The equation relating the x and y components of the parabolic surface is $y = 1/4\ \ F\ x^2$, where F is the focal length of the parabola. It can be shown that all the incoming rays with no x-component will pass through the focus. If D is the diameter or width of the parabola, then this can be written in the normalized form

$$\frac{y}{D/2} = \frac{1}{8\,f} = \left(\frac{x}{D/2}\right)^2 \tag{2.7}$$

where $f = F/D$ is called the f -number of the parabola. Note that if $f = 1/4$, then when $x = D/2$, that is, at the rim of the parabola, $y = D/4 = F$. In other words, for an $f = 1/4$ parabola, the rim height is equal to the focal length.

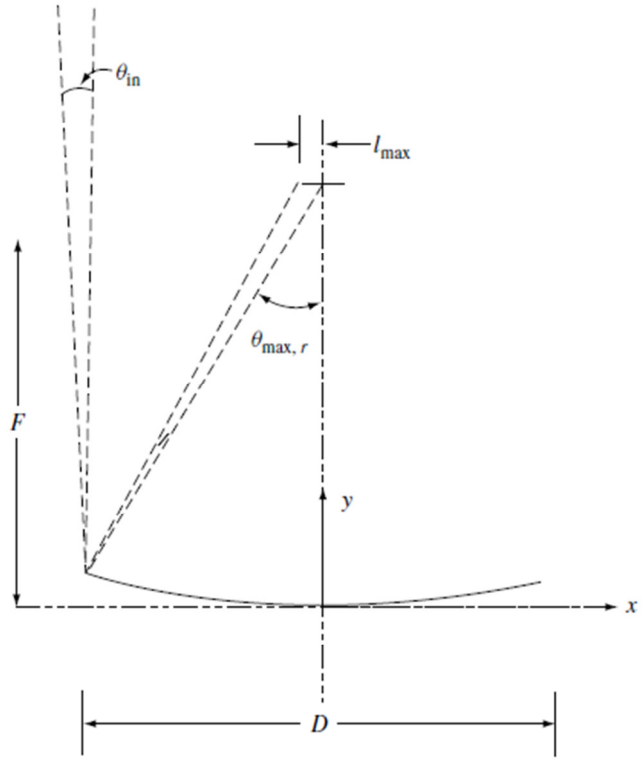

Figure 2.6: cross section of a parabolic reflective concentrator.

Obviously the slope at the rim is then 45◦. Another useful relation that relates the distance from the focus to the parabolic surface, r, to the angle that the ray hits the receiver, θ_r, is

$$r = \frac{2\,F}{1\,+\,cos\theta_r} \tag{2.8}$$

and

$$x = r\,sin\theta_r = \frac{2\,F\,sin\,\theta_r}{1\,+\,cos\,\theta_r}. \tag{2.9}$$

From this we can see that at the rim, when $x = D/2$ and the angle of rays at the receiver is maximum, we have:

$$f = \frac{F}{D} = \frac{1}{4}\,\frac{1\,+\,cos\,\theta_{max,r}}{sin\,\theta_{max,r}} \tag{2.10}$$

Now consider a ray that arrives at a small angle θ_{in} to the normal axis. It can be calculated that it will intercept the receiver at a distance *s* from the focus given by

$$s = \frac{r \sin \theta_{in}}{\cos \theta_r} = \frac{2 F \sin \theta_r}{\cos\Theta_r (1 + \cos \theta_r)} . \tag{2.11}$$

This shows that *s* increases as one moves toward the rim, increasing θ_{r}. Clearly, the rays hitting the rim at $x = D/2$ will have the largest *s*. Noting that the total receiver size, S, required to capture all rays up to incident angles of $\pm \theta_{\max,in}$ is $S = 2\, s_{\max}$, gives

$$S = \frac{4 F \sin \theta_{max,in}}{\cos \theta_{max,r} (1 + \cos \theta_{max,r})} = D \frac{\sin \theta_{max,in}}{\cos \theta_{max,r} \sin \theta_{max,r}}. \tag{2.12}$$

For a three-dimensional paraboloidal concentrator, the concentration ratio is $C = (D/S)^2$, giving

$$C = \cos^2 \theta_{max,r} \left(\frac{\sin \theta_{max,r}}{\sin \theta_{max,in}} \right)^2 \tag{2.13}$$

which at rim angle of 45° becomes

$$C = \frac{1}{4} \left(\frac{1}{\sin \theta_{max,in}} \right)^2 . \tag{2.14}$$

This gives a concentration ratio of 10000 for a perfect paraboloid having $f = 0.6$.

Parabolic dishes are thus capable of quite high-concentration ratios. In practice, slope errors, or waviness in the reflective surface, degrade the performance. This can be analyzed to first approximation by realizing that a slope error of value θ_s will cause the reflected ray to deviate from the intended path by $2\,\theta_s$, and this will add to the angle of arrival $\theta_{max,in}$. A high-quality paraboloid for solar concentration use might have θ_s = 1/8° [Swanson, 2003], thus doubling the divergence of light from the sun from 1/4° to 1/2°. This has the effect of decreasing the concentration by one-fourth, to 2500.

Parabolic concentrators are more highly developed for solar thermal applications in which high temperature is desired and flux uniformity is not so big an issue as with As a matter of facts, reflective dishes can achieve higher concentration than desired

for PV receivers. There is no need for secondary optics s to increase concentration, so in caso of CPV systems, the concentration ratio is usually sacrificed to achieve flux uniformity and pointing tolerance. One method of doing this is the kaleidoscope flux homogenizer. This is simply a box in front of the receiver having internal reflecting walls. The incoming rays are scrambled by reflecting several times and are distributed relatively uniformly over the receiver ([Verlinden et al., 1991]).

2.4 The parabolic concentrator at the University of Trento

Some years ago at the University of Trento (Department of Physics) we built a solar concentrator prototype, which is a part of a full parabolic dish. The ideal paraboloidal surface corresponds to a full dish of 5 m in diameter and is defined by the equations:

$$z = a \cdot \sqrt{(x^2 + y^2)} \tag{2.15}$$

and

$$(x^2 + y^2)^{\frac{1}{2}} \leq 2500 \tag{2.16}$$

with its vertex in x = 0, y = 0, z = 0, a = 10^{-4} mm^{-1}, x, y, z are given in mm and the focal point is located at the position (0, 0, 2500 mm). For this paraboloid number f = 0.5 and rim angle $\theta_{max,r}$ = 53.13°; from Equation 2.13 the maximum concentration would be C = 9216 .

Presently the concentrator is made by three reflective parabolic sectors that can be disassembled and that have angular width of 15°; they are described in Paragraph 2.3. The overall prototype appears like in Figure 2.7. The apparatus is oriented with the x-y plane perpendicular to the incoming sunrays, and thus each sector has an ideal intercepting area of 0.818 m^2.

2.4.1 Tracking

The three sectors (see Figure 2.7) are mounted on a metal frame fixed to a roll axis,

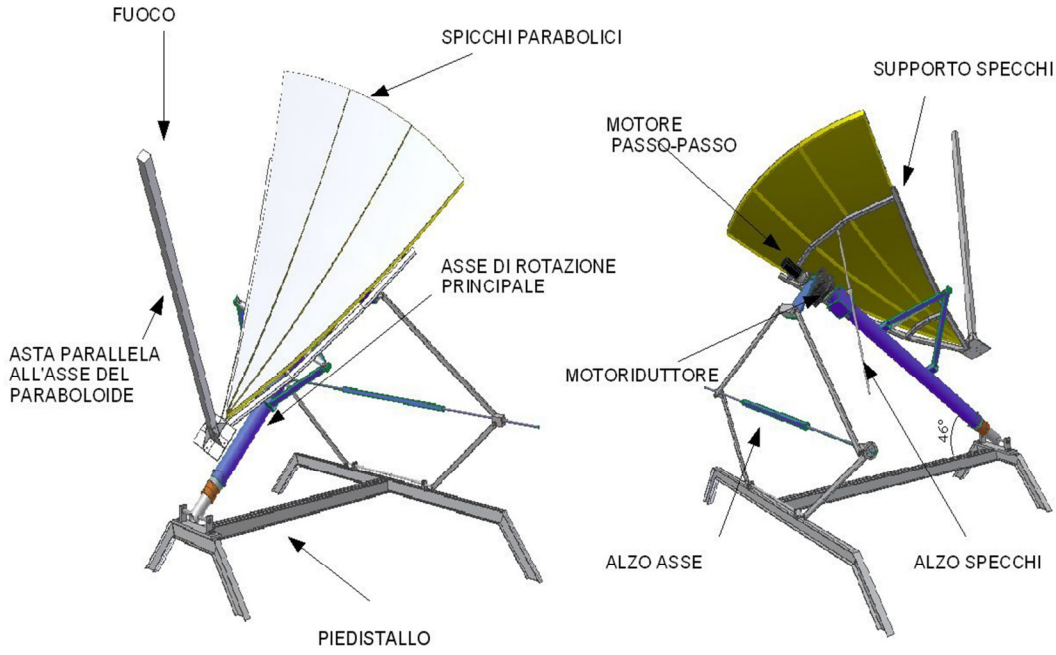

Figure 2.7: schematic representation of the concentrator prototype built at the University of Trento. Some components are shown: the parabolic sectors on the metal frame, the roll axis, the tilting screw, the stepping motor and the shaft supporting the receiver.

which is the main axis of tracking. The roll axis is placed in the north–south direction, and the elevation angle is such that the roll axis is parallel to the Earth axis (polar mount). This angle is of about 46°, as it is shown on Figure 2.7.

The tracking of the sun's position is effected by a chronological tracker, which counteracts the Earth's rotation by turning at an equal rate as the earth, but in the opposite direction. Actually the rates aren't equal, because as the earth goes around the sun, the position of the sun changes with respect to the earth by 360° every year or 365.24 days. The drive method may be as simple as a gear motor that rotates at a very slow average rate of one revolution per day (15° per hour which corresponds to 0.00417°/sec).

Our tracking is achieved with a stepping motor *Oriental Motor PK2913-E4.0T* which needs about 400 steps to realize a full rotation. Two reduction mechanisms (*Bonfiglioli*) with reduction 1:10000 are connected to the stepping motor, resulting in a theoretical resolution of the tracking of $360°/(400 \cdot 10^4) = 0.00009°$. The main limitation to this is the mechanical play of the reduction mechanism.

The daily elevation adjustment of the paraboloid section is made by means of

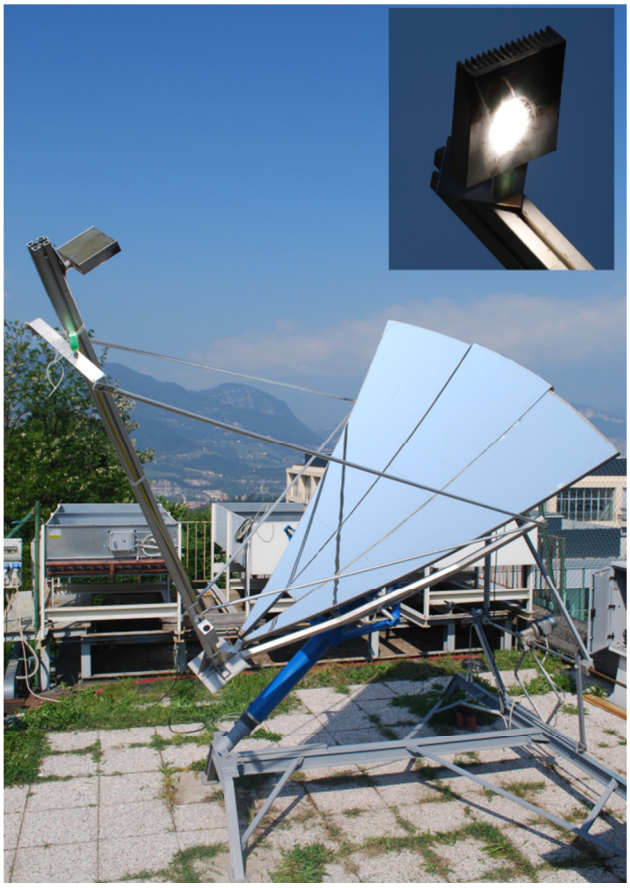

Figure 2.8: picture of the concentrator prototype. The image in the upper frame shows the illumination spot on the receiver.

regulation screw that allows lifting the sectors' frame from the roll axis. Throughout the course of a year the total tilting is of ± 23.5° with respect to the main roll axis, and thus the average variation per day is of 0.128°. The pointing to the sun of the concentrator is manually made by means of a pyroheliometer mounted on the shaft which supports the receiver. The latter has an optical channel which allows correctly pointing the pyroheliometer to the sun. We assume that the concentrator is pointed when the pyroheliometer is pointed. As a final stage, some supporting screws, onto which the sectors are endorsed, allow adjusting the elevation of each sector, in order to concentrate the sunlight in the same region around the sun. In Figure 2.8 is reported a picture of the pointed concentrator and the illumination spot produced at the focus.

2.5 Solar reflective modules

Concave mirrors are called "converging" because they tend to collect light that falls on them, refocusing parallel incoming rays toward a focus. We adopted silvered mirror as reflective material as it combines both high reflectance and good mechanical properties (Poullikkas et al., 2010). Compared with other mirror types, it is preferred for its high reflectance, good specularity, durability, and resistance to distortion from loads.

Despite these advantages, glass is heavy and brittle, requiring massive structural support (SERI, 1985). A good candidate as a structural material with proven rigidity under severe weather conditions is fiberglass. Fiberglass supports formed over a mandrel have been incorporated by Kansas Structural (Gill and Plunkett, 1997) and McDonnell Douglas (NREL, 1998).

Some of most promising results in the construction of solar concentrator mirror facets have been obtained with sandwich construction. In sandwich construction, membranes such as metal or plastic sheets are bonded to the front and back of a core material, and glass mirrors are bonded to one of the membranes (Stone et al. 1993, Shertz, 1986). This construction has the advantage of high strength-to-weigh ratios.
The manufacturing process, here described, is based on the sandwich approach using a PVC panel as a core material, with fiberglass as a back membrane and the glass as a front membrane. Beyond the good optical characteristics, our objective is to develop a solar concentrator module with reasonable material cost, durable and suitable to be used for a mass production. It can be emphasized that this process is not related to a particular curvature or shape of the modules, so it can be applied to different modules types. When facet have to be assembled in a dish, mirror curvature can be parabolic (Johnston, 1995), flat (Kussul and Beidyk, 2008) or spherical (Lovergrove et al., 2010), and different shapes of the modules can be used. We have used manufacturing process to construct sectors of a parabolic dish with a collecting surface of about 0.8 m^2 . The selection of the mirror shape was intended to use identical modules, with relatively large area in order to reduce surface discontinuities between a module and the adjacent module.

2.5.1 Manufacturing process

The dish, defined by Equation 2.15 and 2.16, has been ideally divided in 24 identical basic sectors (modules), every sector having angular width of 15° and 0.818 m^2 nominal area normal to the z axis (net aperture area).

The process to manufacture the modules makes use of a mould made of resin. The lodging wall of the mould is convex and consists of a slice portion of a round paraboloid with upward-directed convexity. The mirror surface will acquire the shape of this wall, so great care must be applied in the refining of the mould. Each parabolic sector was manufactured by shaping a starting plane mirror and a support material in a unique process, resulting in a single composite piece with the desired curvature and continuous reflective surface. The first step to produce a module is the arrangement of a flat 0.8 mm thick silvered mirror (FAST GLASS®) onto the mould, with reflective surface turned towards said convex wall. Afterward, structural layers are deposited above the mirror in the following order: a fiberglass layer, a PVC panel and another fiberglass layer. An alternative module has been successfully produced by substituting the PVC panel with a parabolic-curved wood panel. Shaped thin still plates were inserted in the PVC panel to add stiffness to the whole structure and to help the maintenance of the curvature over time. This has been made in the wood panel, too, by previously curving some transversal and longitudinal fissures.

Figure 2.9: the parabolic sector placed in the mould and inserted in the plastic bag.

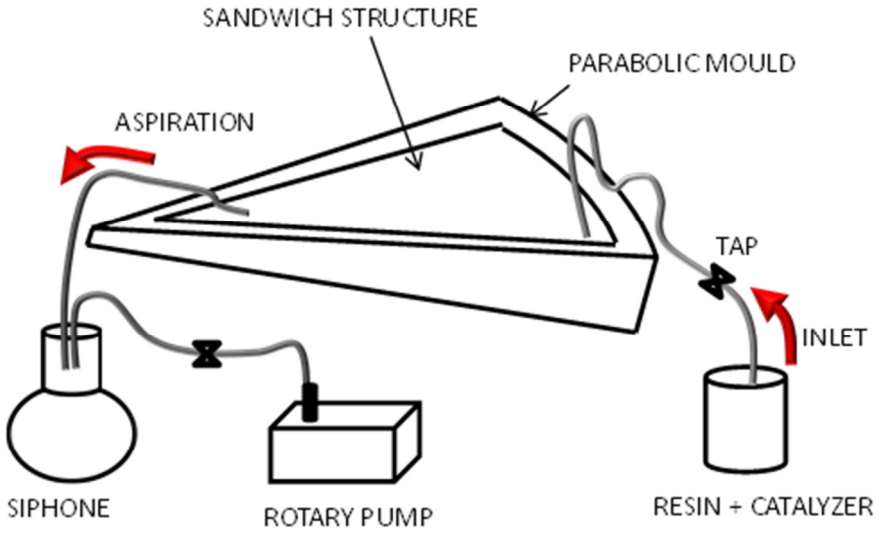

Figure 2.10: representation of the rosin infusion process.

The mould is then inserted inside a soft plastic bag connected to a rotary pump in order to create vacuum (see Figure 2.9). When an adequate vacuum (3 mbar) is reached, the difference from internal and external pressure is used as uniform force which shapes the layers against the mould surface. The same difference of pressure is used to insufflate into the fiberglass matrix a thermosetting epoxy resin; for such purpose, the non-rigid container is placed in communication, through an inflow line, with a resin tank (see Figure 2.10). The fluid resin, filling the non-rigid container, penetrates into the porous fiberglass and glues the stiff PVC layer to the mirror back-surface. The reduced pressure created inside the bag has the advantage of ensuring a gradual and uniformly distributed shaping of the mirror. A siphone has been placed at the end of the aspiration tube in order to protect the pump from resin contamination.

After about 14 hours the manufact is heated by means of warming stripes at ~70° for about 6 hours. The parabolic sector is extracted from the mould when the hardening of the resin, that requires some hours after the end of the infusion, is completed. More details about the different steps of the process are described in the patent [Bettonte et al., 2007].

The manufacturing process satisfies two fundamental requirements for the concentration systems: the good optical quality of the resulting reflector and its reproducibility. In fact five out of six of the built sectors have shown the same optical

characteristics, whereas the remainder has resulted faulty due to the breaking of the plastic bag during the infusion of the resin. In the latter case, rupture was due to the smaller dimensions of the wood panel with respect to the lodging of the mould.

Chapter 3

Characterization of solar collectors

3.1 Introduction

Lack of regulation and standardized specification has led designers to use their own procedures to characterize the optical system for photovoltaic applications. Some difficulties in the characterization procedure are related to the use of materials with unknown optical properties. Lens and mirror manufacturers do not provide some of the parameters needed for the design of a CPV system, or the specifications are not adapted to the designs of photovoltaic concentrators. The solar concentrating prototype designed and built at the Department of Physics at the University of Trento, has been conceived for working both with a dense array PV receiver and with a CSP absorber. In both cases energy conversion efficiencies strongly depend upon the optical properties of the reflective materials and the optical quality of the manufactured elements, which determine the amount of sunlight reflected onto the receiver. This performance is influenced by the sun shape, reflector quality, tracking accuracy, and location of the solar energy plant. Reflector quality is dependent on the solar-weighted reflectance and specularity of the mirror material in addition to the durability and geometrical deviations from the designed shape. These deviations can be of different type, such as surface waviness due to manufacturing process, shape errors of the module, structural distortions due to wind and gravity, alignment errors [Guven and Bannerot, 1985]. The shape errors affect the optical efficiency and the intercept factor, which are introduced in the following.

In the first part of this chapter, Section 3.1, some characterization methods that have been used for concentrator photovoltaic applications are presented. Some of them have been adopted from other applications, since solar collector can be used for concentration solar application (CSP), too. Then the experimental work to evaluate the performance of our solar collector is reported. In particular we have measured the reflectance properties of the mirror material, the shape of the illumination profile e and the total power impinging on the receiver. To perform the last measurement a flat plate calorimeter was built and then a thermal balance study was carried out.

3.2 Optical performance: theory and testing procedures

3.2.1 System preparation

The optical quality of an individual collector, which is part of a concentration photovoltaic system, is independent of the photovoltaic receiver used. In order to measure the performances of collectors, a two-axis solar tracker in which the collector–receiver is mounted and pointed to the sun, is required. The precision of its tracking and in the alignment of both the collector and light sensor will influence the capacity to characterize the collector, and it is independent from the optical quality of the collector itself. Before taking any measurement, the collector and the receiver have to be thoroughly cleaned.

3.2.2 Collector optical efficiency

The overall optical efficiency of the collector is defined as the ratio of the power incident on the receiver (P_{REC}) to the power at its aperture plane (P_{AP}):

$$\eta_{op} = \frac{P_{REC}}{P_{AP}} = \frac{G_X}{G_I X_g} \tag{3.1}$$

where G_I is the irradiance on the collector's aperture plane, measured with the same

acceptance angle as that of the collector and G_X is the average irradiance on the receiver; X_g is the geometric concentration, defined as:

$$X_g = \frac{A_{NC}}{A_{REC}} \tag{3.2}$$

with A_{NC} collector net aperture area and A_{REC} receiver area**.**

The overall optical efficiency can be expressed as the product of two parameters:

$$\eta_{op} = \eta_{op,g} GT(\lambda) \tag{3.3}$$

where $GT(\lambda)$ is the global transmittance/reflectivity coefficient and refers to the intrinsic properties of the material of the collector, λ is the wavelenght, $\eta_{op,g}$ is the geometric optical efficiency depending on the collector geometry and characteristics, especially relating its shape, including the losses not included in $GT(\lambda)$. The micro-imperfection of a reflective surface are mainly contained in $GT(\lambda)$, whereas the macro imperfections impact $\eta_{op,g}$.

The parameter $GT(\lambda)$ depends on the material transmittance or reflectivity characteristics and includes losses due to the material absorption and losses caused by the spectral modification of the solar light at the collector. It is obtained from the following equation:

$$GT[\lambda_1, \lambda_2] = \frac{\int_{\lambda_1}^{\lambda_2} E(\lambda) T(\lambda) d\lambda}{\int_{\lambda_1}^{\lambda_2} E(\lambda) d\lambda} \tag{3.4}$$

where $E(\lambda)$ is the spectral distribution of light falling on the collector; $T(\lambda)$ is the spectral transmittance/reflectivity of the unshaped material. η_{op} depends on the radiation wavelength range $[\lambda_1, \lambda_2]$ trough $GT(\lambda)$. In order to evaluate $GT(\lambda)$, the $T(\lambda)$ coefficient must be known, and its meaning and evaluation procedure are different for specular collectors or lenses. Radiation falling on the collector aperture plane G_I must be measured with a sensor with the same angular acceptance as the concentrator to be characterized. Two cases can be observed.

1. In solar tracking systems, angular acceptance is higher than the size of the solar disc ($\Delta s = \pm 0.275°$), but i tis possible to collect just a small part of

the diffuse radiation coming from the sky. The incoming radiation is measured with a pyrheliometer having an acceptance angle within 5°. Thus

$$G_I = B \tag{3.5}$$

where B is the direct irradiance measured with the pyrheliometer.

2. Systems with angular acceptance higher than 5°, can collect direct irradiance and some of the diffuse irradiance coming from the sky. If no specific measurement system with the same acceptance is available, incoming radiation can be calculated from the measurements obtained by means of a pyrheliometer and a pyranometer. Thus way

$$G_I = B + mD \tag{3.6}$$

where $D = G - B$ is the diffuse irradiance calculated from direct radiation B, measured with the pyrheliometer, and G is the global radiation, measured with the pyranometer; m is the fraction of collected diffuse radiation, evaluated according to the acceptance angle of the collector. In order to measure the radiation spectral distribution $E(\lambda)$, necessary to separate the optical efficiency losses of geometry and shaping $\eta_{op,g}$, from those of the material $GT(\lambda)$, a portable spectrometer is needed. From the measurement, this distribution results as:

$$E_I(\lambda) = G_I e_I(\lambda) \tag{3.7}$$

where

$$\int_{\lambda_2}^{\lambda_1} e_I(\lambda) d\lambda = 1; \tag{3.8}$$

$E_I(\lambda)$ is the absolute spectral distribution (W cm^{-2} nm^{-1}) and $e_I(\lambda)$ is the relative spectral distribution (nm^{-1}).

3.2.3 Intercept factor

The intercept factor of a solar collector is defined as the ratio of the energy intercepted by the receiver (P_{REC}) to the energy reflected by the focusing device, i.e. parabola (P_{REF}) [Sodha et al., 1984]:

$$\gamma = \frac{P_{REC}}{P_{REF}}. \tag{3.9}$$

Its value depends on the size of the receiver, the surface angle errors of the parabolic mirror, and solar beam spread. The errors associated with the parabolic surface are of two types, random and non-random. Random errors are identified as apparent changes in the sun's width, scattering effects caused by random slope errors (i.e. distortion of the parabola due loading) and scattering effects associated with the reflective surface, and can be represented by normal probability distributions. Non-random errors arise from the manufacturing process and/or from the assembling of the optical elements and/or from the pointing or tracking of the collector. These errors can be identified as reflector shape imperfections, misalignment errors and receiver location errors. Random errors are modeled statistically, by determining the standard deviation of the total reflected energy distribution, at normal incidence [Guven and Bannerot, 1986] as specified in equation 3.9:

$$\sigma = \sqrt{\sigma^2{}_{sun} + 4\,\sigma^2{}_{slope} + \sigma^2{}_{mirror}} \tag{3.10}$$

where σ_{sun} is the standard deviation of the energy distribution of the sun's rays at normal incidence, σ_{slope} is the standard deviation of the distribution of local slope errors at normal incidence, and σ_{mirror} is the standard deviation of the variation in reflectivity of the mirror at normal incidence.

Non-random errors are determined from the knowledge of the misalignment angle error β (i.e. the angle between the reflected ray from the center of sun and the normal to the reflector's aperture plane) and of the displacement of the receiver from the focus of the parabola (dr).

Random and non-random errors can be combined with the collector geometric parameters, concentration ratio (C) and receiver diameter (D), to yield error parameters universal to all collector geometries. An asterisk is used to distinguish them from the already defined parameters. Using the universal error parameters the formulation of the intercept factor γ is derived as follows [Guven and Bannerot, 1985]:

$$\gamma = \frac{1+\cos\phi_r}{2\,sin\phi_r}\int_0^{\phi_r}\left\{Erf\left(\frac{\left(sin\phi_r\right)(1+cos\phi)(1-2\,d^{*}sin\phi)-\pi\,\beta^{*}(1+\cos\phi_r)}{\sqrt{2}\pi\sigma^{*}(1+\cos\phi_r)}\right)\right. \tag{3.11}$$

$$\left.-Erf\left(\frac{\left(sin\phi_r\right)(1+cos\phi)(1+2\,d^{*}sin\phi)+\pi\,\beta^{*}(1+\cos\phi_r)}{\sqrt{2}\pi\,\sigma^{*}(1+\cos\phi_r)}\right)\right\}\frac{d\phi}{(1+cos\phi)}$$

where ϕ_r is the collector rim angle (degrees), σ^* is the universal random error parameter ($\sigma^* = \sigma\,C$) and β^* is the universal non-random error parameter due to angular errors ($\beta^* = \beta\,C$).

3.2.4 Solar mirror reflectance

The main parameter for characterizing the performance of planar mirrors for solar-energy applications is the solar-weighted specular reflectance R_S (ρ_{sun}, θ, ϕ); this is the amount of solar power reflected by the mirror within a certain acceptance angle (θ) when a reference standard solar distribution (ρ_{sun}) is incident at a given angle (ϕ) (Figure 3.1). It is essentially the total solar-weighted reflectance minus the light scattered outside a specific acceptance angle due to micro-imperfections of the mirror surface. There is no commercial instrument to quantify $Rs(\rho_{sun}, \theta, \phi)$: the current instruments can only measure specular reflectance at a specified θ in narrow wavelength bands. Therefore $Rs(\rho_{sun}, \theta, \phi)$ must be approximated and, as a consequence, the reflectance values cited in datasheets of commercial solar mirrors often cannot be compared because of differences in measurement methods [Meyen et al., 2010]. Hemispherical reflectance $R_H(\lambda, \theta, \phi)$ is measured over a wavelength range representative of the terrestrial solar spectrum ($\lambda = 250 \div 2500\,nm$) with a UV-Vis-NIR spectrophotometer and an integrating sphere (typically, the incidence angle ϕ is 8°) relative to standards. The spectrum is then weighted by an appropriate standard terrestrial solar spectrum to compute a solar-weighted hemispherical reflectance, R_H ($\lambda = 250 \div 2500\,nm$). The standard ASTM G173 at air mass 1.5 is recommended [ASTM, 4444].

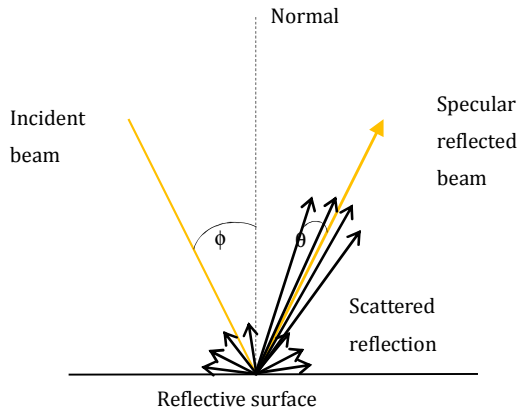

Figure 3.1: Definition of angles.

The specular reflectance $R_S(\lambda, \theta, \phi)$ is measured with a specular reflecto-meter at $\theta = 3.5$, 7.5, and 12.5 mrad with an incidence angle $\phi = 15°$ for $\lambda \approx 660nm$. For highly specular reflectors, specular reflectance can then be described by the ratio of specular reflectance $R_S(\lambda, \theta, \phi)$ to the hemispherical reflectance $R_H(\lambda, \theta, \phi)$ at the same wavelength; this ratio is assumed to be constant and equals the ratio of the solar weighted values. The solar-weighted specular reflectance is then approximated by [Pettit, 1982]:

$$R_S(\rho_{sun}, \phi, \theta) = \frac{R_S(\lambda = 660\ nm, \phi, \theta)}{R_S(\lambda = 660\ nm, \phi, \theta)} \cdot R_H(\rho_{sun}, \phi, \theta) \tag{3.12}$$

3.2.5 Distribution of concentrated light at the receiver

The quality of a collector depends not only on its optical efficiency, but also on the distribution of light on the receiver. In fact, the spot light profile produced by the collector is fundamental to the design of the system. The size of the receiver is usually chosen a priori and is based on technological and economic considerations. On the one hand, the materials chosen affect the optical efficiency through the global transmittance/reflectivity coefficient parameter (GT, equation 3.3), that can be taken equal to the solar-weighted specular reflectance $RS\ (\rho_{sun}, \theta, \phi)$ for solar reflectors; on the other hand, the ability of the manufacturing process to reproduce the theoretical reflective surface determines the distribution of the energy on the receiver and thus

affects the optical efficiency, too.

A tool for measuring the light distribution produced by the collector, therefore, will serve not only to compare manufacturing processes and give the information for designing the receiver, but also to determine the efficiency of the system for a certain concentration level. It is possible that a collector designed for a relatively high concentration level has poor optical quality as a great part of the light falls outside the receiver for which it was designed; at lower concentrations the optical quality in general is higher.

The measurement of concentrated solar flux can be made with radiometric methods, through thermocouples, thermopiles, or photo-sensors and it requires calibration. In [Chong et al., 2011] an optical scanner based on a photodiodes array capable of plotting the flux distribution has been proposed, with the advantage of performing real time and direct measurement of very high-concentrated fluxes without the risk of burning the diffuser.

In spite of this, thanks to its high resolution, the most common procedure to measure the irradiance distribution make use of a CCD camera and a receiver placed in the focusing region of the collector [Parretta et al., 2006; Johnston, 1998]. The collector and the receiver have to be positioned on a two-axis tracker with the camera moving in line with them. In case of high irradiance values, a set of filters are needed in order not to saturate the image obtained. A lambertian plane surface (the angular distribution depends on $cos\ \phi$, where ϕ is the angle to the perpendicular) is used as a receiver. In this way all the radiation coming from the mirror is collected equally, and given that the object is to take a measurement relative to the distribution of the light, the angle at which the camera sees the reflector has no influence. Differently, if the receiver behaved as a reflector, the light power detected by the camera would correspond to a fraction of the mirror area and not to its totality, falsifying the measurement. A lambertian receiver can be obtained with a flat microgranular surface painted matt white.

Some configurations used for this analysis are shown in Figure 3.2. The CCD camera ideally is situated perpendicular to the receiver, but this is not possible in all cases. In order to achieve this situation for a parabolic dish, a small hole in the area of collector shaded by the receiver, as it is shown in Figure 3.2 (b), is made. Another

possible solution is to place the CCD camera behind a lambertian diffuser, in transmittance configuration. The CCD camera provides a matrix of pixels *I* (i, j), which contains the irradiance level for each pixel, whose coordinates are (i, j). The measurements obtained through this process are always relative, although a calibration the system can be carried out in order to find out the absolute value of the irradiance in W/cm^2 [Ulmer et al., 2002].

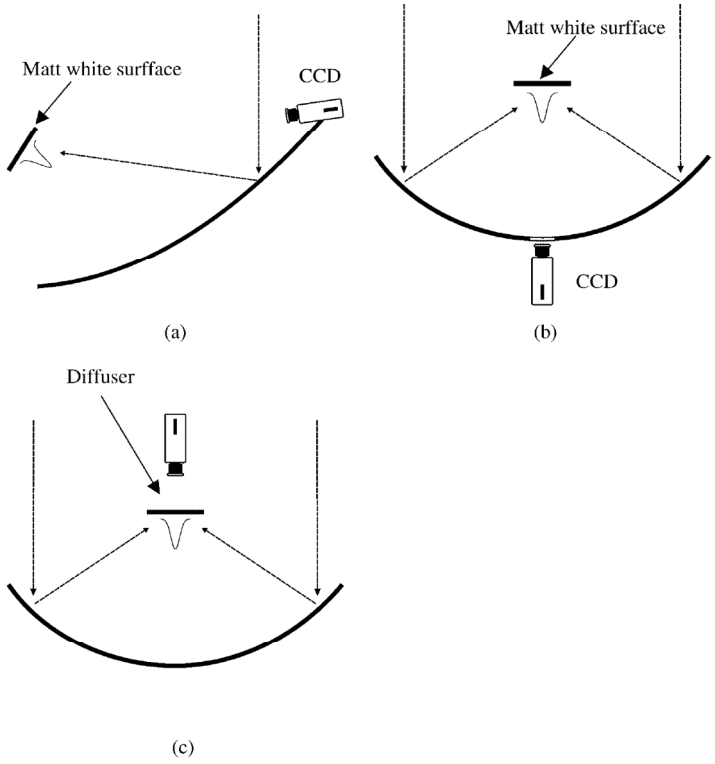

Figure 3.2: Different system configuration in order to measure the light distribution for different solar collectors: (**a**) linear, (**b**,**c**) parabolic dish.

3.2.6 Calorimetry

Despite of many efforts, the apparently simple problem of measuring high concentrated radiative fluxes produced by concentrators remains a problem [Ulmer et al., 2004]. The methods that have been employed for this analysis include both radiometric and calorimetric techniques. In the case of radiometers, the concentrated solar flux is estimated through a variation of temperature measured by a transducer at a given location on the sensor. Thermocouples or thermopiles are commonly used to

carry out this task [Gardon, 1953; Pérez-Ràbago et al., 2006]. The disadvantage of these methods is that all radiometers require calibration, and this is not easy due to spectral response effects.

Calorimeters are used to measure the concentrated flux in a direct way. A device of this type allows exchanging the power produced by the pointed-to-sun concentrator module with a heat transfer fluid, usually water, flowing through the calorimeter body. The incident concentrated flux can be evaluated by determining the heat absorbed by fluid and estimating the external heat losses. This technique requires reducing to a minimum the uncertainties in the measurements of the mass flow rate of the cooling fluid, and of the difference between its inlet and outlet temperatures. One of the calorimetric techniques that have been successfully explored is the Cold Water Calorimetry (CWC) [Buck et al., 2002]. Here very good heat transfer from the concentrated flux to the fluid flow is needed, in order to have the receiving surface of the calorimeter at a temperature close to ambient. This can be achieved by increasing the fluid flow rate. In this way is possible to reduce radiative and convective losses, hopefully eliminating the need for a precise estimation of these losses.

3.3 Experimental

The principal aim of the work here presented is to assess the optical performances of a single manufactured parabolic module. The characterization procedures have been applied just to a single module, because the power resulting from the all three modules would be detrimental for the photovoltaic cells, at the current level of development. The geometry and the structure of this single-module collector, having a collecting aperture area of about 0.8 m^2, are described in Chapter 2 (Section 3.4). In the following, the characterization of the mirror by means of reflectivity measurements is reported. Specular reflectance has been characterized by means of a UV-Vis spectrophotometer, in the 250-1200 nm wavelength range, and of a pyrheliometer, with respect to a direct solar spectrum. The illumination profile of a module mounted on a sun-tracking system was tested by power density measurements in and out of the focal plane, and spots are compared with a theoretical one. In order to evaluate the

high-flux solar energy arriving at the focus of a module, a flat-plate calorimeter was built. The study was carried out by measuring the energy absorbed by the water flow and the external losses due to convection. Based on an energy balance, the intercept factor and the overall optical efficiency of the collector were estimated.

3.3.1 Measurement of reflectance of silvered mirrors

The reflectivity of an ideal (front-surface) silvered mirror is approximately 97%. Since silver degrades quickly in the outdoor environment, more durable back-surface glass mirrors have typically been used at CSP and CPV plants. Glass superstrates result in transmission losses (increased absorption) through the glass medium, with losses increasing as a function of both iron content in the glass and thickness. The reflectivity of typical mass-produced commercial glass exhibit lower reflectivity, ≤90%, due to increased absorption and thickness.

We have used a 0.8 mm thick silvered mirror produced by FAST GLASS® whose reflectivity properties have to been assessed. Microscopic surface irregularities, called specularity errors, in a mirror's substrate or superstrate material slightly reduce a mirror's measured specular reflectivity because they cause non-specular (scattered) reflections that fall outside the acceptance aperture of the measurement instrument. Specularity errors can be measured on small mirror samples and generally have a much smaller impact on plant performance than "slope" and "curvature" errors, which are errors in the shape of the mirror surface over larger macroscopic areas of the surface that must be measured on full-size samples.

The main parameter of interest for solar-energy applications is the solar-weighted specular reflectance R_S (ρ, θ, ϕ) introduced in paragraph 3.2.4; this is the amount of solar power reflected by the mirror with respect to an acceptance angle θ when a reference standard solar distribution ρ_{sun} is incident at a an angle ϕ. It is essentially the total solar-weighted reflectance minus the light scattered outside a specific acceptance angle due to micro-imperfections of the mirror surface. In the present work, the reflectivity properties of the mirror are investigated with two measurements; one to estimate the spectral modification in the solar spectrum shape produced by the optics itself and another to establish an effective value for R_S (ρ, θ, ϕ). Firstly the reflectance of the silvered mirror has been measured with an UV-Vis-NIR spectrophotometer

(Varian Cary 5000) as a function of the wavelength of the incident radiation. The acquisition has been made over a wavelength range $\lambda = 250\text{-}1200$ nm of the scanning radiation and with a fixed incident angle $\theta = 12.5°$. The spectrophotometer was equipped with a PMT detector (250 – 800 nm) and with a PbS detector (800-1200 nm). The measured reflectance $R(\lambda)$ is shown in Figure 3.3. It holds 93.0% ± 0.1 % for $\lambda > 500$ nm, reaching a maximum value of 94.4% ± 0.1 % around 700 nm. At low wavelength values the reflectance decreases to 89.8% at around 465 nm and falls below 80.0 % at 426 nm and below 70 % at 395 nm.

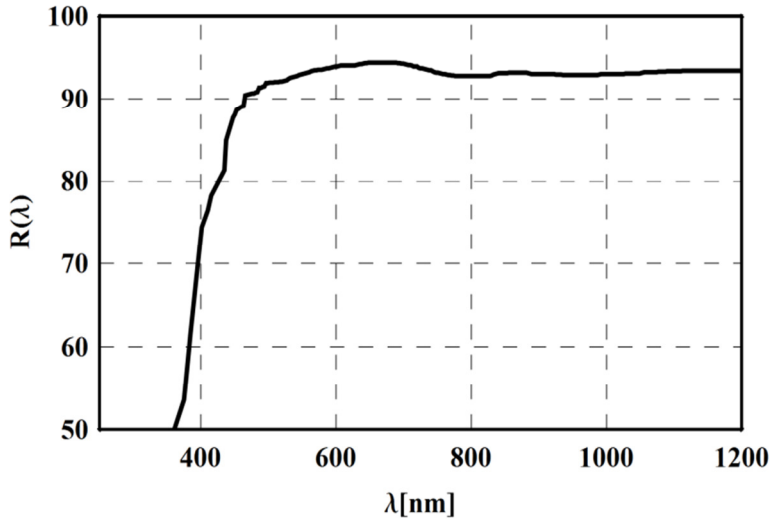

Figure 3.3: reflectance curve $R(\lambda)$ of the unshaped silvered mirror measured with a UV-Vis spectrophotometer.

In Figure 3.4 the standard AM 1.5 direct spectrum ASTM G173-03D (Standard ASTM_G173-03, 2003) is reported with the same spectrum weighted by the measured reflectance $R(\lambda)$ in the range $\lambda = 250 \div 1200$ nm. We refer to this direct spectrum reflected by the mirror in the given spectral range as ASTM G173-03 DR. From the figure it is clear that the spectral modifications introduced by the mirror are almost negligible for wavelengths higher than 500 nm. Differently variations become important for wavelengths lower than 450 nm and actually the mirror's material acts as a filter for wavelengths below 350 nm. In general this has no important influences on a CSP receiver's operation, where the sunlight is converted in heat and the receiver

surface absorption is almost insensitive to the spectral content of the incoming radiation. Differently, if the mirror is used in a Concentration PhotoVoltaic (CPV) application, spectral variations have to be carefully considered. This is particularly true when multijunction cells are the active elements of the receiver, because each sub-cell thickness is designed to satisfy current-matching requirements, that depends upon the spectral distribution of the incident light. The sensitivity of MJ devices to variable spectrum has been studied theoretically [Kurtz et al. 1990], but not yet experimentally to our knowledge.

In our case the reflective material acts as a filter for wavelengths below 400 nm, so it would have an influence on the electrical behavior of every cell that has been

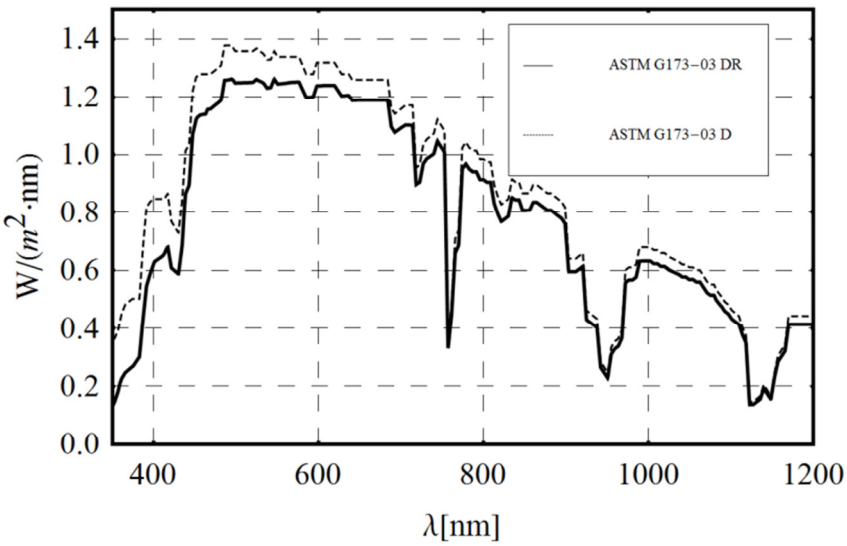

Figure 3.4: standard AM1.5 direct solar spectrum (ASTM G173-03 D) and the same spectrum after reflection by the silvered mirror (ASTM G173-03 DR). This last curve was calculated by using the reflectivity curve shown in Figure 3.3.

designed for an optimum operation with a standard solar spectrum. The parameter of interest, $R_S\,(\rho,\theta,\phi)$ could be approximated by weighting $R(\lambda)$ with the standard spectrum ASTM G173-03D, but this would require the spectrophotometer to measure over a wavelength range representative of the whole terrestrial solar spectrum ($\lambda = 250 \div 2500\,nm$) [Pettit, 1982]. This wasn't possible for the available Varian Cary 5000 at the moment of the measurements. Therefore, in order to assess a solar-weighted reflectance of the mirror material, we performed an outdoor direct

measurement of this parameter. This procedure has the advantage to give an effective value that describes the performance of the mirror material at a given solar radiation condition. The measurement has been carried out with respect to the solar spectrum incident at a given angle of $\theta = 45°$ and along a series of 20 repetitive measurements within half an hour. For this purpose a device supporting a piece of plane mirror and a pyroheliometer, accurately aligned by means of a laser-pen, has been mounted on the solar tracker. The sunlight incident on the mirror at 45° is reflected to the entrance aperture of the pyroheliometer, having an aperture cone $\phi = 5°$.

This way we can define an effective value for solar-weighted reflectance as:

$$R_{eff} = \frac{P_0}{P_i} \tag{3.13}$$

where P_i is the incident solar power measured by the pyroheliometer and P_0 is the power measured after a reflection on the mirror's surface. Power values were measured with the same pyroheliometer, by pointing it alternatively to the sun and to the mirror's output beam. The resulting value for R_{eff} was 89.6 % with a standard deviation of 0.4%. It must be emphasized that this value refers to an incident angle of the sunlight on the plane mirror of 45°, with respect to the rays coming from the center of the solar disk.

When this solar-weighted reflectance R_{eff} is used as a figure of merit for our oriented parabolic sector, the dependence of R_S from the angle of incidence θ is neglected. The angle of incidence θ on the oriented sector ranges between 0° (incident solar rays near the vertex of the sector) and 64° (incident rays on the largest side of sector).

3.3.2 Illumination profile measurement

The illumination power density at the focal plane gives the most significant indication on the optical quality of the manufactured reflector modules. It points out how well the parabolic sectors approximate the designed geometry (equation). Here we report the measurements carried out on a parabolic sector exposed continuously outdoor for more than 2 years. The two-years exposure wasn't under sun-tracking mode but in a rest position pointed upward. The spot-area was investigated on a discrete set of

representative points by using an electrical plotter with x and y movements (Micos) and a powermeter (Ophir Ltd), as it is shown in Figure 3.5. The thermal head (Ophir F150A), which allows to measure average power density up to 15 kW/cm^2, was mounted upon the plotter and was connected to an Ophir Vega display and to a computer. To enhance the spatial resolution of the power density measurement, the 17.5 mm diameter of the thermal head was protected with a water cooled copper shield, with an aperture hole whose area was measured to be 16.66 ± 1.44 mm^2.

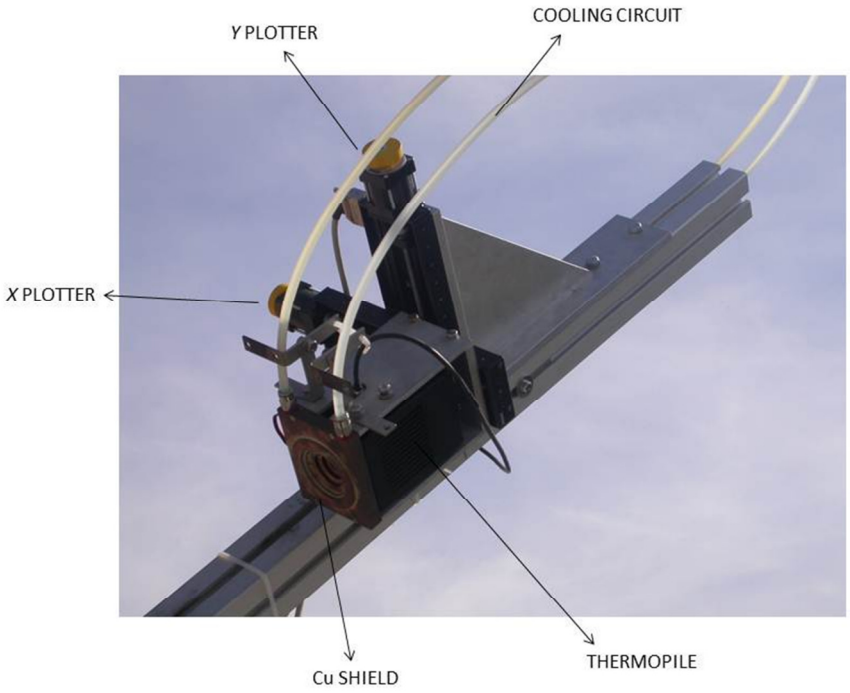

Figure 3.5: experimental apparatus used to scan the illumination profile, mounted on the sun tracking system**.**

The power measurements were performed on a target plane perpendicular to z axis of the paraboloid, at distances of 2460 mm and 2500 mm (theoretical focal point). The capture points belong to a square grid with a spacing of 4 mm, and each measurement was acquired after a thermalization time of 4 seconds in order to allow the thermal head to reach an equilibrium level. During the acquisition at 2500 mm, the mean power value of the direct solar radiation during the acquisition time (25 min) was 835 W/m^2, with maximum variations of about 2%. In order to consider these variations, every power density measurement was multiplied by a factor k = 835 / I_D, with I_D

equal to the instantaneous direct solar radiation express in W/m^2. Solar radiation was measured with a calibrated pyroheliometer (Kippen&ZonenCHP1). Figure 3.6 (left) shows the radiative flux distribution at the focal region in terms of power density units (W/cm^2), as a result of the interpolation of experimental data. The spot shape is close to a Gaussian distribution with a mean power gradient of about 2.23 W/(cm^{2}mm) and a peak flux of 73 W/cm^2, corresponding to a peak concentration ratio of about 870 X.

The spot measured at 2460 mm is shown in Figure 3.6 (right). The mean power value of the direct solar radiation during the acquisition time was 831 W/m^2. In this case the spot loses its symmetry, the illuminated area becomes larger and the peak flux lower (62 W/cm^2).

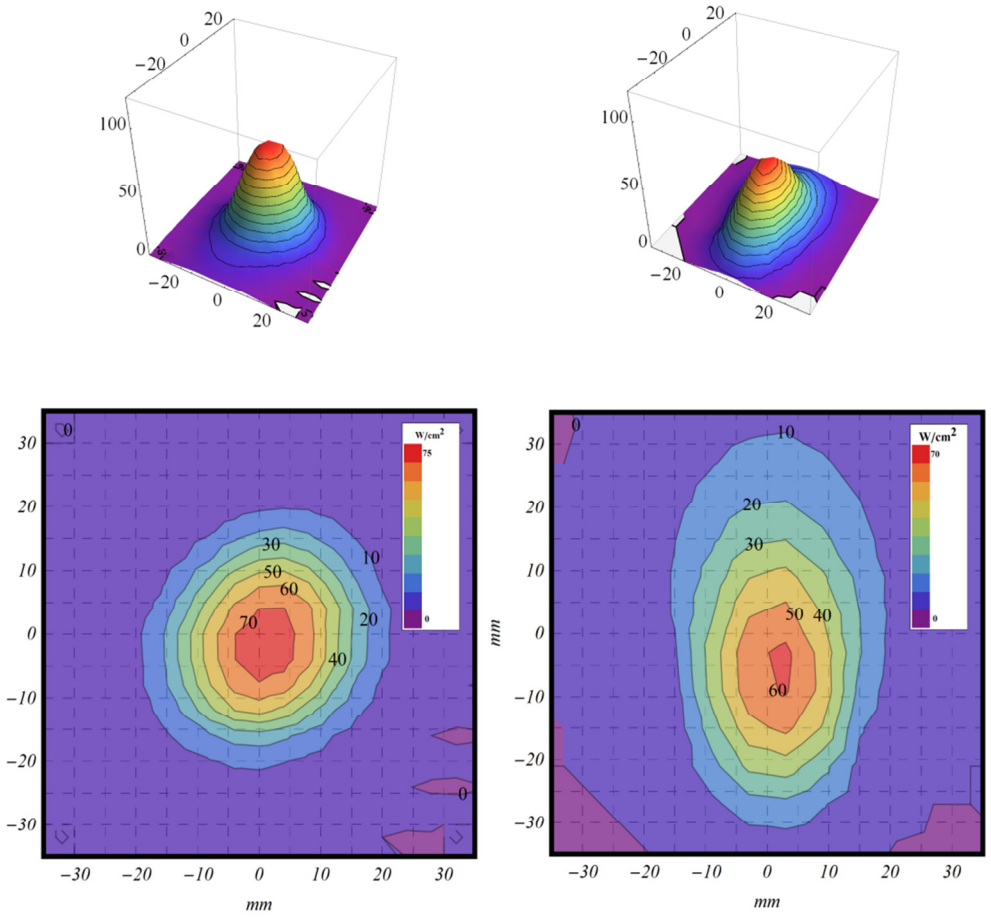

Figure 3.6: 3D profile and 'contour plot' of the power density. The image is referred to the measurements performed on planes perpendicular to the z axis of the paraboloid, at a distance of 2500 mm (**left**) (theoretical focal point) and 2460 mm(**right**) from the origin plane. Values reported on the contours are expressed in W/cm^2

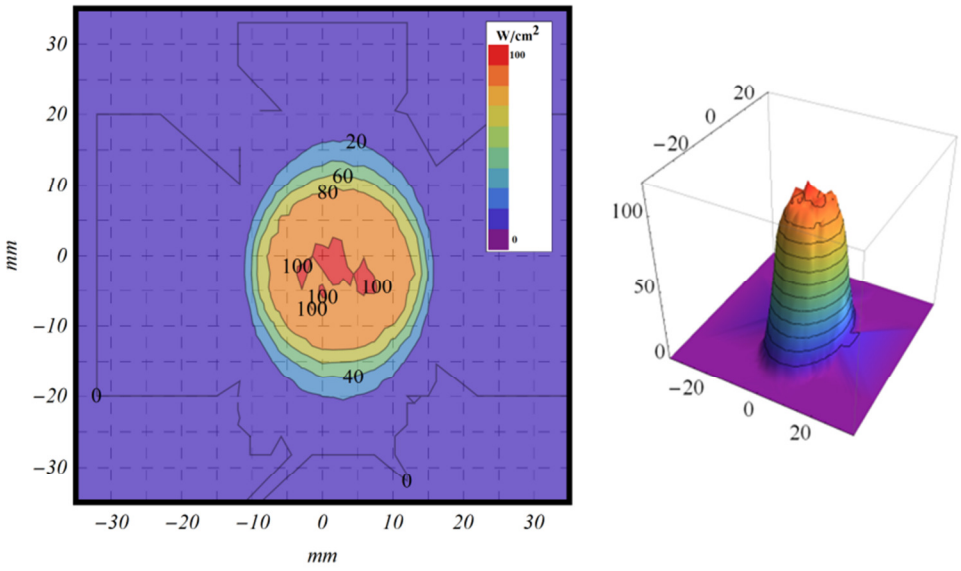

Figure 3.7: calculated 3D profile and 'contour plot' of the density power for a parabolic module. The image is referred to power density expected on a plane perpendicular to the z axis of the paraboloid, at a distance of 2500 mm from the origin plane. The collector is considered and having no surface errors and a weighted-solar spectrum reflectivity of 0.876. Values reported on the contours are expressed in W/cm^2.

In Figure 3.7 is reported the flux distribution simulated with a Monte Carlo (MC) ray-tracing technique. Simulation was performed with a reflector having no surface errors (zero slope error) and in nearly the same conditions of the reflector under testing: same shape, sizes, solar-weighted reflectance of 0.896, as estimated in the previous paragraph, and incident direct solar radiation of 835 Wm^{-2}. A sample of 10^6 sunrays/m^2 in the MC run, and the sunshape model with circumsolar ratio CSR=5% were used [Buie et al, 2003]. In this case the spot is smaller and the peak reaches values of about 110 W/cm^2.

Data obtained from the measurements and the simulation of the density power distribution, are compared in Figure 3.8, in which the power fractions contained into circles of radius R are shown. From this figure it is found that 95% of the total measured power is collected in a region of radius R = 29 mm. For the simulated spot this region has radius R = 18 mm. This difference can be ascribed to imperfections and to deviations from the designed shape of the collector due to the manufacturing process, in addition to surface errors of the given mirror material.

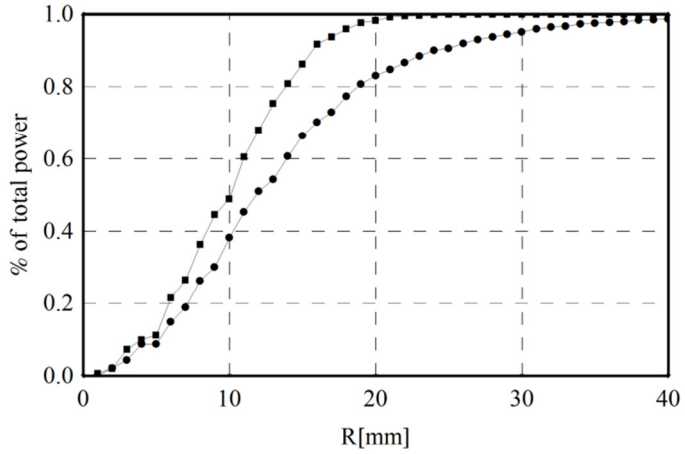

Figure 3.8: measured and calculated power fraction collected in circles of radius *R* at the focal plane of the parabolic sector.

3.3.3 Calorimetric measurement

The aim of this work is to determine the solar energy concentrated by a parabolic module onto the spot region. To achieve this goal is necessary to quantify the global heat losses to the environment, thus establishing the validity of the Cold Water Calorimetry (CWC) for the system. In order to keep the design of the calorimeter as simple as possible, a flat plate device has been built (Jaramillo et al., 2007). In this type of calorimeter concentrated sun rays hit a plate receiver and part of the light is back-reflected. These losses are greatly higher than in a cavity calorimeter (in which the sun rays are reflected inside the cave), but at the same time they are easier to estimate. In order to increase solar absorption, the receiving face of the calorimeter has been chemically oxidized.

Part of the energy absorbed by the calorimeter is lost towards the environment through convective and radiative heat transfer. To calculate this portion of energy, the temperature of the front face of the calorimeter has to be accurately measured.

Description of the calorimeter

The built calorimeter with its sub-components is shown in Figure 3.9. The cylindrical outer casing, machined from stainless steel, houses the insulation layer and the copper receiver. The receiver is a 10 millimeter thick copper plate, having 10 centimeters in diameter. The front face exposed to concentrated energy, has been

oxidized to increase the solar absorption; the rear part has been carved into channels and then covered with a thin copper plate (3 mm), which has been soldered to the body. The section of the channels is a 5 by 5 mm square, while the walls between the channels are 3 mm thick. Water enters from the back of the plate, near the center, flows through the channels alternating clockwise and counterclockwise direction and finally exits near the edge. Along this path, water increases its temperature, subtracting heat from the copper plate. The channels' function is to force the water to keep a steady velocity in the rear part of the plate, avoiding the formation of vortexes and stagnation.

In the walls that separate the channels, 13 holes, 9.5 millimeters deep and horizontally lined up, have been drilled. These holes host 13 type-k thermocouples,

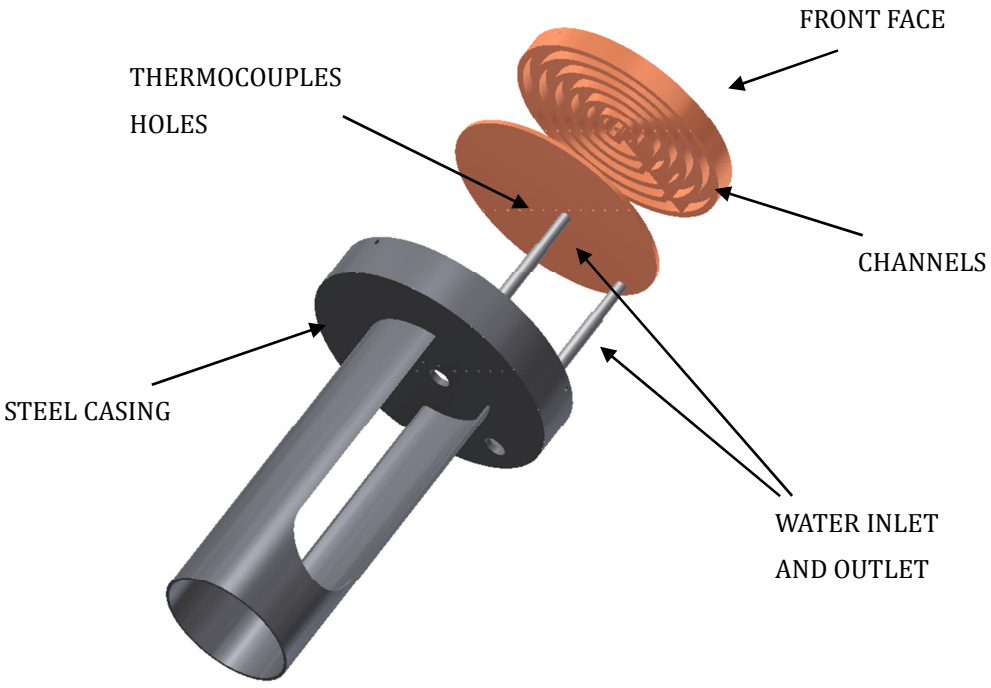

Figure 3.9: exploded representation of the calorimeter. The 12 thermocouples and the insulating material are not drawn.

which directly measure the temperature of the front plate, which will then be used to calculate convection losses.

The sides and the back of the plate have been insulated with 6mm thick pyrogel

6671, an insulation blanket formed of silica aerogel and reinforced with a non-woven, glass-fiber batting. The insulated copper plate is contained into a stainless still, which can be easily fixed to our concentration solar collector. Thermal conductivity of pyrogel is less than 18 mW/(m·K) under 100°C [http://www.teknowoolnanotecnologie.com/documenti/Aspen/Scheda%20tecnica %20Pyrogel_6671.pdf] which is the range of temperature we expect to reach on the front face. This low conductivity layer allows to disregard thermal losses toward the steel stand, and only consider losses from the front face (reflection, convection and radiation). A more detailed description of the calorimeter sub-components is given in Appendix A.

Oxidation process

To obtain a high absorption surface, the copper has been oxidized through a chemical treatment. First, the plate has been lapped with different grade silicon carbide papers; further degreasing was then obtained by dipping it in Rodaclean supra solution (5%) for 3 minutes at 60°C; finally the surface oxide has been removed with a 1% HCL solution. The cleaned copper plate was then immersed into a sealed glass container, containing an alcaline solution (0.1M NaOH) of $K_2S_2O_8$ (0.001M). In this condition, the plate was left still at 70°C for 16 hours. Such oxidation of copper normally proceeds through the precipitation of copper oxide salt on the surface, which then decomposes to produce copper oxide film. After reaction, the sample was taken out, washed with distilled water and dried in air. A dark film was obtained,which covered uniformly the copper substrate.

The process was performed on a small circular copper plate, too, whose reflectivity was then measured with Varian spectrophotometer Cary 5600, equipped with a DRA 2500 integrating sphere and using a spectralon SRS-99 diffuse reflectance standard as reference sample. The measurement has been performed in a range from $\lambda = 280 \div 2000$ nm, and then integrated on a standard solar spectrum to compute a solar weighted absorption (Figure 3.10). The standard ASTM G173-03 Reference Spectra, which considers direct + circumsolar radiation, was used. From this measurement, the solar-weighted absorption coefficient resulted $\alpha = 0.95$. More details about the characterization of the copper oxide layer coated on the calorimeter plate are reported in Appendix B.

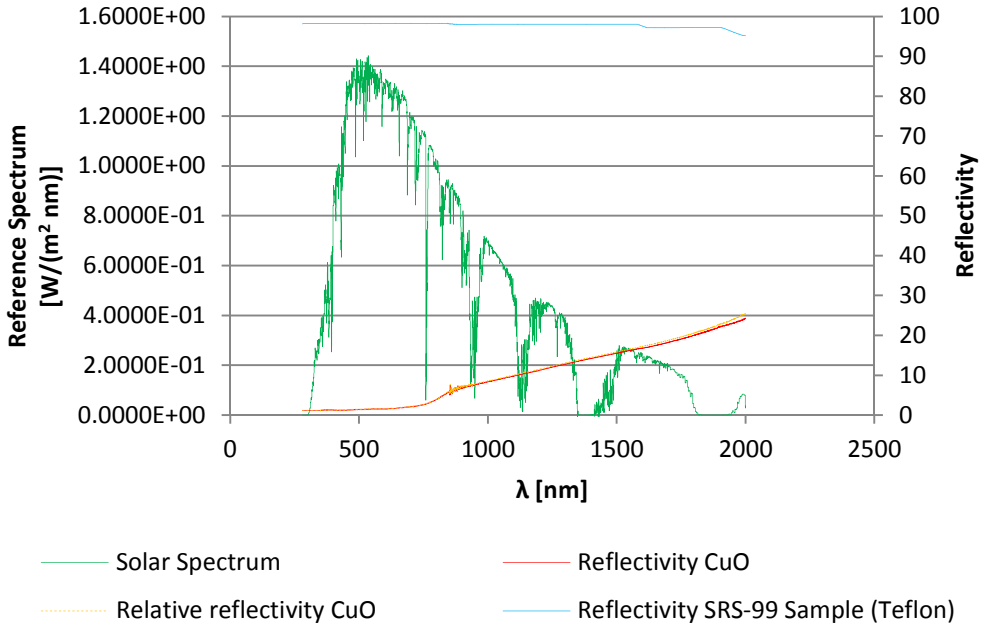

Figure 3.10: diffuse reflectivity of the copper oxide layer (yellow) with respect to the reference Teflon sample (blue). The ASTM G173-03 solar spectrum is also shown (green).

Physical process

When direct sunlight is collected by the parabolic module, part of it is reflected in the focus region and the rest is scattered or absorbed by the glass layer. In case of an ideal dish collector of A_{mod} collecting area, the fraction

$$P_{in}{}^{ideal} = R_S I_d A_{mod} \tag{3.14}$$

would hit the plate of the calorimeter, where R_S is the solar-weighted specular reflectance of the mirror and I_d is the direct solar intensity. In case of a real solar collector, an energy balance on the copper disc has to be carried out in order to determine the impinging high-flux solar energy. Neglecting the losses from the back and lateral faces of the calorimeter, which are insulated, and assuming stationary conditions, the incident power (P_{in}) on the calorimeter is either reflected (P_{ref}), removed from the water flow (P_w) or lost by convection (P_{conv}) and radiation (P_{rad}) from the front face to the ambient air.

The power balance can be written as:

$$P_{cal} = P_{ref} + P_w + P_{conv} + P_{rad} \tag{3.15}$$

and the terms P_{ref}, P_w, P_{conv}, $P_{rad}$of the balance are given in Equations 3.16 to 3.19.

$$P_{ref} = (1 - \alpha)P_{in} \tag{3.16}$$

$$P_w = Q \cdot \rho \cdot C_p \cdot (T_{out} - T_{in}) \tag{3.17}$$

$$P_{conv} = \int h(\vec{r}) \cdot [(T_s(\vec{r}) - T_{amb}(\vec{r})]\, dA \sim A_{rec} \cdot h \cdot (T_s - T_{amb})_{ef} \tag{3.18}$$

$$P_{rad} = \epsilon \cdot \sigma \int \left({T_s}^4(\vec{r}) - {T_{amb}}^4(\vec{r}) \right) dA \tag{3.19}$$

The power arriving on the copper plate that is not absorbed (P_{ref}) can be estimated by Equation (3.16) given the measured absorbance of the oxide layer α. Power absorbed by the water flow (P_w) is estimated by the simplified steady-flow thermal energy equation, Equation (3.17), where Q is the water flow in m3/sec, ρ is water density (1000 kg/m3), Cp is water heat capacity at constant pressure (4183 J/(kg·K)), and T_{in} and T_{out} are respectively the measured temperature of the water at the inlet and outlet of the calorimeter. External convection heat losses to the surroundings are given by Equation (3.18), where $h(\vec{r})$ is the convective heat transfer coefficient, $T_s(\vec{r})$ and $T_{amb}(\vec{r})$ are the calorimeter front surface and the ambient temperatures, respectively, and $\vec{r}$ is the position vector on the surface of the calorimeter. The integration extends to the area of the calorimeter front face ($\vec{r} \in A_{rec}$). For simplicity, Equation (3.18) is linearized by introducing the mean values for h, T_s and T_{amb}. Convective heat coefficient h depends on the wind flow over the surface and on the geometrical characteristics. In particular $h = R_{cal}/2 \cdot k/Nu$, where R_{cal} is the radius of the circular plate, k is air thermal conductivity (0.0263 W/(m·K) at standard temperature), and $Nu = 0.664\, Re^{0.5}\, Pr^{1/3}$ is Nusselt number for laminar flux, Re is Reynolds number, which contains dependency on wind velocity and Pr is Prandl number. Wind velocity was measured every ten minutes by a nearby meteo station, and for every test the simultaneous wind velocity data was used. The corresponding values of h goes from 50 to 60 W/m^{2}K.

The mean plate temperature T_s was evaluated, assuming axial symmetry, as

$$\frac{2\pi \int_0^R r\, T(r)\, dr}{\pi R^2} \tag{3.20}$$

where r is the radial coordinate and $T(r)$ results from interpolation of the thermocouples data.

Radiative losses (P_{rad}) are calculated from Equation 8, where ϵ is copper oxide emissivity, which is 0.8 ± 0.12, σ= 5.670·10^{-8} W/(m^{2}K^4) is the Stefan-Boltzmann constant. Air temperature T_{air} was used instead of sky temperature T_{sky}, as the front face of the calorimeter was pointed toward the ground, so the radiative heat transfer was mainly between the calorimeter and the direct surroundings of the dish collector

With the above considerations, we define the intercept factor as the power found in the spot (P_{in}) over the power expected after reflection ($P_{in}{}^{ideal}$) by the parabolic mirror.

$$\gamma = \frac{P_{in}}{P_{in}{}^{ideal}} = \frac{(P_w + P_{conv} + P_{rad})/\alpha}{R_{eff} I_d A_{mod}}. \tag{3.21}$$

Equation 3.21 accounts for the intrinsic reflectivity properties of the mirror material through the value R_{eff}. For an ideal concentrator, with no shape errors introduced by the module's manufacturing process, γ =1.

The overall optical efficiency of the collector module is defined as the ratio of the power incident on the receiver to the power collected at its aperture plane

$$\varepsilon = P_{in}/P_{coll}\,. \tag{3.22}$$

The uncertainties on the measured and the derived quantities were evaluated as described in the following. For the variables which uncertainties have measurement limitation (α, Q, R_{rec}, A_{mod}, V_{wind}), the instrumental errors were considered as absolute errors. For other measured variables (R_S, I_D, T_s, T_{amb}), the uncertainty was calculated as the standard deviation of their mean value. For example, in case of temperatures data, during the one-minute acquisition (60 points), the temperature has been taken as a mean value with its own standard deviation. For the value of copper oxide emissivity (ε) we have taken the value given in [Siegel, 2002]. We have established a very large error (15% relative error) in order to account for influence of temperature, structure and thickness of the oxide layer. The above mentioned variables propagate as

uncorrelated variables in the calculation of the uncertainty of the derived quantity.
The values P_{conv} resulting from the integral of Equation 3.18 has been computed in the following way. For each test, two Gaussian functions (one for thermocouples 1-7, another for 7-13) have been assumed to interpolate the experimental temperature data. By assuming semi-circular symmetry we integrated these functions (from 0 to π, and from π to 2π, respectively); the integrals give the corresponding mean half-plate temperatures (T_S in Equation 3.18) and the corresponding values of P_{conv}, relative to the half plate. Total P_{conv} is the sum of these two values. In order to calculate the errors, the same procedure has been adopted with the two interpolations on the 13 values $T_i+\Delta T_i$, where ΔT_i is the standard deviation of each temperature value; this results in new value T_S*; the difference T_S*- T_S, for each semicircle was used as error on T_S. This propagates to give the errors in P_{conv}. For the computation of the mean value of T_S^4 and the relative error the same procedure used for T_S was adopted but using the functions T^4.

Measurement equipment.

Water temperature was measured using 2 Delta Ohm TP87 PT100 sensors; plate temperature was monitored in 13 points with k-thermocouples connected to an Agilent 34970A data logger. An additional k thermocouple, connected to the same instrument, was used to measure air temperature. Direct solar radiation was measured with Kipp & Zonen CHP1 Pyrheliometer, connected to an Agilent 34410 Digital Multimeter. Data from all this equipment were recorded every second during the entire measure duration. Wind velocity data were provided by a nearby weather station. 4 measurements of 1 minute were made, in quasi-stationary conditions, and the elaboration was then conducted using mean values over these intervals.

Results.

The results of the measurements done at four different water flows are reported in Table 1. The difference of the outlet and inlet temperature of the water ranged between 6.1 and 23.0 °C, as it is shown in the Figure 3.11. In Figures 3.12–3.15 temperature of the copper receiver measured as a function of the distance from its center are shown together with the corresponding specific convective power (W/cm^2) for the four cases.

The first graph (Figure 3.12) refers to the highest water flow (test A), where the

temperature of the plate is the lowest.

We note that out of the center of the plate convection is negative, and the total convective power P_{conv} results negative, too. In the case of the lowest water flow (TEST D) the plate reaches a maximum temperature of about 63°C. In this condition convective losses are at their maximum (8 ± 2 W), but anyway they are less than 2% of the solar power impinging on the calorimeter surface.

Radiative losses are about ten times lower. These findings show that the assumptions needed for applying the CWC technique are fulfilled with good approximation for the present calorimeter. The calculated (Equation 3.21) intercept factors γ of the parabolic module relative to calorimeter plate dimensions (R=5 cm) are consistent within the uncertainties and range between 0.96 and 0.99 for the four tests. Intercept factor is an intrinsic property of the collector and for this reason, as expected, no significant trend is observed with the change in the values of water flow and incident power. The overall optical efficiency η_{op} of the collector is esteemed to be in the range 86-89 %.

Parameters	**Test**			
	A	**B**	**C**	**D**
Water flow, Q [l/min]	1.20 ± 0.01	0.723 ± 0.005	0.417 ± 0.002	0.259 ± 0.001
Direct solar flux, I_D [W/m^2]	801 ± 4	679 ± 3	717 ± 4	670 ± 3
Collected solar power, P_{coll} [W]	625 ± 11	530 ± 9	559 ± 10	523 ± 9
Air temperature, T_{air} [°C]	31.6 ± 0.5	31.7 ± 0.5	32.1 ± 0.6	31.6 ± 0.5
T_{out}-T_{in} [°C]	6.1± 0.1	8.3 ± 0.1	15.1 ± 0.3	23.0 ± 0.1
Expected power, $P_{in,id}$ [W]	575 ± 13	488 ± 11	515 ± 11	481 ± 13
Water heating power, P_w [W]	508 ± 12	419 ± 8	438 ± 12	415 ± 5
Convective coeff., h [W/m^{2}K]	59 ± 12	52 ± 10	55 ± 11	59 ± 12
Convective power, P_{conv} [W]	-1.4 ± 0.5	0.0 ± 0.3	3 ± 1	8 ± 2
Radiative power, P_{rad} [W]	-0.12 ± 0.04	0.01 ± 0.02	0.3 ± 0.1	0.7 ± 0.2
Intercept factor, γ	0.99 ± 0.07	0.97 ± 0.07	0.96 ± 0.09	0.99 ± 0.08
Overall efficiency, η	0.89 ± 0.06	0.87 ± 0.06	0.86 ± 0.07	0.88 ± 0.06

Table 1: Parameters used to evaluate the intercept factor γ and the overall efficiency ε with the calorimetric measurements by varying the water flow (tests A,B,C,D). γ and ε are reported in the last two lines.

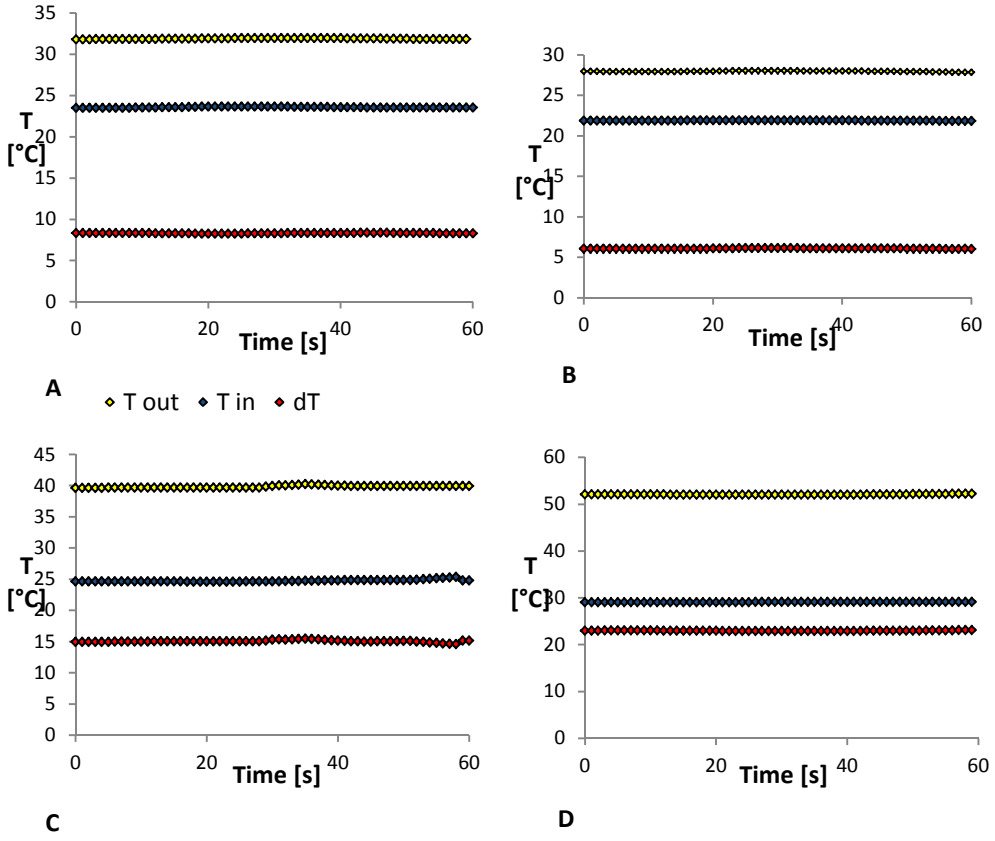

Figure 3.11: water temperatures for the four measurements A-D; outlet temperature (yellow markers), inlet temperature (blue) and their difference (red).

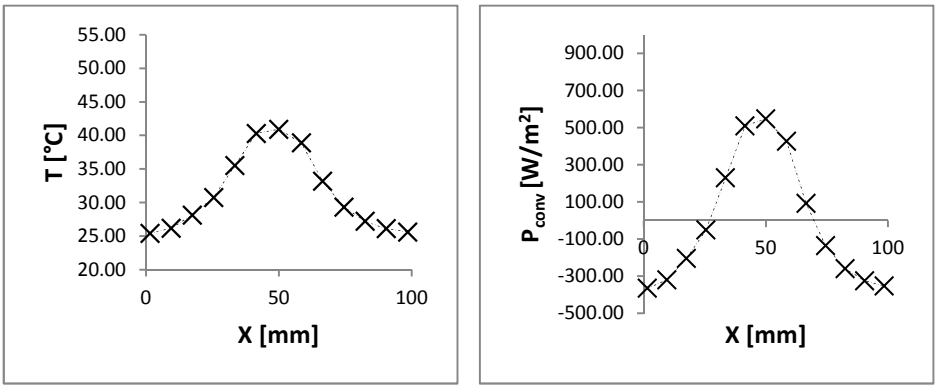

Figure 3.12: temperature and specific convective loss on the front surface for test A.

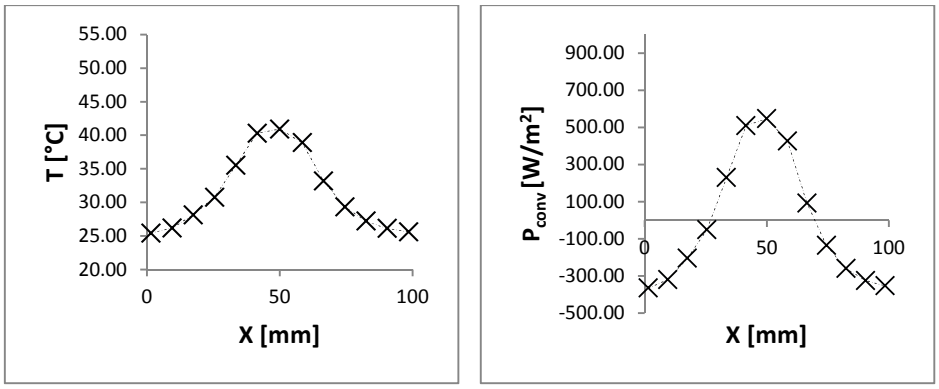

Figure 3.13: temperature and specific convective loss on the front surface for test B.

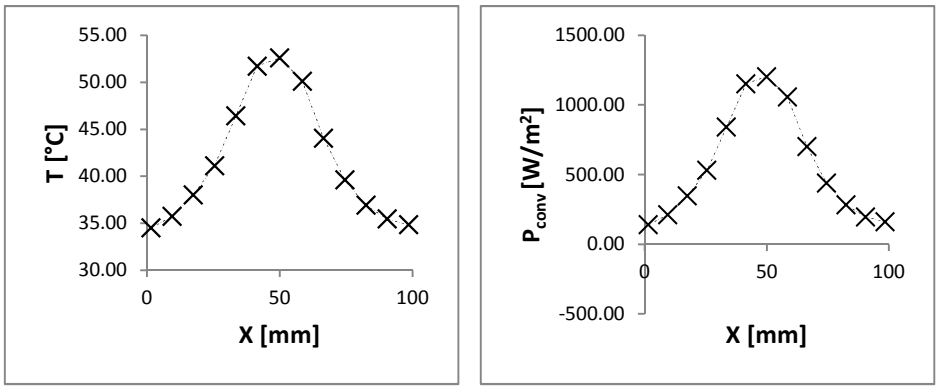

Figure 3.14: temperature and specific convective loss on the front surface for test C.

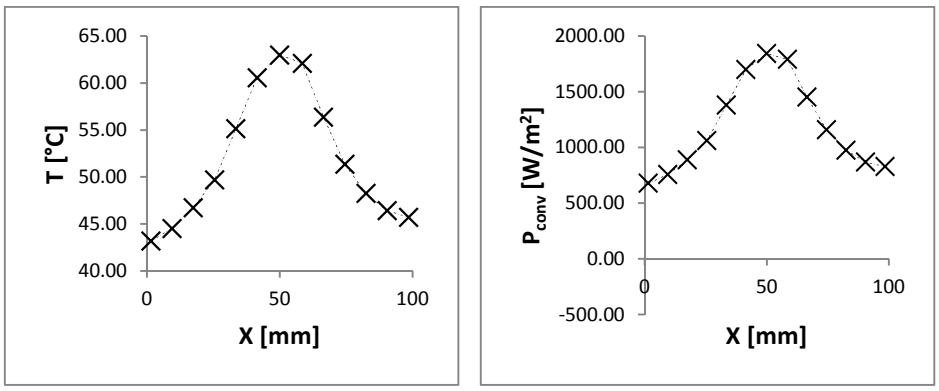

Figure 3.15: temperature and specific convective loss on the front surface for test D.

In order to purpose the present reflective structure to a manufacturer, together with the assessment of the optical performance it should be done a test of reliability of the mirror. A study of environmental durability has not to be done, anyway we can claim that reflector modules was outdoor exposed almost continuously for about two years at

temperature ranging from about -10 °C to 40 °C, without showing any degradation, delamination or silver corrosion due to exposure. This construction has proven to preventing water from coming in contact with the silvered material.

Chapter 4

Multijunction solar cells

4.1 Introduction

The core object of every CPV system, which allows converting the power carried by the sunlight into useful electrical power, is the photovoltaic device, i.e. the solar cell. In the work here presented we have adopted III-V multijunction (MJ) solar cells. These kind of solar cell was firstly introduced in the 70s from the Reasearch Triangle Institute, with the realization of a double junction AlGaAs/GaAs interconnected by a tunnel junction [Bedair et al., 1979]. Shirtly afterwards at the National Renewable Energy Laboratory (NREL) another device was proposed, consisting in a GaInP/GaAs tandem grown on top of a Ge substrate. Briefly this type of solar cell obtained large success in space application, due to the higher radiation tolerance and the lower temperature coefficient $d\eta/dT$ with respect to Si cells (η is the power conversion efficiency). In the early 90s triple junction GaInP/GaAs/Ge reached a record efficiency of 29.5% [Bertness et al., 1994], but the high cost of these materials made their use unsuitable for flat PV technology. For this reason the potential advantages of MJ solar cells in concentration system started to be investigated. In 1995, at NREL, the GaInP/GaAs designed for a direct AM1.5D spectrum demonstred efficiency of 30.2% at 160 suns [Friedman et al., 1995]. In recent years new solution have been introduced to enhance the performance of MJ devices, particularly at Spectrolab, and many worldwide manufactures started to developed this technology. In 2009 the Fraunhofer Institute announced a record efficiency of 41.1% with a 5.09 mm^2 triple-junction cell under a concentration factor of 454 X [Fraunhofer, 2009]. The cell is made out of $Ga_{0.35}In_{0.65}P$ and $Ga_{0.83}In_{0.17}As$ layers on germanium. The Fraunhofer

Institute applies metamorphic crystal growth: the semiconductors in these cells do not have the same lattice constant. The resulting crystal defects are localized in a region of the solar cell that is not electrically active, whereas the active regions of the solar cell remain relatively free of defects. In this way, the metamorphic crystal growth enables the use of much larger range of III-V compound semiconductors for growing multijunction cells, so that completely current matched III-V cells could be grown. This is also a good start for future generation III-V cells with 4, 5 and even 6 junctions. The authors of [Masafumi et al., 2008] and [Law et al., 2008] estimate on the long run the record cell efficiency to climb close to 50%. Commercial triple-junction III-V cells are now in the range of 35% to 39% depending on the manufacturer. These already impressive efficiencies are expected to climb to around 45% in a few years with 4-junction cells. In 2012, the triple junction cell manufactured by Solar Junction has demonstrated a record efficiency (NREL verified) of 44% at 947 suns [www.greentechmedia.com]. Commercial cell efficiencies are usually 2-3 % lower.

In spite of the type of solar cell, the basic knowledge of its operation principles is necessary to understand what is required for an optimal exploitation of the CPV technology A first objective of this chapter is to give a basic understanding of the physical principles that underlie the operation of MJ solar cells. To introduce the matter, a very basic description of the electrical behavior of a semiconductor solar cell is given in Section 4.2. The multijunction approach is then theoretically sketched out in Section 4.3 (a detailed expalnation can be found in [Olson, 2003] and [Cotal et al., 2008]), whereas the used triple junction solar cells (Spectrolab C1MJ) are described in Section 4.4. These type of solar cells has been specifically designed to work under concentration. In Section 4.5 the results of the I-V measurements at different concentration levels for the C1MJ cell are reported.

4.2 Solar cell *I-V* characteristics

A solar cell is simply a semiconductor diode designed to efficiently absorb and convert

the light energy from the sun into electrical energy. The explanation of the physical principles underlying the operation of solar cells can be found in a huge branch of specific literature (for example [Sze, 1981], [Gray, 2003], [Green, 1982]). Here we just give a basic expression for the current-voltage characteristics of a single-junction solar cell that will be useful to understand the behavior of multijunction devices under concentration.

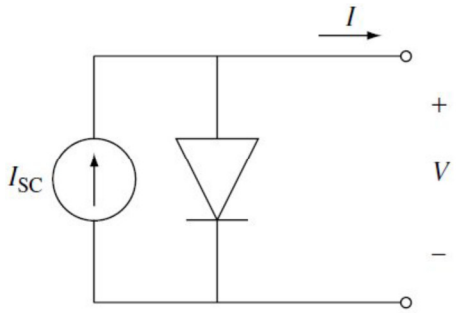

Figure 5.1: simplified solar cell circuit model.

From a circuit perspective, a solar cell can be modeled by an ideal current source in parallel with a diode, as shown in Figure 4.1. The direction of the current source is opposed to the current flow through the diode, that is, it serves to forward bias the diode. The general expression for the current produced by a solar cell as a function of the bias voltage is:

$$I = I_{SC} - I_0\left(e^{qV/nkT} - 1\right) \tag{4.1}$$

where I_{SC} is the shirt-circuit current, I_0 the dark saturation current, q the electron charge, k the Boltzmann's constant and T is the Kelvin temperature; n is the ideality factor and ranges between 1 and 2. This formulation is valid by neglecting the presence of series and shunt resistances.

At small applied voltages, the diode current is negligible and the current is just the short-circuit current, I_{SC} (Figure 5.2). When the applied voltage is high enough so that the diode current becomes significant, the cell current drops quickly. At open circuit ($I = 0$), all the light-generated current is flowing through the diode, so the open circuit voltage can be written as

$$V_{OC} = \frac{kT}{q} ln \frac{I_{SC} + I_0}{I_0}. \tag{4.2}$$

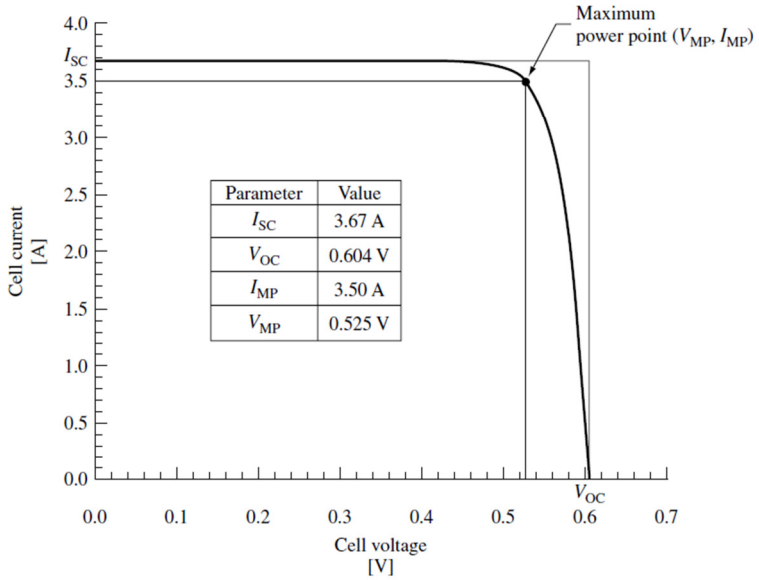

Figure 5.2: current-voltage characteristic of a typical silicon solar cell.

Of particular interest is the point on the $I-V$ curve where the power produced is at a maximum. This is referred to as the *maximum power point* with $V = V_{MPP}$ and $I = I_{MPP}$. The rectangle-defined V_{OC} and I_{SC} provides a convenient means for characterizing the maximum power point. The fill factor, FF, is a measure of the squareness of the $I-V$ characteristic and it is defined as the ratio of the areas of the two rectangles shown in Figure 5.2:

$$FF = \frac{P_{MPP}}{V_{OC}\, I_{SC}}. \tag{4.3}$$

The most important figure of merit for a solar cell is its power conversion efficiency, defined as

$$\eta = \frac{P_{MPP}}{P_{IN}} = \frac{FF\, V_{OC}\, I_{SC}}{P_{IN}} \tag{4.4}$$

where P_{IN} is the incident solar power.

4.2.1 Effects of concentration

The operation under concentrated illumination offers an advantage in the solar cell efficiency. If sunlight is concentrated by a factor of X (X sun illumination), the short

circuit at that concentration is

$$I_{SC}{}^{Xsuns} = XI_{SC}{}^{1sun}. \tag{4.5}$$

This is valid by assuming that the semiconductor parameters are unaffected by the illumination level and that the cell's temperature doesn't change. These are not necessarily valid assumptions especially at very large X, that is, X > 100. However, they will allow the demonstration of the potential efficiency of concentrator solar cells. Substituting Equation 4.5 into Equation 4.4 gives

$$\eta = \frac{FF^{Xsuns}\, V_{OC}{}^{Xsuns}\, I_{SC}{}^{Xsuns}}{P_{IN}{}^{Xsuns}} = \frac{FF^{Xsuns}\, V_{OC}{}^{Xsuns}\, I_{SC}{}^{1sun}}{P_{IN}{}^{1sun}} \tag{4.6}$$

From Equation 4.2, by assuming $I_{SC} \gg I_0$,

$$V_{OC}{}^{Xsuns} = V_{OC}{}^{1sun} + \frac{kT}{q} ln\, X \tag{4.7}$$

and so

$$\eta^{Xsuns} = \eta^{1sun} \left(\frac{FF^{Xsuns}}{FF^{1sun}} \right) \left(1 + \frac{\frac{kT}{q} ln\, X}{V_{OC}{}^{1sun}} \right). \tag{4.8}$$

Both factors multiplying the 1 sun efficiency increase as the illumination concentration increases. Therefore, the efficiency of concentrator cells increases as the illumination concentration increases. Of course, there are many obstacles to achieving this. Concentrator cells must be cooled, since an increase in operating temperature reduces V_{OC}, and hence the cell efficiency. The FF^{Xsuns} eventually decreases with increasing X and current due to the parasitic series resistance. The dependence of efficiency on concentration level is shown for a multijunction cell in the next section.

4.3 III-V Multijunction solar cells

Let's consider an ideal single junction (SJ) solar cell with a characteristic bandgap

energy E_g. A photon with energy $h\nu < E_g$ has almost zero probability to be absorbed and so it doesn't contribute to the photovoltaic process. On the other end, a photon incident with $h\nu > E_g$ is absorbed, but only a fraction $E = E_g$ can be converted in electric energy, whereas the excess energy in wasted in heat. Given that the solar spectrum spreads in the range 0-4 eV, the efficiency of a SJ cell is much lower than the efficiency that could be reached for monochromatic light ($E = E_g$).

Multijunction solar cells can make better use of the solar spectrum by having multiple semiconductor layers with different E_g. Each layer, usually a III-V semiconductor, is designed to absorb a different portion of the spectrum. Let's suppose to divide the full spectrum in three regions $(h\nu_1, h\nu_2)$, $(h\nu_2, h\nu_3)$, $(h\nu_3, \infty)$, where $h\nu_1 < h\nu_2 < h\nu_3$. The solar energy correspondent to these three regions can be converted in as much subcells having bandgap $E_{g1} = h\nu_1$, $E_{g2} = h\nu_2$ and $E_{g3} = h\nu_3$, where the top subcell has the largest bandgap (E_{g3}) and the bottom cell has the lowest bandgap (E_{g1}) as in Figure 5.3. This way the top subcell absorbs the photons with $h\nu > E_{g3}$, the middle one absorbs in the region $E_{g2} < h\nu < E_{g3}$ and the bottom one in the region $E_{g1} < h\nu < E_{g2}$.

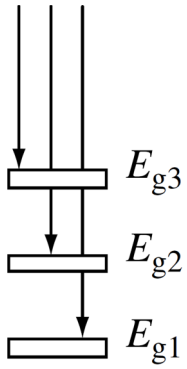

Figure 5.3: multijunction stacked approach.

By increasing the number of the spectral regions and thus reducing the energy intervals of each region, the energy losses through thermalization can be reduced. In fact, it can be demonstrated that the ideal efficiency limits at 1000 suns in case of 1,2 ,3 and 36 partitions of the solar spectrum, are 37, 50, 56 and 72% , respectively [Henry, 1980].

Several mechanisms prevent the cell's efficiency to reach these theoretical values.

First of all, the loss probability for a photogenerated carrier increases with the number of the interfaces inside the multilayer structure, that are preferential locations for electron-hole recombination. In practice, the feasibility of a device with more than 3 or 4 junctions is improbable.

4.3.1 Subcells interconnection

The most effective and economically affordable multijunction approach is the multilayer stacked one. The junctions are fabricated each one atop the last, starting from a single substrate and where the subcells are series-connected. This configuration requires the subcells to be of the same polarity and the photocurrents of the subcells to be closely matched, since in series connection the subcell with the least photocurrent limits the current generated by the entire device. This current-matching constraint puts relatively tight constraints on the selection of band gaps.

The connection between two subcells is realized through a tunnel junction (TJ) diode. Without the TJ, the base layer of a cell and the emitter layer of the contacting one would form a p-n junction having a polarity voltage that is in opposition to that of the top or bottom cells, and, when illuminated, would produce a photovoltage that could roughly negate the photovoltage generated by the top cell. The existence of high-quality monolithic TJ interconnects means that these stacks can be made as monolithic SJ structures with metallization at the very top and bottom of the stack only. This way such devices can be integrated into modules with the same simplicity afforded by traditional devices.

4.3.2 Choice of materials

A typical triple junction solar is composed by about 20 layers with thicknesses between 10 nm (TJ) and about 100 μm (active layers). The Figure 5.4 shows the structure of a cell with three p-n junctions $Ga_{0.5}In_{0.5}P$, $Ga_{0.99}In_{0.01}$ and Ge. The non-active layers have different compositions and consist, beyond the TJs, of passivation layers and barrier layers for the internal processes of atomic diffusion.

All the high-efficiency III-V multijunction solar cells are produced by epitaxial growth on a single substrate. Many techniques allow depositing layers of monocrystal semiconductors, as molecular epitaxy or the liquid epitaxy, and presently the leading

technique is the organometallic vapor phase epitaxy (OMVPE) [Stringfellow, 1999]. In order to fabricate an efficient MJ structure some restrictions have to be satisfied for the materials to be used. First of all, given a substrate (for example Ge), the layers on top must have similar lattice constants. Otherwise, the reticular mismatch

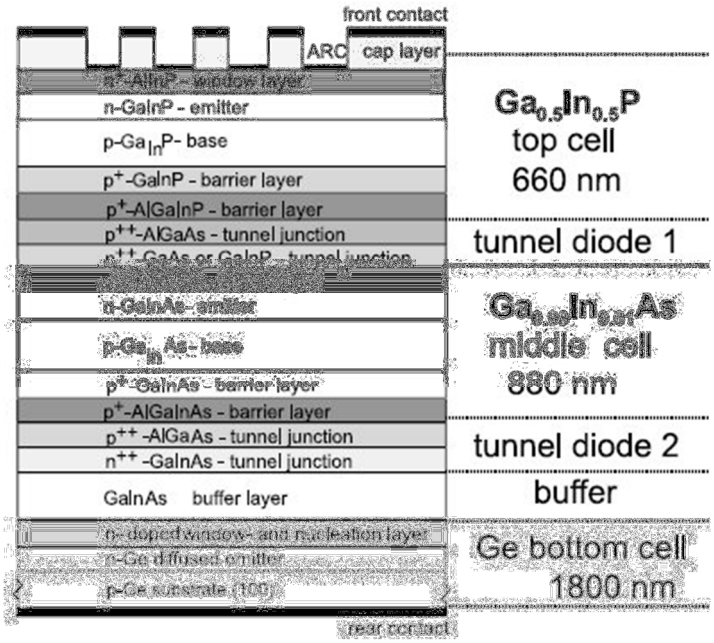

Figure 5.4: Typical structure of a monolithic triple junction solar cell.

determines the nucleation and the propagation of dislocations and other defect types along the layers' interfaces. These interface defects behave like non-radiative recombination centers; the resulting effect is that of limiting the lifetime or the diffusion length for the photogenerated carries, thus reducing the efficiency of the device. The choice of the materials has to consider materials with certain bandgap energies and with about the same lattice constant.

Figure 5.5 shows the possible combinations with materials of the IV group and alloys from the III-IV groups. The lines through binary compound represent ternary alloys with middle composition between binary compounds. For example, the compound $Ga_xIn_{1-x}P$ with x = 0.5 has about the same lattice constant of GaAs and Ge.

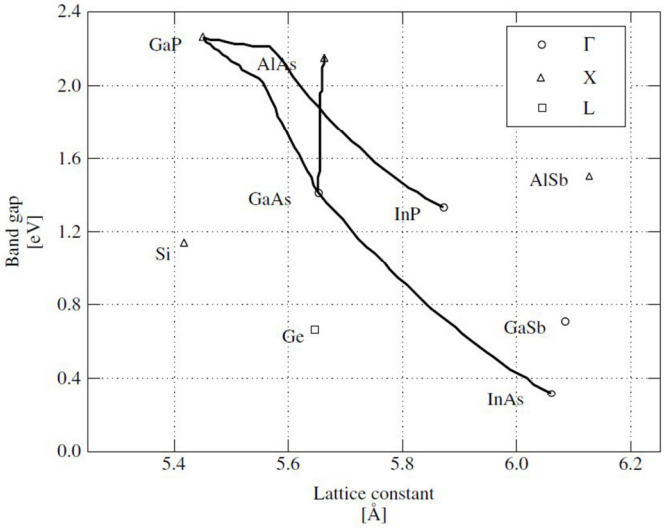

Figure 5.5: bandgap energies and lattice constants for different semiconductor material [Olson et al., 2002].

4.3.3 Current-voltage curves and working conditions.

The electrical behavior of a multijunction cell can be determined with good approximation if the individual current-voltage (I-V) characteristics of the subcells are known. For a stack of series connected subcells, given the characteristic $V_i(I)$ voltage for the *i*-esim subcell, the overall curve is given by:

$$V(I) = \sum_{i=1}^{n} V_i(I) \tag{4.9}$$

that is, the voltage at a current value is equal to the sum of the correspondent subcells's voltages. Every cell has its own maximum power point (V_{MPi} , I_{MPi}). The currents of the various subcells are forced to have the same value, so each cell can work in its MPP just its I_{MP} is the same for all the subcells, i.e. $I_{MP1} = I_{MP2} \ldots . = I_{MPn}$. If this condition is satisfied, the maximum power of the MJ device is the sum of the various maximum powers of the subcells $V_{MPi} \cdot I_{MPi}$; otherwise some subcell is constrained to work out of its MPP.

This consideration makes it clear the first reason why the working efficiencies of the MJ are lower than the efficiencies measured under indoor solar simulators. In fact, a certain bandgap combination (and the relatives thicknesses of the subcells) is

optimized for a certain shape of the incident solar spectrum, in order to reach the current matching for the subcells. For example, the efficiency of MJ solar cells is given for an incident AM1.5D spectrum, which in real operation conditions is different most of the time and depends on parameters like latitude, local time, season, weather conditions, spectral variations introduced by optical elements of the CPV system.

Others main factors that limit the efficiency of single MJ solar cells in operative conditions with respect to reference conditions, are temperature and illumination non-uniformity. Actually, the temperature of a working MJ solar cell in a CPV system can be much higher than 25 °C. The deleterious effect of increasing temperature (that will be briefly sketched in Paragraph 7.2.1) can be seen by example from the case of a 2J GaInP/GaAs solar cell, which shows an open voltage reduction $\frac{dV_{OC}}{dT} = -4\ mV/°C$ [Friedman, 1996].

The distribution of the illumination on the cell produced by the concentrating optical element is not uniform across the cell's surface. By example, the RXI concentrator at the University of Madrid has a mean concentration value of about 1000 suns and peak values of nearly 3000 suns [Algora et al., 2000]. In case of both SJ or MJ solar cells, the transversal gradient of the photocurrent (due to the non-uniform photogeneration) involves an increase of the transversal current's components. The global effect is similar to that resulting from the increase in the series resistance of the cell itself, thus reducing the photovoltaic conversion efficiency. An in-depht analysis of non-uniform illumination on solar cells can be found in [Algora, 2007] and [Anton et al., 2001].

4.4 Spectrolab C1MJ

The photovoltaic multijinction devices that have been used in the present work are the Specrolab CDO-100-C1MJ[2] solar cells, that are commercially available since 2006. The datasheet here reported can be found in [Spectrolab, 2010].

[2] Currently the 4th generation C4MJ is available, with typical efficiency of 40% (http://www.spectrolab.com/dataSheets.html).

C1MJ e cells have a structure based on GaInP, GaInAs and Ge in reticular matching conditions, and have an aperture area of 98.8 mm^2. The top contacts are realized with silver metallization on busbars (0.5 mm width) and grid fingers (Figure 5.6). On the back surface, the silver metallizations is coated with a 500 Å gold layer.

Spectrolab declares that the operating temperature has to be lower than 100 °C and that this structure can resist to temperatures up to 350 °C. The efficiencies at 25 °C and for a AM1.5D spectrum present a distribution from about 34.5 to 39.5 %, with a peak volume of devices with 37 % efficiency. A current-voltage curve at 50 W/cm^2 is

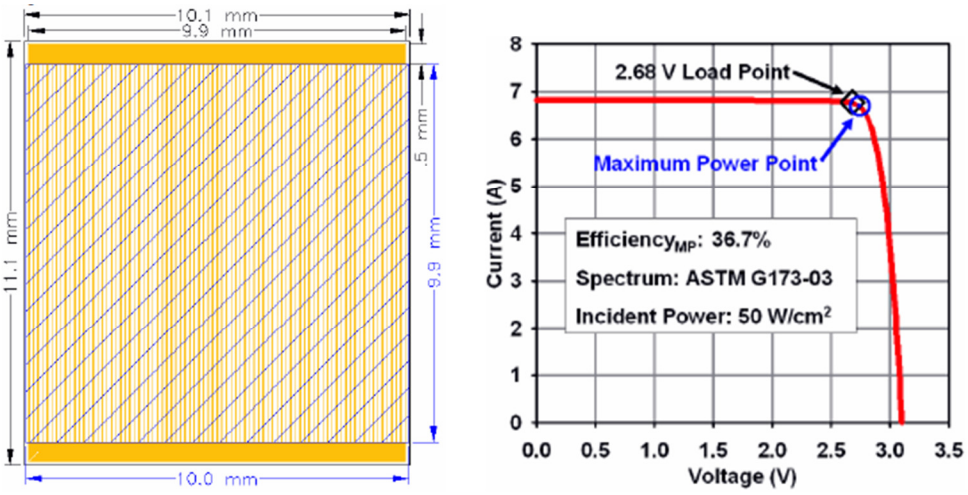

Figure 5.6: dimensions of the C1MJ solar cell (left); current-voltage characteristic (right).

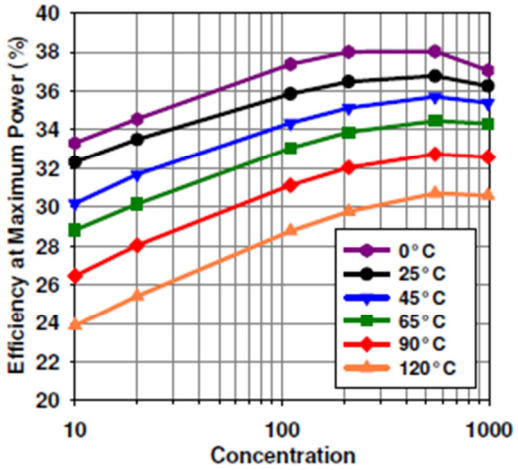

Figure 5.7: efficiency of the C1MJ solar cell as a function of the concentration for different temperatures.

also reported in Figure 5.6; shirt circuit current reaches a value close to 7 A.

The behavior of the C1MJ cell for different concentrations (10-1000 suns) and temperatures (0-120 °C) is displayed in Figures 5.7 and 5.8. The efficiency increases almost uninterruptedly from 10 suns to 1000 suns, reaching a maximum value between 500 and 600 suns. For example, it starts from 33% at 0 °C, reaches a maximum of 38.5 % and then decreases to 37% at 1000 suns. Every 20 °C of increase in temperature, the efficiency loss is between 1 and 2%: from 24 °C to 120 °C a rate of $\frac{d\eta}{dT} \approx -0.06 \div 0.08\ \%$ is estimated. The trends for the voltage at maximum power point V_{MP} are similar, and an approximate rate value of $\frac{dV_{OC}}{dT} \approx -5\ mV/°C$ can be extracted.

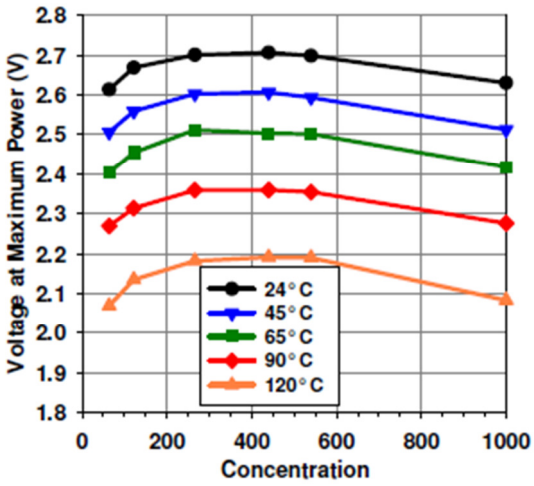

Figure 5.8: voltage at the maximum power point for the C1MJ solar cell as a function of the concentration for different temperatures.

4.5 Concentration measurements

The present electrical measurements of a C1MJ cell under concentration have been performed to evaluate the reliability of the measurement process itself, and to reproduce the trends of the cell's parameters supplied in the Spectrolab datasheet.

A single cell was soldered to a copper heat sink (4 mm thick, water cooled), and

two copper flexible cables were welded to the cell's busbars in order to realize the front contacts. This PV receiver assembly was placed in the illumination spot produced by the concentration system, with just one parabolic sector mounted on the sun-tracking structure, a little out of focus (2490 mm from the paraboloid origin) in order to enhance the illumination uniformity. The precise position of the cell in the concentration plane was checked by means of a laser pen fixed on the concentrator's shaft. The sky was clear and the illumination conditions were stable (12/06/09), so that no important variations have occurred during the measure's time. Before mounting the PV receiver, several illumination spots at different concentration levels were acquired with the thermopile/plotter system. The variation of concentration levels on the cell was obtained by progressively shadowing some portions of the mirror's surface by means of a rotating metal shield (pivot on the origin of the paraboloid). Seven illuminations have been acquired, correspondent to 2°-8° portions of the reflecting parabolic sector. The original idea was to assess the power incident on the cell's frame as the mean power measured on 9 point, 0.5 mm far one each other. Unfortunately, this procedure has turned out unreliable; the illumination level on the cell was too difficult to reproduce and evaluate due to the difficulty in exactly placing the device in the spot frame, which was previously scanned. Moreover the shadowing of the sector's slices wasn't precise enough. For this reasons, the concentration I-V curves have been measured without assessing the power conversion efficiency.

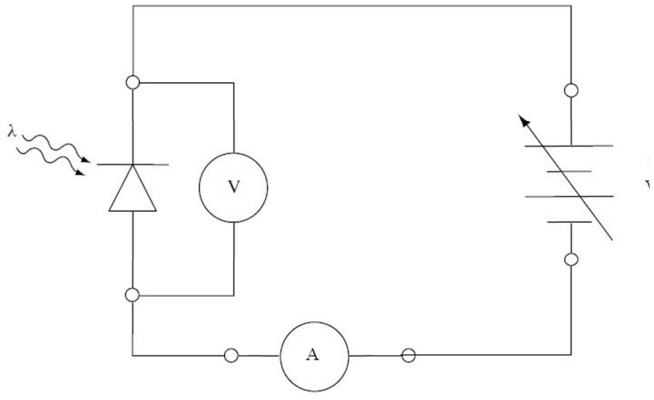

Figure 5.8: electrical schematic for the I-V measurements; the cell and the measurements devices are connected to an external variable load.

The measurements has been performed with an ammeter, a voltmeter and an electronic variable load (R ≥ 0.6 Ω), according to the schematic of Figure 5.8. The entire measurement process has required less than 25 min. The first measurement refers to non-concentrated sunlight; a cell was fixed on the sun-tracking system turned over the sky and pointed to sun[3]. The pointing was made with the assistance of a pyroheliometer, but the incident power was measured with a pyranometer, in order to consider the diffuse part of the light content, too.

4.5.1 Results

The measurement under non-concentrated sunlight (solar flux of 940 W/m^2) reveals a maximum power delivered to the load P_{MP} = 27.4 ± 0.1 mW, and in this point the efficiency is 29.1 ± 0.7% (see Figure 5.9). During this acquisition the temperature, as measured on the copper receiver near the cell with a k-thermocouple, was 23.5 °C. The efficiency could be slightly lower than the expected one (extrapolating the 1-sun efficiency from the Spectrolab datasheet at 25 °C), probably due to the fact the

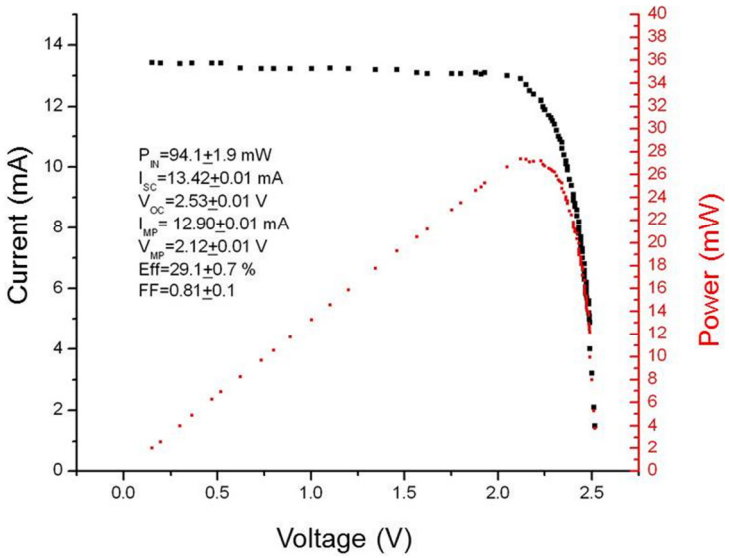

Figure 5.9: I-V and P-V curves for the C1MJ under non concentrated sunlight (global solar flux 940 W/m^2).

[3] The mirror was obscured; the placing of the cell in the CPV system was only aimed to the properly pointing to the sun.

incident light refers here to a global spectrum instead of a direct spectrum (these cells have been designed and optimized to work under the direct AM1.5D spectrum). Anyway, the Fill Factor (FF) is 0.81 ± 0.01, which is a similar value to the FF reported in [King et al., 2007] for a C1MJ cell in standard conditions.

In the graphs of Figures 5.10-5.15 are shown the I-V curves for increasing illumination power on the cells. These power levels correspond to the illumination produced by slices of de-shielded mirror from 2° to 7°. The values for the open circuit voltage (V_{OC}) have been calculated with a linear fit through the I-V points near the zero current points. At the same way the shirt circuit currents have been extrapolated from linear trends, even if the points near to $V = 0$ haven't been measured due to the

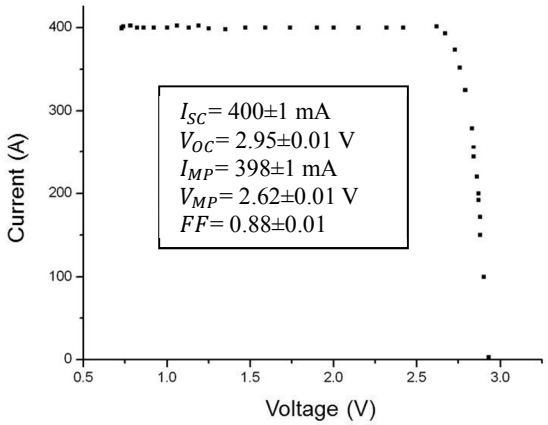

Figure 5.10: I-V curve for a 2°aperture of the parabolic sector.

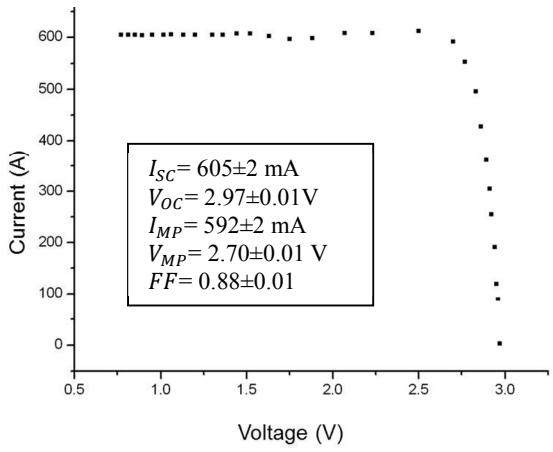

Figure 5.11: I-V curve for a 3°aperture of the parabolic sector.

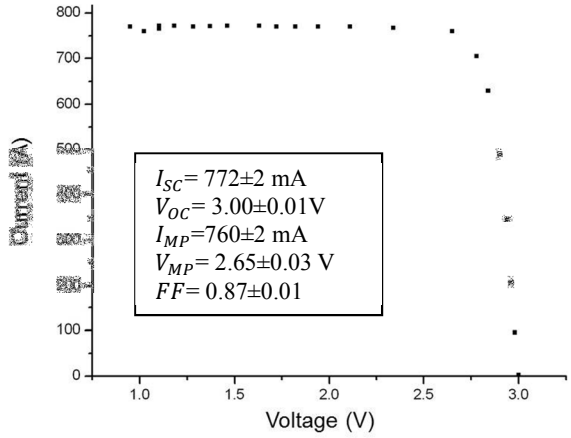

Figure 5.12: I-V curve for a 4°aperture of the parabolic sector.

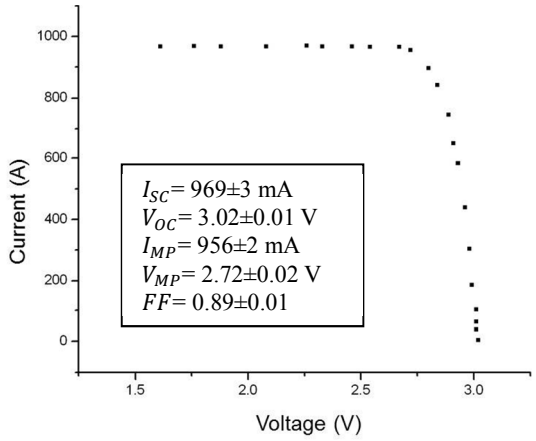

Figure 5.13: I-V curve for a 5°aperture of the parabolic sector.

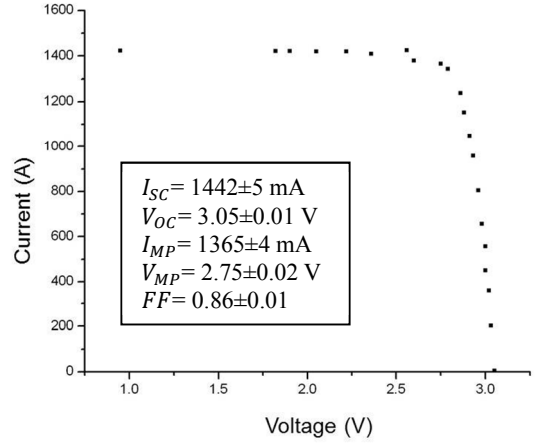

Figure 5.14: I-V curve for a 6°aperture of the parabolic sector.

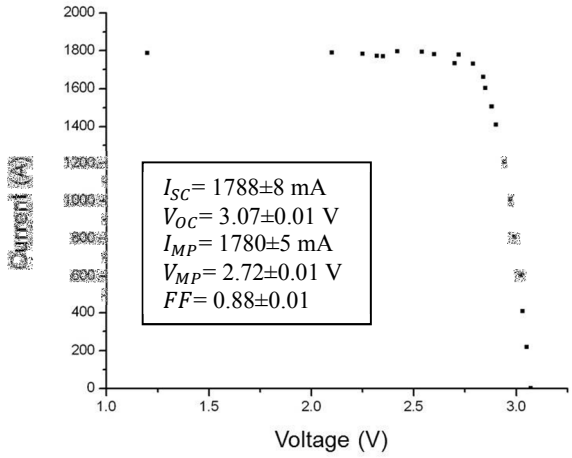

Figure 5.15: I-V curve for a 7°aperture of the parabolic sector.

electrical resistances of the measurement apparatus (~1.3 Ω). In the last acquisitions, a I-V point bypassing the electronic load has been measured. The temperature on the heat sink remained in the range between 17.5 and 18.7 °C, and thus the possible increases of the cell's temperature are consequence of the assembly process only. The highest current that has been measured is of about 1.8 A, and this leads to suppose a concentration levels incident on the cell of about 130 suns (by assuming a linear relation between I_{SC} and incident solar power).

The FF values are in the range between 0.87 ± 0.01 and 0.89 ± 0.01, and they agree with the values reported in [King et al., 2007]. The FF parameter is not influenced by the evaluation of the incident power P_{IN}, but only depends upon the electrical behavior of the cell itself. In particular the increase of FF with respect to the case of non-concentrated sunlight (0.81 ± 0.01) states that the ratio I_o/I_{SC}, with I_o dark saturation current, decreases under concentration. This points out that these cells take advantage of the operation in CPV systems. Actually the FF is expected to constantly increase with the concentration level, at least to a certain limit value. This hasn't been verified, but it should be considered that the present working conditions (spectrum, illumination uniformity, temperature) may have been significantly different than standard conditions. In [Olson et al., 2002] it has been simulated that FF strongly depend upon the current matching condition between the subcells within the multijunction structure. The sub-current matching can be perturbed by both the real incident spectrum and by the non-uniform illumination on the cell. In fact, non-

uniform incident light cause temperature and band-gap variations, that impact the fractions of absorbed sunlight and the correct current distribution. Moreover the non-uniformity causes an increase of the equivalent series resistance of the cell (R_S), that could have degraded the FFs due to the Joule effect losses. Low FF values in semiconductor solar cells often indicate high R_S.

During the acquisition at the 8° mirror's aperture, the cell broke. This was established and confirmed by the open circuit voltage V_{OC} = 0.18 V under non concentrated sunlight (~850 W/m^2), much lower than the expected 2.5 V. The most probable reason for this failure is the different thermal expansions between the copper and the cell's materials that, as the temperature increases, may have led to stress accumulation and mechanical cracks phenomenon. This situation could have deteriorated due to the presence of voids in the solder layer. The possibility of re-melting of the solder material has been ruled out pursuant to an observation with the optical microscope.

Chapter 5

Problem of non-uniform illumination in dense array receivers

5.1 Introduction

When a parabolic dish of large area (more than 0.3 m^2 aperture area at 500 X) is used for CPV applications, the electrical power conversion cannot be managed by a single solar cell, so a multi-cell receiver is required. Parabolic dish receivers, in general, use a 'parquet' of solar cells arranged in rectangular arrays having a certain number of rows and columns [Verlinden et al., 2006]. Main problems related to the dense array receivers are: i) high thermal flux to be dissipated to keep the cell working at ambient temperature ii) gradient of power density on the cell, iii) differences in illumination and temperature between the cells of the array.

This chapter is focused on the solution of the last problem which is the main responsible of two technological issues known as 'current matching' and 'maximum power point tracking'. The I-V curve of the array depends on which types of connections have been used to realize the array and therefore it is related to the 'current matching' issue, that is the choice of the appropriate type of connection with respect to the operative working situation (incident solar radiation, temperatures, types of cells) to ensure the maximum power transfer to the load. In order to reduce the Joule I^2R losses, series connection is required at least partially so that more power can

be conveyed with lower current. 'Maximum power point tracking' problem is the research of the maximum power point (MPP) along the total *IV* curve of the array, even in presence of externals changes like solar radiation and temperature fluctuations.

The following sections are organized as follows. Firstly, the effects of current mismatching between the connected cells are discussed. Then a theoretical analysis of electrical behavior of CPV multijunction array is presented, with respect to the current mismatching level. Finally the problem of power transfer to the load is treated. Two new types of electrical connections between the cells are presented, and they are validated trough simulation. The experimental proof is the subject of Chapter 6.

5.2 Effects of current mismatch

Cell current mismatch is a main problem for CPV system, above all in case of dense array system where the illumination level on the cells is not uniform. Flat panel photovoltaic is affected by the same problem as well, for example it occurs when a cell in a series connected string is shaded or damaged preventing it from generating current equal to the other cells. Here it will be explained why mismatch results in degradation to the module and to lower power output from a general point of view.

5.2.1 Formation of hot spots and bypass diodes

Figure 5.1 (a) shows the equivalent circuit of two cells series connected in short circuit condition. The two cells are both generating equal current, shown in green, which flows through the external circuit. The voltage across each cell is zero so there is no forward bias current flowing through the diode of the cell [http://pveducation.org/pvcdrom/modules/mismatch-for-cells-connected-in-series22]. Figure 5.1 (b) shows the open circuit conditions of the two cells generating matched currents. No current flows through the external circuit so each cell is forward biased by its own photogenerated current. The open circuit voltage of the entire module is equal to the sum of the open circuit voltage of the two cells.

The same cell configuration in short circuit but with cell mismatch is shown in

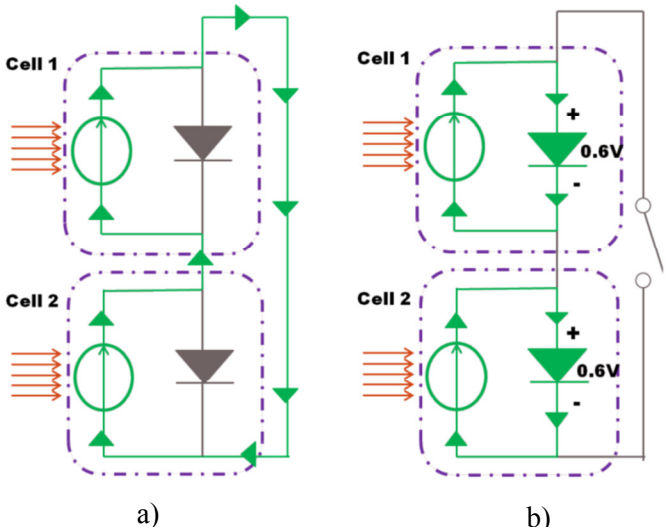

Figure 5.1: The equivalent circuit of two matched solar cells in a) short circuit and b) open circuit conditions

Figure 5.2 (a). Cell 2 has half the photogeneration current with respect to Cell 1. The current generated by the weak cell is the maximum that can flow through the external circuit limiting the current output of the two cells. Cell current produced is unable to flow through the external circuit so the extra current flows though the diode forward biasing the cell. In short circuit conditions the net voltage over the two cells must

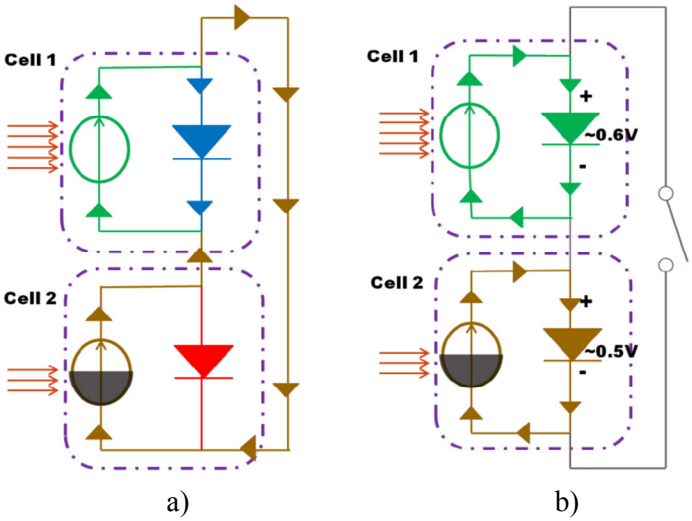

Figure 5.2: The equivalent circuit of mismatched cells under a) short circuit and b) open circuit conditions.

be zero and to maintain this condition the Cell 2 must be reverse biased in magnitude equal to the forward bias of Cell 1. When a cell is reverse biased it changes from a power generator to a current dissipater and may generate heat. This localized heat generation results in a hot spot which can cause damage to the cell material, melting the interconnection solder, and cracks in the protection glass [Meyer and Dik, 2004].

Performance degradation and hot spot formation due to cell current mismatch can be prevented by the use of bypass diodes. Bypass diodes are connected in parallel over the cells as indicated in the scheme of Figure 5.3 (a). In matched current conditions the bypass diodes are reverse biased and have no effect [Overstraeten and Mertens, 1986] However in presence of current mismatch, instead of the weak cell being reverse biased as in Figure 5.2 (a) the bypass diode is forward biased and conducts the extra current produced by the good cell as seen in Figure 5.3 (b). The weak cell is still reverse biased but only by about 0.5 V, which is the activation voltage of the bypass diode. The current through the external circuit is now not limited by the weak cell once the bypass diode is activated.

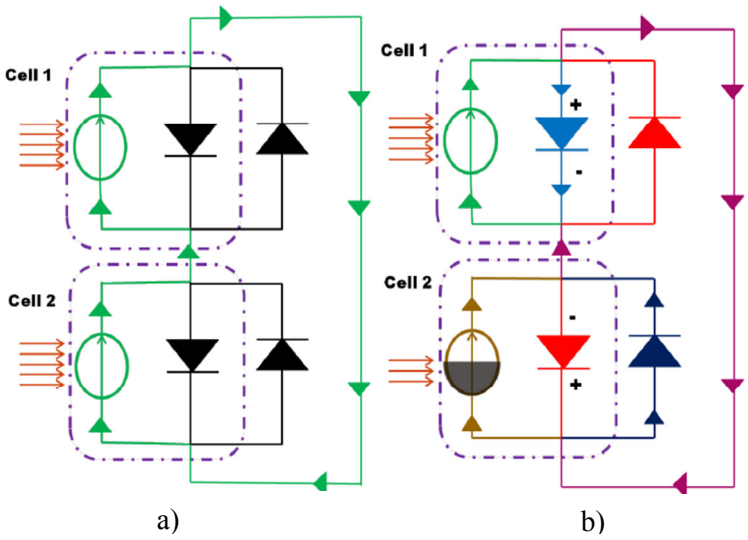

Figure 5.3: The equivalent circuit of two solar cells with parallel bypass diodes in short circuit conditions with a) matched and b) mismatched currents

In this simple example a bypass diode is parallel connected to each cell. This is not practical in large flat PV module, and usually bypass diodes are connected over series connected strings of cells. Differently in CPV receivers, where the number of cells is lower, bypass diodes are connected to each cell. The presence of the diodes is not

problematic for a CPV Fresnel lens panel: in this case there is a large spacing between the cells receiving concentrated sunlight, so that the bypass diodes can be placed near their relative cell. The situation is different for a dense array CPV receiver, where the placement of the cells' parquet must be optimized in order to maximize the luminous power absorbed by the cells themselves. The effects of bypass diodes activation on the I-V characteristic curve are discussed further in the next section.

5.2.2 Effect of current mismatch on 3 series connected cells

When cells are connected in series the total current is limited by the weakest cell while the voltages add as normal. In Figure 5.4 one cell out of three series connected cells present a photocurrent reduced by about 50%.

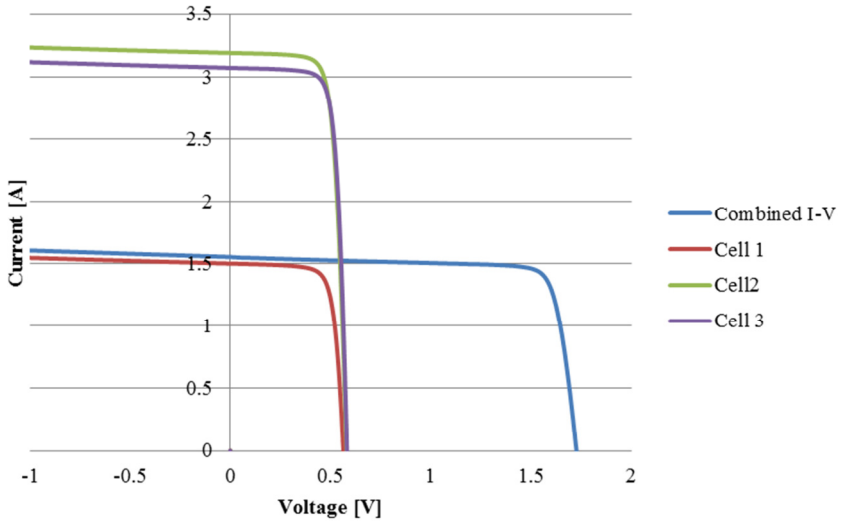

Figure 5.4: The effect of mismatch in series string of three cells with one cell shaded 50% [King et al., 1996].

The effects of mismatch can be mitigated by using bypass diodes connected in parallel over the cells. The activation of the bypass diode (when the reverse bias in the weak cell equals the transmission voltage of the bypass diode) results in a step in the I-V curve. This can be seen for three series connected cells with bypass diodes parallel connected across them, where one cell present a 50% photocurrent (Figure 5.5). The resultant curve has a step related to the activation of the bypass diode over the mismatched cell.

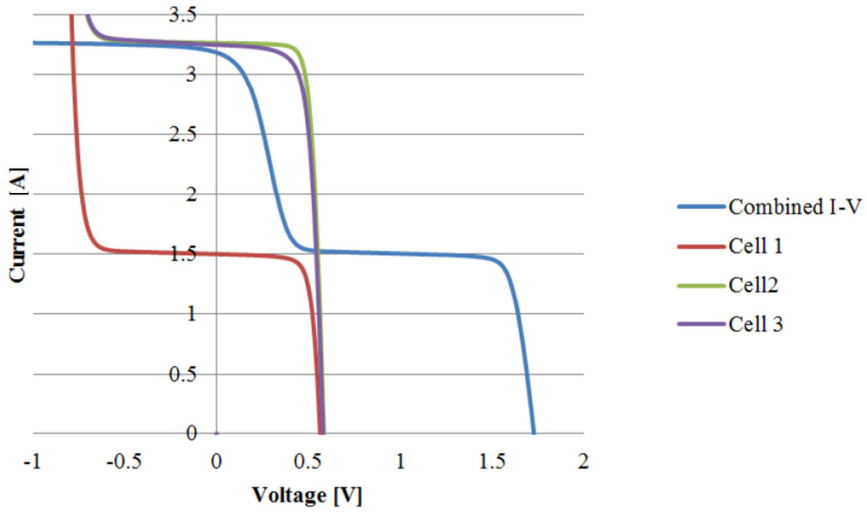

Figure 5.5: The effect of shading one cell in a 3 cell series string by 50% on the resultant I-V curve with bypass diodes connected across each cell [King et al., 1996].

5.3 Mismatch analysis of a CPV multijunction array.

In the previous section, the mismatch effect on a simple generic PV module is presented. In order to understand the effect on a more complex CPV multijunction array, a theoretical modeling is needed, with reference to the mismatch level and series resistance effects. The present analysis follows the approach proposed in [Minuto et al., 2010], which analyze the I-V curve of a photovoltaic module composed by a certain number of series connected receivers (made up of a certain number of parallel connected photovoltaic cells), each connected to a bypass diode. This analysis is here adapted to an array comprising N series connected MJ. It will be shown useful for predicting the I-V curve and the maximum power point of the array.

5.3.1 Theoretical mismatch analysis

The modeling of a CPV array made of a number N of series connected MJ cells is developed starting from some assumptions on the array equivalent circuit. First of all, in each sub-cell making part of a multijunction solar cell, the generation–recombination current in the depletion layer is neglected, since it is assumed that the

high concentration of solar light produces enough carriers to saturate the energy level of the defects. The cell shunt resistance effects are neglected, too, since they can be usually hidden by more relevant mismatch problems. It can be shown that, under the above assumptions, a given multi-junction solar cell (labeled with i) is formally equivalent to a single-junction solar cell which is characterized by three equivalent parameters: $I_{0,i}$, the equivalent inverse saturation current; n_i, the equivalent ideally factor; $R_{S,i}$, the cell series resistance [Timò et al., 2010]

When the cells are exposed to sunlight, if no spectral mismatch between the three sub-cells is considered, a single shirt circuit current is associated to each MJ cell, $I_{SC,i}$. The connecting cables are taken in count by introducing their resistance R_{CAB}. Let's write the I-V characteristic for each cell and the current and voltage identities for the array made up of N series connected MJ cells:

$$I_i(V_i) = I_{SC,i} - I_{o,i}\left\{\left[\frac{\exp[q(V_i + I_i R_{S,i})}{n_i\, KT}\right] - 1\right\} \tag{5.1}$$

$$I = I_1 = I_2 = \ldots\ldots\ldots = I_i \tag{5.2}$$

$$V_{array}(I) = \sum_i V_i(I) \tag{5.3}$$

where $i = 1, 2, \ldots N$ numerates the cells, I is the series current load and $V_{array}(I)$ is the array voltage.

By assuming equal ideally factors $= n_1 = n_2 = \ldots\ldots\ldots = n_i$, which is a reasonable assumption for identical cells, and defining $\frac{q}{nKT} = m$, the following equation describes the I-V curve of the array:

$$V_{array}(I) = \frac{1}{m}\sum_{i=1}^{N} \ln\left(\frac{I_{SC,i} - I}{I_{o,i}} + 1\right) - I\sum_{i=1}^{N} R_{S,i} - IR_{CAB} \tag{5.4}$$

Now let's consider the presence of bypass diodes. Each cell has a parallel connected bypass diode that allows, in case of current mismatch between the cells, the protection of the cells from inverse polarization and, in some cases, to partially recover the array electrical power. If the cells are sorted in function of their shirt circuit current value, from the highest to the lowest one, the array voltage can be written as:

$$V_{array}(I) = \sum_{i=1}^{N}\left[\sum_{z=1}^{i}\frac{1}{m}\ln\left(\frac{I_{SC,z}-I}{I_{o,z}}+1\right) - I\ln\left(\frac{I_{SC,i}-I}{I_{o,i}}+1\right)\right. \tag{5.5}$$

contribution of the i – active cells

$$\left. -I\left(\sum_{i=1}^{N}R_{S,i}+R_{CAB}\right) - \sum_{z=1+i}^{N}\frac{KT}{q}n_{by}ln\left(\frac{I-I_{SC,z}}{I_{o,by}}+1\right)\right]\cdot w_i(I)$$

drop on the circuit resistances drop of the N- i bypass diodes of the N- i passive cells

where n_{by} is the ideally factor of the bypass diodes, $I_{o,by}$ is the inverse saturation current of the bypass diodes I is the current load and $w_i(I)$ is defined as:

$$w_i(I) = \begin{cases} 1 & if \quad I_{SC,i+1} < I \leq I_{SC,i} \\ 0 & for\ all\ other\ cases \end{cases} \tag{5.6}$$

Equation 5.5 is valid if the cells are sorted from 1 to N by starting from the highest I_{SC} to the lowest. All the cells producing $I_{SC} > I$ give a voltage contribution. These voltage values are summed, while the other cells are inverse-biased and the voltage drops associated to their bypass diodes have to be subtracted.

Before discussing the general theoretical implications, it is useful to define the following quantities. The i-cell mismatch degree within the array is defined by introducing the maximum cell shirt circuit current ($I_{SC,max}$):

$$M_i = \frac{I_{SC,max} - I_{SC,i}}{I_{SC,max}} \tag{5.7}$$

The k index, with k=*1…N*, is the cell mismatch order. The cell mismatches are sorted in function of their mismatch value, with k decreasing. This way the cell with k=*1,* has the highest current mismatch, $M(k=1)$, while the cell with k=*N* is considered without mismatch.

The array power loss ($PL_{\%}$) is referred to the maximum electrical power that would be delivered in case of zero mismatch (P_{max}), and to the measured electrical power (P_{meas}):

$$PL_{\%} = 100\ \frac{P_{max}\ - P_{meas}}{P_{max}} \tag{5.8}$$

From Equation 5.8, it can be shown that the *I-V* curve of the array presents a maximum number of current steps equal to the number of mismatched cells (the number of mismatched cells can be higher than the number of current steps), and this is due to the presence of the bypass diodes connected to each cells. The curve of an array having mismatched cells but without bypass diodes doesn't have current steps. As a consequence, while the *P-V* curve of the array without by-pass diode presents a single canonical power peak (P_0), power extra-peaks are found for the array with bypass diodes. The maximum number of these extra-peaks is again equal to the number of mismatched cells.

The value of voltages corresponding to the power extra-peaks decreases with the mismatch order, so that, for example, the cell without mismatch corresponds to the highest voltage peak. The value of the power extra peak of k order is indicated by P_k. This value is a decreasing function of the cells mismatch values having higher mismatch order

$$P_k = f[M(k+1), M(k+2) \ldots M(N-1)] \tag{5.9}$$

and doesn't depend on the mismatch values of the cells having lower mismatch order $M(k-1), M(k-2)\ldots$

A critical cell mismatch value M_{cr} can be defined. When $M(1) > M_{cr}$ ($M(1)$ is the highest one) it exists a power extrapeak whose value is higher than the canonical power peak: $P_k > P_0$. In general the critical receiver mismatch is a function of the number N and of the number of mismatched cells. If $M(1) > M_{cr}$ the bypass diode allows to partially recovering the array electrical power, while if $M(1) < M_{cr}$, the bypass diode is not effective in recovering the electrical power. Therefore, the electrical configurations which correspond to a lower value of M_{cr} are more effective in enhancing the electrical power extraction from the photovoltaic array.

When there is only one cell presenting current mismatch, the critical mismatch M_{cr} is the lower possible and is dependent of N only. In particular this critical mismatch value, here denoted by $M_{cr}*$, decreases with the increasing number of series

connected cells in the array (N). When the mismatched cells are several (a number t), this relation holds:

$$M_{cr}{}^{*} < M_{cr} < M_{cr}{}^{*} + \frac{(t-1)}{N} \tag{5.10}$$

The above considerations allow predicting the effects of a certain mismatched condition on the I-V curve and on the maximum power point of an array made up of N series connected cells. This analysis approach can be extended to more complex module configurations, for example a module consisting of a L series connected receivers made up of N parallel connected cells. Another benefit of this analysis is the possibility to identify the cells mismatches starting from the experimental I-V curve of the array.

The Figure 5.6 shows an example of I-V and P-V curves of a simulated CPV array composed by 18 series connected MJ cells [Timò et al., 2010]. Two power extra peak are present, due to as many mismatched cells. The current steps are also visible.

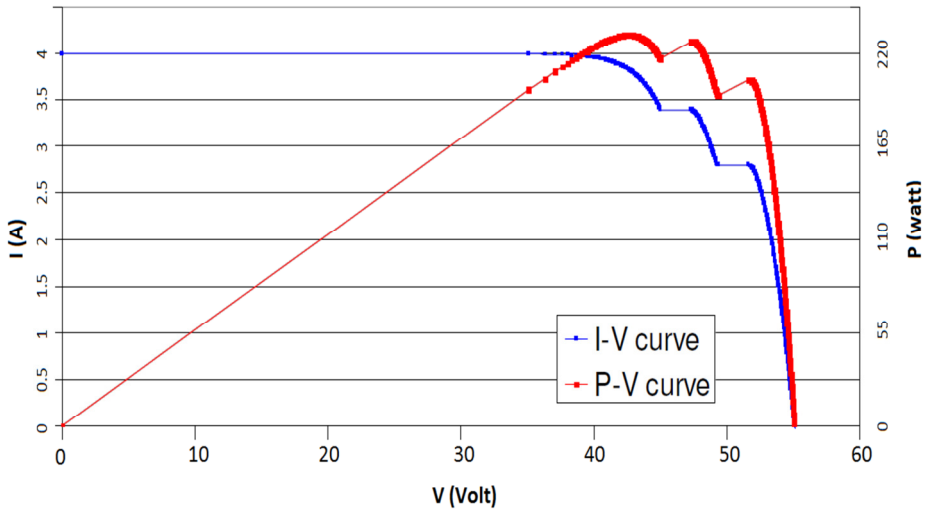

Figure 5.6: simulation of the electrical behavior of an array made up of 18 series connected MJ cells, among them 2 cells present a current mismatch. Both the I-V curve and the P-V curve show the presence of two extra- peaks.

5.4 Power transfer to the load

5.4.1 Parallel and series connections.

When working with flat panel photovoltaic technology, the series or parallel connections are good solutions for the 'current matching' problem; as a consequence the general approach of these studies is aimed to solve the 'maximum power point tracking' problem ([Koutroulis et al., 2001], [Brunelli et al., 2009] and [Hua and Shen, 1998]).

For a single array realized with N cells connected in series or in parallel, the power transferred to the load can be written as:

$$P = \sum_{j=1}^{N} V_{Cj} \cdot I_{Cj} \tag{5.11}$$

where j stands for the j-esim cell and the couple (V_{Cj}, I_{Cj}) is the j-esim cell working point. Maximum electrical power is defined as:

$$P_{MAX} = \sum_{j=1}^{N} V_{MPP,j} \cdot I_{MPP,j} \tag{5.12}$$

where the couple $(V_{MPP,j}, I_{MPP,j})$ is the j-esim cell MPP. The subscript MPP stands for maximum power point of the j-esim cell of the array. Thus P_{MAX} corresponds to the power obtainable if each cell is connected to an optimal load $R_j = V_{MPP,j} / I_{MPP,j}$

In some special cases, the series or parallels arrays can be perfectly matched to the load and the maximum electrical power (defined in Equation 5.12) coincides with the MPP of the array and with the power transferred to the load. Some examples are: a) series or parallel connections of identical cells, under uniform illumination and with the same temperature, b) series array and cells with identical $I_{MPP,j}$, c) parallel arrays and cells with identical $V_{MPP,j}$. Other special cases can be obtained for arrays realized with both series and parallel connections. In flat panel photovoltaic technology these special cases can be practically obtained by selecting 'quasi identical' cells, while the

uniform solar radiation condition is acceptably achieved in a clean day. Thus in flat panel photovoltaic, special cases are generally the most probable cases in which the arrays will work and the series or parallel connections can be considered the optimal solution to the 'power matching' problem. The situation is not very different for CPV panel based on Fresnel lenses, where the cells are illuminated in the same way except for optical misalignments. Actually, these misalignments becomes quite relevant with the aging of the panel

When working with an array of *N* cells realized with series connections some constraints for the system have to be taken in to account. Considering $I_{C_{j1}}, \ldots\ldots, I_{C_N}, I_0$ the *N*+1 free variables of the system, the constraints are:

$$V_0(I_0) = \sum_{j=1}^{N} V_{C_j}(I_{C_j}) \qquad (5.13)$$

$$I_{C_1} = I_0$$

$$\ldots\ldots$$

$$I_{C_N} = I_0$$

where $V_0(I_0)$ is the load voltage-current relation. The first term in Equation 5.13 takes into account that sum of the single cell voltages must be equal to V_0. The next *N* terms are the identical current I_0 constraint for series elements. The system has zero degrees of freedom (*N*+1 free variables and *N*+1 constraints) thus the cells working points are fixed. They can be calculated using Equation 5.13 and the *N* I-V curves $V_{Cj}(I_{Cj})$, where the I-V curves are established by single cell illumination and temperature. In conclusion, the power transferred to the load is fixed and generally less than the maximum achievable power expressed in Equation 5.12. In fact, maximum power can be achieved only for the special case: $I_{MPP,j} = I_0 \quad \forall j \in N$ and $V_0(I_0) = \sum_{j=1}^{N} V_{MPP,j}(I_0)$. For example, this situation can be verified in case of flat photovoltaic panel with identical cells under uniform solar radiation and temperature.

When working with an array of *N* cells realized with parallel connections, the constraints for the system are:

$$I_0(V_0) = \sum_{j=1}^{N} I_{Cj}\,(V_{Cj}) \tag{5.14}$$

$$V_{C1} = V_0$$

$$\ldots\ldots$$

$$V_{CN} = V_0$$

where $V_{C1}, \ldots V_{CN}, V_0$ are the free variables. By proceeding with the same considerations of the series case we obtain that the system still has zero degrees of freedom and thus the power transferred to the load is fixed and generally lower than the maximum achievable power expressed in Equation 5.12.

5.4.2 Power transfer efficiency

We will define the power transfer efficiency ε_T, and the maximum electrical efficiency ε_{MAX}, in relation with the total electrical efficiency of the array ε.
With reference to Figure 5.7, the net power is defined as:

$$P_N = I_0 \cdot V_0 - P_{EXT} \tag{5.15}$$

where I_0 and V_0 are respectively the current and the voltage measured on the load and the P_{EXT} term takes into account of any possible external power supplied to the array. In classical series or parallel array $P_{EXT} = 0$, but helping the array with any other active circuit causes $P_{EXT} > 0$. The total electrical efficiency is:

$$\varepsilon = \frac{P_N}{P_{SUN}} \tag{5.16}$$

where the P_{SUN} is the total solar power radiation incident on the array. Multiplying by $1 = \frac{P_{MAX}}{P_{MAX}}$, where P_{MAX}, defined in Equation 5.12, is the maximum electrical power obtainable from the cells of the array, the electrical efficiency can be written as:

$$\varepsilon = \frac{P_{MAX}}{P_{SUN}} \cdot \frac{P_N}{P_{MAX}} \tag{5.17}$$

Since P_{MAX} depends on conditions like solar radiation level, temperature, and individual parameters of each cell, but is totally independent on the type of connections used to realize the array, the first term in Equation 5.17 is totally independent of the type of connections; it represents the maximum electrical efficiency:

$$\varepsilon_{MAX} = \frac{P_{MAX}}{P_{SUN}} \tag{5.18}$$

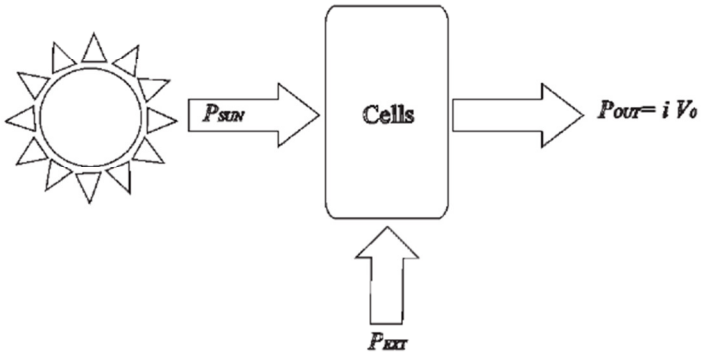

Figure 5.7: Scheme used for the definition of the power transfer efficiency and the maximum electrical efficiency. P_{SUN} is the total solar incident radiation, P_{EXT} is the external power supplied to the system and P_{OUT} is the power on the load.

Differently, the second term in Equation 5.17 is dependent on the type of connection, because of the net power term. This quantity, named ε_T ('power transfer efficiency'), represents the fraction of the maximum power P_{MAX}, transferred to the load:

$$\varepsilon_T = \frac{P_N}{P_{MAX}} \tag{5.19}$$

With previous considerations electrical efficiency ε can be written as:

$$\varepsilon = \varepsilon_{MAX} \cdot \varepsilon_T \tag{5.20}$$

From Equation 5.20 we can see that maximum electrical efficiency, ε_{MAX}, can be achieved only if $\varepsilon_T = 1$, that is, with an appropriate type of connection. Note that in

classical series or parallel connection $\varepsilon_T = 1$ only for the special cases discussed in the introduction.

5.5 A proposal for dense array connection in CPV systems

In dense array CPV technology, where the most probable operative condition is normally characterized by high differences in incident illumination and temperature between the cells, the array doesn't work in a special case abovementioned and the 'current matching' problem is anything but solved.

The most frequently adopted partial solution for large-area dish concentrators (those of more than 100 m^2 of aperture area) is to use planar facet mirrors mounted on an approximately parabolic dish, to provide a more uniform intensity distribution at the focus [Lovengrove et al., 2009]. This requires individual orientation of each facet and it is cost effective only for very large collectors. Other methods of managing the losses associated to non-uniform illumination, make use of secondary optics between the collector and the receiver [Kreske et al., 2002; Ries et al., 1997]; in this cases illumination uniformity is considerably enhanced, but the very high optical losses are unavoidable. An interesting solution using a radial arrangement of the cells into circular sectors is under development at the University of Madrid, but it does not match to the conventional square or rectangular solar cells [Vivar et al., 2010].

We propose a different approach to solve the current matching problem: instead of homogenize the flux, two new types of electrical connections are investigated [Salemi et al. 2011]; in fact, how it will be shown later, in these cases, other type of connections can achieve a power amount larger than the classical series or parallel connections. This type of connections has the advantage of making unnecessary the secondary optics or at least to limit the restriction on their design.

The two connections have a non-zero number of degrees of freedom, oppositely to parallel as series connection as it is shown in section 5.3.3. Because of this fact, the working points of each cell can be chosen and the power transfer to the load can be

increased. This corresponds to find a better solution to the 'current matching' problem. Since the two proposed connections make use of DC-DC converter modules, the physical model of DC-DC converter module that we consider will be discussed. These two types of connection are compared with classical series or parallel connections, with some examples of operative conditions. In Appendix D we discuss the procedure to maximize the power transfer efficiency for the two types of proposed connections, that is, a method to find the MPP of the two connections.

5.5.1 DC-DC converter model

The two types of connections proposed in this paper make use of DC-DC converter modules. The model of the DC-DC converter that we have considered will be defined in the following. The model for a real DC-DC converter module, shown in Figure 5.8 (a), is described by the equations:

$$\begin{cases} \varepsilon_A(V_{IN}, I_{IN}, V_{OUT}, I_{OUT}) \cdot P_{IN} = P_{OUT} & if \quad P_{OUT} > 0 \\ P_{IN} = K(V_{IN}, I_{IN}) & if \quad P_{OUT} = 0 \end{cases} \tag{5.21}$$

In Equations 5.21, the term K takes account of the power dissipated by the DC-DC converter module even with $P_{OUT} = 0$, if the DC-DC converter is power supplied by an external source with power P_{IN}; ε_A is the measured DC-DC converter module efficiency. The power dissipated by the DC-DC converter module, even with $P_{OUT} = 0$, can be simply reduced to 0 using the active circuit as shown in Figure 5.8 (b). In fact, the output power P_{OUT} can be null in 2 cases: $I_{OUT} = 0,\ V_{OUT} \geq 0$ and $I_{OUT} > 0,\ V_{OUT} = 0$.

Therefore, in the first case, by opening the switch A, the source power P_{IN} is disconnected from the DC-DC converter module, thus no power can be lost on the module and $K(V_{IN}, I_{IN}) = 0$ (an eventually switch C can be used to physically disconnect the DC-DC converter module if some current is absorbed by the DC-DC converter). In the second case, closing the switch B, $V_{OUT} = 0$ and any current can flow in the circuit, while opening switch A the source power P_{IN} is disconnected from

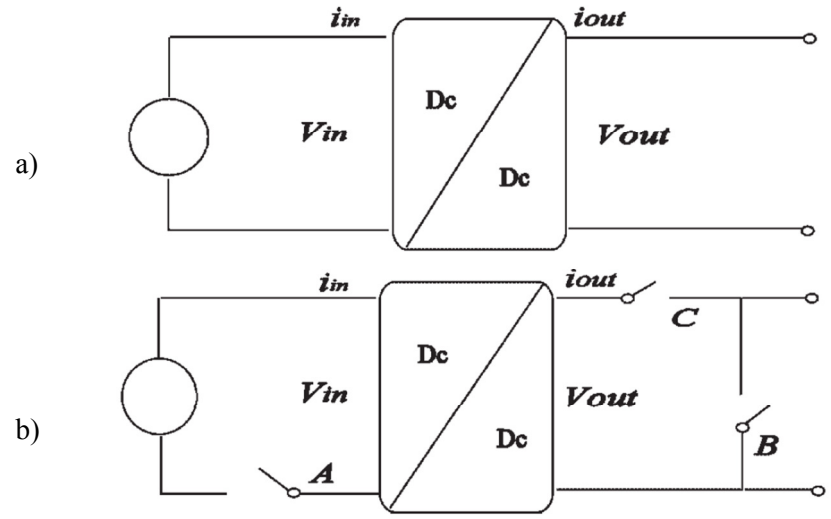

Figure 5.8: (a) scheme of the DC-DC converter module, **(b)** scheme of the DC-DC converter module with 3 switches added. Switch A disconnects the source power, switch B shortcuts the output and switch C is used if some current is absorbed by the module. This is the 'real DC-DC converter module' considered in this paper.

the DC-DC converter module, thus $K(V_{IN}, I_{IN}) = 0$. By using this circuit, term K vanishes and Equations 5.21 can be rewritten as:

$$\begin{cases} \varepsilon_A(V_{IN}, I_{IN}, V_{OUT}, I_{OUT}) \cdot P_{IN} = P_{OUT} & if \quad P_{OUT} > 0 \\ P_{IN} = 0 & if \quad P_{OUT} = 0 \end{cases} \tag{5.22}$$

In the next sections for 'real DC-DC converter module' we intend the DC-DC converter shown in Figure 5.8 (b) and described by Equation 5.22. If ε_A is constant with respect to $V_{IN}, I_{IN}, V_{OUT}, I_{OUT}$, we obtain an ideal efficiency. Commercial DC-DC converter modules can be considered ideal for certain values of $V_{IN}, I_{IN}, V_{OUT}, I_{OUT}$, typically specified in the datasheets.

In the two type of proposed connections each DC-DC converter module will be connected to a photovoltaic cell, then the number of DC-DC converter modules could be greater. Fortunately, low power DC-DC converters are needed and then relatively low cost can be supposed.

5.5.2 Connection of the first type

The connection of the first type (1st type, hereafter) makes use of DC-DC converter

modules, one for each cell of the array. Figure 5.9 shows that each cell is the power source for the DC-DC converter module and the power out of the DC-DC converter is directly transferred to the load. By considering that 20 W is today about the maximum electrical power for a photovoltaic cell, for the 1st type, we need 'low power' non isolated DC-DC converters. Some configurations in which PV arrays have been used as power source of DC-DC converter modules (or dc-ac converter modules) have been already proposed (see for example [Koutroulis, 2001] and [Walker and Sernia, 2004]). 1st type connection is a new type of connection characterized by a different MPP with respect to the classical series connection. As a consequence, different amount of power can be transferred to the load.

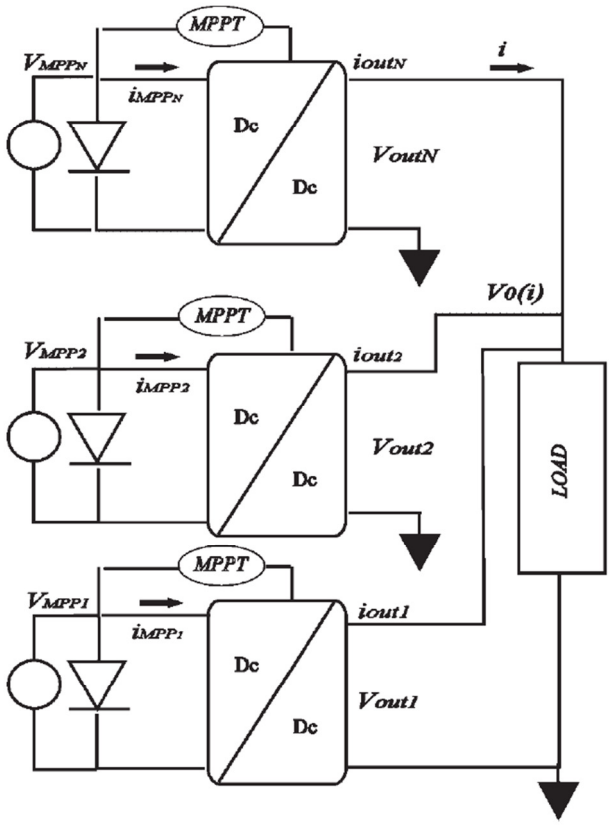

Figure 5.9: schematic of the 1st type connection. The cells are the power source of the DC-DC converter module and the output power is directly transferred to the load. An MPP trackers circuit is supposed to maintain each cell in its MPP.

Suppose to have an array of *N* cells. Looking at Figure 5.9, with the 1st type connection the only constraint for the system is:

$$I_0 = \sum_{j=1}^{N} I_{OUT,j}\,(I_{Cj}) \tag{5.23}$$

where the N +1 free variables are $I_{C1}, \ldots\ldots, I_{CN}, I_0$, the current of the cell and through the load, respectively, and the current $I_{OUT,j}$ is the output current of the DC-DC converter module supplied by the j-esim cell. 1st type connection has *N* degree of freedom and the working point of each cell can be chosen. Here DC-DC converter modules are assumed to have equal and constant efficiency I_{CN}. If each cell is maintained at its MPP, for example by using an MPP tracker, then Equation 5.21 gives the j-esim power out for the DC-DC converter:

$$P_{OUT.j} = P_{MMP,j} \cdot \varepsilon_A \tag{5.24}$$

If the array is realized with *N* cells, the power transferred to the load is thus:

$$I_0 \cdot V_0 = \sum_{j=1}^{N} P_{MPP,j} \cdot \varepsilon_A = \varepsilon_A \cdot P_{MAX} \tag{5.25}$$

The net power P_N is:

$$P_N = I_0 \cdot V_0 - P_{EXT} \tag{5.26}$$

where, in this case, P_{EXT} is the external power supplied to the MPP tracker circuits. By using Equation 5.19, the power transfer efficiency ε_T results to be :

$$\varepsilon_T = \varepsilon_A - \frac{P_{EXT}}{P_{MAX}} \tag{5.27}$$

Working with CPV systems, P_{MAX} can be some hundreds of watts and since of MPP trackers are low power circuits ($P_{MAX} >> P_{EXT}$) the second term of Equation 5.27 can be neglected. Power transfer efficiency ε_T , becomes:

$$\varepsilon_T = \varepsilon_A \tag{5.28}$$

Note that $\varepsilon_T = 1$ can be obtained only if the DC-DC converter modules efficiencies

are ε_A. In this case the power transferred to the load coincides with the maximum electrical power defined in Equation 5.12, in any operative condition.

5.5.3 Second type connection

In the connection of second type (2nd type, hereafter) each cell is connected to the output of an isolated DC-DC converter module and the DC-DC converter module is power supplied from an external source. Another DC-DC converter module, named L, is used to adjust the output voltage V_0 on the load. Figure 5.10 shows the 2nd type schematic for an array of *N* cells, where the sub elements 'cell-DC-DC converter' are connected in series. We will examine the case of *N* 'sub-elements' connected in series, but the parallel case leads to the same conclusions. Suppose to have *N* cells. In 2nd type there are 2 *N*+3 free variables (see Figure 5.10): $V_{C1}, \dots, V_{CN}, I_{OUT,1}, I_{OUT,N}, V_L, I_{OUT,L}, I$, where $I_{OUT,J}$ is the output current of the DC-DC converter module connected to the j-esim cell, $V_L, I_{OUT,L}$ are respectively output voltage and output current of the DC-DC converter L, I is the current that flows in the circuit, and $V_{C1}, \dots, V_{CN}$ are the voltage's cells. There are N+2 constraints:

$$\begin{cases} V_0(I) = V_L + \sum_{j=1}^{N} V_{Cj} \\ I_{C1}(V_{C1}) + I_{OUT,1} = I \\ \dots\dots \\ I_{CN}(V_{CN}) + I_{OUT,N} = I \\ I_{OUT,L} = I \end{cases} \tag{5.29}$$

First of Equations 5.29 takes into account that the voltages sum for the *N* sub elements 'cell-DC-DC converter' plus the voltage V_L must be equal to the voltage $V_0(I)$ across the load. Remaining equations are the identical current constraints, for series elements. Thus the system has *N*+1 degree of freedom and, for example we can impose the set of working points $S = \{V_{Cj},\ I_{Cj}\ (V_{Cj})\}$ plus the value for V_L. Because of DC-DC converters modules can't absorb current, this conclusion is physically meaningful only if the chosen value for the set S and for V_L drive the variables $I_{OUT,1}, \dots\ I_{OUT,N}, I_{OUT,L}, I$ to be positive.

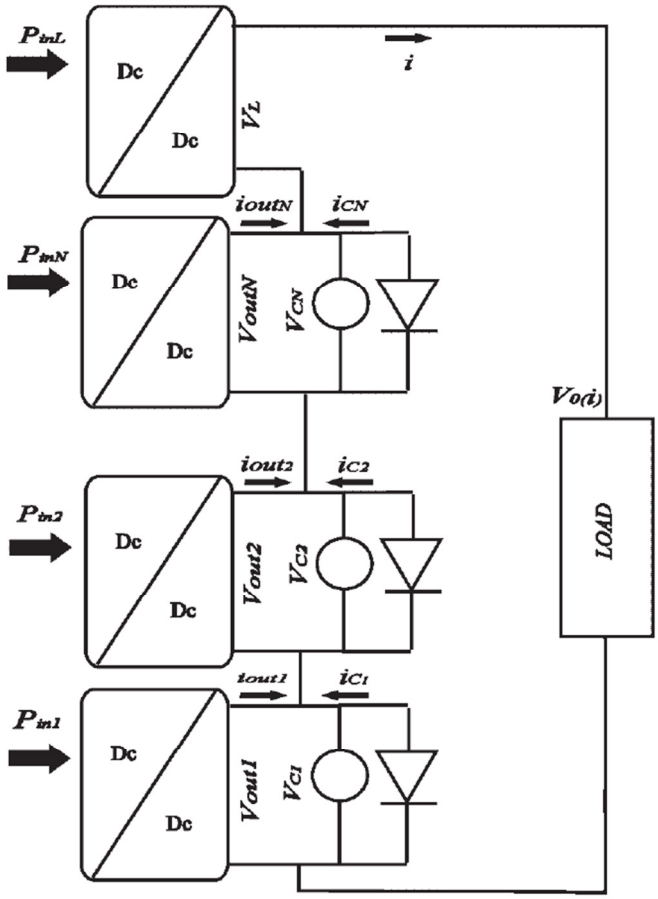

Figure 5.10: schematic of 2nd type in the series case. For an array realized with N cells there are N sub elements 'DC-DC converter module-cell' connected in series, in which the output of each DC-DC converter is connected in parallel with the cell. Another DC-DC converter module L is connected in series with the N sub element for adjusting the voltage value V_0 on the load.

In the following treatment the power transfer efficiency for the 2nd type is calculated. For the DC-DC converter connected to the j-esim cell the output power can be written as:

$$P_{OUT,j} = V_{Cj} \cdot (I - I_{Cj}) \tag{5.30}$$

where it was taken into account that $V_{OUT,j} = V_{Cj}$ and $I_{OUT,j} = (I - I_{Cj})$ because of the output parallel connection and the series elements constraints, respectively. External input power supplied to the DC-DC converter module can thus be written using Equations 5.12:

$$P_{IN,j} = \frac{V_{Cj} \cdot (I - I_{Cj})}{\varepsilon_{Aj}(V_{OUT,j}, I_{OUT,j}, V_{IN,j} I_{IN,j})} \tag{5.31}$$

where $\varepsilon_{Aj}(V_{OUT,j}, I_{OUT,j}, V_{IN,j} I_{IN,j})$ is the *j*-esim DC-DC converter module efficiency. Next we consider DC-DC converter module with the ideal efficiency ε_A (ideal efficiency has been defined in section 3). Given the electrical power delivered by the j-esim cell $P_{Cj} = V_{Cj} \cdot I_{Cj}$, we can rewrite the external input power supplied as:

$$P_{IN,j} = \frac{V_{Cj} \cdot I - V_{Cj} \cdot I_{Cj}}{\varepsilon_{Aj}} = \frac{V_{Cj} \cdot I}{\varepsilon_{Aj}} - \frac{P_{Cj}}{\varepsilon_{Aj}} \tag{5.32}$$

External input power supplied to DC-DC converter module indicated with letter L in Figure 5.10 is obtained in the same way. Using the equality $V_L = V_0(I) - \sum_{j=1}^{N} V_{Cj}$, the power input of the DC-DC converter L becomes:

$$P_{IN,j} = \frac{\left(V_0(I) - \sum_{j=1}^{N} V_{Cj}\right) \cdot I}{\varepsilon_{A,L}} = \frac{V_0(I) \cdot I}{\varepsilon_{A,L}} - \frac{I \cdot \sum_{j=1}^{N} V_{Cj}}{\varepsilon_{A,L}} \tag{5.33}$$

In the net power calculation we must take into account the total external power P_{EXT} , that is the sum of all the external power supplied to all the DC-DC converter modules:

$$P_{EXT} = P_{IN,L} + \sum_{j=1}^{N} P_{INj} \tag{5.34}$$

Making use of the previous equations, considering equal and ideal efficiencies for all the DC-DC converters modules: $\varepsilon_{Aj} = \varepsilon_A \ \forall j \in N$ and$\varepsilon_{A,L} = \varepsilon_A$, P_{EXT} becomes:

$$P_{EXT} = \frac{V_0(I) \cdot I}{\varepsilon_A} - \frac{\sum_{j=1}^{N} P_{Cj}}{\varepsilon_A} \tag{5.35}$$

The net power $P_N = I \cdot V_0 - P_{EXT}$, using Equation 5.35 results:

$$P_N = \frac{\sum_{j=1}^{N} P_{Cj}}{\varepsilon_A} - I \cdot V_0(I) \cdot \frac{(1 - \varepsilon_A)}{\varepsilon_A} \tag{5.36}$$

Finally, substituting Equation 5.36 into 5.19, the power transfer efficiency can be calculated as :

$$\varepsilon_T = \frac{\sum_{j=1}^{N} P_{Cj}}{\varepsilon_A \cdot P_{MAX}} - I \cdot V_0(I) \cdot \frac{(1-\varepsilon_A)}{\varepsilon_A \cdot P_{MAX}} \tag{5.37}$$

where P_{MAX} has been defined in Equation 5.12.

The 2nd type power transfer efficiency ε_T can result unitary even if ε_A <1. This happens when $I_{MPP,J} = I \ \forall j \in N$ and $V_o(I) = \sum_{j=1}^{N} V_{MPP,j}(I)$, the same special case for classical series connections.

Note that for each sub-element 'cell/DC-DC converter', the DC-DC converter module output voltage is $V_{OUT,j} = V_{Cj}$, where V_{Cj} is the output voltage of the *j*-esim cell (see Figure 5.10). Thus, because of the N+1 degree of freedom, we can decide the working point of each cell simply by setting the output voltages $V_{OUT,j}$ of the DC-DC converter. Given an operative condition the optimal output voltage of the DC-DC converters can be found by maximizing the power transfer efficiency ε_T with respect to the working points of the cells ($V_{Cj} = I_{Cj}$).

5.6 Comparison of 2nd type with classical connections and 1st type with 2nd type.

In this section the 2nd type will be compared with the classical series connections realized without DC-DC converter modules. The same results would be obtained by comparing the 2nd type with classical parallel connections. In the following discussion, for 'operative condition' we mean: incident illumination on the cells, temperature of the cells, type of cells.

5.6.1 Theoretical comparison between classical series connections and 2nd type

It will be shown that the comparison between 2nd type and classical series connections leads to conclude that 2nd type is more efficient than the classical series connections. Suppose to have 2 arrays each constituted of N cells. The first array connections are simply classical series connections (we denote this array with the letter A) while the

second array connections are of 2nd type (we denote this array with the letter B). The N cells of each array can be different between them and the array A is composed by the same cells of array B (i.e. array A is identical to array B except for the type of electrical connections).

Any operative condition σ forces the cells of the array A in a set of working points $I_\sigma = \{V_{Cj,\sigma}, I_{Cj,\sigma}\}$ where the subscript σ refers to the particular operative condition. Note that the set of working points I_σ is fixed for A, because the array realized with classical series connections has zero degrees of freedom. Because of the constraints on A (see Equation 5.13) all the currents must be equals $I_{Cj,\sigma} = I_\sigma \quad \forall j \in N$, where I_σ is the current that flows in the circuit and the cells voltages relation must be $\sum_{j=1}^{N} V_{Cj,\sigma} = V_0$ where V_0 is the load voltage value. We denote with $\varepsilon_{T(\sigma,A)}$the power transfer efficiency for A with respect to the operative condition Taking into account that for classical connections no external power is supplied (P_{EXT} = 0), Equation 5.19 gives, the power transfer efficiency for the array A:

$$\varepsilon_{T(\sigma,A)} = \frac{\sum_{j=1}^{N} P_{Cj,\sigma}}{P_{MAX}} \tag{5.38}$$

Under the same operative condition σ, we can reproduce on the array B the same set of working points $I_\sigma = \{V_{Cj,\sigma}, I_{Cj,\sigma}\}$ of A, by simply setting the DC-DC converter modules output voltages at the values: $V_{OUT,j} = V_{Cj,\sigma} \quad \forall j \in N$ and $V_L = 0$ and thus obtaining the same power transfer efficiency $\varepsilon_{T(\sigma,I,B)} = \varepsilon_{T(\sigma,A)}$. The term $\varepsilon_{T(\sigma,I,B)}$ is the power transfer efficiency obtained with the array B in the operative condition σ and the set of working points I_σ.

Because of the fact that for any operative condition σ, the same power transfer efficiency of A can be obtained with B too, we conclude that: $\varepsilon_{T(\sigma,C_{MAX\sigma},B)} \geq \varepsilon_{T(\sigma,A)}$ where $C_{MAX\sigma}$ is a different set of working points with respect to the set I_σ that maximizes the power transfer efficiency of the array B in the operative condition σ and $\varepsilon_{T(\sigma,C_{MAX\sigma},B)}$is the maximum power transfer efficiency for B in the same operative conditions. The procedure to maximize the power transfer efficiency for the 2nd type is exposed in Appendix D.

The demonstration of the previous assertions comes by writing the Equation 5.37

and by taking into account that we have imposed to the array B the same set of working points I_σ obtained for A and that the output voltage of DC-DC converter L has been set to zero ($V_L = 0$). Power transfer efficiency becomes:

$$\varepsilon_{T(\sigma,I,B)} = \frac{\sum_{j=1}^{N} P_{Cj,\sigma}}{\varepsilon_A \cdot P_{MAX,\sigma}} - I_\sigma \cdot V_0(I_\sigma) \cdot \frac{(1-\varepsilon_A)}{\varepsilon_A \cdot P_{MAX,\sigma}} \tag{5.39}$$

The terms $P_{Cj,\sigma} = V_{Cj,\sigma} \cdot I_{Cj,\sigma}$ are the j-esim cell electrical power and $P_{MAX\ \sigma}\, P_{MAX,\sigma}$ is the maximum electrical power achievable under operative condition σ by the N cells. Using the relation $\sum_{j=1}^{N} V_{Cj,\sigma} = V_0$, Equation 5.39 can be simplified as:

$$\varepsilon_{T(\sigma,I,B)} = \frac{\sum_{j=1}^{N} P_{Cj,\sigma}}{P_{MAX,\sigma}} = \varepsilon_{T(\sigma,A)} \tag{5.40}$$

The array B (2nd type) can give in any operative condition the same power transfer efficiency obtainable with A. After maximization of power transfer efficiency for B, generally:

$$\varepsilon_{T(\sigma,C_{MAX\sigma},B)} \geq \varepsilon_{T(\sigma,I,B)} = \varepsilon_{T(\sigma,A)} \tag{5.41}$$

where the sign "equal" between first and second members occurs if the 2 sets of working points are the same ($C_{MAX\sigma} = I_\sigma$).

Equation 5.37, the derived Equation 5.39, the maximization of the power transfer efficiency ε_T exposed in Appendix A, are based on the assumptions of real DC-DC converter modules with ideal and equal efficiency ε_T. Despite this, Equation 5.41 preserves its validity in the real case, too. In fact, supposing DC-DC converter modules with real efficiencies, potentially different one each other and dependent on $V_{OUT,j}, I_{OUT,j}, V_{IN,j}, I_{IN,j}$, the net power on the load can be written, starting by Equations 5.32 and 5.33, as:

$$P_N = V_0(I) \cdot I - \left[\sum_{j=1}^{N} \left(\frac{V_{Cj} \cdot I}{\varepsilon_{Aj}} - \frac{P_{Cj}}{\varepsilon_{Aj}} \right) + \frac{V_{0j} \cdot I}{\varepsilon_{AL}} - \sum_{j=1}^{N} \frac{V_{Cj} \cdot I}{\varepsilon_{AL}} \right] \tag{5.42}$$

where ε_{Aj} is the real efficiency of the j-esim DC-DC converter module and ε_{AL} is the

real efficiency of the L DC-DC converter module.

Imposing the cells of array B to work in the points I_σ obtained for the array A in the σ operative condition, the net power using Equation 5.42 becomes:

$$P_N = V_0(I_\sigma)\cdot I_\sigma - \left[\sum_{j=1}^{N}\left(\frac{V_{Cj,\sigma}\cdot I_\sigma}{\varepsilon_{Aj}} - \frac{P_{Cj,\sigma}}{\varepsilon_{Aj}}\right) + \frac{V_0(I_\sigma)\cdot I_\sigma}{\varepsilon_{AL}} - \sum_{j=1}^{N}\frac{V_{Cj,\sigma}\cdot I_\sigma}{\varepsilon_{AL}}\right] = \sum_{j=1}^{N} P_{Cj,\sigma} \tag{5.43}$$

And by using Equation 5.19 , the power transfer efficiency results:

$$\varepsilon_{T(\sigma,I,B)} = \frac{\sum_{j=1}^{N} P_{Cj,\sigma}}{P_{MAX,\sigma}} = \varepsilon_{T(\sigma,A)} \tag{5.44}$$

In conclusion, the array B realized with 2nd type can achieve the classical series connection power transfer efficiency obtained for the array A also with DC-DC converters with real and different efficiencies. Since a maximum power transfer efficiency $\varepsilon_{T(\sigma,C_{MAX\sigma},B)}$ always exists, Equation 5.41 is still valid.

5.6.2 Theoretical comparison between 1st and 2nd type and their application in operative conditions

In the previous section it was shown that 2nd type results more efficient than classical connections. Then in the cases where 1st type will result to be more efficient than 2nd type, the 1st type will be more efficient than classical series connections, too. We suppose to have 2 arrays each constituted by N cells. The first array connections are 1st type connections (we denote this array with the letter A) while the second array connections are 2nd type connections (we denote this array with the letter B). The N cells of each array can be different between them and the array A is composed by the same cells of array B (i.e. array A is identical to array B except for the type of electrical connections). The DC-DC converters modules used for A have the same efficiency of those used for B.

The comparison between the proposed 1st and 2nd type connections is strictly related to the DC-DC converter modules efficiency and to the I-V curves of the cells. As a consequence, in this case there is not an a priori type of connection that results more efficient than the other one. It depends from the operative conditions. Thus we suppose to have a CPV system and to be in an operative condition σ. For example an operative condition could be a CPV working at midday, at a given position on the Earth's surface and in a predetermined day.

In Appendix D it is shown a procedure to obtain and to set the working points for the cells in order to have the maximum transfer power efficiency with 2nd type connection. Since this procedure does not give a analytical formula for the maximum transfer power efficiency $\varepsilon_{T(\sigma,C_{MAX\sigma},B)}$, to make a comparison with 1st type, we chose the power transfer efficiency $\varepsilon_{T(\sigma,I^*,B)}$ in which each cell is working in its MPP. In the operative condition σ, $\varepsilon_{T(\sigma,I^*,B)}$ for array B is written as :

$$\varepsilon_{T(\sigma,I^*,B)} = \frac{1}{\varepsilon_A} - I_\sigma \cdot V_0 \cdot \frac{(1-\varepsilon_A)}{\varepsilon_A \cdot P_{MAX,\sigma}} \tag{5.45}$$

where the subscript I^* indicates that the transfer power efficiency is obtained by imposing at the cells the set of working points: $I^* = \{V_{MPPj,\sigma}\,,\ I_{MPPj,\sigma}\}$ and adjusting V_L in a way that the current that flows in the circuit results to be $I_\sigma = max\{\ I_{MPPj,\sigma}\}$. $P_{MAX\ \sigma}$ is the maximum electrical power in the operative condition σ defined by Equation 5.12. Power transfer efficiency used for the array A in any operative condition is ε_A, that is, the DC-DC converter modules efficiency (see Equation 5.28).

We suppose that in the operative condition σ, it results $\varepsilon_{T(\sigma,I^*,B)} > \varepsilon_A$, that is, array B works better than the array A. When the operative condition σ changes (for example at the sunrise or at the sunset), does array B still work better than the array A? By naming σ' the new operative condition, the power transfer efficiency for array B in the operative condition σ' is:

$$\varepsilon_{T(\sigma',I'^*,B)} = \frac{1}{\varepsilon_A} - I_{\sigma'} \cdot V_0 \cdot \frac{(1-\varepsilon_A)}{\varepsilon_A \cdot P_{MAX,\sigma'}} \tag{5.46}$$

where I'^* indicates that the transfer power efficiency is obtained by imposing at the

cells the set of working points: $I^* = \{V_{MPPj,\sigma'}\ ,\ I_{MPPj,\sigma'}\}$ and adjusting V_L in a way that the current that flows in the circuit results to be: $.I_{\sigma'} = max\{\ I_{MPPj,\sigma'}\}$. $P_{MAX,\sigma'}$ is the maximum electrical power in the new operative condition σ'. Writing:

$$\frac{I_{\sigma'}}{P_{MAX,\sigma'}} = \frac{1}{K} \cdot \frac{I_{\sigma}}{\varepsilon_A \cdot P_{MAX,\sigma}} \tag{5.47}$$

where *K* is an adimensional factor. Equation 5.46 can be written as:

$$\varepsilon_{T(\sigma',I'^*,B)} = \frac{1}{\varepsilon_A} - \frac{I_{\sigma}}{K \cdot P_{MAX,\sigma}} \cdot V_0 \cdot \frac{(1-\varepsilon_A)}{\varepsilon_A} \tag{5.48}$$

After a change in the operative condition, array B still works better than array A only if the relation:

$$\varepsilon_{T(\sigma',I'^*,B)} \geq \varepsilon_A \tag{5.49}$$

is satisfied. Using Equation 5.48, deriving the term $\frac{I_\sigma}{P_{MAX,\sigma}}$ from Equation 5.45 as a function of $\varepsilon_{T(\sigma,I^*,B)}$ and solving with respect to *K* one obtains the condition:

$$K \geq \frac{(1-\varepsilon_{T(\sigma,I^*,B)} \cdot \varepsilon_A)}{(1-{\varepsilon_A}^2)} \tag{5.50}$$

In the following some useful examples to explain physical meaning of K will be reported. For this purpose we suppose that the two arrays have been realized with the C1MJ-CDO100 Spectrolab cells. For next calculations, data from Spectrolab datasheet will be used [Spectrolab, 2010].

5.6.3 Uniform decrease of illumination

In this example we suppose that the change in operative condition σ consists in a uniform decrease of illumination. This can be the case of sunset or sunrise with respect to the operative condition of the CPV working at midday. Thus if $P_{Sj,\sigma}$ is the concentrated solar power incident on the j-esim cell in operative condition σ, then:

$$P_{Sj,\sigma'} = P_{Sj,\sigma} \cdot g \tag{5.51}$$

is the solar power incident on the j-esim cell in the new operative condition σ'. The

factor g is lower than 1 and points out the decrease in the solar radiation intensity (in this example we use g = 0.5; $P_{Sj,\sigma'}$ and $P_{Sj,\sigma}$ are measured in suns). By hypothesis in the operative condition σ, $\varepsilon_{T(\sigma,I^*,B)} \geq \varepsilon_A$ and thus 2nd type connection is more efficient than 1st type. Using the efficiency and V_{MPP} curves reported in [Spectrolab, 2010], the I_{MPP} curves, shown in Figure 5.11, can be derived. The I_{MPP} curves can be considered independent from the temperature in the 25°C - 90°C range up to 600 suns and a linear relation with respect to the concentrated incident solar power on the cell can be obtained:

$$I_{MPP} = m \cdot P + q \tag{5.52}$$

where m = 0.0136 and q = 0.039. For the array B (2nd type), $I_{\sigma'}$ can be derived as function of g and I_σ by using Equations 5.51 and 5.52:

$$I_{\sigma'} = I_\sigma \left(g + \frac{q}{I_\sigma}(1-g) \right) \tag{5.53}$$

From the Spectrolab datasheet, at 500 suns the MPP current of the C1MJ-CDO100 cell is I_{MPP} = 6.8 A. Supposing to work with g = 0.5 and with values of I_{MPP} of 2 A (or higher); the term $\frac{q}{I_\sigma}(1-g)$ results to be lower than 0.01 and the second term in bracket in Equation 5.53 can be neglected thus obtaining a proportional relation between currents:

$$I_{\sigma'} = I_\sigma \cdot g \tag{5.54}$$

where $\varepsilon\left(P_{Sj,\sigma'}, T\right)$ is the efficiency of the *j*-esim cell with $P_{Sj,\sigma'}$ incident solar power and $\varepsilon\left(P_{Sj,\sigma}, T\right)$ is the efficiency of the *j*-esim cell with $P_{Sj,\sigma}$ incident solar power, as taken from [Spectrolab, 2010]. By introducing the factor $h_j = \frac{\varepsilon\left(P_{Sj,\sigma'},T\right)}{\varepsilon\left(P_{Sj,\sigma},T\right)}$ and using Equations 5.55, 5.47, and 5.54, the *K* factor results to be:

$$K = \sum_{j=1}^{N} \frac{P_{Mj,\sigma}}{P_{MAX,\sigma}} \cdot h_j \tag{5.56}$$

In Figure 5.11 the $h_j\left(P_{Sj,\sigma}, T\right)$ curves are shown for g = 0.5. The curves have been

derived by the efficiency curves of [Spectrolab, 2010], as a function of the concentrated incident power on the cell $P_{Sj,\sigma}$.

For example, suppose that the power transfer efficiency in the operative condition σ for 2nd type is $\varepsilon_{T(\sigma,I^*,B)} = 0.85$ and that DC-DC converter modules efficiencies are $\varepsilon_A \cong 0.8$. By replacing these two values in Equation 5.50 we obtain the condition $K \geq 0.89$. That is, if after an uniform decrease of illumination of g it results $K \geq 0.89$, then the 2nd type connection is still more efficient than 1st type. Looking at Figure 5.11, and with the hypothesis that in the starting operative condition σ, all the incident powers

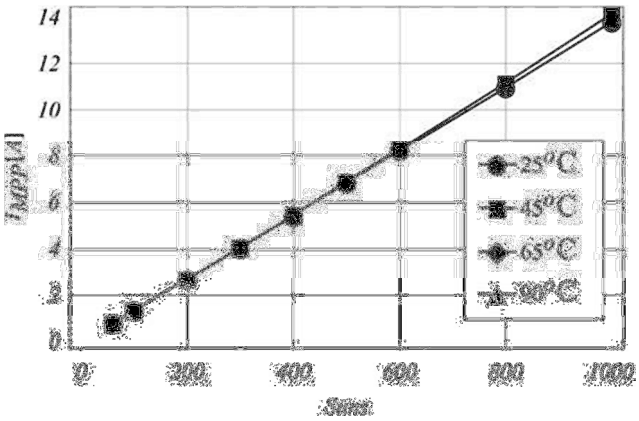

Figure 5.11: the $I_{MPP}(P,T)$ curves of the C1MJ-CDO100 cells, derived by the efficiency and the V_{MPP} curves from Spectrolab datasheet ([Spectrolab, 2010]). P is the incident power on the cell express in suns and T is the cell temperature.

on the cells, are comprised between 200 and 600 suns and all temperatures are lower than 90 °C, one obtains: $h_j \geq 0.96\ \forall j$ where j is the cell index. By using Equation 5.56, it results $K \geq 0.96$ and thus the condition $K \geq 0.89$ is satisfied.

Given a CPV system, a procedure to calculate the K factor value can be also outlined. The $\varepsilon_{T(\sigma,I^*,B)}$ can be calculated by measuring, for example, the maximum electrical powers of the cells in the 'midday' operative condition. The g factor can be derived by the ratio between the direct solar power measured at the 'sunrise operative condition' and the direct solar power measured at the 'midday operative condition' (Equation 5.51). The h_j curves are extracted from the efficiency curves reported in the datasheet. Finally, knowing the DC-DC converter modules efficiencies, the K factor can be calculated with Equation 5.56 and used in Equation 5.50.

5.6.2 Breakdown of a cell

We suppose now the array A is realized with the 1st type and the array B with 2nd type. The DC-DC converter modules efficiencies are $\varepsilon_A \cong 0.8$ and under the initial operative condition σ, the relation between the power transfer efficiencies is $\varepsilon_{T(\sigma,I^*,B)} > \varepsilon_A$ (all the cells are working). In a second operative condition σ', the cell j is out of order. Defining $P_{Mj,\sigma}$ the electrical power of the j-esim cell at its MPP, in the given operative condition σ, and

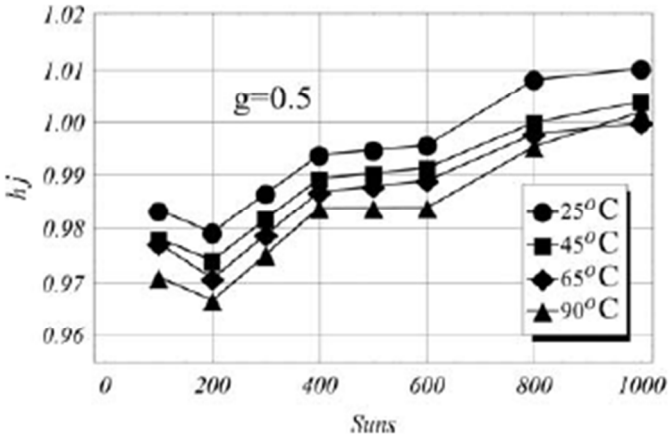

Figure 5.12: the $h_j(P_\sigma, T)$ curves derived for the Spectrolab cells. The curves have been derived by the efficiency curves in [Spectrolab, 2010] as a function of the concentrated incident power P_σ in the operative condition σ and taking into account that the concentrated incident power in the operative condition σ' is $P_{\sigma'} = P_\sigma \cdot g$, where g = 0.5 represents the uniform decrease of illumination. The curves have been used to evaluate the K factor.

$P_{MAX,\sigma} = \sum_{j=1}^{N} P_{Mj,\sigma}$ the maximum electrical power of the cells of the array in the operative condition, the maximum electrical power of the cells of array in the operative condition σ' is:

$$P_{MAX,\sigma'} = P_{MAX,\sigma} - P_{Mj,\sigma}\left(1 - \frac{P_{Mj,\sigma}}{P_{MAX,\sigma}}\right) \tag{5.57}$$

The current that flows in the circuit can or cannot change, depending on which cell of the array is out of order. We use $\varepsilon_{T(\sigma,I^*,B)}$ as power transfer efficiency of array B that implies that the current that flows in circuit is: $I_\sigma = max\{I_{MPPj,\sigma}\}$. If the $i_{MPP_{j\,\sigma}}$ of the j cell in operative condition σ is $I_{MPPj,\sigma} < I_\sigma = max\{I_{MPPj,\sigma}\}$, then the current

that flows in the circuit in the operative condition σ' remains unchanged as:

$$I_{\sigma} = I_{\sigma'} \tag{5.58}$$

On the contrary, if the $I_{MPPj,\sigma}$ of the *j*-cell in operative condition σ is $I_{MPPj,\sigma} = I_{\sigma} = max\{I_{MPPj,\sigma}\}$, then the current that flows in the circuit in the operative condition σ' changes as:

$$I_{\sigma} < I_{\sigma'} \tag{5.59}$$

In the first case, the K factor defined in Equation 5.47 can be determined by using Equations 5.57 and 5.58

$$K = \left(1 - \frac{P_{Mj,\sigma}}{P_{MAX,\sigma}}\right). \tag{5.60}$$

By using Equations 5.50 and 5.60 and solving for $\frac{P_{Mj,\sigma}}{P_{MAX,\sigma}}$:

$$\frac{P_{Mj,\sigma}}{P_{MAX,\sigma}} \leq 1 - \frac{(1 - \varepsilon_{T(\sigma,I^*,B)} \cdot \varepsilon_A)}{(1 - {\varepsilon_A}^2)} \tag{5.61}$$

Equation 5.61 gives a limit for the relative electrical power of the *j*-cell at its MPP with respect to the maximum electrical power of the array. For example, we suppose an operative condition σ with $\varepsilon_{T(\sigma,I^*,B)}$= 0.8 and $\varepsilon_A \cong 0.8$. By replacing these values in Equation 5.61 it comes out that the array B (2nd type) is always more efficient than array A (1st type) after the breakdown of the *j*-cell if the relative contribution of the *j*-esim cell to the maximum electrical power of the array is $\frac{P_{Mj,\sigma}}{P_{MAX,\sigma}} \leq 0.11$.

In the above mentioned case, in which $I_{MPPj,\sigma} = I_{\sigma} = max\{I_{MPPj,\sigma}\}$, according to Equation 5.59 the current flowing in the circuit after the breakdown of the *j*-esim will be lower than I_{σ}. The circuit current relative to the operative condition σ' will be determined by another cell, marked by the subscript *k*, and it results $I_{MPPk,\sigma} = I_{\sigma'} = max\{I_{MPPi,\sigma}\}$, where the subscripts indices *i* and *k* are different from *j*. Defining $f = \frac{I_{MPPk,\sigma}}{I_{MPPi,\sigma}}$, the current that flows in the circuit in the condition σ' can be written as:

$$I_{\sigma\prime} = I_{MPPk,\sigma} = f \cdot I_{\sigma} \tag{5.62}$$

Note that f is lower than 1. The maximum electrical power of the cells of the array $P_{MAX,\sigma\prime}$is the same as defined in Equation 5.57. The K factor defined in Equation 5.47 can be determined by using the Equations 5.57 and 5.62:

$$K = \frac{\left(1 - \frac{P_{Mj,\sigma}}{P_{MAX,\sigma}}\right)}{f} \tag{5.63}$$

By using the Equations 5.50 and 5.63 and solving for $\frac{P_{Mj,\sigma}}{P_{MAX,\sigma}}$:

$$\frac{P_{Mj,\sigma}}{P_{MAX,\sigma}} \leq 1 - \frac{(1 - \varepsilon_{T(\sigma,I^*,B)} \cdot \varepsilon_A)}{(1 - \varepsilon_A{}^2)} \cdot f \tag{5.64}$$

Equation 5.64 set a limit of the relative electrical power of the *j*-cell with respect to the maximum electrical power of the cells of the array when the broken cell *j* is the cell that in the operative condition σ produces the highest current value. For example, by considering $\varepsilon_{T(\sigma,I^*,B)}$= 0.85, $\varepsilon_A \cong 0.8$ and f = 0.85. After the breakdown of the *j*-esim cell, array B is still more efficient than array A if the relative contribution of the *j*-esim to the maximum electrical power of the array in the initial condition σ is $\frac{P_{Mj,\sigma}}{P_{MAX,\sigma}} \leq$ 0.24.

5.7 Numerical Simulation with a twenty cells array

In this section we will compare, in a possibly realistic case, the power transfer efficiency ε_T (Equation 5.19) when 1st type, 2nd type, and classical series connection are adopted. DC-DC converters with an ideal efficiency $\varepsilon_A = 0.85$ are chosen for the 1st type and 2nd type connections. The example is carried out by simulating an array realized with 20 cells of area 1 cm^2 . The model of each cell is described by the ideal diode equation:

$$I = I_{SC} - I_0\left(e^{q(V+IR)/kT} - 1\right) \tag{5.65}$$

where I_{SC} is the short current and it is related to the incident power P_S (in suns) by the linear relation $I_{SC} = P_S \cdot 0.01$ A, $R = 0.005\ \Omega$ is the series resistance, and $I_0 = 10^{-5}$ A is the dark current. We will calculate the power transfer efficiency for the three connections in the following operative conditions:

a) The cells of the array are irradiated with an incident density power given by the profile P1 shown in Figure 5.12.

b) The cells of the array are irradiated with an incident density power given by the profile P2 shown in Figure 5.12. The profile simulates an uniform decrease of illumination characterized by a factor $g = 0.5$, that is P2 = 0.5 P1.

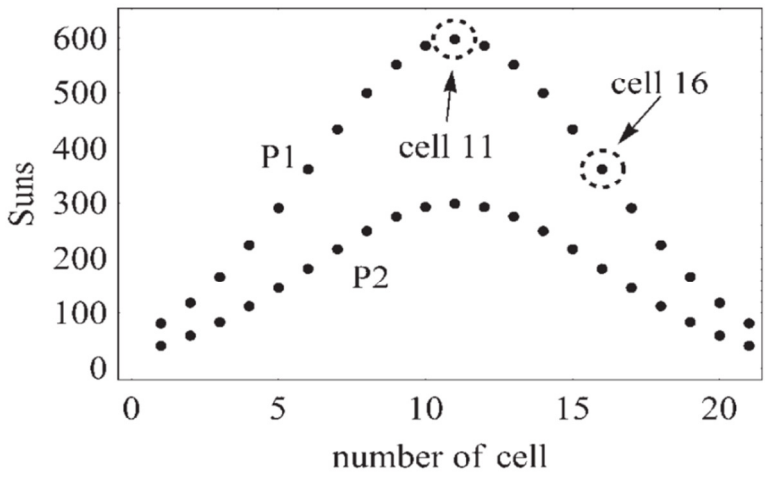

Figure 5.12: incident density power profiles on the array. Profile P2 is the profile P1 multiplied by a factor $g = 0.5$. The total incident power on the array with the profile P1 is 723,43 W. The marked cell 11 is the cell with higher current in its MPP, while the marked cell 16 is another cell with less current in its MPP.

c) There is a breakdown of one cell of the array: the cell with the higher current in its MPP (cell number 11) in both cases P1 and P2.

d) There is a breakdown of a one cell of the array: a generic cell, we have chosen cell number 16, in both cases P1 and P2.

The calculated values of the maximum electrical power PMAX (Equation 5.12) are

P1	P1–breakdown of cell 11	P1–breakdown of cell 16	P2	P2–breakdown of cell 11	P1–breakdown of cell 16
204.28 W	187.37 W	194.03 W	101.89 W	93.44 W	96.78 W

Table 5.1: calculated values of the maximum electrical power P_{MAX} (Equation 5.12) for the operative condition of the array composed by twenty cells under illumination with density power profile P1 and P2 and after breakdown of one cell

reported in Table 5.1 for the above six cases. The ε_T for classical series connection was obtained by calculating the I-V curve of the system and determining the MPP. It was assumed that each cell is connected to a bypass diode of zero forward voltage and that the voltage on the load is $V_0 = V_{MPP}$, where V_{MPP} is the output voltage of the array in its MPP. The ε_T for 2nd type was obtained by Equation 5.37 using I^* as set of working point ($\varepsilon_T = \varepsilon_{T(P1,I^*)}$, where the subscript P1 stands for operative condition relative to illumination profile P1). It is assumed that the voltage on the load is given by :

$$V_0(I) = \sum_{j=1}^{N} V_{MPP}\,(I) \tag{5.66}$$

That means $V_L = 0$. The ε_T for 1st type is equal to the DC-DC converters efficiency. The values calculated are reported in Table 5.2.

The 2nd type connection results the best connection in all the cases due also to the choice of the DC-DC converter efficiency. The best connection between the 1st type and 2nd type can be directly evaluated by using the K factor discussed in the sections 5.6.1 and 5.6.2. This will be outlined by reporting two examples in which the starting operative condition is the array under the P1 profile and connected by 2nd type ($\varepsilon_{T(P1,I^*)}$= 0.87). As it has been assumed in section 5.6.2, 2nd type works better than 1st type in the starting operative condition, that is $\varepsilon_{T(P1,I^*)} > \varepsilon_A$.

In the first example, a uniform decrease of illumination from the density power profile P1 to P2 (g = 0.5). From section 5.6.2 the condition for which 2nd type results to be better than 1st type is obtained by substitution $K \geq 0.36$ and ε_A = 0.85 in Equation 5.50: the condition requires $K \geq 0.36$. To evaluate the K factor of the system we first

calculate h_j. By Equation 5.55 (numerical calculation) all the cell efficiencies result to lie in the range between 0.270 to 0.285 when the incident density power is going from 20 to 1000 suns. For g = 0.5, the term h_j is greater than 0.27/0.285 = 0.95 and so, by Equation 5.56, it results $K \geq 0.95$. Thus 2nd type is better than 1st type after the decrease of the solar radiation. This conclusion is confirmed by the value of $\varepsilon_{T(P1,I^*)}$= 0.87 (where the subscript P2 stays for the operative condition relative to profile P2) reported in Table 5.2.

Operative conditions	**Connections**		
	Classical series	2nd type	1st type
	ε_T	ε_T	ε_T
P1 profile	0.57	0.87	0.85
P1-breakdown of cell 11	0.56	0.86	0.85
P1-breakdown of cell 16	0.59	0.87	0.85
P2 profile	0.57	0.87	0.85
P2-breakdown of cell 11	0.56	0.87	0.85
P2-breakdown of cell 16	0.59	0.87	0.85

Table 5.2: calculated values of the power transfer efficiency for the operative condition of the array composed by twenty cells under illumination with density power profile P1 and P2 and after breakdown of one cell. The power transfer efficiency ε_T is shown for the three type of connection.

In the second example, there is the breakdown of the cell number 16, and, as in the first example, it results $K \geq 0.36$. By Equation 5.50, the condition on the K factor becomes a condition for the relative power of the cell with respect to the total power. One obtains the condition: $\frac{P_{M16,P1}}{P_{MAX,P1}} \leq 0.64$, where $P_{M16,P1}$ is the maximum electrical power of the cell number 16 and $P_{MAX,P1}$ is the maximum electrical power of the array (the values refer to the starting profile P1). The numerical simulation gives $P_{M16,P1}$ = 10.25 W and $P_{MAX,P1}$= 204.28. The relative power results $\frac{P_{M16,P1}}{P_{MAX,P1}}$ = 0.05. Thus 2nd type is better than 1st type after breakdown. This conclusion is confirmed by the value of $\varepsilon_{T(P1-16,I^*)}$ = 0.87 (the subscript P1-16 stands for the operative condition of profile P1 with the breakdown of the cell 16) as reported in Table 5.2.

Chapter 6

Experimental proof of the new type of connection

6.1 Introduction

The proposed new types of connection are expected to give advantages over the classical series and parallel connections. This has been theoretically proved in the last chapter. The next step consisted in measuring the electrical behavior of this new type of connection and we have decided to test the 2nd type. The first experiment here presented has been performed indoor and made use of test-PVcells: these devices have PV cell-equivalent circuit and are powered by a DC power supply instead of solar power. The second experiment evaluated the electrical behavior of more 2nd type connected PV cells under concentrated solar light. The comparison with the I-V characteristic predicted for the series connected circuit will show the actual effectiveness of the new type of connection for some given illumination distributions over the cells.

6.2 Indoor proof 2nd type connection with test cells.

The operation of the 2nd type of connection was here tested on a PV-like array whose cells were differently illuminated. These devices were not real PV devices; they were constituted by test-circuits, each one made by a diode and a current generator.

Hereafter in this chapter, the word ‘cell’ will be used in place of this PV-like circuit. The use of this circuit allowed making the test operations easier and working with more precision with respect to the experimental proof with PV cells under concentrated solar power.

6.2.1 Electrical layout

The tested circuit is shown in Figure 6.1. Every cell was simulated by three series-connected diodes and an electrical current generator (model Agilent E3631A). The current generator allows setting the current flowing

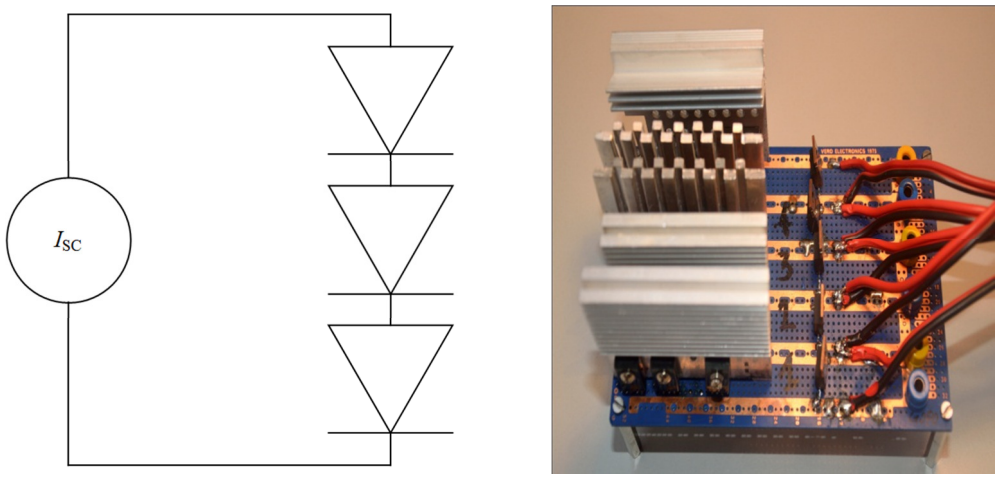

Figure 6.1: Electrical scheme for a test PV cell (left) and a picture of the three cells circuit (right).

through the circuit: this variable current simulated the variable solar power incident on a real solar cells, given that shirt circuit current ISC is proportional to the illumination level. Three diodes have been used in order to reproduce working conditions similar to those that would be obtained by using triple junction C1MJ-CD100 from Spectrolab (see Chapter 4). In fact, with three of the present diodes the I-V curves exhibit a maximum power point voltage VMPP around 2.6 V, similar to the cited cells one. This value corresponds to the required voltage range for the Vicor VE-JWY-YE DC-DC converter, used to realize the 2nd type of connection.

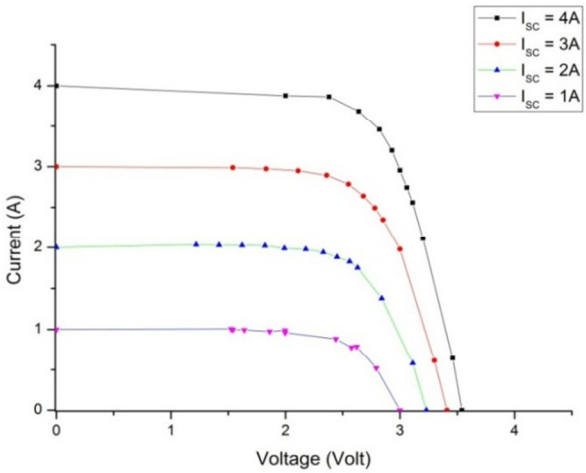

Figure 6.2: I-V characteristics for Cell 1 at 1, 2, 3 and 4 A.

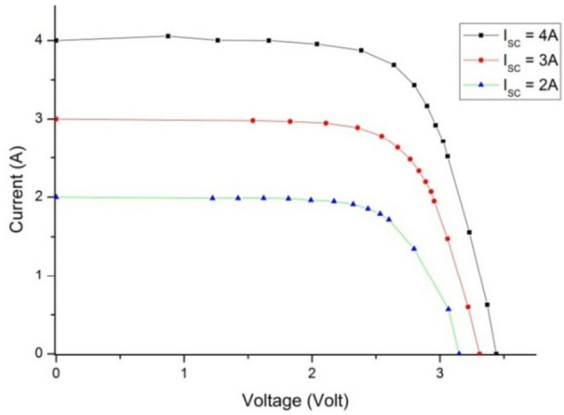

Figure 6.3: I-V characteristics for Cell 2 at 2, 3 and 4 A.

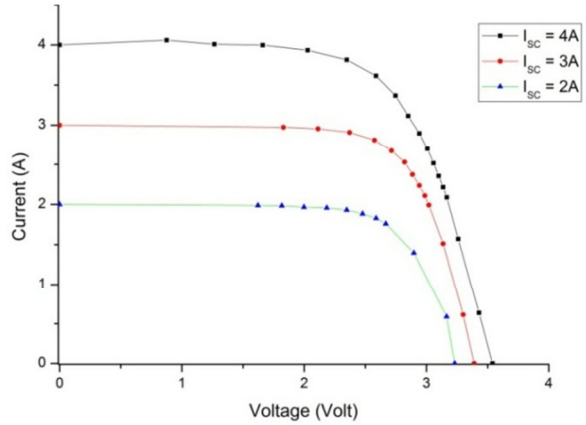

Figure 6.4: I-V characteristics for Cell 3 at 2, 3 and 4 A.

Before performing the test, each cell has been characterized with different I_{SC} values: 4 A, 3 A, 2 A, 1 A. As already written, they have to be considered as different illumination levels incident on each PV cell. The I-V curves measured for each I_{SC} value are reported in Figures 6.2, 6.3 and 6.4. Cell 2 and cell 3 are measured just with 2, 3 and 4 A, since they won't be supplied with 1 A. These curves show that the present circuits actually act as photovoltaic cells.

6.2.2 Circuit under testing

The 2nd type of connection assumes that every cell of the array is parallel connected to a DC-DC converter. Then the elements cell-DC-DC converters are connected in series. In the present test, 3 elements of such were used to realize a test array, as can be seen in the schematic of Figure 6.5. The working voltages of the cells V_1, V_2 and V_3 and the value for the external load R_0 arise from theoretical calculations and they have been use to set up the circuit for the optimal operation of the 2nd type of connection under given operative conditions. The measured quantities are the input current and voltages of the DC-DC converters, V_{IN} and I_{IN} respectively, and the output voltage across the load, V_{OUT}.

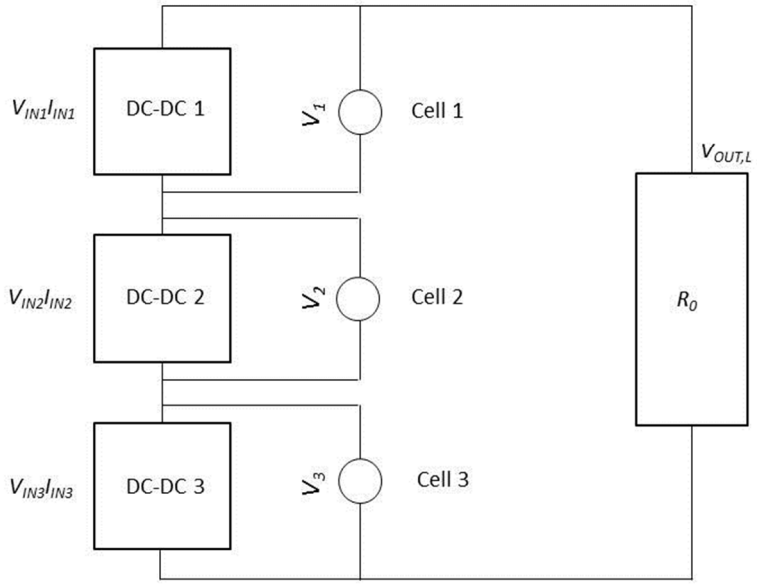

Figure 6.5: electrical schematic for the circuit under testing composed by three test cells connected in the 2nd type of connection.

The different illumination conditions have been simulated by imposing a certain combination of I_{SC} currents on the cells by means of 3 current generators.
For example, using the I_{SC} values, the condition 4A-4A-2A stands for:

- the I-V curve for Cell 1 is that of Figure 6.2 with I_{SC} = 4 A;
- the I-V curve for Cell 2 is that of Figure 6.3 with I_{SC} = 4 A;
- the I-V curve for Cell 3 is that of Figure 6.4 with I_{SC} = 2 A.

For every illumination condition the quantities to consider to evaluate the operation of the 2nd type of connection are the following:

- P_{MAX}, the maximum power obtainable from the cells, which is the sum of the MPP powers;
- R_0, the resistance to use as external load;
- V_1, V_2 and V_3 , voltages to set up across the cells;
- ε_T, the maximum efficiency (power transfer efficiency to the load) calculated for 2nd type of connection; if it would be 1, net power would equal P_{MAX} (see Equation 5.12);
- ε_{SERIES}, overall efficiency predicted for 3 series connected cells (classical connection without use of DC-DC converters).

The value of P_{MAX} is immediately defined by the illumination condition, which is equivalent to specify the three I-V curves and thus their relative maximum power points. With the procedure exposed in Chapter 5, knowing the I-V curves and the efficiencies of the DC-DC converters, we calculate the values for R_0, V_1, V_2 and V_3 to set up in order to maximize the power transfer efficiency to the load ε_T. Imposing the working voltages of the cells means to adjust the output voltage of each DC-DC converter to the desired value, since they are forced to have the same voltage value ($V_{OUT1} = V_1 \ldots$). Before describing the present measure steps, the working efficiencies of the DC-DC converters were evaluated.

6.2.3 Characterization of the DC-DC converters

The 2nd type of connection requires external electrical power to supply the DC-DC converter. In order to know the power transfer efficiency to the load ε_T the efficiency ε_A, of each DC-DC has to be measured (see Equation 5.37).

The devices we used are Vicor VE-JWY-YE, that have an input voltage of 24 V, an

output maximum voltage of 3.3 V and a temperature range between -0 °C and 100 °C. The operation of the DC-DC converters can be described by the following equations relating to the input and output electrical power:

$$\begin{cases} P_{OUT1} = \varepsilon_{A1}(I_{IN1}, V_{IN1}, I_{OUT1}, V_{OUT1}) \cdot P_{IN1} \\ P_{OUT2} = \varepsilon_{A2}(I_{IN2}, V_{IN2}, I_{OUT2}, V_{OUT2}) \cdot P_{IN2} \\ P_{OUT3} = \varepsilon_{A3}(I_{IN3}, V_{IN3}, I_{OUT3}, V_{OUT3}) \cdot P_{IN3} \end{cases} \quad (6.1)$$

where the subscripts refer to the corresponding devices. In Equations 6.1 it is explicated the dependency of ε_A from input and output currents and voltages. The DC-DC converter are supplied with 24 V, and their output voltage can be set up trough a potentiometer; by measuring the input and output currents as a function of the output power of each device, the efficiency curves shown in the Figures 6.6, 6.7 and 6.8 have been found for the DC-DC converter 1, 2 and 3, respectively. Efficiency is here defined as P_{OUT}/P_{IN} where $P_{IN} = I_{IN} \cdot V_{IN}$ is the power input to each device and $V_{IN} = 24$ V. These measured curves show that efficiency increases of about 10% by increasing the output power from 3 W to 16 W. For values of P_{OUT} of about 16.2 W, efficiency is higher than 70%, wherease for values lower than 3 W, efficiency falls under 50%. The dependency on the output voltage is weaker, but in general efficiency improves with the growth of P_{OUT}. With good approximation, the 3 devices present the same behaviour, and we will consider them as identical in the further treatment.

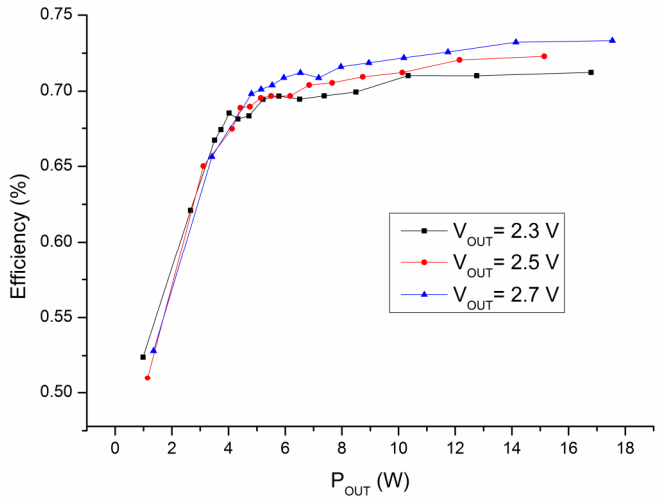

Figure 6.6: efficiency curves for DC-DC converter 1 for three value of V_{OUT} of each device and for V_{IN} = 24 V. Lines through data point are eye-guiding lines only.

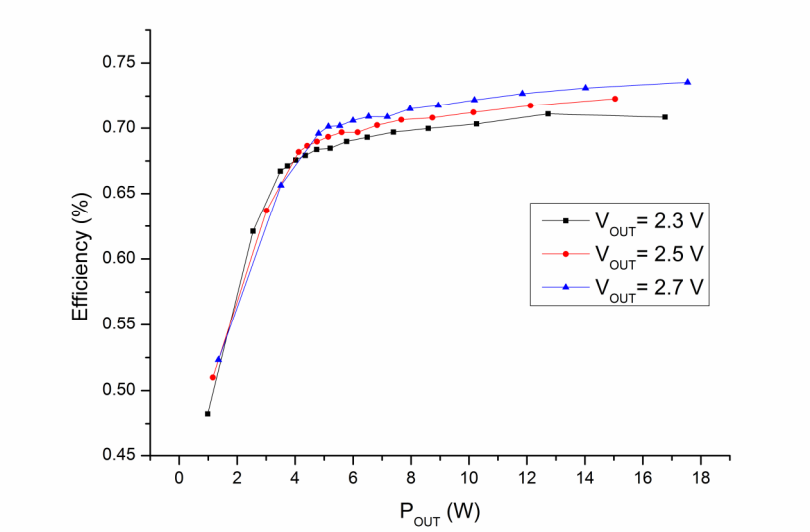

Figure 6.7: efficiency curves for DC-DC converter 2 for three value of V_{OUT} of each device and for V_{IN}= 24 V. Lines through data point are eye-guiding lines only.

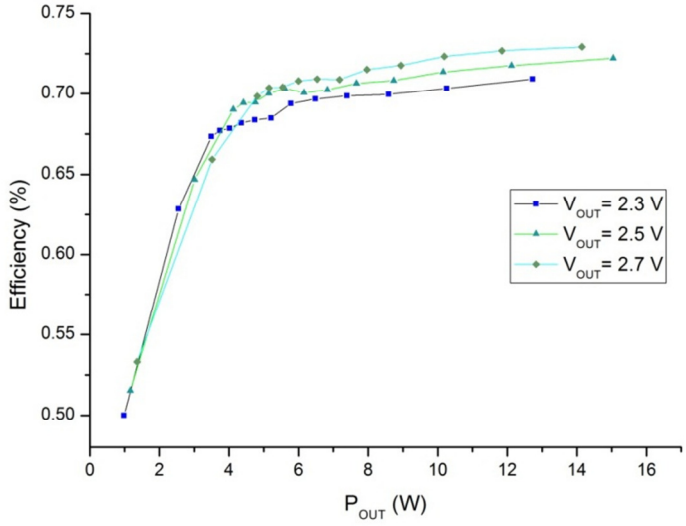

Figure 6.8: efficiency curves for DC-DC converter 3 for three value of V_{OUT} of each device and for V_{IN}=24 V. Lines through data point are eye-guiding lines only.

6.2.4 Measurement procedure and analysis

Given an operative illumination condition and calculated the values for V_1, V_2, V_3 and R_0 in order to maximize the power transfer efficiency ε_T, the testing procedure goes as the following:

1. DC-DC converters are set up to $V_{OUT1} = V_1, V_{OUT2} = V_2, V_{OUT3} = V_3$;

2. a resistance load R_0 is connected; the DC-DC converters are supplied at 24 V and the voltage across the load $V_{OUT,L}$ are measured;
3. the input currents and voltages of the three DC-DC converters are measured.

Voltages and currents have been measured with two digital multimeters. The external electrical power to the DC-DC converters was given by a power supply Agilent E 3631A (maximum ± 25 V @ 1 A). The board build to realize the circuit of Figure 6.5 will be shown in Chapter 6.3.3. The variable load is realized trough a box of resistances.

The analysis of the performance consisted in evaluating the power transfer efficiency of the circuit, and in comparing it with the theoretical value ε_T. From the previous measurements at point 3 and 4, the analysis steps are:

1. calculate the overall power to the load P_{OUT}, obtained from the relationship $P_{OUT} = {V_{OUT,L}}^2/R_0$;
2. calculate the electrical power supplied to the every DC-DC converters, $P_{IN} = I_{IN} \cdot V_{IN}$;
3. calculate the net power given to the load by subtracting the external supplied power $P_N = P_{OUT} - P_{IN1} - P_{IN2} - P_{IN3}$;

calculate the power transfer efficiency to the load given by $\varepsilon_T = \frac{P_N}{P_{MAX}}$ (Equation 5.19) , where P_{MAX} is the maximum power obtainable from the cells, depending on the particular illumination condition;

4. verify that the theoretical power transfer efficiency ε_T predicted for the values of corresponds to the real efficiency.

6.2.5 Results and discussion

The results obtained by the test are reported in Table 6.1. The different illumination conditions are specified by the values for the I_{SC} currents of the cells (I_{SC1}, I_{SC2}, I_{SC3}). Five different conditions were considered.

As it shown in second to last line of Table 6.1, the real efficiency values are found to be very near to the predicted theoretical efficiency values. Some percentage of difference can be ascribed to the impossibility to use resistance loads that exactly equal the calculated R_0 values (we have used a combination of resistances). From this

consideration, the operation of the 2nd type of connection can be reasonably thought as verified.

From the last two lines of Table 6.1 the advantage given by the 2nd type of connection with respect to the classical series connection, results evident. In four cases out of five the efficiency given by the 2nd type is higher than the efficiency that would be obtained with series connection; in the remaining case the efficiencies are roughly the same.

	(4A, 4A, 2A)		**(4A, 3A, 2A)**		**(1A, 4A, 2A)**		**(1A, 2A, 3A)**		**(1A, 3A, 2A)**	
	Calc.	**Meas.**	**Calc.**	**Meas.**	**Calc.**	**Meas.**	**Calc.**	**Meas.**	**Calc.**	**Meas.**
P_{MAX}**(W)**	23.63		21.13		16.31		13.76		13.81	
V_{OUT1}**(V)**	2.75	2.79	3.10	3.08	2.39	2.36	2.39	2.35	2.39	2.37
V_{OUT2}**(V)**	2.74	2.83	2.60	2.60	2.84	2.85	2.50	2.50	3.01	2.97
V_{OUT3}**(V)**	2.61	2.60	2.61	2.60	2.60	2.59	2.86	3.09	2.61	2.53
R_0 **(Ohm)**	2.35	2.36	3.11	3.04	2.42	2.34	4.31	4.29	4.42	4.41
V_{IN} **(V)**		24.00		24.00		24.00		24.00		24.00
I_{IN} **(A)**		0.285		0.213		0.585		0.193		0.142
ε_T	0.92	0.92	0.87	0.83	0.73	0.73	0.77	0.73	0.78	0.77
ε_{SERIES}	0.80		0.78		0.59		0.74		0.75	

Table 6.1: calculated and measured electrical parameters for the 3 cell connected with the 2nd type of connection. In the last two lines, transfer efficiencies to the load for this connection and for the classical series connection are shown. Series efficiency is calculated only.

We note that the DC-DC converter connected to the most illuminated cell shouldn't consume electrical power, since it's not necessary to supply current to the cell actually determining the current of the circuit. In practice, however, a supplied DC-DC converter consumes power, and this would decrease the measured efficiency with respect to the predicted one. In order to solve this issue it is possible to disconnect the power supply from such DC-DC converter; the theoretical voltage

across the cell would be anyway obtained. This consideration can be extended to more devices. In order to make it clear, it is useful to look at the results of situation 1A-3A-2A. The configuration of maximum theoretical efficiency requires the DC-DC converters 2 and 3 not to consume electrical power. The efficiency measured with these two devices connected to the external supply resulted 0.67. By switching off DC-DC converter 2, efficiency roses up to 0.75. By disconnecting both the devices, efficiency resulted 0.77 (see value in Table 6.1).

6.3 Outdoor proof 2nd type connection with PV cells.

6.3.1 Introduction

The predicted benefits of the 2nd type connection have previously been proved by means of an indoor experiment making use of test devices that have equivalent circuit to the PV cells. The present experiment consists in measuring the electrical behavior of more 2nd type connected PV cells under concentrated solar light. The comparison with the I-V characteristic recorded for the series connected circuit will show the actual effectiveness of the new type of connection for some given illumination distributions over the cells.

In order to realize this experiment, we decided to keep the electronic configuration as simple as possible, thus using just three MJ cells, which is the minimum number of cells that make sense. The three cells were assembled in a water-cooled receiver, which allows singly connecting the cells to the external circuit. The detailed description of the receiver components and construction is the subject of Chapter 7, and here is mentioned only. Measurements were performed by placing the receiver in the illumination spot produced by a parabolic sector, mounted on the sun-tracking CPV system. Several proofs were previously performed indoor, under the illumination produced by a 400 W halogen lamp and a focusing lens. These test resulted useful to arrange the instrumental configuration of the experiment, but the luminous power was too low to evaluate the performance of the 2nd type connection with the present DC-DC converters devices.

6.3.2 The photovoltaic receiver

The present prototype of receiver is aimed to host the cells to be tested under concentrated solar power with the 2nd type connection. The device supports six 1 cm × 1 cm cells (Spectrolab C1MJ) (see Figure 7.9 in Chapter 7) even if just three cells were used in the current experiment. In case of break of some cells, other cells are ready to be connected to the external circuit. The receiver allows both cooling the cells and singly connecting the cells themselves. The support upon which the cell are placed is an insulating AlN plate with dimensions 50 mm × 50 mm × 0.25 mm; this plate is soldered to a copper body which is water cooled. On the top surface of the plate, 10 μm copper traces for the electronic connection of the cells are coated. The cells are tin soldered to the traces, whereas the front contacts are realized with copper wires. In Figure 6.9 the whole PV receiver is shown: the copper traces collect the current produced by the cells and let out in small electric connecting blocks, which realize the connection to the external circuit. A copper water cooled shield was placed in front of the receiver, in order to shadow the fiberglass material used to fix the connection cables.

Figure 6.9: photograph of the PV receiver mounted in the focus of the concentrator. The illumination spot is focused on a protection copper shield.

6.3.3 Measurement equipment

In the present experiment the operation of the PV receiver is evaluated with the cells that are at first electrically independent one each other, in order to singly acquire the I-V characteristics, and then connected together by the 2nd type of connection

(schematic of Figure 6.5). Before describing the measurement process, we briefly present the tools that have been employed.

The I-V curves are acquired by means of a source measurement unit (SMU), model Keithley 2651A, which is specifically designed to characterize and test high power electronics [up to 2000 W of pulsed power (±40 V, ±50 A) or 200 W of DC power (±10 V @ ±20 A, ±20 V @±10 A, ±40 V @ ±5 A)]. It can be used as a voltage or current generator, precision power supply, digital multimeter, precision electronic load. The embedded TSP Express software is a utility that easily creates runnable scripts for the SMU unit. By using TSP Express is it possible to set up sweep in voltage values and measure the corresponding values for the current. An I-V curve of the connected device is finally obtained. The output files from TSP Express are .csv files containing the info about the acquisition setting, a column for voltage values and another one for the corresponding current values.

- A program (*conversion.xlsm*) has been written in Visual Basic; it converts the .csv files into .txt files containing just two columns, one for the voltage values and another for the current values.
- A personal computer is connected to the SMU unit through the Ethernet port; it serves to run the I-V acquisitions and to perform the calculations for the 2nd type of connection' operation (software *output.vbproj* below described).
- The DC-DC converter are supplied at 24 V by the Agilent power supply model E3634 (maximum ± 25 V @ 7 A).
- The DC-DC converters are grouped in the board of Figure 6.10. This circuit allows supplying the DC-DC converters at 24 V with a single power supply, switching on/off each DC-DC converter and connect it to the corresponding cell according to the 2nd type of connection. The output voltage of the DC-DC converters can be adjusted by simply regulate the trimmer (a screw on top of them).
- The electronic load is an Eutrom LUR 150. It allow setting a load in order to work in constant current (CC) up to 25 A, constant resistance (CR) up to 1.2 Ohm or constant voltage (CV) up to 120 V. In order to set the calculated value of the electronic load (or equivalently the value for the current of the circuit), the instrument is tuned by means of a power supply Agilent E 3631A

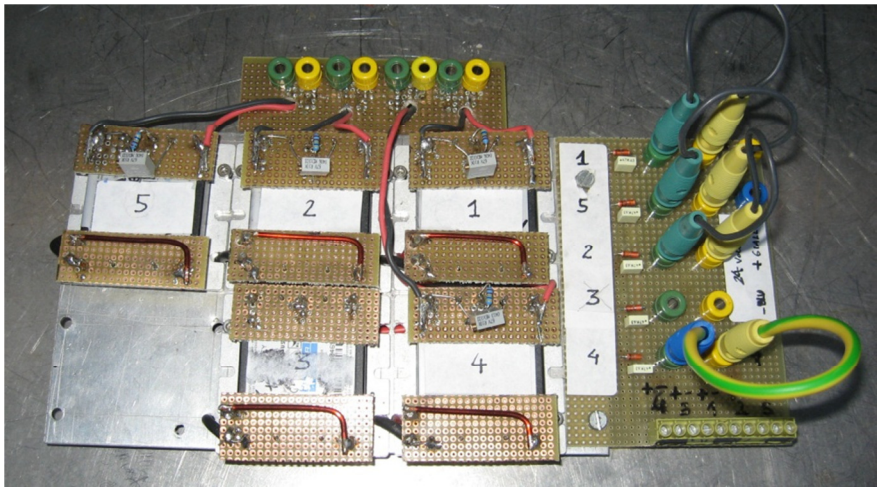

Figure 6.10: board with five DC-DC converters: four PV cells can be connected.

(maximum ± 25 V @ 1 A) before being connected to the circuit of Figure 6.5. When the required load is to high, a rheostat is connected to the electronic load.

- Two digital multimeters are used to measure currents and voltages.
- The software *output.vbproj* has been written in Visual Basic language to predict the situation in which 2nd type of connection optimizes the power transfer efficiency. The program, whose interface is shown in Figure 6.11, takes the I-V files for each cell (output .txt file from the SMU unit, containing the experimental I-V data points) and performs a fit through this data points (a simplified 1-diode equation for solar cells). A .txt file with the fitting parameters is created and this process is repeated for all the I-V curves. The ranges of the parameters of the diode equation have to be set up. Next, by using the files containing the fitted I-V curves, the program evaluates which DC-DC converters have to be turned on and calculate their own output voltages. It eventually considers the power consumption of the operating DC-DC converters. In order to perform this calculation, the files with the efficiency curves of the DC-DC converters have to been imported

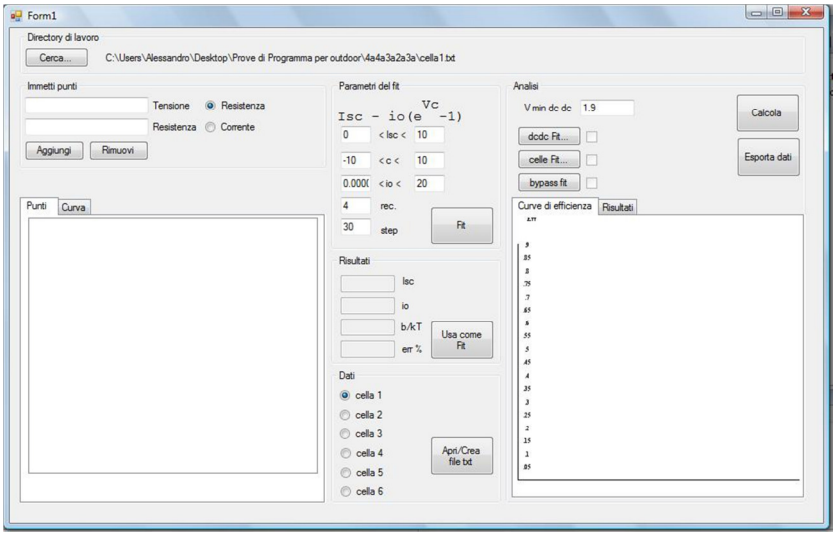

Figure 6.11: graphic interface for the program outdoor.vbproj designed to predict the optimal set up of the DC-DC converter, given a certain illumination condition. On the left part, the experimental I-V files in .txt format are loaded and a fit is traced. On the right part, DC-DC efficiency files are loaded and theoretical efficiencies calculated for the optimal configuration.

(fitted curves on the measured data points of Figures 6.6, 6.7 and 6.8). The program calculates the power output, the current output and the efficiency for the optimized configuration (basically the values for V_1, V_2 and V_3) in the 2nd type connected circuit of Figure 6.5. This optimal configuration is the one which maximizes the power transfer efficiency ε_T (Equation 5.19). At the same moment, the program calculates the efficiency of a classical connected receiver in the same condition of the present one. For these reason, a file containing the I-V curve of a typical bypass diode is also required as input.

6.3.4 Measurement procedure

Before acquiring the single I-V cells, the PV receiver was mounted on the spot region of the concentration system, accurately cleaned to remove powder residuals, water cooled and protected with a cooled shield made of copper. The measurements have been performed with just a parabolic module mounted on the tracking system, and part of it has been shadowed in order to progressively increase the illumination level on the PV cells. The collector is pointed to the sun by means of the pyroheliometer, as explained in Chapter 2, and tracker is switched on.

Two cables for each cell are fixed and they allow singly connecting them to the

SMU unit. The different level of solar power is due by the non-uniform illumination at the receiver plane, and it can change by simply changing the mirror's parts under shadowing. The measurement procedure occurs with receiver exposed to the concentrated spotlight and it is the following.

1. A cell is connected to the input port of the SMU unit. The TSB software allows setting the parameters for the I-V acquisition. Here a voltage sweep is made in the 0-2.8 V range (range both for source and measurement), with # points = 50. The instrument is configured in the high-capacity mode in order to avoid capacity effects that may affect the measurement. The first cell is characterized this way, then it is disconnected and the operation is repeated for the other two cells. The final output files (*cell1.csv*, *cell2.csv*, *cell3.csv*) contain the experimental I-V data points and the measurement specifications.

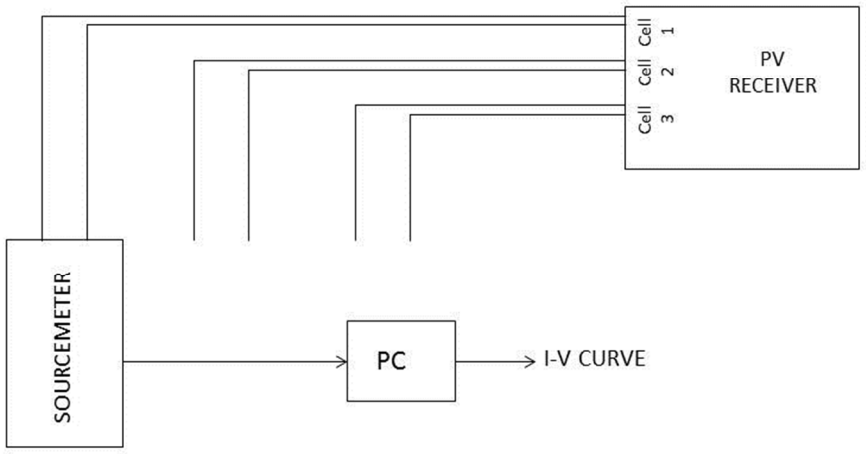

Figure 6.12: electrical schematic for the single I-V measurements. The cells are connected to the SMU one after other.

2. These files are converted in simpler files (*cell1.txt*, *cell2.txt*, *cell3.txt*) containing just a column for the volts (reading) and a column for the Amperes (reading), where shirt circuit currents are defined as positive. This is accomplished with the program *conversion.xlsm*.

   The program *output.vbproj* is launched. The file cell1.txt is opened, and a fit is created and saved as fit1.txt. The same for cells 2 and 3. After having inserted

the files for the efficiency of the DC-DC converters and for the electrical behavior of a bypass diodes, the program calculates and displays the settings to obtain the optimal configuration of the 2nd type of connection: which DC-DC converter has to be connected, the values for the voltages to be forced across each cell V_1, V_2 and V_3 and the corresponding currents, the value to be used for the external load R_0. Moreover, the program calculates the efficiency for the cells connected in series (ε_{SERIES}) and in the 2nd type of connection (ε_T) at their maximum power point; in the last case, a curve showing efficiency as a function of the overall current trough the load is built.

3. Given the results from the calculations, the circuit of Figure 6.5 is set up. The DC-DC are switched on or off as required from the theoretical evaluation. The values V_1, V_2 and V_3 are regulated through the trimmer on top of the devices and by checking the values by means of a voltmeter.
4. Before to be connected, the electronic load Eutron LUR 150 is adjusted to the calculated value in constant current (CC) mode. This means that the overall current (predicted) of the circuit is set up and this is equivalent to the setting of the load R_0(when needed, a rheostat is connected in series in order to reach a certain resistance value).
5. Then the three cells are connected to the board of Figure 6.10, and the electronic load close the circuit from cell 1 to cell 2 (see Figure 6.13). At this point, the output voltages of the DC-DC converters have to be checked again, since they may have been changed.
6. An ammeter is connected in series to the board and to the electronic load to measure the current that flows through the circuit.
7. The voltage across the load (for less than voltage drops on the connections, $V_{OUT,L} \cong V_1 + V_2 + V_3$) and current through the load itself (which is the current flowing through each cell+DC-DC converter block, I_C) are measured.
8. At this point, the power consumption (P_{IN}) of each DC-DC converter is calculated by measuring their output current and voltages, and their efficiencies (see Equation 5.21).
9. At the final stage, the power transfer efficiency with respect to the given illumination condition is calculated by (Equation 5.37).

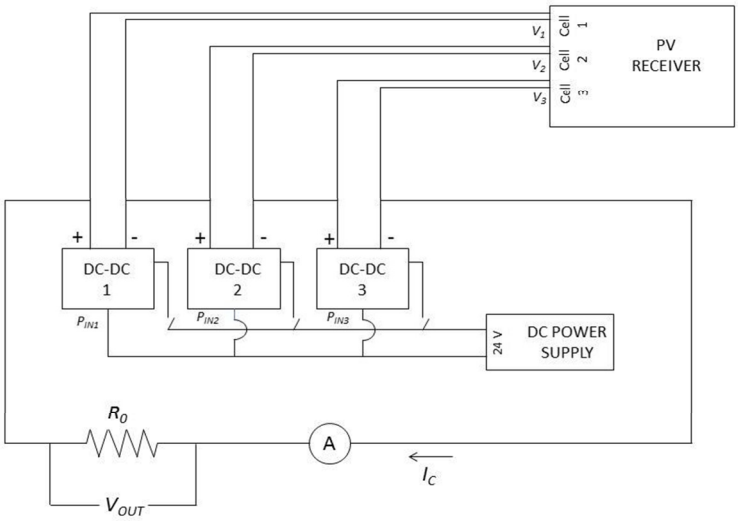

Figure 6.13: electrical schematic for the measurement of the 2nd type of connected circuit. The switches at the input of the DC-DC converters allows supplying them or not.

It's important to underline that the I-V measurements with the SMU instrument have been made in the two-wire mode, since the connection cables were thick enough (copper cables with 2.5 mm^2 section) to make the voltage drops on them negligible. Most of the total drop occurs at the soldering joints above the receiver, and they wouldn't be avoided by making use of the four-wire mode.

The entire measurement process, from point 1 to point 10, requires about 5-6 min; we consider the illumination conditions inside this interval as constant, even if we cannot verify the veracity of this assumption; a little bit of variability is unavoidable due the tracking movement of the system. Actually, the measurements can be made just in a very clean day with no clouds. The present ones have been performed on December 12th and 13th, 2012.

6.3.5 Results

In the present paragraph, the results for the testing of 2nd type of connection are reported for five different cases (Test A-E) in the Figures 6.14-6.23 and in the Tables 6.2-6.16. The difference in the illumination conditions was obtained by simply changing the shielded parts of the parabolic collector. Other influences in the I-V curves are related to the relative temperatures of the operating cells and to possible

differences of the cells themselves (as fabricated and after being soldered).

The measured I-V data points are reported (for example, Figure 6.14 in the case of Test A), and their relative values for the circuital parameters are calculated on the fitted curves (Table 6.2). The fitted curves, the setting of the parameters for the circuit and of the DC-DC converters for each test, the working points (V_{OUT}, I), are calculated by the program *output.vbpro* (Table 6.3). The external power supplied to each DC-DC converter is $P_{EXT} = \frac{I_{OUT} \cdot V_{OUT}}{\varepsilon_A}$, where I_{OUT} and V_{OUT} are the relative output current and voltage; the efficiency of each DC-DC converter, $\varepsilon_A = \frac{P_{OUT}}{P_{IN}} \cdot \frac{I_{OUT} \cdot V_{OUT}}{I_{IN} \cdot 24\,V}$, is derived from the polynomial fits extrapolated from the measured curves of Figures 6.6-6.8. The power transfer efficiency, $\varepsilon_T = \frac{P_{OUT,L} - P_{EXT}}{P_{MAX}}$, is then automatically calculated by *output.vbproj* and is reported in the graph as a function of the overall output current flowing through the circuit I_C(Figures 6.15). In particular, (see Table 6.3) the maximum power transfer efficiencies calculated for the 2nd type of connection (ε_T) and for the series connection (ε_{SERIES}), are compared to the measured value (ε_{MEAS}) at the same I_C value. In order to highlight the potential advantages obtainable from the 2nd type of connection over the classical series connection, an enhanced power transfer efficiency ($\varepsilon_T{}^*$) is calculated by assuming an highest efficiency of the DC-DC converters $\varepsilon_A = 0.9$. The series connected circuit has not been measured, because of the high risk of breaking for the differently illuminated cells in case of reverse bias. The operation of connecting the cells to bypass diodes would have been quite complicated due to the small sizes of the bus bars on top of the cells, and would have been too time consuming to guarantee reasonably steady illumination conditions.

Test A

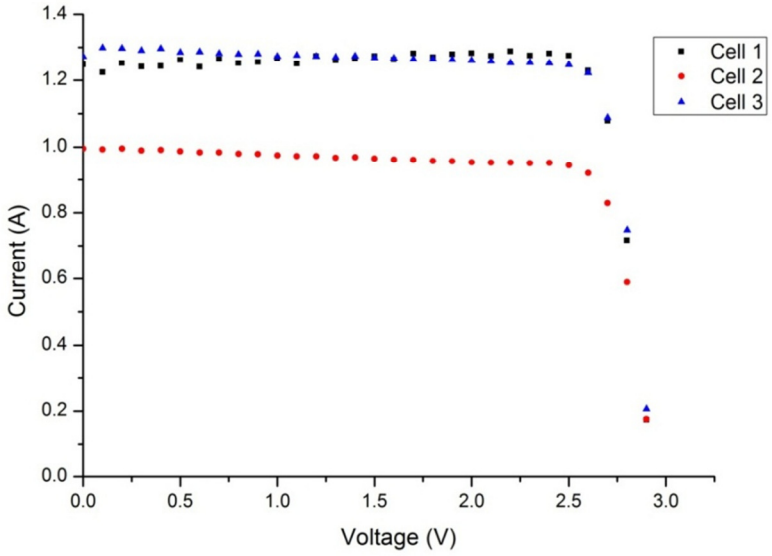

Figure 6.14: I-V characteristics for the three cells measured during Test A.

Cell	V_{MPP} (V)	I_{MPP} (A)	P_{MPP} (W)	V_{OC} (V)	I_{SC} (A)
1	2.45	1.29	3.16	2.94	1.34
2	2.38	0.95	2.26	2.93	1.03
3	2.45	1.28	3.14	2.94	1.35

Table 6.2: solar cell parameters for Test A resulting from the single diode fits (made by *output.vbproj*) on the I-V curves.

Cell	V_{OUT} (V)	I (A)	St. DC-DC	ε_A
1	2.53	1.25	Off	-
2	2.18	1.00	On	0.43 ± 0.01
3	2.53	1.25	Off	-

Table 6.3: the setting of the parameters for solar cells and DC-DC converters that results from theoretical calculations for the three I-V curves of Test A. V_{OUT} is the output voltage of each DC-DC converter; the working point of the cells are given by (V_{OUT}, I). The status (connected/non connected) and the efficiency ε_A of the DC-DC converters relative to their output voltage are also indicated.

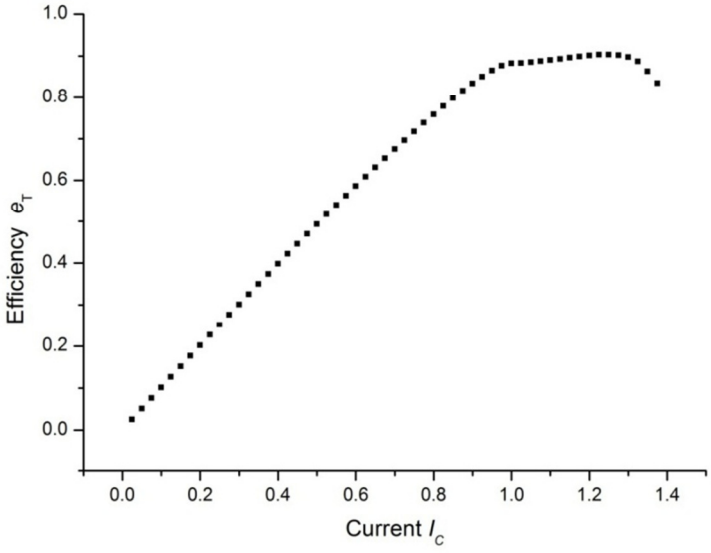

Figure 6.15: calculated power transfer efficiency ε_T as a function of the current flowing through the load I_C (Test A).

$V_{OUT,L}$ (V)	7.25
$P_{OUT,L}$ (W)	9.06
P_{MAX} (W)	8.56
P_{EXT} (W)	1.26
R_0 (Ohm)	5.8
ε_{SERIES}	0.88 @ I_C = 1.00 A
ε_T	0.90 @ I_C = 1.25 A
$\varepsilon_T{}^*$	0.98 @ I_C = 1.25 A
ε_{MEAS}	0.81 ± 0.05

Table 6.4: calculated electrical values that maximize ε_T for Test A. In the last 4 lines, ε_T is compared to the calculated efficiency for the series connection (ε_{SERIES}), the calculated one in the case of DC-DC converter efficiency $\varepsilon_A = 0.9$ instead of 0.43 ($\varepsilon_T{}^*$) and the measured one (ε_{MEAS}).

Test B

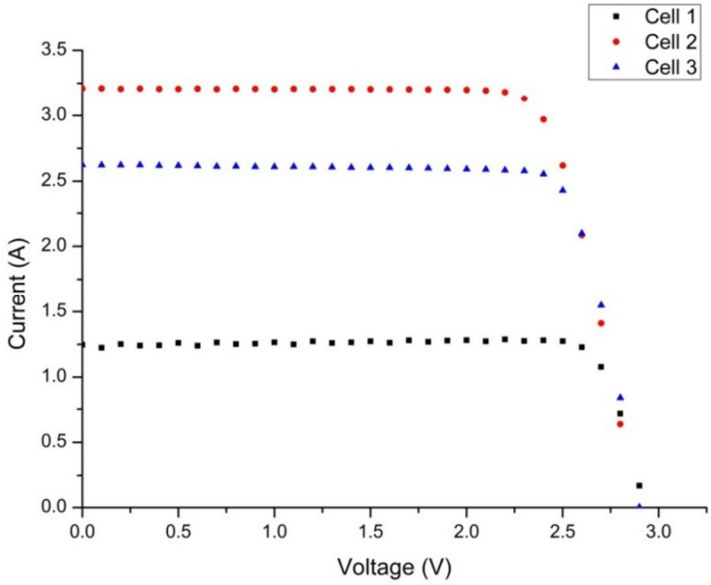

Figure 6.16: I-V characteristics for the three cells measured during Test B.

Cell	V_{MPP} (V)	I_{MPP} (A)	P_{MPP} (Watt)	V_{OC} (V)	I_{SC} (A)
1	2.45	1.30	3.18	2.94	1.34
2	2.36	2.87	6.80	2.87	3.35
3	2.33	2.53	5.89	2.88	2.68

Table 6.5: solar cell parameters for Test B resulting from the single diode fits (made with *output.vbproj*) on the I-V curves.

Cell	V_{OUT} (V)	I (A)	St. DC-DC	ε_A
1	2.384	1.325	On	0.64 ± 0.01
2	2.526	2.575	Off	-
3	2.279	2.575	Off	-

Table 6.6: the setting of the parameters for solar cells and DC-DC converters that results from theoretical calculations for the three I-V curves of Test B. V_{OUT} is the output voltage of each DC-DC converter; the working point of the cells are given by (V_{OUT}, I). The status (connected/non connected) and the efficiency ε_A of the DC-DC converters relative to their output voltage are also indicated.

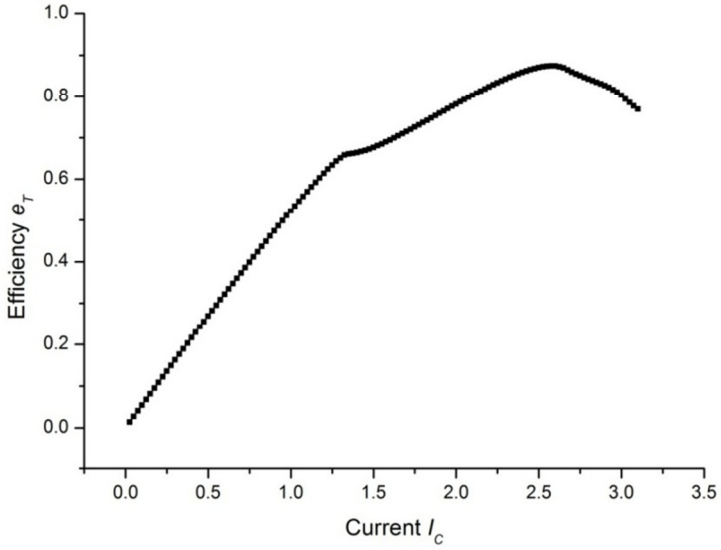

Figure 6.17: calculated power transfer efficiency ε_T as a function of the current flowing through the load I_C (Test B).

$V_{OUT,L}$ (V)	7.19
$P_{OUT,L}$ (W)	18.51
P_{MAX} (W)	15.97
P_{EXT} (W)	4.63
R_0 (Ohm)	2.79
ε_{SERIES}	0.72 @ I_C = 2.60 A
ε_T	0.87 @ I_C = 2.575 A
$\varepsilon_T{}^*$	0.95 @ I_C = 2.575 A
ε_{MEAS}	0.79 ± 0.04

Table 6.7: calculated electrical values that maximize ε_T for Test B. In the last 4 lines, ε_T is compared to the calculated efficiency for the series connection (ε_{SERIES}), the calculated one in the case of DC-DC converter efficiency $\varepsilon_A = 0.9$ instead of 0.64 ($\varepsilon_T{}^*$) and the measured one (ε_{MEAS}).

Test C

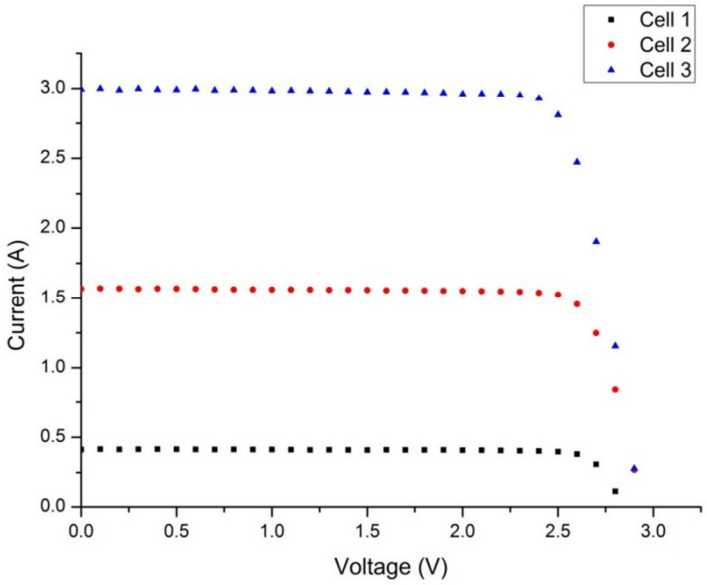

Figure 6.18: I-V characteristics for the three cells measured during Test C.

Cell	V_{MPP} (V)	I_{MPP} (A)	P_{MPP} (W)	V_{OC} (V)	I_{SC} (A)
1	2.21	0.33	0.71	2.84	0.34
2	2.42	1.58	3.81	2.97	1.72
3	2.37	2.82	6.7	2.91	3.10

Table 6.8: solar cell parameters for Test C resulting from the single diode fits on the I-V curves (made with *output.vbproj*).

Cell	V_{OUT} (V)	I (A)	St. DC-DC	ε_A
1	2.207	0.325	On	0.70 ± 0.02
2	2.328	1.625	On	0.61 ± 0.01
3	2.492	2.625	Off	-

Table 6.9: the setting of the parameters for solar cells and DC-DC converters that results from theoretical calculations for the three I-V curves of Test C. V_{OUT} is the output voltage of each DC-DC converter; the working point of the cells are given by (V_{OUT}, I). The status (connected/non connected) and the efficiency ε_A of the DC-DC converters relative to their output voltage are also indicated.

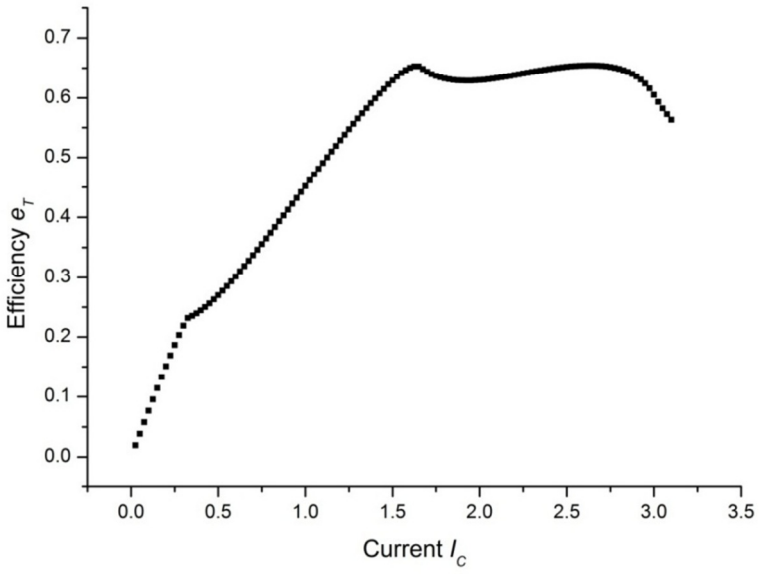

Figure 6.19: calculated power transfer efficiency ε_T as a function of the current flowing through the load I_C (Test C).

$V_{OUT,L}$ (V)	7.03
$P_{OUT,L}$ (W)	18.45
P_{MAX} (W)	11.23
P_{EXT} (W)	11.10
R_0 (Ohm)	2.68
ε_{SERIES}	0.68 @ I_C = 1.650 A
ε_T	0.65 @ I_C = 2.625 A
$\varepsilon_T{}^*$	0.92 @ I_C = 2.625 A
ε_{MEAS}	0.67 ± 0.03

Table 6.10: calculated electrical values that maximize ε_T for Test C. In the last 4 lines, ε_T is compared to the calculated efficiency for the series connection (ε_{SERIES}), the calculated one in the case of DC-DC converter efficiencies of $\varepsilon_A = 0.9$ instead of 0.70 and 0.61 ($\varepsilon_T{}^*$) and the measured one (ε_{MEAS}).

Test D

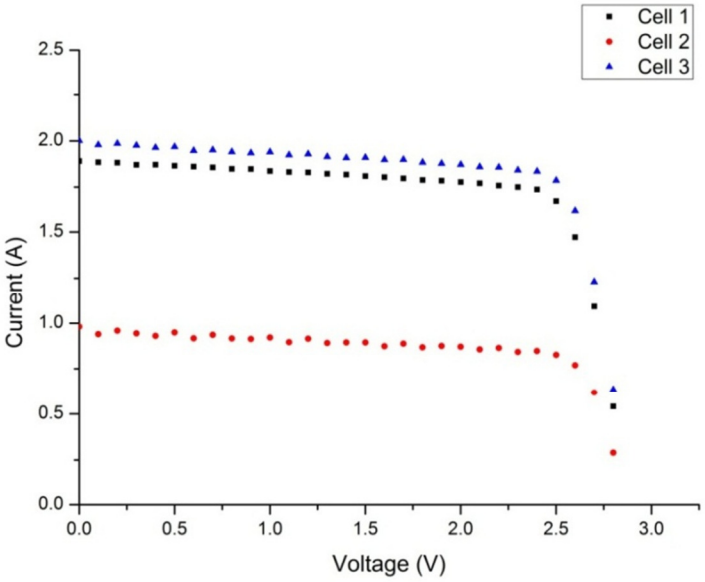

Figure 6.20: I-V characteristics for the three cells measured during Test D.

Cell	V_{MPP} (V)	I_{MPP} (A)	P_{MPP} (W)	V_{OC} (V)	I_{SC} (A)
1	2.39	1.6	3.83	2.90	1.72
2	2.25	0.9	2.03	2.91	1.03
3	2.33	1.9	4.44	2.89	2.07

Table 6.11: solar cell parameters for Test D resulting from the single diode fits (made with *output.vbproj*) on the I-V curves.

Cell	V_{OUT} (V)	I (A)	St. DC-DC	ε_A
1	2.349	1.625	Off	-
2	2.105	0.950	On	0.54 ± 0.01
3	2.550	1.625	Off	-

Table 6.12: the setting of the parameters for solar cells and DC-DC converters that results from theoretical calculations for the three I-V curves of Test D. V_{OUT} is the output voltage of each DC-DC converter; the working point of the cells are given by (V_{OUT}, I). The status (connected/non connected) and the efficiency ε_A of the DC-DC converters relative to their output voltage are also indicated.

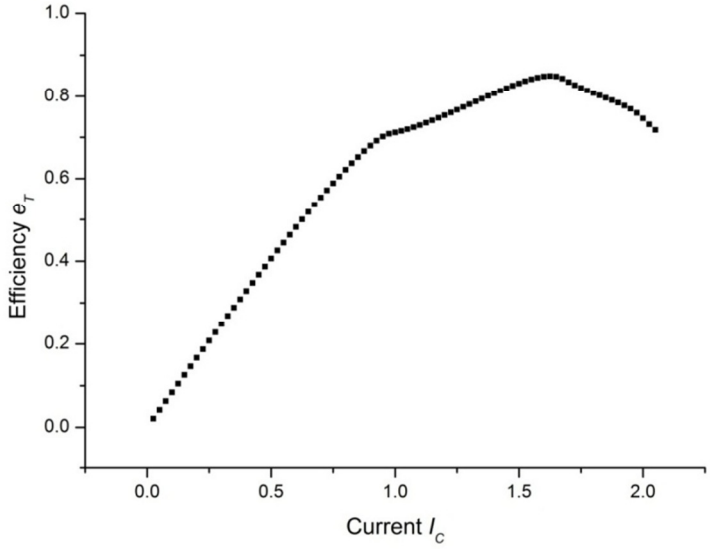

Figure 6.21: calculated power transfer efficiency ε_T as a function of the current flowing through the load I_C (Test D).

$V_{OUT,L}$ (V)	7.01
$P_{OUT,L}$ (W)	11.38
P_{MAX} (W)	10.29
P_{EXT} (W)	2.63
R_0 (Ohm)	4.31
ε_{SERIES}	0.72 @ $I_C = 1.625$ A
ε_T	0.85 @ $I_C = 1.625$ A
$\varepsilon_T{}^*$	0.95@ $I_C = 1.625$ A
ε_{MEAS}	0.77 ± 0.04

Table 6.13: calculated electrical values that maximize $\varepsilon_T$for Test D. In the last 4 lines, ε_T is compared to the calculated efficiency for the series connection (ε_{SERIES}), the calculated one in the case of DC-DC converter efficiency $\varepsilon_A = 0.9$ instead of 0.54 ($\varepsilon_T{}^*$) and the measured one (ε_{MEAS}).

Test E

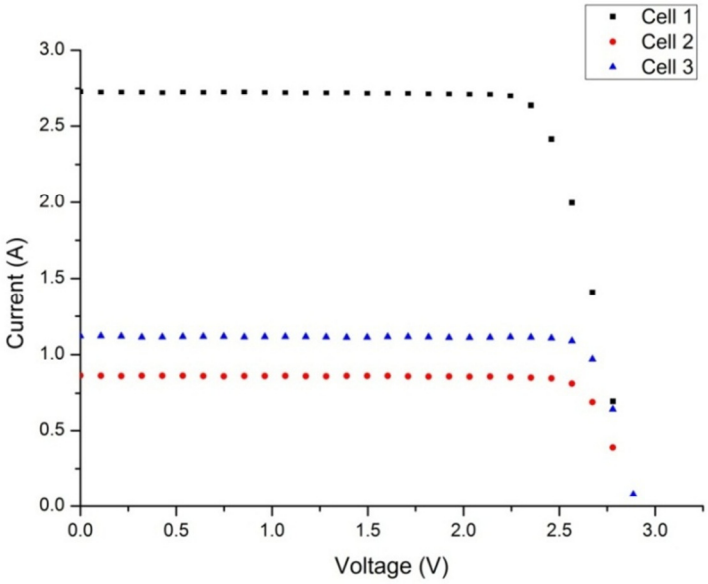

Figure 6.22: I-V characteristics for the three cells measured during Test E.

Cell	V_{MPP} (V)	I_{MPP} (A)	P_{MPP} (W)	V_{OC} (V)	I_{SC} (A)
1	2.28	0.80	1.83	2.88	0.88
2	2.26	2.43	5.48	2.91	2.76
3	2.29	1.08	2.46	2.89	1.19

Table 6.14: solar cell parameters for Test E resulting from the single diode fits (made with *output.vbproj*) on the I-V curves.

Cell	V_{OUT} (V)	I (A)	St. DC-DC	ε_A
1	2.033	0.85	On	0.43
2	2.753	1.10	Off	-
3	2.223	1.10	Off	-

Table 6.15: the setting of the parameters for solar cells and DC-DC converters that results from theoretical calculations for the three I-V curves of Test E. V_{OUT} is the output voltage of each DC-DC converter; the working point of the cells are given by (V_{OUT}, I). The status (connected/non connected) and the efficiency ε_A of the DC-DC converters relative to their output voltage are also indicated.

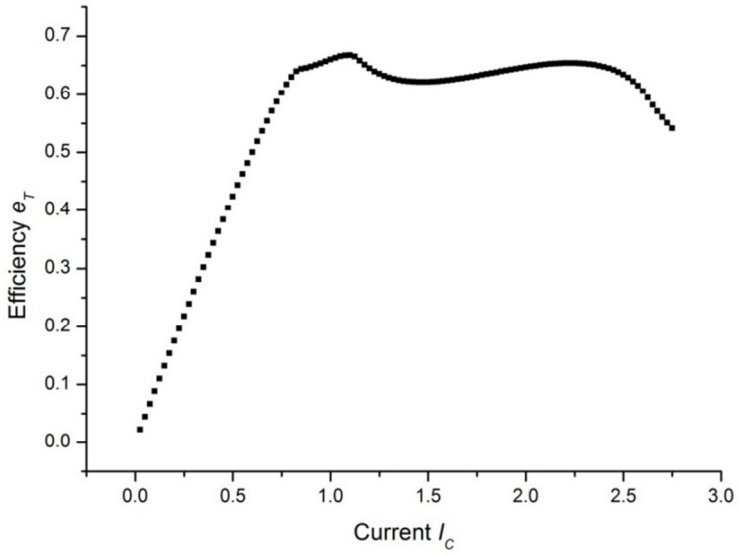

Figure 6.23: calculated power transfer efficiency ε_T as a function of the current flowing through the load I_C (Test E).

$V_{OUT,L}$ (V)	7.01
$P_{OUT,L}$ (W)	7.71
P_{MAX} (W)	9.76
P_{EXT} (W)	1.19
R_0 (Ohm)	6.37
ε_{SERIES}	0.64 @ I_C = 0.85 A
ε_T	0.67 @ I_C = 1.10 A
$\varepsilon_T{}^*$	0.73 @ I_C = 1.10 A
ε_{MEAS}	0.63 ± 0.04

Table 6.16: calculated electrical values that maximize ε_T for Test E In the last 4 lines, ε_T is compared to the calculated efficiency for the series connection (ε_{SERIES}), the calculated one in the case of DC-DC converter efficiency $\varepsilon_A = 0.9$ instead of 0.43 ($\varepsilon_T{}^*$) and the measured one (ε_{MEAS}).

Error analysis notes

The theoretical efficiencies values ε_{SERIES}, ε_T and $\varepsilon_T{}^*$ above reported have been automatically calculated by *output.vbproj*, which has been programmed to return just the fitting parameters without considering their error bars. The cell parameters are evaluated in the same way; in fact, the estimation of the parameters reported in the previous tables was only aimed to evaluate the best configuration of the DC-DC converters for each situation. The only one quantity which is reported with its own error is the measured efficiency ε_{MEAS}. In the following, the error calculation method for ε_{MEAS} is briefly explained. By writing $\varepsilon_{MEAS} = \frac{P_{OUT,L} - P_{EXT,L}}{P_{MAX}}$, where $P_{OUT,L}$ and P_{EXT} are measured and $P_{MAX} = \sum_{i=1}^{3} P_{MPP}$ results from three fitted parameters, it is clear that the error $\Delta\varepsilon_{MEAS}$ arises from the propagation of the corresponding errors $\Delta P_{OUT,L}$, ΔP_{EXT}, and ΔP_{MAX}.

- The power on the load ($P_{OUT,L} = I_C \cdot V_{OUT,L}$) is given by the current and voltage values measured on the load by an ammeter and a voltmeter, respectively. Their errors have been evaluated as instrumental errors only, that are ΔI_C= 1 mA and $\Delta V_{OUT,L}$= 0.1 mV.
- The externally supplied power is $P_{EXT} = \frac{I_{OUT} \cdot V_{OUT}}{\varepsilon_A}$, where the output current and voltage values of the connected DC-DC converter have been considered as instrumental only (in case of more connected DC-DC converters, the same analysis is made on $P_{EXT} = \sum_{i=1}^{3} P_{EXT,i}$, where i is the cell index). The DC-DC converter efficiency $\varepsilon_A(V_{OUT}, P_{OUT})$, for each device, has been graphically evaluated from the measured efficiency curves of Figures 6.6-6.8 for V_{OUT}= 2.3 and 2.5 V. A linear relationship $\varepsilon_A = k \cdot V_{OUT}$ has been established in order to extrapolate ε_A as a function of V_{OUT} and for a given value of P_{OUT}. This extrapolation has been made with respect to the linear fits on (I, V) data points in the region below 5 W (see Figures 6.6-6.8). The choice of using the curves relative to V_{OUT}= 2.3 and 2.5 V (and not to V_{OUT}= 2.7) is due to the facts that in all cases $V_{OUT} < 2.5$ V. A reasonable error of 0.1 is assigned to the ε_A values.
- The main contribute to $\Delta\varepsilon_{MEAS}$ is given by ΔP_{MAX}. As already mentioned, the values for P_{MAX} reported in the previous tables have been automatically

calculated by *output.vbproj* without the relative errors. In order to evaluate ΔP_{MAX}, the errors on P_{MPP} have to be assed, since $\Delta P_{MAX} = \sum_{i=1}^{3} P_{MPP,i}$. To accomplish this goal, the fits on each I-V curve have been remade at a later stage by using a data analysis software (Origin 8.1); the data points have been inserted with their own uncertainty bars, and the software calculates the cell parameters (in particular P_{MPP}) with their own error estimation. These errors, as returned from the software, have been propagated to calculate ΔP_{MAX} and thus $\Delta \varepsilon_{MEAS}$.

6.3.6 Discussion

The present experiment essentially proves the potential advantages of the 2nd type of connection that have been already predicted (Chapter 5) and indoor assessed (Paragraph 6.2), at least in some illumination cases. This can be seen from the results shown in Tables 6.4, 6.7, 6.10, 6.13 and 6.16; the discussion is here made easier by summarizing these results in Table 6.17.

For each of the illumination conditions in the present experiment just only one cell is connected to the DC-DC converter, unless for Test C, where two cells are power supplied. In this case the three cells have quite different I_{SC} values one each other (0.34 A, 1.72 A, 3.10 A), so that in order to enhance the efficiency, it is better to supply two cells and leave the other one to work near its P_{MPP}.

In all cases the calculated power transfer efficiency (ε_T) is found to be higher with respect to the one calculated for the classical series connection (ε_{SERIES}).
This is particularly true for the case of Test D, where two cells present I_{SC} values that are similar one each other and considerably higher than the third one. In this case, the DC-DC converter supplies one cell and allows preserving the electrical power that can be delivered by the other two cells, which can work near their maximum power point. The advantage is confirmed by the measured efficiency ε_{MEAS} = 0.77 which is greater than the series efficiency ε_{SERIES}= 0.72. We note that the gains in efficiency are expected even if the current flowing through the circuit (I_C) is slightly different from the optimal one; this can be seen from the graph of ε_T as a function of I_C.

	Test A	Test B	Test C	Test D	Test E
# DC-DC	1	1	2	1	1
ε_A	0.43±0.01	0.64±0.01	0.70±0.01 0.61±0.01	0.54±0.01	0.53±0.01
ε_{SERIES}	0.84	0.72	0.63	0.72	0.64
ε_T	0.90	0.87	0.69	0.85	0.67
$\varepsilon_T{}^*$	0.98	0.95	0.92	0.95	0.73
ε_{MEAS}	0.81±0.05	0.79±0.04	0.67±0.03	0.77±0.04	0.63±0.04

Table 6.17: summary of the efficiency values resulted from the five measurement test.

In general, ε_T is greater than ε_{MEAS}. A possible explanation of this trend is the difficulty in setting the right parameters calculated by *output.vbproj* during the measuring procedure. In particular it was difficult to set the working points of the cells through the output voltages of the DC-DC converters (V_1, V_2, V_3). Actually, these voltages were regulated through the trimmers on top of each DC-DC converter, that didn't allow tuning precisely the voltages to the last digit. Moreover, the voltages were set before of connecting the DC-DC converters to the cells; once the cells were connected, the voltage values slightly changed and had to be regulated again. This has resulted problematic: after that all the circuit was connected, each voltage value slightly varied again. Another situation that makes ε_{MEAS} lower than ε_T is the variability in the solar power incident on each cell, which causes the I-V curves to change with respect to the ones used to compute the optimal configuration. The measurements have been made over time ranges with weather conditions as constant as possible (the data of direct solar radiation, as measured by a pyroheliometer mounted on the tracking system, were used as indicators for the illumination condition steadiness). As a matter of facts, this steadiness can't be guaranteed, due to the continuous motion of the PV receiver with the tracking system. That said, the measured ε_{MEAS} values are found to be higher than their corresponding calculated ε_{SERIES} values. In two cases (Test A and E), ε_{MEAS} is slightly lower than ε_{SERIES}, but this difference is consistent with the uncertainty bars.

It is important to underline that higher efficiency gains could be obtained by using

more efficient DC-DC converters in the voltage range of interest. This can be seen from the $\varepsilon_T{}^*$ values, that are the power transfer efficiencies calculated in case of DC-DC efficiencies ε_A = 0.9. The case where the difference between ε_T and $\varepsilon_T{}^*$ is more relevant (0.92 in place of 0.69), is Test C, where two DC-DC converters would offer the benefit of their efficiency increase. Anyway, the efficiency would reach high values also in the other cases: for example for Test A, $\varepsilon_T{}^*$ reaches 0.98, which is like to have all the cells delivering their maximum power ($P_{OUT} \approx P_{MAX}$) to the load.

Chapter 7

Thermal management and dense-array receiver building

7.1 Introduction

One of the main concerns when designing CPV systems, above all for high concentration levels, is the thermal management of the photovoltaic receiver. All the radiation absorbed by the cell that is not transformed in useful electric power increases the cell's temperature and determines the thermal load[4]. Due to excess temperatures, cells may experience both short-term (efficiency loss) and long-term (irreversible damages) degradation. The requirement for an efficient way to dissipate the heat, establish the basis to realize a dense array receiver, which is the entire packaging to be exposed to the light focused by the optical system. Usually the dense array CPV receiver is considered to be the whole object that receives the concentrated illumination and it is made of a) an active part in the photovoltaic process, i.e. the cells, and b) a passive part, which is required to give suitable operative conditions for the electrical energy extraction and is composed by a mechanical support and by the electrical connections. In particular the support, upon which the cells are placed, has to accomplish the functions of interconnection between the cells (and separation between anode and cathode) and of heat removal; therefore its design must to take in consideration both these features.

[4] A straightforward consequence of this is that cells connected to a well-matched electrical load will be subject to a lower thermal load than cells in open circuit of short circuit configuration.

The present chapter treats the thermal management of a dense array CPV receiver and presents our trials to build a working multi-cell assembly. The effects of the heat on solar cells are firstly introduced in Section 7.2. In the following, Section 7.3, the structure of a cell to heat exchanger interconnect is discussed, and an evaluation of the thermal behavior for different subcomponent materials is made. In Section 7.4, the receiver prototypes we built are presented, with a description of the whole manufacturing processes. In Section 5 the differential equations that drive the heat transfer are solved in order to understand the response of different types of receiver to a given thermal load. COMSOL Multiphysics has been taken as a tool for making this analysis.

7.2 Requirement for cooling

7.2.1 Effects of Temperature on Solar Cells

The effects of the temperature on the cell's electrical behavior can be understood from the analytical expression of the cell parameters. The derivation of the I-V characteristic for a p-n junction can be found elsewhere, for example [Nelson, 2003], here we just list the most relevant expressions showing the dependency of the cell performance on junction temperature T [Gray, 2003]. The extension of this treatment to a triple junction cell, seen on a first approximation as an assembly of three series connected p-n junctions, is straightforward.

The open circuit voltage (V_{OC}) of an illuminated solar cell decreases with the increasing temperature and this can be seen as the effect of an increase in the diode-dark current. The dark saturation current due to recombination in the quasi neutral regions (I_{o1}) and in the space-charge region (I_{o2}) depends on the intrinsic carrier concentration (n_i):

$$I_{o1} \propto n_i \tag{7.1}$$

$$I_{o2} \propto {n_i}^2 \tag{7.2}$$

An increase in the intrinsic carrier concentration increases the dark saturation (recombination) current and results in a decrease in the open-circuit voltage, as can be seen from equation [Gray, 2003]:

$$V_{OC} \approx \frac{kT}{e} ln \frac{I_{SC}}{I_{o1}} \tag{7.3}$$

where k is the Boltzmann constant, e the electron charge, and I_{SC} the shirt circuit current. The intrinsic carrier concentration is given by

$$n_i = 2\left(m_n m_p\right)^{3/4} \left(\frac{2\pi kT}{h^2}\right)^{3/2} e^{-E_G/2kT} \tag{7.4}$$

where h is the Planck constant, E_G the bandgap energy, and m_n and m_p the effective masses for electrons and holes, respectively. The band gap decreases with temperature, wherease the effective masses generally show a weak dependency. It is clear that as the temperature increases, n_i increases, and thus recombination increases, and cell performance is impaired. The reduction in the bandgap also serves to increase n_i and downgrade the cell performance.

Since the short-circuit current is relatively unaffected by temperature under typical operating conditions, the temperature dependence of the open-circuit voltage can be shown to be expressed as

$$\frac{dV_{OC}}{dT} = -\frac{\frac{1}{q}E_G(0) - V_{OC} + \alpha\frac{kT}{q}}{T} \tag{7.3}$$

that is, V_{OC} varies roughly linearly and inversely with temperature. For silicon at 300 K it corresponds to about −2.3 mV/◦C. Following the decrease in Voc, it can be shown that the overall cell efficiency decreases almost linearly with the temperature, for a given light flux [Antonini, 2006].

In general, temperature is not uniform across the cell. The front junction is the most critical part because it is the farthest away from the heat exchanger, and also because the photons with higher energy are absorbed in the first few microns of the cell. A mitigating effect for CPV cells is the fact that the temperature coefficient improves with the concentration level. For example, the HCPV Amonix silicon solar cells have a voltage temperature sensitivity of about −1.78 mV/◦C at 1 sun and about −1.37

mV/°C at 250 suns [Yoon et al., 1994], whereas for GaAs it is from −2.4 mV/°C to −1.12 mV/◦C at 250 suns [Siefer et al., 2001]. For a multijunction cell, the expression for $\frac{dV_{OC}}{dT}$ is a little more complicated than Equation 7.3 [Nishioka et al., 2006], but anyway a value of – 4.3 mV/°C has been derived under 40 suns [Kinsey et al., 2009].

7.2.2 Mechanical Effects of Temperature

Another important issue related to CPV receivers is the mechanical impact of the receiver temperature varying during the on-off state. The problem arises from the fact that the receiver includes several different materials, in direct contact, having different thermal expansion coefficient (CTE). During the operation of the system, the temperature of the receiver changes following, at least, a day/night cycle. As a consequence, the components unavoidably undergo dimensional changes with the build-up and release of mechanical tension. Breakage (or failure) can follow the build-up of critical stress levels inducing immediate failure in fragile components or cyclical buildup and release of sub-critical levels inducing fatigue. Fatigue is often related to the formation and growth of micro-cracks and voids. This is a key issue also in the electronics design, where the most critical part is known to be the solder interconnect layer [Stam and Davitt, 2001] between the component and the printed circuit board (PCB) substrate.

7.3 Cell to heat sink interconnect

The cell-cooling problem is common to dense array and Fresnel-like systems, even if in the latter case it is relatively easy to cool the system due to the large space between the cells and plenty of dissipative surface on the back of each element.

From the thermal point of view the top surface of the cell must be considered the source of the heat. The purpose of a proper thermal design is to minimize the global thermal resistance of the cell assembly and, consequently, the cell operating temperature. Typical cells have one contact on the front surface and the opposite contact on the back surface, and both sides must be electrically connected either to

other cells' front (for series connection) or, in a more general way, to external circuitry. In dense array receivers, where many cells are typically mounted on the same substrate, it is also necessary to insulate each cell back-surface from the nearby ones. The solution is therefore to have a patterned copper layer providing the desired cells' interconnection on the top of a structural substrate being a thermal conductor and an electrical insulator.

Following the state of the art in power electronics two are the main solution to this issue, directly bonded copper substrate (DBC) and insulated metal substrate (IMS); the first, and most common, is where a layer of copper (from 25 to 200 μm thick) is bonded at high temperature on both sides of a ceramic plate. The top copper layer can be patterned by selective chemical etch to obtain the desired cell interconnection layout. The bottom layer is often used to solder it on a heat spreader or heat exchanger. The ceramic layer is the main contributor to thermal resistance of the stack and to the thermal mismatch with the cell material. Materials used in DBC include:

1. Alumina (Al_2O_3), the most commonly used material due to cost; brittle and not the optimal thermal conductor.
2. Aluminium nitride (AlN), more expensive but a better thermal conductor.
3. Beryllium oxide (BeO), good thermal conductor but with toxic effects.

In Figure 7.1 a prototype of cell assembly based on Alumina substrate and using $1cm^2$ cell and a bypass diode for the protection from "dark current" is shown; the copper pattern is Au/Ni plated to prevent corrosion and to promote a wet surface for solder.

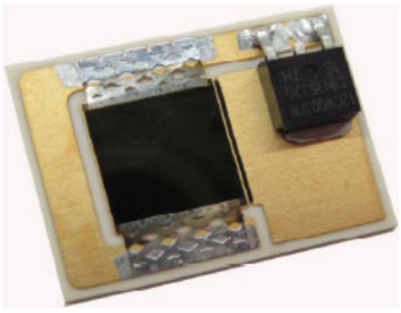

Figure 7.1: example of a cell assembly on alumina substrate [Cotal and Frost, 2010]; a bypass diode is connected for protection.

The cheap alternative is the insulated metal substrate (IMS) constituted by a metal baseplate (aluminium is commonly used) covered by a thin layer of dielectric (usually epoxy based) and a layer of copper. The thermal resistance is higher with respect to DBC, and for this reason it isn't a good choice for CPV receivers.

The interconnection between the metalized cell back-surface and the copper pattern is preferably obtained by soldering the cells. Computer-aided pick and place, components self-alignment and reflow soldering techniques allow industrializing this phase of cell assembly. In a typical configuration, cells will be soldered on standard DBC substrates with standard machinery. The DBC to heat exchanger soldering occurs at a second stage, causing potential problems of solder re-melting. The lead-free regulation worsens the problem; with lead-based solder materials, it is possible to perform this second stage with low melting point compounds ($Sn_{62}Ag_2Pb_{36}$ at 179 °C), whereas the cells are soldered by lead-free compounds at around 217 °C. An easier solution is to attach the DBC to the heat exchanger with a conductive epoxy, which doesn't require to be melted but has lower thermal conductivity.

Another issue to consider is the thermal contact between different surfaces. Due to the finite level of flatness of real surfaces, the contact between two surfaces actually occurs only in a limited number of points greatly affecting the resulting thermal conductivity. The mechanical pressure applied to the stack could be not enough and could be deleterious since cells and the DBC itself are fragile materials.

7.3.1 Thermal resistances evaluation

All the layers contribute to the global thermal resistance being the sum of each separate component. Here we employ a simple steady-state thermal resistance model for a 10 ×10 mm sample, and evaluate just the heat exchange through the x direction (normal direction) by conduction. The heat transfer by conduction for each layer is depicted in Figure 7.2, where the two sides have temperature T_1 and T_2, and where $T_1 > T_2$. If λ is the thermal conductivity of the medium, A is the cross-sectional area for heat flux, and d is the thickness of the plane, from the one-dimensional Fourier's low the heat flux results:

$$Q = -\frac{\lambda A}{d}(T_1 - T_2) = \frac{\Delta T}{d/\lambda A} \tag{7.3}$$

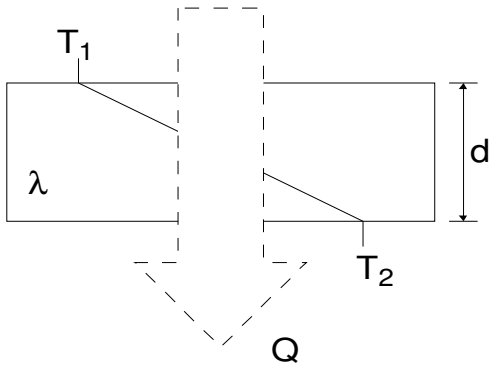

Figure 7.2: the heat Q diffuses from T_1 side to T_2 side. In the steady-state, Q is a constant at random cross-section, and assuming the plane uniform, the thermal conductivity λ is a constant with no dependence on temperature.

In a way that is analogous to Ohm's law governing electrical current flow through a resistance, it is possible to define a conduction thermal resistance as:

$$R = \frac{\Delta T}{Q} = \frac{d}{\lambda A} \tag{7.3}$$

and so $Q = \frac{\Delta T}{R}$. The first layer is the cell itself, and we modelize it by an assembly of three layers since we are going to use triple junction cells Spectrolab C1MJ (GaInP/GaAs/Ge); heat analyses of tunnel junctions and metal layer are ignored. The solder ($Sn_{95}Ag_5$) level is assumed to have a thickness of 50 μm and a thermal conductivity of 37.8 W cm^{-1} K^{-1} [Cotal and Frost, 2010]. The use of a thicker solder layer introduces an increase in thermal resistance but allows for a better relief of the mechanical stress caused by differential thermal expansion of the upper (semiconductor) and lower (DBC) layers during thermal cycles. The following level is the copper layer with thickness of 300 μm. This thickness can be reduced, but due to the high electric currents that will be produced by the cells, a choice of at least 100 μm is advisable. In any case, the high thermal conductivity of copper (4 W/(cm K)) makes its contribution to the global thermal resistance negligible.

The inner substrate of the DBC is taken to be alumina (Al_2O_3), aluminum nitride (AlN) or beryllium oxide (BeO). Standard thickness is of 0.635 mm. The back of the ceramic is then covered with another level of copper, having generally the same

thickness of the front one[5], which is used for adhesion to the heat exchanger.
The thermal characteristic of each layer are shown in Table 7.1. Thermal conductivity and the thermal expansion coefficient for the materials, except for solder and epoxy, have been taken from the Ioffe database (http://www.ioffe.ru/SVA/NSM/Semicond). The corresponding thermal resistances for each layer are calculated for a 1 cm^2 area.

The cell can be considered as made of a 200 μm Ge layer only. For this simplified 1-D model, the temperature variation across the cell (ΔT) in case of a heat flux of 50 W/cm^2 is expected to be 1.7 °C. The contribution to the thermal resistance of the solder paste (here we use $Sn_{95}Ag_5$) isn't high, but it should be considered that the presence of voids into this layer could dramatically decrease the thermal runaway.

Substrate and Thickness (μm)	Th. conductivity (W/(m K)	Th. expansion coefficient (K^{-1})	Th. resistance for 1 cm^2 (K/W)
GaInP 0.7	53	5.4×10^{-6}	< 0.001
GaAs 4	55	5.7×10^{-6}	< 0.001
Ge 200	58	5.8×10^{-6}	0.034
$Sn_{95}Ag_5$ 50+50	37	$25\text{-}35 \times 10^{-6}$	0.027
Epoxy 100	1-4	flexible	1.00 - 0.25
Cu 300+300	38	17×10^{-6}	0.158
Al_2O_3 635	24	7.1×10^{-6}	0.265
AlN 635	180	4.5×10^{-6}	0.035
BeO 635	280	7.0×10^{-6}	0.023

Table 7.1: characteristic for the interconnect structure, considering a C1MJ cell and typical materials used as interconnect to the heat sink. Thermal resistances at room temperature are calculated for a 1 cm^2 area.

Care must be taken not to put a too thick layer of solder, which would increase the thermal resistance, and a not too thin layer, which may cause a non-homogeneity or a lack of solder. In principle, the thermal behavior of the solder is expected to be much better than the epoxy's one. For a 100 μm epoxy layer, a flux of 50 W/cm^2 could result in a ΔT of 50 °T, much higher than the solder's one (about 1.4 °C for a 50 μm layer). Anyway, as a matter of facts, a possible failure mechanism is caused by the solder

[5] This way, the stress introduced by the copper layer, and large CTE, will be balanced on both sides of the ceramic, preventing unwanted bending.

layer shear stresses building up due to different CTE of each layer [Nurmi et al., 2004]. In fact, this is a problem in conventional electronic devices, due the limited yield and large CTE of the solder.

The use of epoxy could give some advantages in terms of relief of the thermo-induced mechanical stresses. In fact flexible species like the epoxy materials have the ability to store lots of mechanical energy: given a certain stress, the strain can be very small. Despite this, if stress is too high, a delamination or cracking of the layer can occur. The thermal conductivity [Hodgin and Estes, 1999] and the thermal resistance for a 100 μm layer of epoxy are the higher among the ones reported in Table 7.1: in case of a thermal flux of 10 W/cm^2, they would give a thermal difference of 10 °C from a surface to the other of the layer itself.

As a check for the cell's thermal resistance, we have tried to perform a direct measurement of this parameter, but unsuccessfully. A MJ cell was soldered to a copper substrate (water cooled), with front contacts made by soldered copper wires. On top of the cell, a Pt100 thermocouple was fixed and encapsulated by a polymide (Kapton) tape, covering the whole cell's surface. At the bottom of the cell, a small hole was dug inside the copper, and a K-thermocouple was inserted, sealed with a thermo-conductive silver paste. A heat flux to the cell was applied by injecting a current through the cells (from 2 A to 10 A), and it was established by measuring the electrical resistance of the cell (Joule effect power). The measurement has failed because of the fact that the difference of temperature measured by the two thermocouples hasn't increase significantly with the increasing of the current (less than 1 °C from 2 A to 10 A). Probably, the thermal runaway at the edges of the cell wasn't negligible, and besides this, the accuracy of the temperature measurements was too low.

7.4 Building of the CPV dense-array receivers

As already said, parabolic dish CPV receivers in general use a 'parquet' of solar cells and for this reason they are called dense array receivers. The essential requirements for a receiver are the realization of the cooling and of the electrical interconnections

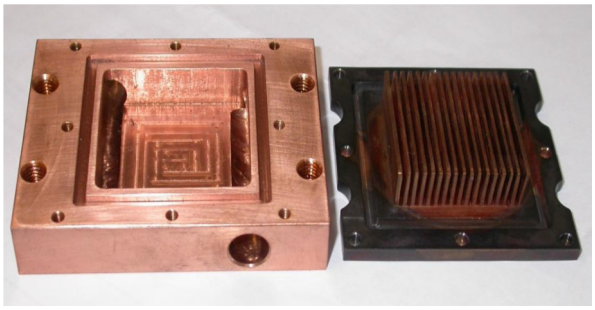

Figure 7.3: the water-cooled copper body and the support with thermal exchange winglets.

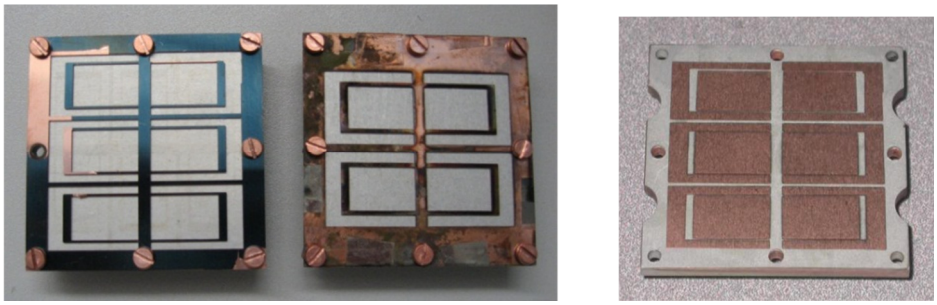

Figure 7.4: the 6-cells and 4-cells masks fixed Al/Al_2O_3 supports. At the right is shown the receiver after the R.F. sputtered copper layout.

(between them and to the external circuitry) of the cell. The materials that can be used and a typical 1-cell assembly prototype have been presented in the previous section. Here we expose our trials to realize a working dense array receiver.

The starting object is a body (6 cm × 6 cm and 4 mm thick, Figure 7.3 right) made of aluminum or copper, which serves as a support for the other layers with the PV cell at the top. This support is fixed to a copper object (7.6 cm × 6.0 cm × 1.5 cm, Figure 7.3 left), which realizes the active cooling of the receiver through an input and an output channel. The support is provided with a series of winglets aimed to enhance the thermal exchange with the cooling water.

The next layer has to be electrically insulated in order to separate the current flowing through the cells, but it simultaneously would be required to be a good thermal conductor. We have used for this layer alumina (Al_2O_3) coatings or aluminum nitride (AlN) plates. The details will be described in the following.

On the top of the insulating material, the conductive traces for the cells interconnections have been realized with a copper deposition having thickness of about 10 mm and coated by R.F. sputtering. The traces layout resulted from the

shadowing of the substrate during the copper deposition with a metal mask. Two kinds of mask have been used; the resulting conductive layouts have 4 o 6 places for the cell to be soldered and separate traces to collect the front contact for each cell (see Figure 7.4). Several attempts have been made to realize an AlN coating on top of the aluminum support, with the goal of reducing the thermal resistance between the PV cell and the heat sink. Unfortunately, in all the samples the film has resulted so porous, that the copper traces coated were in shirt circuit. These depositions are described in Appendix C. The same problem has occurred with the deposition of Diamond-Like-Carbon (DLC) film, have been realized by three different external companies[6] with both chemical (CVD) and physical (PVD) vapor deposition techniques. The advantage that could be given by AlN and by DLC can be seen in Table 7.2, where some oxides and nitrides with low electrical conductivity and good thermal conductivity, are listed.

Material	Thermal conductivity [W/(m K)]	Electrical resistivity (Ω cm)
DLC	> 1100	$> 10^{14}$
AlN	140 - 180	$> 10^{14}$
BN	70 - 120	$> 10^{14}$
Al_2O_3	25 - 35	$> 10^{14}$
SiC	40 - 120	$> 10^{2}$ - 10^{8}
Si_3N_4	~ 27	$> 10^{12}$

Table 7.2: some possible candidates as electric insulators. Values relative to ambient temperature are reported (http://www.ioffe.ru/SVA/NSM/Semicond).

7.4.1 Receiver prototypes

A.

The aluminum supports (fac-simile to the one shown in Figure 7.3 right) have been anodized by the company Gallox S.p.a. (Rovereto, Italy); the result of the anodization process is a 10 μm thick alumina (Al_2O_3) coating. The receiver, before of the soldering of the cells, appears as in Figure 7.4 (right). The soldering process we have tuned is

[6] The three coating manufactors are Argor-Heraus SA (CH), Lafer S.p.a. and Zuani S.p.a. (IT).

described in the next section. The solder layer is consider to be ~ 50 µm in thickness, as is used in [Cotal and Frost, 2010].

PV cell	200 µm
SOLDER	~ 50 µm
Cu	10 - 15 µm
Al_2O_3	~ 10 µm
Al support	4 mm

Figure 7.5: material structure of the A receiver prototype.

B.

The structure B is like A, but with a 250 µm Kovar sheet interlayer, soldered on the copper trace.

PV cell	200 µm
SOLDER	~ 50 µm
KOVAR	250 µm
SOLDER	~ 50 µm
Cu	10 - 15 µm
Al_2O_3	~ 10 µm
Al support	4 mm

Figure 7.6: the configuration B is like the A one with a Kovar plate at the bottom of the cell.

C.

In this case the support is a copper body. The insulating layer is instead an AlN plate (commercial), with 5 cm × 5 cm dimensions; two thicknesses for these plates have been used, 250 µm and 1000 µm. The copper traces have been coated on top surface of

the plate, whereas at the bottom surface a uniform copper coating, 1 μm thick, has been evaporated. This layer is needed to solder the plate to the underlying support.

PV cell	200 μm
SOLDER	~ 50 μm
Cu	10 - 15 μm
AlN	250 / 500 μm
SOLDER	~ 50 μm
Cu support	4 mm

Figure 7.7: material structure of the C receiver prototype.

D.

The electrical insulation between the cell and the heat exchanger is here made through a commercial DBC plate, like the one shown in Figure 7.1 and supplied by Angelantoni S.p.A. It is composed of a ceramic 300 μm tile (AlN) with a 200 μm sheet of copper bonded to both sides by a high-temperature oxidation process. The copper is Au coated to prevent corrosion and oxidation.

	PV cell	200 μm
	SOLDER	~ 50 μm
DBC	**Cu / Au plated**	200 μm
DBC	**AlN**	300 μm
DBC	**Cu / Au plated**	200 μm
	SOLDER	**~ 50 μm**
	Cu support	4 mm

Figure 7.8: material structure of the D receiver prototype.

7.4.2 Cell soldering and voids

The first built receiver of type A (the full assembly is shown in Figure 7.9), starting from the Al/Al_2O_3 support of Figure 7.4, was assembled in two different steps: the soldering of the cells to the copper traces together with the busbar contacts, and then the fixing of the external contacts to the fiberglass board. The operation of the cells' soldering has been developed as follows.

1) The support is placed on a heating plate at 200°C, and the copper traces are tinplated with a $Sn_{62}Pb_{36}Ag_2$ solder paste (Multicore SN62 RM89 AAS 85 V, melting point 179 °C).
2) Cleaning in an acetone bath at 100 °C for 5 min.
3) Placement of small solder drops (about 1 drop/2 mm^2) on the back-contact trace and on the busbars.
4) Cells placement with a sucker-pen. Protection and lock of the cells with a polymide (Kapton) ribbon.
5) Placement of the contacts on the busbars.
6) Heating for 5 min, at 230 °C (heating plate temperature).
7) Cooling down and washing in hot acetone (100 °C for 5 min) and hot isopropanol (100 °C for 5 min).

The receiver was finally tested by means of a digital multimeter; all the cells were working. Nevertheless, after problems occurred after the exposure to concentrated solar radiation (described in paragraph 7.4.3), we have decided to enhance the whole process.

Actually, one of the main causes of damage to the welds between the various components of a CPV receiver is the presence of voids in the solder layer. Voids in the solder are a common problem and are usually tolerated if they are present at levels less than 3 % and if they are small enough [Lathrope, 2003]. Large voids prevent the exchange of heat between the various layers and can bring to the formation of so called "hotspot" that causes premature component failure, a loss of performance, or both. The characteristics and the dimensions of the voids are mainly dependent on the materials that are joined and from the type of technology used for welding.

For this reason we have tried another solution for the soldering of the cells to the

receiver. Instead of heating the assembly on a heating plate, we have performed the soldering process inside a vacuum chamber. The receiver was inserted inside a tube connected to a vacuum pump, and this tube was inserted inside a furnace. The aspiration of a vacuum pump is expected to drain the air bubbles from the inside of the solder layer. The final stage of development of this process has been the following.

1) Receiver preparation as above (solder placement, cell fixing, Kapton ribbon). In case of B, C and D type receivers, more components are present and two solder layers are needed.
2) Insertion of the receiver in a stainless steel tube connected to the vacuum chamber under 10^{-6} mb.
3) Heating in a furnace at 220 °C (furnace temperature) for 20 min.
4) Cooling down and cleaning as above.

The realization of the front contacts in this case is separated from the cells fixing process.

7.4.3 Electrical connections and front contacts

The realization of the connections to the busbar metalization on top of small area concentrator solar cells is an issue common to both fresnel-like assemblies and dense array receivers. Most of the commercial receivers prototypes (fresnel-like) are realized with ultrasonic wire-bonding techniques [Harman, 1997], that we tried to use and will be discussed further. Another strategy (see Figure 7.1) is adopted by Spectrolab, which used a proprietary process to directly solder a metal sheet to each busbar [King, 2008].

In the present work we made several attempts to solder metal contacts to the cells' busbars. The first built prototype, receiver A shown in Figure 7.9, had these contacts made of small curved pieces silver ribbon, having 10 mm width and 0.1 mm thickness, soldered in a unique process together to the fixing of the cells. The contacts are collected by means of a silver ribbon having a width of 10 mm: a flat-shaped ribbon for the front contact, and another one arch-shaped for the back contact. In order to solder these connections, the receiver with the fiberglass board was placed on a heating plate at about 160°C, that didn't melt the solver layer at the bottom of the

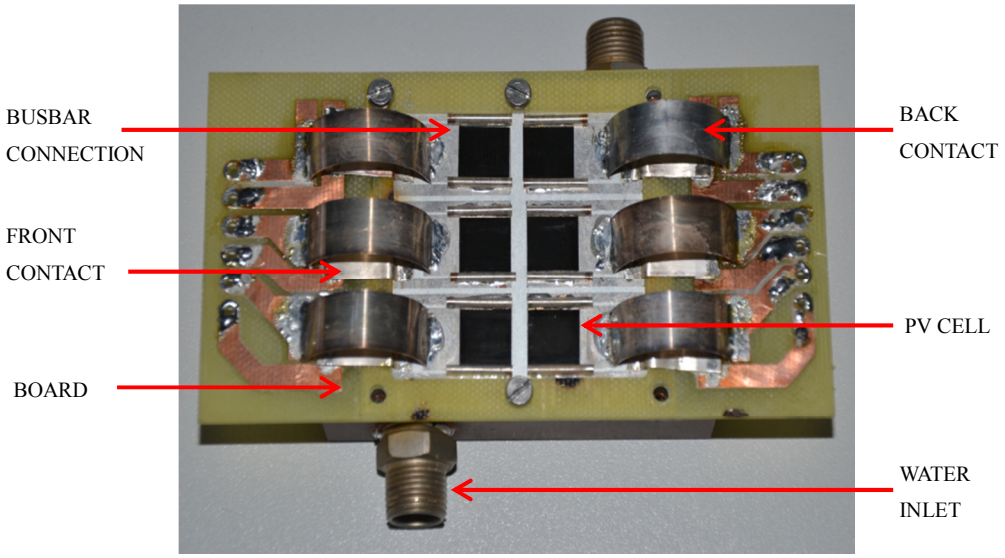

Figure 7.9: receiver A with 6 cells soldered and mounted on the copper body (heat sink). The front and back contacts are realized by means of a Ag strip and collected on a fiberglass electronic board. The water inlet and outlet for the active cooling are inserted on the heat sink.

cells[7]. This served as pre-heating for the contacts to be soldered, that was completed with a Weller soldering tip at 450°. After proper cleaning with acetone and isopropanol, these contacts have all shown to be mechanically robust, and the electrically functioning after a check with a digital multimeter. A problem could arise from thermally induced expansion of the metallic ribbon. Moreover, it was difficult to precisely control the placement of the solder past on the busbar. For these reasons other approaches have been explored.

After that other attempts using Ag and Au ribbons have proven complications, we decided to use thin wires for the busbar connection. In Figure 7.10 is shown a prototype of receiver B. The contacts to the external board have been realized here by means of smaller Ag strips, whereas the contacts to the busbar have been made by copper wires (1/10 inch in diameter). This method required a small portion of solder paste on the busbar and the placement of a U-shaped wire contacting the busbar in two points; the connection was realized by pre-heating and a soldering tip.

[7] The temperature at the base of the cells was much lower, and the used solder past melts at about 178 °C.

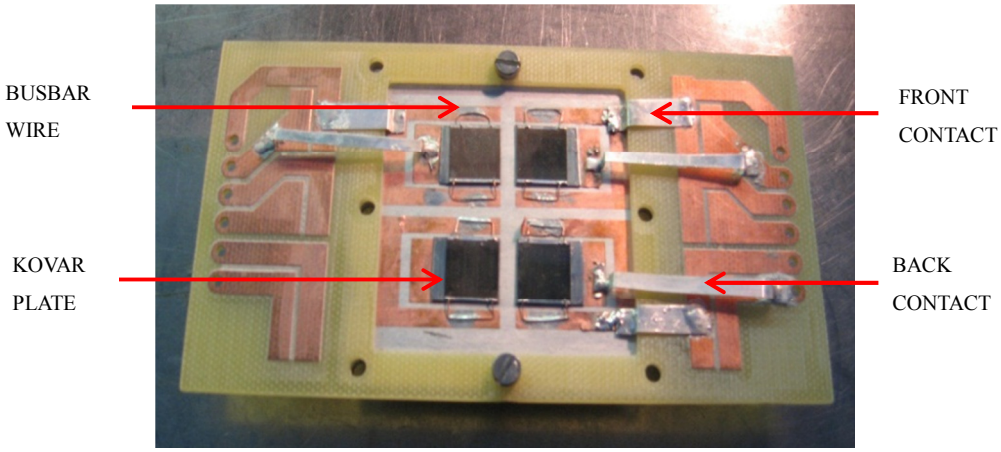

Figure 7.10: receiver B with 4 connected cells; the front contacts are collected through copper wires soldered to the busbar contacts on top of the cell.

A slightly different shape for the wires is shown in Figure 7.11. This L-shape has proven to strike the balance between reliability and ease of manufacturing, and was used in the further receiver assembling.

Some trials have been made with wire-bonding techniques, too, by using with two different apparatus. In case of *Aluminum Wedge-Wedge Bonding*, with 20 µm wires, the connection weren't solid enough, probably due to oxidation problems. In addition, for the optimized process, two out of six cells have resulted damaged. In case of Gold Ball-Wedge Bonding the results have instead been satisfying. The realized connections have been made with copper wires with diameter of 18 µm and by adjusting the machine parameters. Conversely to what is reported in [Rey-Stolle and Algora, 2003], where 30 cells have been wire-bonded and about 30% of them showed damage. This was verified on 6 wire-bonded cells (10 bondings for each cell), by measuring the pre-bond and post-bond dark I-V currents (at 1 V). The dark current hasn't changed significantly, and this proves that solar cell performances haven't suffered degradation. A possible reason for the success of our bonding operation is the mechanical damaged due to the ultrasonic power, in our case no one cell was fact that we performed each bonding in two different steps: firstly, a gold ball is laid on the copper trace and then pushed with a wedge bonding; secondly, another ball is pushed to the first one, and the wedge is made on the cell's bus-bar. This way, the first bond (on the copper trace) results more solid; the transmission of the vibrational energy to the second bond could be more efficient, allowing to decrease the ultrasonic power and thus to reduce the risk

of mechanical damage. Even if many bonding points should be applied to each bus-bar (around 10 for the gold wires under a 5 A current), the wire-bonding technique could be a good solution, and this should be outdoor tested in operative conditions. We have chosen to abandon this technique for now because of the fact that the ball bonding machine is not present at the Department of Physic at Trento.

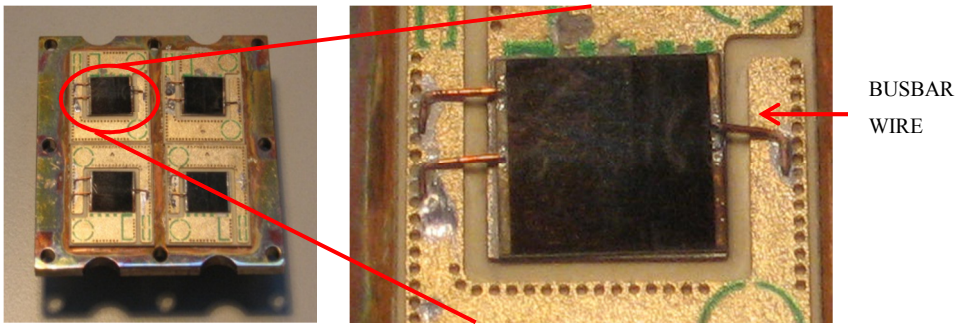

Figure 7.11: receiver D with 4 DBC plates and 4 cells; the copper wires having L-shape used as front contacts are showed.

7.4.4 Preliminary evaluation after exposure to sun.

Before using the receiver to prove the 2nd type of connection and to perform a thermal response test, we have observed preliminary facts as regard to the material configurations A-D for the receiver under working conditions, i.e. under exposure to concentrated solar radiation. Actually the first built receiver, the Al/Al_2O_3 of configuration A, as shown in Figure 7.9, was ready to be tested. All the six cells were fully functioning after the soldering processes (cells and front contacts); this was established by the measurement of the open circuit voltages V_{OC} ~2.5 V under the illumination produced by a halogen lamp. As soon as this receiver, fixed to the water-cooled copper receiver was mounted on the solar tracker, a couple of cells started to fail (V_{OC} = 0). After other four exposure cycles, required to measure the I-V curves (about 1-2 minute of sun-exposure for each cycle), the receiver was brought in laboratory. After a brief time in which the receiver cooled down, just two cells showed $V_{OC} \neq 0$, and anyway at least one of them had a not optimal voltage (1.4 V).
The cells have then been observed with the microscope and they looked like the new cells; there was no evidence of craters or black portions due to charred moisture on top

surface of the cells. The possibility of re-melting for the solder paste, which may shoot down the cell parallel resistance, has also been excluded.

The most probable cause of damage is the mechanical stress due to different CTE between aluminum and germanium (PV cell). During the manual soldering operation, differential expansion can result in the formation of micro-cracks that may not be detected during the manufacturing process and result in a less than expected field lifespan. Moreover, some hot-spots in the cell' slice can occur because of voids in the solder layer under the cell itself.

To reduce the stress, we have chosen a material with a better matched CTE, which is AlN. Another attempt has been made with configuration B, in which a Kovar alloy plate has been placed under the cell. Kovar has a CTE of 5.9 ppm/K (http://www.cleanroom.byu.edu/CTE_materials.phtml). One of the receivers realized with B structure, is shown in Figure 7.12. Unfortunately, they all had the problem of the lifting of the copper traces, which happened after the heating cycle (soldering of the cells). This was a problem of the R.F. sputtering deposition, and impeded us to further use these receivers.

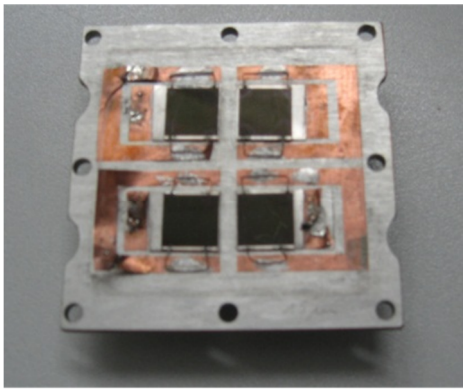

Figure 7.12: receiver B showing the Kovar plates at the base of the cells; after the soldering process most of the copper traces resulted lifted.

7.5 Thermal simulation of the receivers

7.5.1 Heat transfer mechanisms

Energy transfer in the heat form occurs when temperature difference exists between different sides of a material. Heat is always transferred from the hotter object to the colder one and it occurs through three basic transfer mechanisms: conduction, convection, and radiation. A detailed description of these three mechanisms can be found in [Chengel, 2006].

- **Conduction**

For a one-dimensional transfer in a plane wall, the amount of heat flux by conduction is proportional to the normal temperature gradient dT/dx and the cross sectional area A:

$$\dot{Q} = -\lambda A \frac{dT}{dx} \tag{7.4}$$

where λ [W/(m K)] is the thermal conductivity of the material and the minus sign means that heat is transferred in the direction of decreasing temperature. On the basis of conservation of energy, the balance of heat-conduction energy for a medium is expressed by the *heat diffusion equation*, that in rectangular coordinates is:

$$\lambda\left(\frac{\partial^2 T}{\partial x^2} + \frac{\partial^2 T}{\partial y^2} + \frac{\partial^2 T}{\partial z^2}\right) + \dot{g} = \rho C_P \frac{\partial T}{\partial t} \tag{7.5}$$

where C_P [J/(kg K)] is the specific heat, ρ [kg/m^3] is the density and $\dot{g}$ [W/m^3] is the rate of heat generation inside the infinitesimal volume $\Delta x \Delta y \Delta z$. This equation, with specific boundary conditions, has analytical solution for the temperature distribution inside a solid. In the next chapter, when the simulation program COMSOL will be used to solve heat transfer problem, the boundary conditions are reported.

- **Convection**

When the thermodynamic system is a fluid, in general the heat transfer is accompanied by macroscopic transport of matter. Convection is the transfer of energy between a solid surface and the adjacent fluid in motion, and involves the combined effects of conduction and mass transport. It can be distinguished in two categories depending on the characteristics of the motion of the fluid: natural convection (the fluid motion is caused by forces induced by the difference in density, due to the variation of temperature) or forced convection (motion caused by external means). The basic formula of calculating convective heat transfer rate is the Newton's law of cooling:

$$\dot{Q} = h\,A\,(T_S - T_\infty) \tag{7.6}$$

where h [W/(m^2 K)] is the convective heat transfer coefficient, A [m^2] is the area and $T_S - T_\infty$ [K] is the temperature difference between the surface and the fluid. The coefficient h depends on several factors, as, the geometry of the surface, the nature of the motion, the properties and the speed of the fluid. By using known relationships derived for particular conditions and geometries, one can get h in certain situations, even if in case of complex geometries it is better to evaluate h through the measurement of all the heat transfers between an object and the surroundings. In any case h is directly related to the Nusselt number Nu, that is the ratio of convective to conductive heat transfer across (normal to) the boundary [Chengel, 2006]:

$$Nu = \frac{h\,L}{k_f} \tag{7.7}$$

where k_f is the thermal conductivity of the fluid. L is the characteristic lenght, a dimension that defines the scale of a physical system. For example, in the case of an horizontal cylinder the characteristic length is equal to the

diameter. In the case of laminar flow, as in the natural convection, over a flat plate, the Nusselt number is given by a relation with Prandtl (Pr) and Reynolds number (Re):

$$Nu = 0.332\ Re^{1/2}\ Pr^{1/3} \tag{7.8}$$

Both Re and Pr are dimensionless number that can be derived for any particular situation [Chengel, 2006], given the velocity of the fluid, the geometry and the nature of the viscous motion (turbulent or laminar flow) .

- **Radiation**

Radiation differs from the other modes in two important aspects; first, no medium is required for transport of energy by radiation, and second, the rate of heat dissipation by radiation varies approximately as the fourth power of the absolute temperature, while that by the other modes varies approximately as the first power of temperature. For these reasons radiation becomes the dominant mode of heat transfer at high temperatures [Touloukian, 1970], and anyway is very important as regard to the temperatures that can be reached in a CPV heat sink.

The flux emitted [W] from a real body radiator is given by Stefan-Boltzmann equation:

$$\dot{q} = A\ \varepsilon\ \sigma\ T^4 \tag{7.9}$$

where A is the emitting surface, $\sigma = 5.6697 \times 10^{-8}$ W/(m^2 K^4) is the Planck constant and ε is the emissivity of the surface.

7.5.2 Heat transfer with COMSOL Muliphysics

The present simulations have been performed by using the basic features of COMSOL *Heat Transfer Module*. To simulate heat transfer processes the following steps have been followed:

1. Geometry modelling. Depending on integration volume and on physical parameters,a model (1D, 2D, or 3D) was established.

2. Physics settings. We can select the packages that we want to include, i.e. the physics that we want to simulate (AC/DC, acoustic, chemical transport, fluid flow, heat transfer, structural mechanics), and then if we want to simulate a stationary or time-dependent study. In our case we needed the heat transfer package and a stationary study.
3. Selection of parameters that define the model, for example in our case the ambient temperature, the initial temperature of the sample or the emissivity of the surface.
4. Geometry definition. Through the built-in software functions, or thanks to the tools that allow to import a geometry already drawn with appropriate programs, it is possible to define the geometry of the problem, the size and to select parts of the systems to which assign specific physical properties.
5. Materials setting. One can use the built-in library of materials to assign specific physical properties such as specific heat, density, thermal conductivity, and others (Figure 7.13).

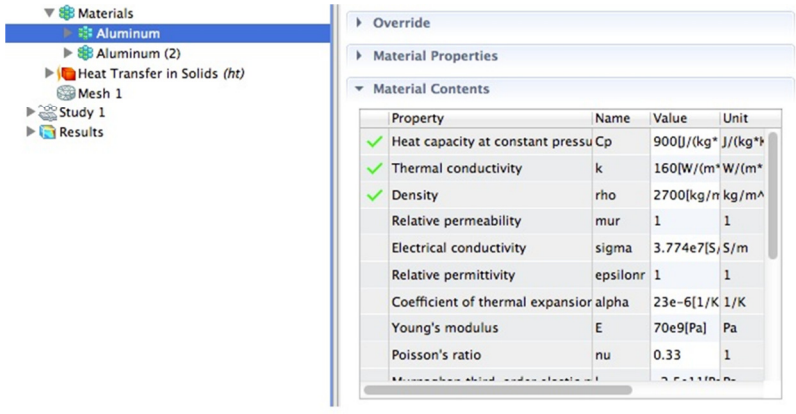

Figure 7.13: example of the library of physical properties: the built-in Aluminium.

6. Setting the physics for a specified problem. Some default settings are already selected, for example Heat transfer in solids is assigned to all domains of the problem. For a stationary study (like the present one) we

had to set the boundary conditions of the problem.

7. Mesh setting. The mesh is the collection of vertices, edges, and faces that defines the shape of objects and divides it in finite elements (where the temperature is uniform). Mesh can be set with default settings or with user-defined settings (shape, distribution and dimensions).
8. Computation. With the software functions one can start the simulation and also select variables that must be calculated.

For our simulations we used the package Heat transfer in Solids with basic features. In the Model Builder window we had added to our model the heat transfer mechanisms. Depending on whether the phenomenon is surface or volume, we can assign a heat flow to a boundary or to a domain. As we already said, Heat transfer in solids is assigned by default to all domains of the problem. If the thermal conductivity k is isotropic (homogeneous solid), the velocity is set to zero, one get the equation governing pure conductive heat transfer that is equal to Equation 7.5.
The convection in the basic Heat transfer module is simulated by assigning to the boundaries an heat flux that enters in the energy balance with the equation:

$$-\mathbf{n} \cdot (-k\,\nabla T) = h \cdot (T_{ext} - T) \tag{7.10}$$

where T is the temperature of the selected surfaces, T_{ext} is the ambient temperature (e.g. air surrounding an heat sink), $\mathbf{n}$ is the vector normal to the boundary and h is the convective heat transfer coefficient. The radiation contribution can be inserted in the model by the function Surface-to-Ambient Radiation and it can be assigned to the boundaries of the considered object. The equation for the radiative heat flux that enters in the energy balance is:

$$-\mathbf{n} \cdot (-k\,\nabla T) = \varepsilon\,\sigma({T^4}_{amb} - T^4) \tag{7.11}$$

If we want to consider a constant power input through a boundary surface we can insert it by the function:

$$-\mathbf{n} \cdot (-k\,\nabla T) = \frac{Q_{tot}}{A} \tag{7.12}$$

where Q_{tot} is the total power through the boundary surface of area A.

7.5.3 Thermal simulation conditions

The objects utilized in thermal analysis are prototypes of CPV receivers to be exposed to the concentrated solar flux. For simplicity, each object is just 1 cm^2 in area, and consists of a MJ solar cells and the interconnections layer, made by the materials of Table 7.1, to the copper heat sink. The cell is connected to the substrate layer trough a conductive $Sn_{60}Pb_{40}$ paste (30 μm) or a Ag filled epoxy (50 μm). In the following, the various types of receiver' structures that have been considered are listed in Table 7.3. They are labeled with symbols S_A ...S_E, in order not to create confusion with prototypes of paragraph 7.4.1. The analyzed materials include Al/Al_2O_3, an AlN plate and two coatings (AlN and DLC).

Receiver	Structure
S_A	Ge 200μm / $Sn_{60}Pb_{40}$ 30μm / Cu 15μm / Al_2O_3 10μm /Al 4mm
S_B	Ge 200μm / $Sn_{60}Pb_{40}$ 30μm / Cu 15μm / AlN 250μm / $Sn_{60}Pb_{40}$ 30μm / Cu 4mm
S_C	Ge 200μm / $Sn_{60}Pb_{40}$ 30μm / Cu 15μm / AlN 2μm / Cu 4mm
S_D	Ge 200μm / $Sn_{60}Pb_{40}$ 30μm / Cu 15μm / DLC 2μm / Cu 4mm
S_E	Ge 200μm / epoxy 50μm / Cu 15μm / Al_2O_3 10μm / Al 4mm

Table 7.3: receiver's structures utilized in the thermal simulation with *Comsol Multiphysics*.

After the setting of the geometry and the assignment of material for each layer, the stationary study in the *Heat transfer in solids* has been selected. The initial condition (boundary condition for the differential equation of heat transfer) considers the temperature of the stack equal to room temperature 293.15 K. Instead of adding the fluid study to the 3D model, considering the thermal transfer between the cooling fluid and the heat exchanger, we fixed a temperature at the base of the substrate (bottom surface of the copper or aluminum support) of 17 °C. This assumption doesn't change the behavior of the structures under analysis (this conclusion has been indeed verified).

Subsequently, the physical processes for the model are added: an incoming heat

flux on the top surface of the cell and convective cooling (surface-to-ambient radiation). Heat transfer by conduction is enabled by default. Natural convection has been considered, for a horizontal plate, upside oriented.

The physical properties (thermal conductivity) of the materials used to build up the module, that represent the input data of the model itself, are taken from the software database except for those of solder [8], λ = 50 W/(m K), DLC and AlN depositions. Generally, thermal conductivity of deposited thin films is different from their bulk form due to the special nature of the microstructure resulting from the growth process, and they can range across several decades. For these reason the thermal conductivities have been taken of 2 W/(m K) for both AlN and DLC films. These values are in agreement with the results reported in [Ducquenne et al., 2012] and [Shamsa et al., 2006], respectively. The thermal distributions in the receivers' domain are evaluated at equilibrium for heat flux values ranging from 10 to 100 W/cm^2.

7.5.4 Results

In Figure 7.14 the temperature distribution on the receiver S_E for an incoming heat flux of 50 W/cm^2 is shown (this is the heat flux that would be produced by a 1000 X optical concentrator with optical losses of 20% and a cell efficiency of 30%). In this case the temperature at the top surface of the cell reaches about 38.5 °C and is the the highest among the ones here calculated. In fact, the epoxy layer negatively affects the thermal runaway from the cell to the heat sink, with respect to solder. The graph in Figure 7.15, relative to Figure 7.14 and derived from a cut line vertically drawn at the center of the receiver's stack, shows the temperature as a function of the distance from the cell's surface. The main contribution, about 12 °C of temperature gradient, is given by the epoxy layer, whereas the contribution of the thin layer of copper and alumina are negligible. The variation across the aluminum substrate is of about 8 °C. It could easily be reduced by a factor 2 by simply decrease the aluminum thickness to 2 mm. This thickness can't be reduced too much, because the support has to guarantee mechanical support and an uniform temperature distribution.

[8] http://alasir.com/reference/solder_alloys/

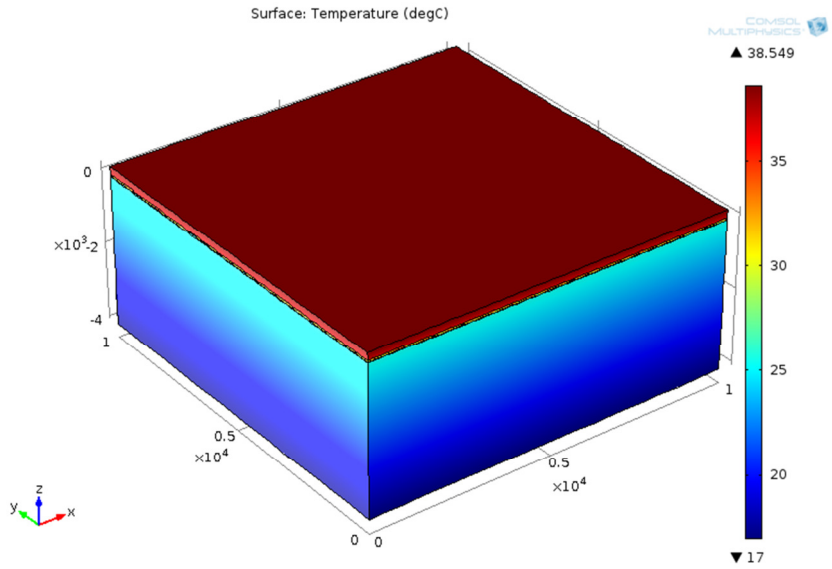

Figure 7.14: surface temperature distribution simulated with Comsol for receiver S_E exposed to an heat flux of 50 W/cm^2. The bar indicates the temperature in °C.

The temperatures on receiver S_C under 50 W/cm^2 can be seen in Figure 7.16. In this case the main contribution to the temperature gradient is given by the copper substrate itself, whereas a temperature excursion lower than 0.5 °C is calculated across the 30 μm solder layer. The comparison between the five types of CPV receiver is aided by the Table 7.4. The temperature distributions for S_C and S_D are the same, since the

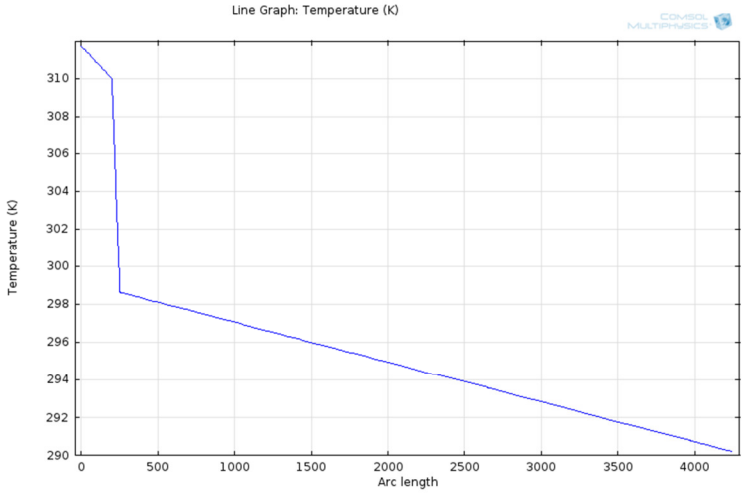

Figure 7.15: vertical temperature distribution for receiver S_E under 50 W/cm^2. The base of the cell is the origin for the length coordinate. The main contribution is given by the epoxy layer.

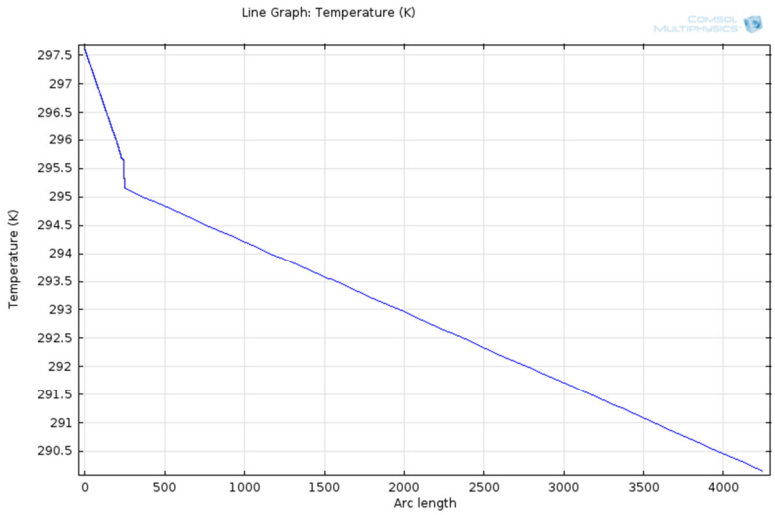

Figure 7.16: vertical temperature distribution for receiver S_C under 50 W/cm^2. The base of the cell is the origin for the length coordinate. The main contribution is given by the copper substrate.

Heat flux (W/cm^2)	S_A ΔT (°C)	S_B ΔT (°C)	S_C/S_D ΔT (°C)	S_E ΔT (°C)
10	2.20	1.59	1.48	4.29
20	4.24	3.18	2.96	8.61
30	6.37	4.78	4.45	12.83
40	8.49	6.38	5.72	17.23
50	10.62	7.98	7.43	21.95
60	12.75	9.59	8.93	25.90
70	14.89	11.20	10.42	30.24
80	17.09	12.81	11.92	34.58
90	19.93	14.43	13.46	38.94
100	21.70	16.05	14.94	43.31

Table 7.4: thermal excursion across the receivers for different incoming heat fluxes resulting from the simulation. The temperature at the base of the stack is fixed at 17 °C.

contribution given by AlN and DLC films (2 μm) is negligible. These material's configurations are the most effective as thermal stacks among the simulated ones. The other extreme is the receiver using epoxy, as already said. It is interesting to note that

the thermal performance of receiver S_B are better than those of S_A one, even if the latter is a thicker structure and includes two solder layers instead of one.

It should be outlined the range of heat fluxes is consistent with real CPV illumination levels. Let's suppose a concentration value of 500 X, and a direct solar flux 900 W/m^2 incident on the CPV optical element. By supposing a reasonable optical efficiency of 90%, and a power conversion efficiency of 30 % for the cell, the incoming heat flux would be of about 285 W/cm^2. In this case the temperature at the top of the cell is expected to be lower than 22 °C for receiver S_B and lower than 34 °C for receiver S_E.

An important aspect that has to be considered is the influence of voids in the solder layer on the thermal performance. Large voids prevent heat transfer and can cause premature component failure, loss of performance or both. Their origins are not well understood but are typically faulted as a failure of the solder fillet to thoroughly expel flux remnants during the reflow process. As a matter of facts, it is more difficult to control the uniformity of the solder with respect to epoxy, because of the reflow soldering process. The amount of solder voiding can vary significantly within an assembly, between different flux formulations, solder alloys and component metallization. The deleterious effect of voids is shown for receiver S_B in Figures 7.17-7.20.

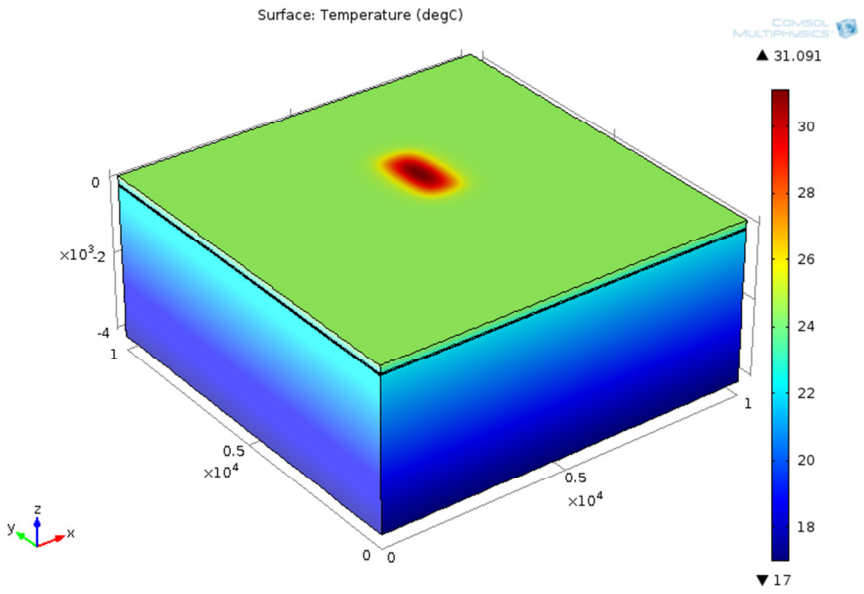

Figure 7.17: surface temperature distribution simulated with Comsol for receiver S_C exposed to a heat flux of 50 W/cm^2 and with a solder void of 1×2 mm^2.

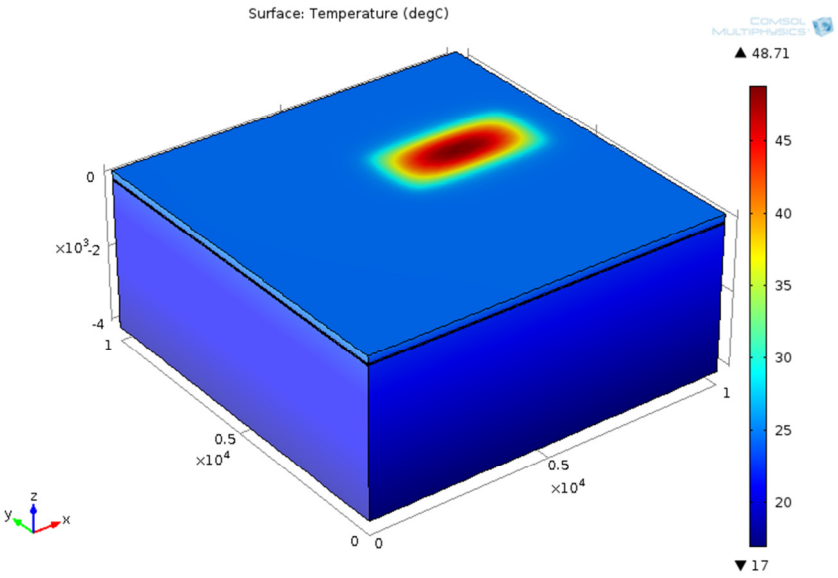

Figure 7.18: surface temperature distribution simulated with Comsol for receiver S_C exposed to a heat flux of 50 W/cm^2 and with a solder void of 2×4 mm^2.

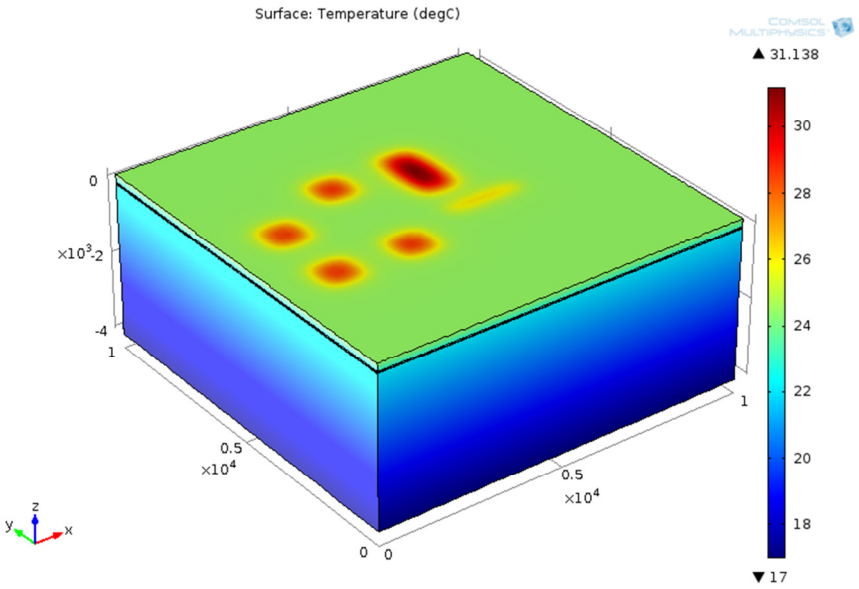

Figure 7.19: surface temperature distribution simulated with Comsol for receiver S_C exposed to a heat flux of 50 W/cm^2 and with a given solder void distribution (total voids 6.8 mm^2).

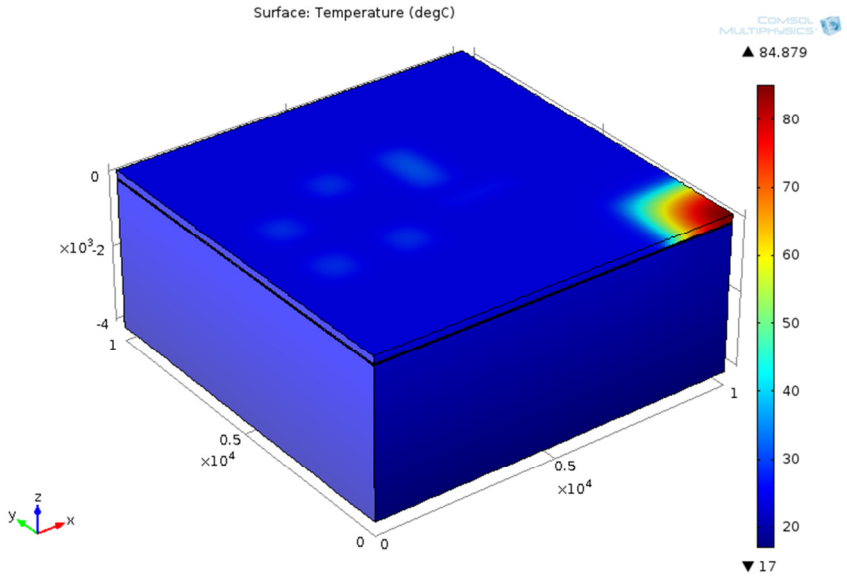

Figure 7.20: surface temperature distribution simulated with Comsol for receiver S_C exposed to a heat flux of 50 W/cm^2. The solder void distribution (total voids 10.8 mm^2) presents a corner void.

For a single void of 1×2 mm^2 the temperature increases up to 31 °C (instead of 24.4 ° C), and if the same void is enlarged to 2×4 mm^2 dimensions, it reaches 48.7 °C. These temperature non-homogeneities and the associated mechanical stresses may accumulate and bring to the cell breakage. In the Figure 7.19 and 7.20, the effects of other two voids distribution in the solder layer are shown for receiver S_C under 50 W/cm^2. In the first case the voids cover a total area of 6.8 mm^2; in the second case a corner void is added and the total void area is 10.8 mm^2 and temperature reaches a very high value of 84.9 °C. The corner voids has a large impact on the cooling, because it is the zone where the thermal runaway to the heat sink is less effective.

7.6 Conclusion

The realization of a dense array receiver is the most crucial part of a parabolic dish-like CPV system. Then, in order to build a reliable system we have to identify its critical points and try to achieve an affordable solution. In the present work it results

clear that reliability can be obtained just with a robust receiver able to endure several sun-exposure cycles (thermal cycles) and thus able to both cool the PV cells and to accommodate the arising mechanical stress. We have considered different materials that are both thermal conductors and electrical insulators. The Al/Al_2O_3 has been proven to cause the cell failure because of the high stress due to the different CTE between Al and PV cell, and a possible solution which has to be evaluated is the use of Kovar as interconnecting layer.

The best receiver we have developed makes use of a 5×5 cm, 250 μm thick AlN plate as insulating material. The AlN plate has been soldered to a water cooled copper support; on top of the plate a 10 μm copper layout has been R.F. sputtered in order to fix the cells and collect the electrical power. The realization of the front connections has been realized by means of copper wires having L-shape and directly soldered to the cell busbars. The choice of AlN is validated by a 3D model in which conduction, convection and radiation are used to simulate the thermal response of different sandwich structures to an incoming thermal flux. From this simulation we have shown the better thermal behavior of solder with respect to epoxy adhesives, and of AlN-based structure with respect to the Al/Al_2O_3 one. The best structure would use a thin film as interconnection insulating layer; we have tried to realize two different coatings (AlN, DLC), but without success. From the simulation we have also shown the importance of getting a solder layer with voids as small and few as possible. For this reason the cell soldering process has been made in a vacuum chamber. The final receiver realized with 6 MJ cells soldered to an AlN plate under vacuum has been exposed to several working cycles without showing any breakage or degradation of performance.

Appendix A

Calorimeter sub-components

The description of the calorimeter, used to quantify the optical efficiency of the concentrator prototype (with a single parabolic module) has already been given in Chapter 3 (Section 3.3). Here some more details and pictures of the sub-components are provided.

The receiver is a 10 millimeter thick copper plate, 10 centimeters in diameter, whose front face (oxidized, Figure A3) is exposed to concentrated solar energy, and whose rear face is wetted by the cooling water. The rear part looks like in Figure A1; it has been carved into channels and then covered with a thin copper plate (3 mm), which has been soldered to the body.

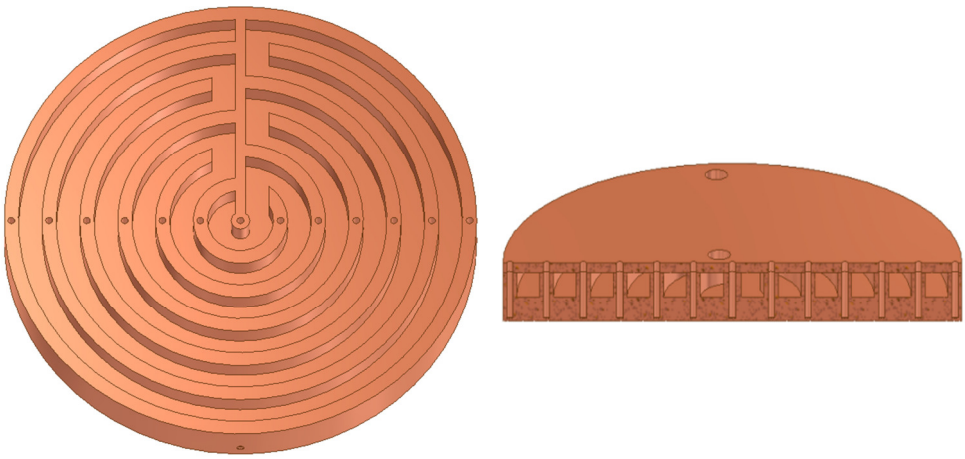

Figure A1: Copper plate with channels for the water and holes for k-type thermocouples (a), Copper plate with rear cover soldered (b) and section of the copper plate (c)

The sides and the back of the plate have been insulated with 6mm thick pyrogel 671. Thermal conductivity of pyrogel is less than 18 mW/(m K) under 100°C (Figure A2),

which is the range of temperature we expect to reach on the front face.

The insulated copper plate is contained into a stainless still cylinder, which can be easily attached to our concentration solar collector. The low conductivity pyrogel layer allows us to disregard thermal losses toward the steel stand, and consider only losses from the front face, being those reflection, convection and radiation.

The stainless steel housing and the assembly with the copper plate, the pyrogel and the thermocouples appear like in Figure A4. The Figure A5 shows the completely assembled flat plate calorimeter, with the 13 k-type thermocouples inserted in the holes. The calorimeter is also shown during the measurements.

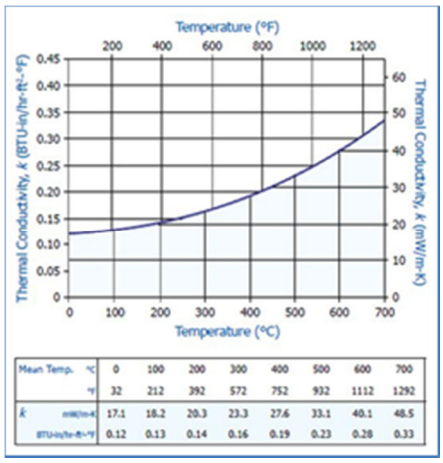

Mean Temp. °C	0	100	200	300	400	500	600	700
°F	32	212	392	572	752	932	1112	1292
k mW/m-K	17.1	18.2	20.3	23.3	27.6	33.1	40.1	48.5
BTU-in/hr-ft²-°F	0.12	0.13	0.14	0.16	0.19	0.23	0.28	0.33

Figure A2: thermal conductivity of Pyrogel 6671.

Figure A3: copper plate built as a receiver for the calorimeter: the front face has been oxidized; on the rear face, the holes for the thermocouples and inlet and outlet pipes are visible.

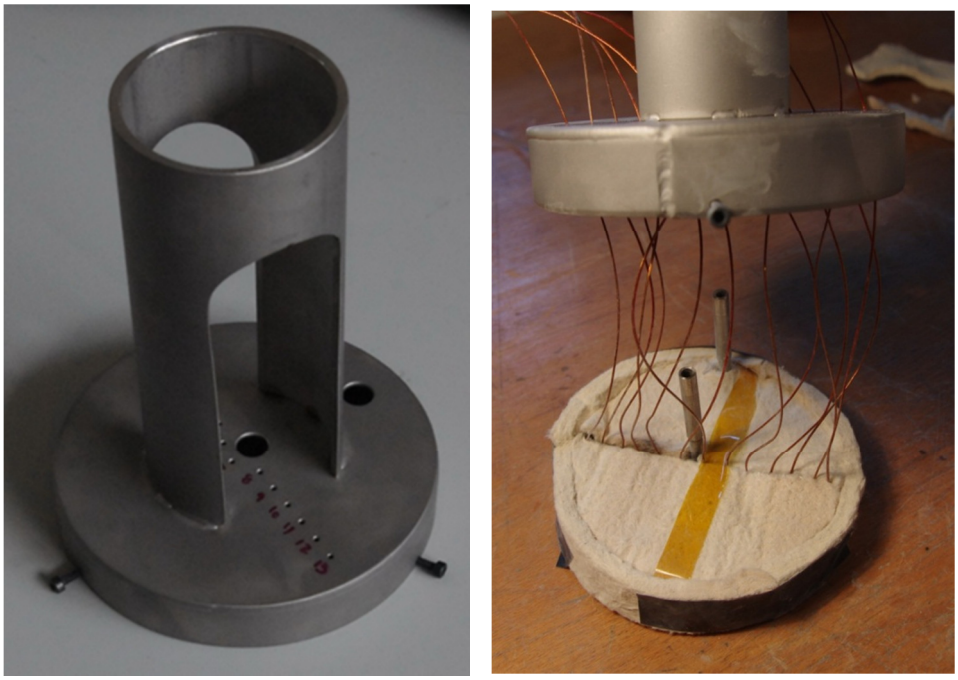

Figure A4: stainless steel housing, on the left, and assembling phase, on the right.

Figure A5: completely assembled flat plate calorimeter. On the right, it is mounted on the concentrator

.

Appendix B

Copper oxide observations.

The copper plate of the calorimeter has been oxidized in order to enhance solar absorption. The full process of synthesis of the CuO film is described in Chapter 3, Section 3.3. We used a chemical reaction in which by just immersing the copper substrate in the chemical, with proper composition, for certain period of time will lead to the chemical oxidation. Important advantage with this technique is that by just changing the precursor composition and exposure time will lead to the formation of range of textures on the surface. These include geometrically roughened surfaces and coatings with microcrystalline metal particle gradients or artificially produced optical constant gradients formed through changes in the composition of the oxide coatings. The film deposited by PVD is usually flat and shiny which does not provide the texture effects for enhance absorption. To obtain irregular surface it is necessary to optimize the deposition condition which is time consuming and this may also lead to deteriorate the adhesion properties.

Some images of the structure of the copper oxide film have been acquired in order to have information on the resulting films, and to optimize the chemical process (evaluated with absorbance measurements). The present images are relative to the final film that has been deposited.

Scanning electron microscopy (SEM) images have been obtained by using a JSM-7001F, JEOL whereas compositional studies of the films were carried out by Energy Dispersive Spectroscopy (EDS, INCA PentaFET-x3) attached with the SEM.

Figures A6 (A) and (B) present the digital photos of copper substrate before and after formation of copper oxide by chemical conversion method, respectively. The reflection of the digital camera is clearly observed, while taking the photo, on the surface of the polish copper substrate (Figure A6 (A)) indicating the mirror like surface with high reflectance. The chemical oxidation treatment of the copper

substrate causes the formation of total black color copper oxide (Figure A6 (B). SEM images of the copper substrate before and after formation of copper oxide are reported in Figures A6 (C) and (D) respectively. Polished copper substrate seems to be quite flat and smooth with some small pit marks, whereas the other image (D) reveals the formation of porous black copper oxide film with high surface to volume ratio. The copper oxide surface is formed of nano-petals like structures with a thickness of around 5-10 nm. These petals grow with their surface perpendicular to Cu substrate and intermesh with each other to form continuous porous film. Thus immersing a piece of copper substrate into hot NaOH solutions leads to the formation of 3D structure on its surface.

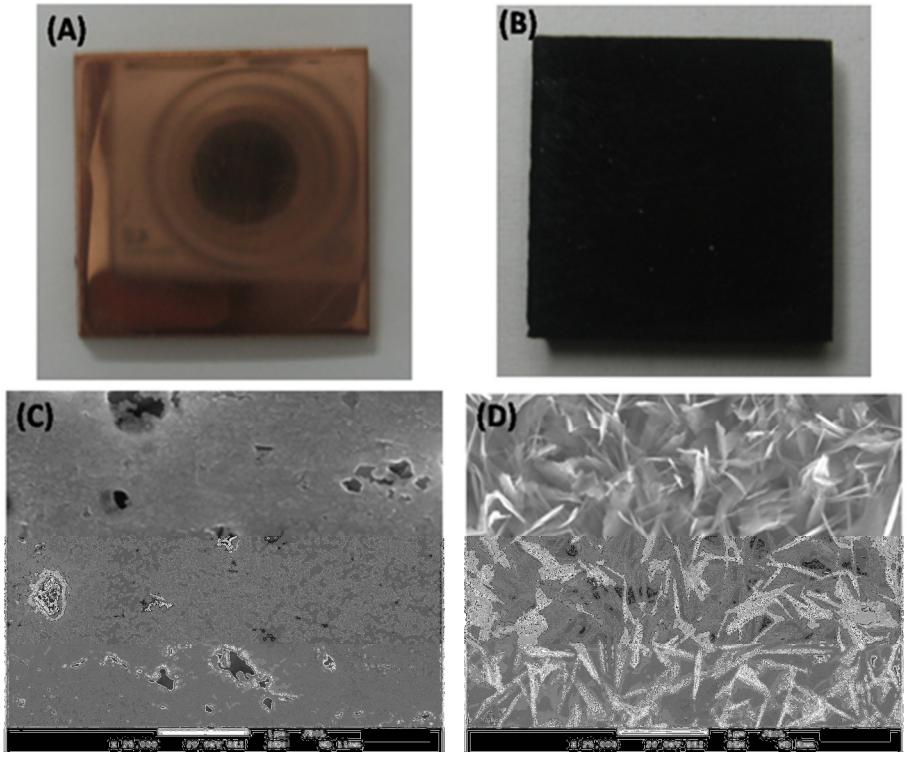

Figure A6: Digital photographs of copper substrate (A) before and (B) after formation of coppe oxide. SEM images of copper substrate (C) before and (D) after formation of copper oxide at 25000 X.

The SEM images of surface texture obtained at different magnification for copper oxide surface is shown in Figure A7. At low magnification 2D nanosheets with quite

uniform distribution is observed. However at high magnification one can clearly see the nano-petal like structure where at some places these 2D nano-petals self-assemble into 3D flowerlike architectures with their long axes pointing toward a common center. Significant importance of such kind of surface is given by the gaps between nano-petals which vary from 1-2 microns to 50-100 nm. Thus it is able to cause the surface texture effect for higher absorption in which surface irregularities such as grooves and pores with dimensions large as compared to the wavelength of the incident radiation simply increase the solar absorbance by multiple reflections. In the present case, for visible wavelengths which are small compared to the actual gaps between the nano-petals, the surface looks rough and radiation may be trapped through multiple forward reflections and partial absorptions in the micro-cavities.

The above results shows that the high absorption of the incident radiation is due to the combined effect of black colored nature of copper oxide and the texturing effect on the surface which arises by the formation 3D structure with the cavities in the range of

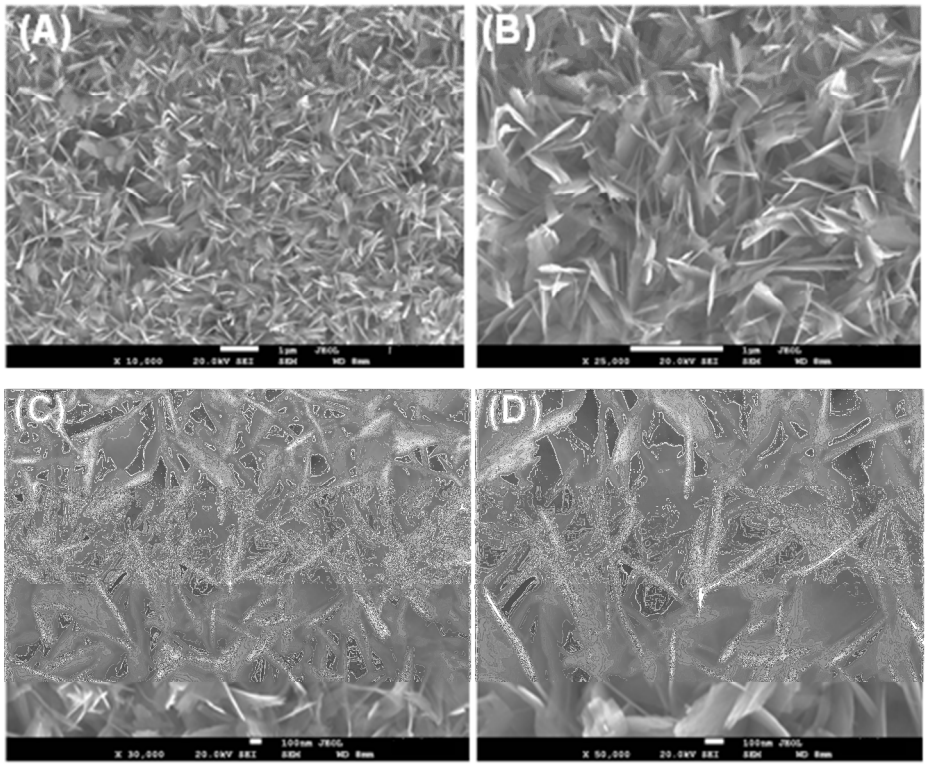

Figure A7: SEM micrographs of copper oxide surface at different magnification (A)10,000 X, (B) 25,000 X (C) 30,000 X and (D) 50,000 X.. The withe burs under the images indicate a 100 nm length.

incident wavelengths.

EDS spectrum (Figure A8) obtained from the surface of the copper oxide shows presence of some impurities (Si, C, and Ca) in addition with copper and oxygen. The atomic percentage of each element is summarized in Table A1. The atomic percentage of copper and oxygen showed nearly similar values indicating the formation of CuO phase which is confirmed by structural characterization. Silicon and carbon are present in the copper substrate while the presence of calcium was really surprising because none of the chemical used during the cleaning or oxidation treatment contains calcium. However the amount of calcium is quite low to affect the absorption properties of the copper oxide. This calcium is present in form of loose particles on the surface (Figure A9) which can be removed by proper rinsing or cleaning in distilled water. An XRD spectrum presented in Figure A 10 clearly shows the intense peak of Cu substrate in addition with low intensity peaks of CuO phase. Single peak of $CaCO_3$ is also observed in the spectra indicating the presence of $CaCO_3$ particles on the surface of the copper oxide

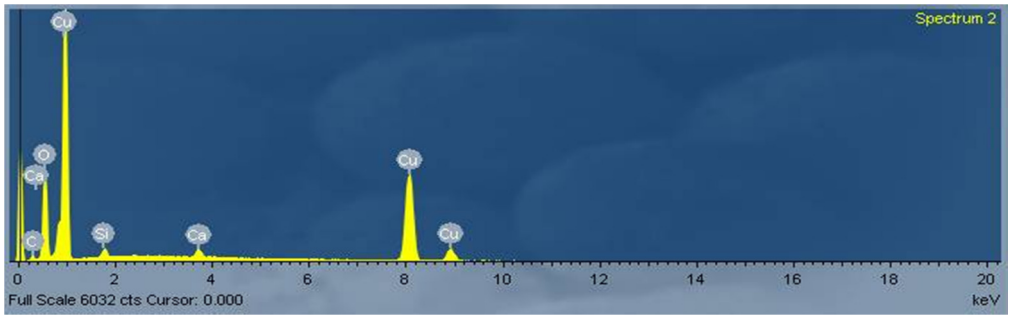

Figure A8: elemental composition plot of the copper oxide surface obtained by EDS measurement.

Element	At%
Cu	43.09
O	44.87
Ca	1.01
Si	1.34
C	9.69

Table A1: elemental composition plot of the copper oxide surface obtained by EDS measurement.

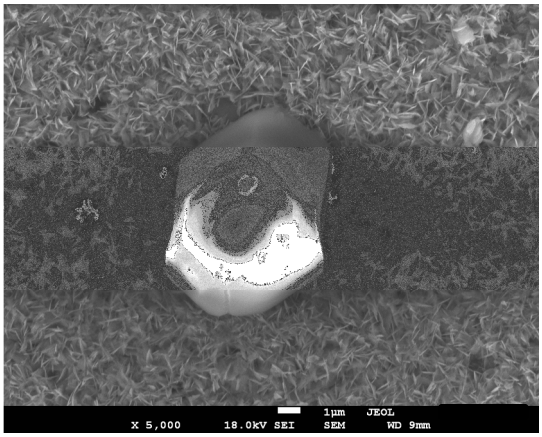

Figure A9: SEM micrographs of copper oxide surface with calcium particle.

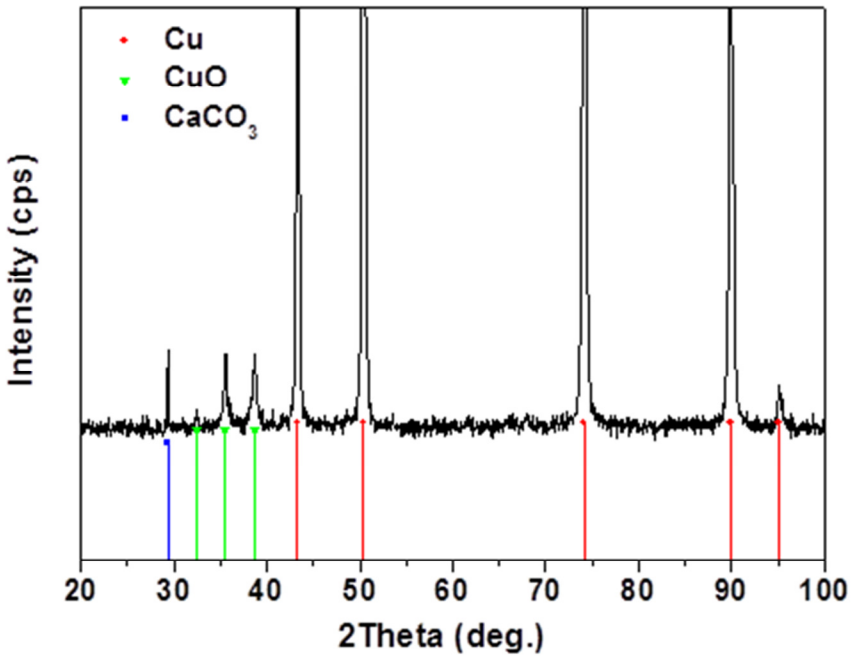

Figure A10: XRD spectra of the copper oxide samples synthesized by chemical conversion method.

Appendix C

Deposition of AlN films on Cu substrate

There are several oxides and nitrides which have low electrical conductivity and at the same time are thermal conductors, as it has been shown in Chapter 7, Section 7.4. We have chosen AlN was because it has the highest thermal conductivity among other materials (except for DLC), and we used chose RF sputtering technique as it is the best technique of deposition for electrically insulating targets.

AlN films were deposited using two different target materials namely AlN and Al. During deposition the base vacuum was 4x 10^{-7} mbar. Deposition temperature range was 150 to 200 °C. Deposition time was 2-3 hours and the average thickness ranged from 1.5 to 2.2 microns.The observations are as follows.

AlN Films deposited using AlN target:

In order to improve bonding with Cu substrate a layer of Al (100 nm) was deposited prior to AlN.

1) Deposited films were white / transparent in color when a gas mixture of Ar+N_2 was used during sputtering. N_2 was used in order to achieve reactive sputtering which helps in deposition of stoichometric nitride films. The XRD analysis showed formation of AlN films with (002) as preferred orientation.
2) The film thickness was lowered (1.2 to 1.6 microns) as compared to those deposited using Al target. Films with higher thickness showed cracking due to compressive stresses.
3) In SEM analysis film surface showed a globular pattern (Figure A11 and A12). In cross section the film appears to have a column like growth.
4) Films deposited on Si showed almost no porosity. Films deposited on copper

showed pore formation on the surface (Figure A14). EDS analysis showed that some of these pores were throughout the film thickness, i.e. substrate was exposed. These pores act as short circuit path when a conducting layer is deposited on top of AlN.

5) Films deposited using a substrate bias of 20 W/ -50 V showed cracking due to generation of compressive stresses (Figure A13).
6) AlN films deposited using only Ar were Violet / Black in color and showed (110) orientation in XRD analysis.

AlN Films deposited using Al target

In order to improve bonding with Cu substrate a layer of Al (100 nm) was deposited prior to AlN deposition. For AlN film deposition gas mixture of $Ar+N_2$ was used. Deposition temperature was 150-200^{0}C.

1) Deposited films were violet / black in color. The XRD analysis showed formation of AlN with (002) as preferred orientation.
2) The film thickness was higher (1.8 to 2.2 microns) as compared to those deposited using AlN target.
3) In SEM analysis film surface showed a globular pattern. In cross section the film appears to have a column like growth.
4) Films deposited on Si showed almost no porosity. Films deposited on copper showed pore formation on the surface. EDS analysis showed that some of these pores were throughout the film thickness, i.e. substrate or Al inter layer was exposed. These pores act as short circuit path when a conducting layer is deposited on top of AlN.
5) Films deposited using a substrate bias of 20 W/ -50 V showed cracking due to generation of compressive stresses.

Films deposited on copper showed porosity. It was observed that copper substrate (commercial grad) shows porosity after polishing. This could be one of the reasons resulting into film porosity. Deposition carried out using Cu gasket (OFHC grade copper) showed no sign of porosity (Figure A15). We did some test deposition using

OFHC copper block but film deposited on this substrate showed some porosity which resulted in short circuit after Ag coating. The coating thickness was about 1.3 microns. We need to deposit a thicker layer in order to eliminate the coating porosity. Thicker AlN layer due to its compressive stresses causes cracks or coating peeling off (Figure A16). If we are able to control the stresses using some technique like substrate bias voltage we can deposit thicker layer of AlN. Other option could be to deposit other oxide / nitride films which have lower thermal conductivity but can have higher thickness.

XRD analysis of AlN coating deposited under various deposition conditions

The samples were deposited at various percentages of N_2 (Spectrum a: 0 %, b: 25 %, c: 50 %, d: 75 %). In Figure A17 the spectra show films with well-defined crystal peaks. The spectra indicates that at higher nitrogen % the films have (002) as preferred orientation (which has lower stress level) and these films are visibly transparent.

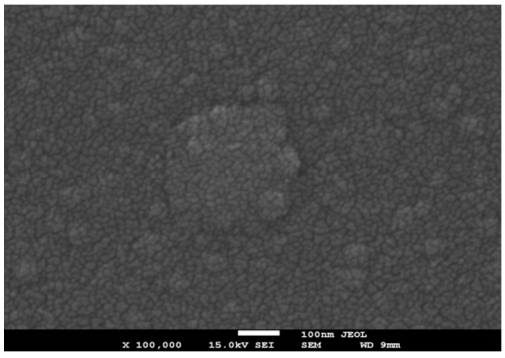

Figure A11: AlN deposited on Si showing globular pattern.

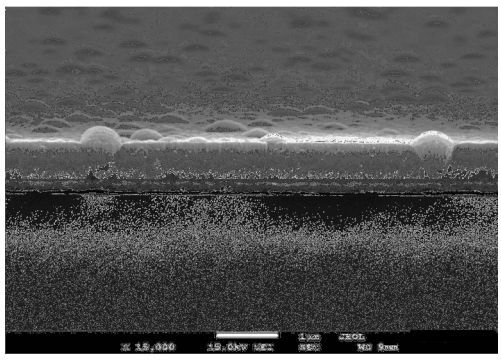

Figure A12: AlN deposited on Silicon cross section view.

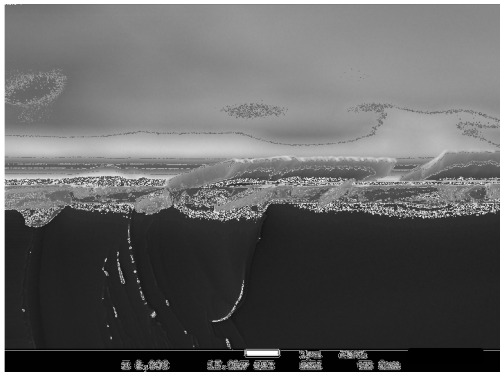

Figure A13: AlN deposited on copper with bias voltage. The crack due to stress is shown.

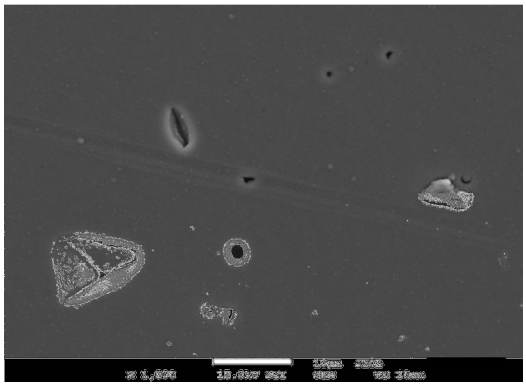

Figure A14: pores on the AlN film deposited on copper.

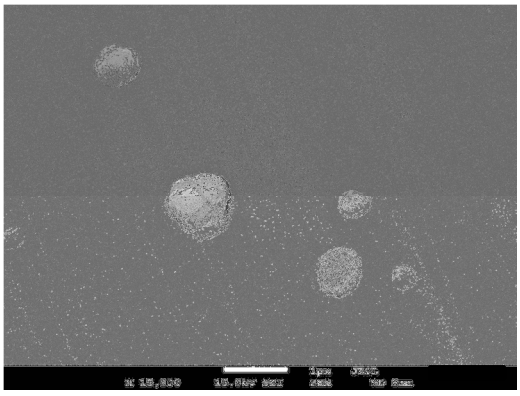

Figure A15: surface of Cu gasket coated with AlN.

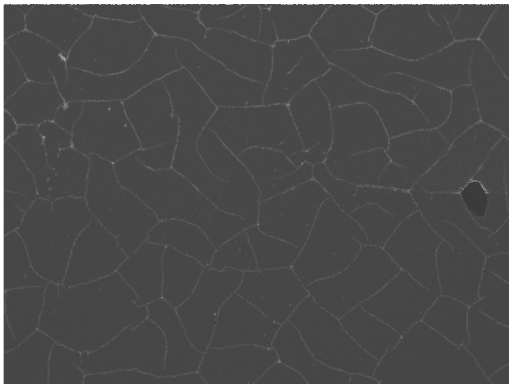

Figure A16: thicker (3.0 microns) AlN coating on Si showing cracks.

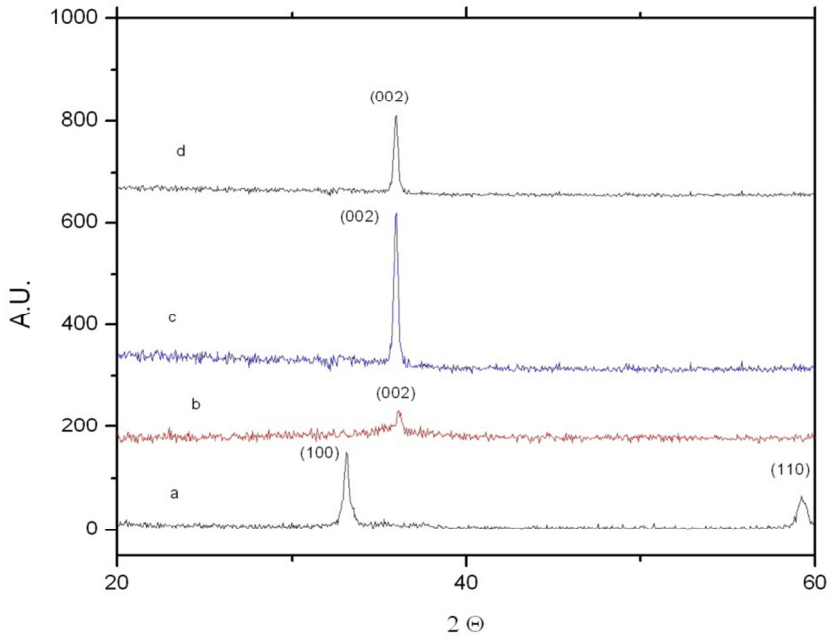

Figure A17: XRD spectra for AlN deposited on Cu at different N_2 concentration..

Appendix D

Maximization of efficiency for the 2nd type of connection

A procedure to maximize the power transfer efficiency of a series array of N cells, 2nd type connected, is developed. In 2nd type connection each cell is connected in parallel with the output of a DC-DC converter module and each sub element 'cell/DC-DC converter' is connected in series with the others (see Fig. 4). The current I flowing in the circuit can be written as $I = I_{OUT} + I_{C,J}$, where I_{OUT} is the output current of the DC-DC converter in parallel with the cell j and $I_{C,J}$ is the output current of the cell J. The DC-DC converter output currents must be greater than zero because of the DC-DC converter modules can't absorb current and, as a consequence, the minimum current that can flow in the circuit is $I = I_{C,k}$ where $I_{C,k}$ is the maximum current produced by one of the N cells ($I_{C,k}$= max$\{I_{C,J}\}$). We suppose that the CPV is working in the operative condition σ that establishes the I-V curves of the cells. As said in Chapter 5 (Paragraph 5.5.3), it is possible to impose the working point of each cell by setting the relative DC-DC converter output voltage. The maximization procedure starts by forcing each cell to its MMP and the current flowing in the circuit to its minimum value. That is, the cells are forced to the set of working points, $I^* = \{V_{MPPj,\sigma}\,,\ I_{MPPj,\sigma}\}$ while the minimum current $I_\sigma = \max\{I_{MPPj,\sigma}\}$ can be fixed by setting the voltage on the load $V_0\,(I)$ at the value $V_0\,(I_\sigma)$. The output voltage on the load can be varied by changing the output voltage V_L of the DC-DC converter L: $V_0\,(I) = V_{L\sigma} + \sum_{i=1}^{N} V_{MPPj,\sigma}$.

In the following we assume:

i) the voltage-current relation of the load to be monotonic, i.e. when the absorbed current increases, the voltage load increases and conversely. For

example, this assumption is true for a resistor or for a battery at each charging time.

ii) monotonic behavior of the I-V curves of the cells, i.e. if the current of the cell increases then the voltage of the cell decreases and conversely.

Using Equation 5.37 the power transfer efficiency relative to the set of working points I* and to the minimum current reads:

$$\varepsilon_{T(\sigma,I^*)} = \frac{\sum_{j=1}^{M} P_{Mj,\sigma}}{\varepsilon_A \cdot P_{MAX,\sigma}} + \frac{\sum_{j=M}^{N} P_{Mj,\sigma}}{\varepsilon_A \cdot P_{MAX,\sigma}} - I_\sigma \cdot V_0(I_\sigma) \cdot \frac{(1-\varepsilon_A)}{\varepsilon_A \cdot P_{MAX,\sigma}} \qquad \text{(D.1)}$$

where $P_{MAX,\sigma}$ is the maximum electrical power of the array and $P_{Mj,\sigma}$ is the electrical power of the cell *j* at its *MPP*. In Equation D.1. the *M* (*M* < *N*) cells that determine the current flowing in the circuit ($I_\sigma = I_{MPPj,\sigma}$ with $j \in M$) and of the *N* - *M* cells that produce a lower amount of current ($I_\sigma > I_{MPPj,\sigma}$) with $k \in$ (*N* - *M*) have been separated in two first terms.

Some observation can be done regarding Equation D.1:

1. Any change of one (or more) of the *N-M* cells working points, with respect to the set I^*, causes a decrease of the second term in Equation D.1. This is because the electrical power of the cell after any change of its working point is lower than the electrical power in its *MPP*. Thus power transfer efficiency $\varepsilon_{T(\sigma,I^*)}$ decreases. The 1st and the 3rd terms are unaffected because they depend by the *M* cells only.
2. Any change of one (only one) of the *M* cells working points decreases $\varepsilon_{T(\sigma,I^*)}$. In fact, for any voltage output of the cell different from $V_{MPPj,\sigma}$, the first term in Equation D.1 decreases, because the electrical power of the cell is lower than the electrical power in its *MPP*. Second term in Equation D.1 is unaffected because it is dependent by the *N* - *M* cells only. Third term is unaffected if the value of the voltage output imposed on the cell is greater than $V_{MPPj,\sigma}$ because I_σ is unaffected. The third term decreases if the value of the voltage output imposed on the cell is lower than $V_{MPPj,\sigma}$: in this case the output current of the cell will be greater than $I_\sigma = I_{MPPj,\sigma}$ (see point ii)), thus the minimum current flowing in the circuit ($I_\sigma = \max\{I_{Cj}\}$) and the voltage value on the load will

result increased (see point i), and consequently third term will decrease.

Resuming points 1 and 2: any change of one (or more) of the N - M cells working points or any change of one (only one) of the M cells working points causes a decrease of the power transfer efficiency $\varepsilon_{T(\sigma,I^*)}$.

3. The set of the working points I^* can be changed by increasing all the voltages output of the M cells in such a way that all the output currents of the M cells result to be equal. This causes the decrease of the minimum current that can flow in the circuit (see point ii) and the decrease of the voltage value on the load (see point i), then third term increases. First term decreases because of the sum of the electrical powers of the M cells is lower than the sum of the maximum electrical powers of the M cells. 2nd term is unaffected.
4. The set of the working points I^* can be changed by decreasing all the voltages output of the M cells but in this case 1st term decreases because of the sum of the electrical powers of the M cells is lower than the sum of the maximum electrical powers of the M cells and third term decreases because of the minimum current flowing in the circuit and the voltage value on the load increase.

In conclusion, starting by the power transfer efficiency $\varepsilon_{T(\sigma,I^*)}$, any change of the set of working points I^*, except that in point 3, implies a decrease of the power transfer efficiency. Conversely, acting as described in point 3, both decrease or increase are possible.

After having measured the I-V curve of each cell in an operative condition and from previous observations, maximum power transfer efficiency $\varepsilon_{T(\sigma,C_{MAX})}$, of a N series array can be found. C_{MAX} will be the set of working points that in the operative condition maximizes the power transfer efficiency.

For the maximization procedure the following steps can be done by using a computer:

a. calculate $\varepsilon_{T(\sigma,I^*)}$;
b. calculate the power transfer efficiency after an increasing of the voltages of the M cells.

If, after the point b, the power transfer efficiency results to be lower than $\varepsilon_{T(\sigma,I^*)}$ then $\varepsilon_{T(\sigma,I^*)}$ is the maximum power transfer efficiency, because any other change of the set of working points I^* decreases the power transfer efficiency (see points 1, 2, 3, 4). In this case the configuration $C_{MAX} = \{V_{MPPj,\sigma}\,,\ I_{MPPj,\sigma}\}$ and the value used for $V_{L,\sigma}$ is the configuration that maximizes the transferred power efficiency.

If, after the point b, the power transfer efficiency results to be greater than $\varepsilon_{T(\sigma,I^*)}$, then the point b must be repeated until on obtains $\varepsilon_{T(\sigma,I^{k+1})} < \varepsilon_{T(\sigma,I^k)}$ where the superscript k stands for the number of times that the point b has been repeated. In this case the configuration $C_{MAX} = I^k$ and the value used for $V_{L,\sigma}$ is the configuration that maximizes the transferred power efficiency and $\varepsilon_{T(\sigma,I^k)}$ is the maximum power transfer efficiency. After the maximization procedure, the voltages configuration C_{MAX}must be imposed to the cells by setting the DC-DC converters output voltages.

Bibliography

Antonini, A. Flat facetted PV concentrator systems and dichroic evolution. PhD thesis, Ferrara, Italy, 2006.

Algora, C., Minano, J.C., Benıtez, P., Rey-Stolle, I., Alvarez, J.L., Dıaz, V., Hernandez, M., Orti, E., Munoz, F., Pena, R., Mohedano, R., Luque, A., Smekens, G., de Villers, T., Andreev, V., Khvostikov, V., Rumiantsev, V., Schvartz, M., Nather, H., Viehmann, K., Saveliev, S. Proc 16th EPSEC, 2241-2244, 2000.

Algora, C. Concentrator photovoltaics. Springer, Heidelberg, 2007.

Anton, I., Solar, R., Sala, G., Pachon, D. IV testing of concentration modules and cells with non-uniform light patterns. Proc. 17th EPSEC, 611-614, 2001.

ASTM G173-03. Standard Tables for Reference Solar Spectral Irradiances: Direct Normal and Hemispherical on 37° Tilted Surface, American Society for Testing and Materials, 2003.

Boes, E. Photovoltaic Concentrators. Proc. IEEE Photovoltaic Specialists Conference, 944-951, 1980.

Bedair, S., Lamorte, M.F., Hauser, J.R. Appl. Phys. Lett., 34:38–40, 1979.

Bertness, K.A., Kurtz, S.A., Friedman, D.J., Kibbler, A.E., Kramer, C., Olson, J.M. App. Phys. Lett., 65:989–991, 1994.

Bett, A.W., Baur, C., Lerchenmuller, H., Siefer, G., Dimroth, F. Fraunhofer Institute

for Solar Energy Systems. The FLATCON concentrator PV technology. International Conference on Solar Concentrators for the Generation of Electricity or Hydrogen; 2005.

Bettonte, M., Brusa, R.S., Miotello, A. Solar Concentrator, method and equipement for its achievement. PCT/EP2007/011181. Available from: http://www.sumobrain.com /patents/wipo/Solar-concentrator-method-equipment-its/WO2008074485A1.pdf, 2007.

Brunelli, D., Moser, C., Thiele, L. Design of a Solar-Harvesting Circuit for Batteryless Embedded Systems. IEEE Transaction on circuits and systems. 56, N. 11, 2519-2528, 2009.

Buck, R., Brauning, T., Denk, T., Pfander, M., Schwarzbozl, P., Tellez, F. Solar-hybrid gas turbine-based power tower systems (REFOS). Trans. ASME J. Sol. Energy Eng. 124, 2–9. 2002.

Burgess, E.L., Pritchard, D.A. Performance of a one kilowatt concentrator array utilizing active cooling. Proc. 13th IEEE Photovoltaic Specialists Conf. (New York), 1121‑1124, 1978.

Cengel, Y. A. Heat transfer and mass transfer: a practical approach. Vol. 32. McGraw-Hill, 2006.

Chong, K. K., Yew, T.K., Wong, C.W., Lau, S. Study of image quality of mirror via solar flux distribution measurement using a high speed optical scanner. Applied Optics, Vol. 50, N. 25, 2011.

Cotal, H., Fetzer, C., Boisvert, J., Kinsey, G., King, R., Hebert, P., Yoon, H., Karam, N. Energy Environ. Sci. 2, 174–192, 2009.

Cotal, H., Frost, J. Heat transfer modeling of concentrator multijunction solar cell assemblies using finite difference techniques. Proc. 35th IEEE Photovolt. Spec. Conf.,

2010, 000213–000218, 2010.

Duquenne, C., Besland, M.P., Tessier, P.Y., Gautron, E., Scudeller, Y., Averty, D. Thermal conductivity of aluminium nitride thin films prepared by reactive magnetron sputtering. J. Phys. D: Appl. Phys. 45, 015301, 2012.

Ferrier, A., Rivoire, B. An instrument for measuring concentrated solar radiation: a photo-sensor interfaced with an integrating sphere. Solar Energy 72, 187–193, 2002.

Fraunhofer ISE. World Record: 41.1% efficiency reached for multi-junction solar cells at Fraunhofer ISE. Press release, January 2009.

Friedman, D., Kurtz, S.A., Bertness, K.A., Kibbler, A.E., Kramer, C., Olson, J.M, King, D.L., Hansen, B.R. Accelerated publication 30.2% efficient GaInP/GaAs monolithic two-terminal tandem concentrator cell. Prog. Photovolt.: Res. Appl., 3:47–50, 1995.

Friedman, D.J.. Proc. 25th NREL Photovoltaic Specialists Conference, 89‑92, 1996.

Gill, S.R., Plunkett, J.D. Fabrication of Four Focusing Solar Collector Segments of Widely Differing Geometries From Fiber-Reinforced Polymer Honeycomb Composite Panels. Final Report Submitted to Sandia National Laboratories, Albuquerque, NM, 1997.

Garboushian, V. A Novel High Concentration PV Technology for Cost Competitive Utility Bulk Power Generation. First World Conference on Photovoltaic Energy Conversion ,Hawaii, 1994.

Gardon, R. An instrument for the direct measurement of intense thermal radiation. Rev. Sci. Instrum. 24, 366–370, 1953.

Gray, L. J. Handbook of photovoltaic science and engineering, Chapter 3. John Wiley & Sons Ltd, Chichester, West Sussex PO19 8SQ, England, 2003.

Green, M. Solar Cells: Operating Principles, Technology, and System applications, Prentice Hall, Englewood Cliffs, NJ, 1–12, 1982.

Guven, H.M., Bannerot, R.B. Derivation of Universal Error Parameters for Comprehensive Optical Analysis of Parabolic Troughs. Proceedings of the ASME - ASES Solar Energy Conference, Knoxville TN, 1985.

Guven H.M. and Bannerot R.B. Determination of Error Tolerances for the Optical Design of Parabolic Troughs for Developing Countries, Solar Energy, no. 36, pp. 535-550, 1986.

Harman, G. Wire Bonding in Microelectronics Materials, Processes, Reliability, and Yield. 2nd edition, McGraw-Hill, New York, 1997.

Hazlehurst, A. Economic Analysis of Solar Power: Achieving Grid Parity http://energyseminar.stanford.edu/sites/all/files/eventpdf/AHazlehurst_Solar%20Economics_102809.pdf

Henry, C. J. Appl. Phys., 51:4494‑4450, 1980. King, R.R., Law, D.C., Edmonson, K.M., Fetzer, C.M., Kinsey, G.S., Yoon, H., Sherif, R.A., Karam, N.A. App. Phys. Lett., 90, 183516, 2007.

Hodgin, M. J., Estes, R.H. Advanced boron nitride epoxy formulations excel in thermal management applications. Proceedings of the Technical Programs, NEPCON WEST 1999 Conference, Feb 23–25th, 359-366, Anaheim, CA,1999.

Hua, C., Shen, C. Study of maximum power tracking techniques and control of dc-dc converters for photovoltaic power system, Proc. 29th Annu. IEEE PESC. 1, 86–93, 1998.

Jaus, J., Fleischfresser, U., Peharz, G., Dimroth, F., Lerchenmüller, H., Bett, A. Heat Sink Substrates for Automated Assembly of Concentrator Modules. Proceedings of the 21st European Photovoltaic Solar Energy Conference, Dresden, Germany, 2120-2123, 2006.

Johnston, G., Lovergrove, K., Luzzi, K. Optical performance of spherical reflecting elements for use with paraboloidal dish concentrator. Solar Energy 74,133-140, 2003.

Jeffery L. Gray *Handbook of Photovoltaic Science and Engineering*. Chap 3. Edited by A. Luque and S. Hegedus. John Wiley & Sons, Ltd, 2003.

Johnston, G. Focal region measurements of the 20 m^2 tilted dish at the Australian National University. Solar Energy Vol. 63, No. 2, 117–124, 1998.

King, D. L., Dudley, J. K., Boyson, W. E. PVSIM: A Simulation Program for Photovoltaic Cells, Modules, and Arrays. Proceedings of the 25th IEEE PVSC, Washington, DC, May 13-17, 1996.

King, R.R. Ultra-High Efficiency Multijunction Cell and Receiver Module,
Phase 1B: High Performance PV Exploring and Accelerating Ultimate Pathways. NREL Final Subcontract Report, 2008.

Kinsey, G. S., Pien, P., Hebert, P., Sherif, R.A. Operating characteristics of multijunction solar cells. Solar Energy Materials & Solar Cells 93, 950–951, 2009.

Koutroulis, E., Kalaitzakis, K. Development of a Microcontroller-Based, Photovoltaic Maximum Power Point Tracking Control System. IEEE Transaction on power electronics, 16, N.1, 46-54, 2001.

Kreske, K. Optical design of a solar flux homogenizer for concentrator photovoltaics. Applied Optics Vol. 41, N. 10, 2002.

Kurtz, S., Faine, P., Olson, J., 1990. Modeling of two-junction, series-connected tandem solar cells using top-cell thickness as an adjustable parameter. J. Appl. Phys. 68, 1980.

Kurtz, S. Opportunities and Challenges for Development of a Mature Concentrating Photovoltaic Power Industry. Technical Report NREL/TP-5200-43208, November 2012.

Kussul, E., Baidyk, T., et al. Flat Facet Parabolic Solar Concentrators with support cell for one and more mirrors. WSEAS TRANSACTIONS on POWER SYSTEM 8,577-586, 2008.

Lathrop, R.R. Defining Solder Paste Performance via Novel Quantitative Methods, Apex Proceedings, Anaheim CA, 2003.

Mokri, A., Emziane, M. Concentrator photovoltaic technologies and market: a critical review. World Renewable Energy Congress 2011, 8-13 May, Linkoping, Sweden, 2011.

Law, D.C., King, R.R., Yoon, H. Future technology pathways of terrestrial III‑V multijunction solar cells for concentrator photovoltaic systems. Solar Energy Materials & Solar Cells July, 2008.

Lovegrove, K, Burgess, G, McCready, D, Pye, J. ANU's new 500 m^2 paraboloidal dish solar concentrator, LSAA Conference, 2009.

Lovegrove, K., Burgess, G., Pye J., 2011. A new 500 m^2 parabolic dish solar concentrator. Solar Energy 85, 620, 2011.

Masafumi, Y, Ken-Ichi N, Takuo S. Novel materials for high efficiency III‑V multi-junction solar cells. Solar Energy 82:173‑80, 2008.

Meyen, S., Lüpfert, E., Pernpeintner, J., Fend, T. Optical Characterization of Reflector Material for Concentrating Solar Power Technology. SolarPaces Conference, 2009.

Meyer, E.L., Van Dyk, E.E. Assessing the reliability and degradation of photovoltaic module performance parameters. IEEE Transactions on Reliability 53, 83-92, 2004.

Minuto, A., Timò, G., Groppelli, P., Sturm, M. Concentrating photovoltaic multijunction (CPVM) module electrical layout optimisation by a new theoretical and experimental " mismatch" analysis including series resistance effects. Photovoltaic Specialists Conference (PVSC), 35th IEEE. 3081–3086, 2010.

Nelson, J. The Physics of Solar Cells Imperial College Press, London, 2003.

Nishioka, K., Takamoto, T., Agui, T., Kaneiwa, M., Uraoka, Y., Fuyuki, T. Annual output estimation of concentrator photovoltaic systems using high-efficiency InGaP/InGaAs/Ge triple-junction solar cells based on experimental solar cell's characteristics and field-test meteorological data, Solar Energy Mater. Solar Cell 90 (1) 57–67, 2006.

NREL Final Report. Solar Thermal Component Manufacturing for Near-Term Markets. Subcontract ZAP-5-15299-02, Golden, CO, 1998.

Nurmi, S., Sundelin, J., Ristolainen, E., Lepisto, L. The effect of solder paste composition on the reliability of SnAgCu joints. Microelectron Reliability 44, 485–494, 2004.

Olson, J.M., Friedman, D.J., Kurtz, S. Handbook of photovoltaic science and engineering, Chapter 9. John Wiley & Sons Chichester, West Sussex PO19 8SQ, England, 2003.

Overstraeten, R.J., Mertens, R.P. Physics, Technology and Use of Photovoltaics. Adam Hilger, Bristol, 1986.

Parretta, A., Privato, C., Nenna, G., Antonini, A., Stefancich, M. Monitoring of concentrated radiation beam for photovoltaic and thermal solar energy conversion applications. Appl. Opt. 45, 7885–7897, 2006.

Pérez-Higueras, P., Munoz, E., Almonacid, G., Vidal, P.G. High Concentrator PhotoVoltaics efficiencies: Present status and forecast. Renewable and Sustainable Energy Reviews 15, 1810–1815, 2011.

Pettit, R.B. Characterizing Solar Mirror Materials Using Portable Reflectometer. Sandia Report, Albuquerque, SAND 82-1714, 1982.

Photon International. A Complicated Hybrid., p. 158, June 2008.

Photon International. Market survey on concentrating PV, p.146. November 2008.

Poullikkas, A., Kourtis, G., Hadjipaschalis, I. Parametric analysis for the installation of solar dish technologies in Mediterranean regions. Renewable and Sustainable Energy Reviews 14, 2772–2783, 2010.

Rey-Stolle, I., Algora, C. Analysis of Wirebonding Techniques for Contacting High Concentrator Solar Cells. IEEE transaction on advanced packaging, Vol. 26, No. 1, 2003.

Ries, H., Gordon, J.M., Lasken, M. High flux photovoltaic solar concentrator with kaleidoscope-based optical. Solar Energy. Vol. 60, N. 1, 11-16, 1997.

Sala, G., Antòn, I. Handbook of photovoltaic science and engineering, Chapter 10. Edited by A. Luque and S. Hegedus, John Wiley & Sons Ltd, Chichester, West Sussex PO19 8SQ, England, 2011.

Salemi, A., Eccher, M., Miotello, M., Brusa, R.S. Dense array connections for

photovoltaic systems in concentration. Progress in Photovoltaics: Research and Applications 19, 4, 379–390, 2011.

Shamsa, M., Liu, W.L., Balandin, A.A., Casiraghi, C., Milne, W., Ferrari, A.C. Thermal conductivity of diamond-like carbon films. Applied Physics Letters 89, 161921, 2006.

Siefer, G., Abbott, P., Baur1, L., Schleg, C.T., Bett, A.W. Determination of the temperature coefficient of various III-V solar cells. Proceedings of 20th European Photovoltaic Solar Energy Conference, 6–10 June, Barcelona, Spain, 2005.

Siegel, R., Howell, J. Thermal Radiation Heat Transfer, 4th edition, Taylor & Francis, New York, 2002.

Sodha, M.S., Mathur, S.S., Malik, M.A.S. Review of Renewables Energy Resources, Vol.2, Wiley Eastern Ltd, 1984.

Spectrolab link (http://www.spectrolab.com/DataSheets/TerCel/C1MJ_CDO-100.pdf), 2010.

Stam, F.A., Davitt, E. Effects of thermomechanical cycling on lead and lead-free (SnPg and SnAgSu) surface mount solder joints. Microelectron Reliability 41, 1815–1822, 2001.

Stringfellow, G. B. Organometallic Vapor-Phase Epitaxy. Academic Press, San Diego, 2nd edition, 1999.

Sze, S. Physics of Semiconductor Devices, 2nd Edition, John Wiley & Sons, New York, NY, 1981.

Timò, G., Minuto, A., Groppelli, P. and Sturm, M. Modelling and new Identification

procedures to evaluate concentrating photovoltaic multi-junction (MJ) module equivalent parameters and MJ-cells junction temperature in operative outdoor conditions**.** 25th Photovoltaic European Conference, 2010.

Touloukian, Y. Thermal radiative properties: metallic elements and alloys. IFI/Plenum, 1970.

Ulmer, S., Reinalter, W., Heller, P., Lupfert, E., and Martinez, D. Beam Characterization and Improvement With a Flux Mapping System for Dish Concentrators. J. Sol. Energy Eng., 124, 182–188., 2002.

Ulmer, S., Lupfert, E., Pfander, M., Buck, R. Calibration corrections of solar tower flux density measurements. Energy 29, 925–933, 2004.

Verlinden, P.J., Lewansdoswki, A., Kinsey, G.S., Sherif, R.A., Lasich, J.B. Performance and realiability of multi-junction III–V dense array modules for concentrator dish and central receiver applications. 4th IEEE World Conference on Photovoltaic Energy Conversion, Hawaii, USA, 2006.

Vivar, M., Anton, I. and Sala, G. Radial CPV receiver Prog. in Photovoltaics: Res. Appl. 18:353–362, 2010.

Yoon, S., Garboushian, V. Reduced temperature dependence of high concentration photovoltaic solar cell open circuit voltage (V_{oc}) at high concentration levels, 1st World Conference on Photovoltaic Energy Conversion, 1500–1504, 1994.

Walker, G.R., Sernia, P.C. Cascaded DC–DC Converter Connection of Photovoltaic Modules. IEEE Transaction on power electronics. 19, N. 4, 1130-1139, 2004.

SERI (Solar Energy Research Institute). Silver/Glass Mirrors for Thermal Systems. Report SERI/SP-271-2293. Solar Energy Research Institute, Golden, CO, 1985.

Stone, K.W., Radtke, C.W., Blackmon, J.B. Status of Glass Reflector Technology for Heliostats and Concentrators. Proceedings of the 28th Intersociety Energy Conversion Engineering Conference, Atlanta, GA, 1993.

Swanson, R. Handbook of photovoltaic science and engineering, Chapter 11. Edited by A. Luque and S. Hegedus, John Wiley & Sons Ltd, Chichester, West Sussex PO19 8SQ, England, 2003.

Verlinden, P., Sinton, R., Swanson, R., Crane, R. Single-Wafer Integrated 140 W Silicon Concentrator Module. Proc. IEEE Photovoltaic Specialists Conference, 739-743, 1991.

Zubi, G., Bernal-Agustın, J.L., Fracastoro, G.V. High concentration photovoltaic systems applying III-V cells. Renewable and Sustainable Energy Reviews 1, 2645-2652, 2009.

.

.